Dynamic analysis of a mechanical connection between an installation vessel and a floating offshore wind turbine

J.J.A Kortekaas

Technische Universiteit Delft

Dynamic analysis of a mechanical connection between an installation vessel and a floating support structure during the installation of a floating offshore wind turbine.

by

J.J.A Kortekaas

Master Thesis

in partial fulfilment of the requirements for the degree of

Master of Science
in Mechanical Engineering

at the Department of Maritime and Transport Technology
of Faculty Mechanical, Maritime and Materials Engineering
of Delft University of Technology

to be defended publicly on Thursday, June 22nd, 2023, at 14:30.

Student number:	4315871	
MSc track:	Multi-Machine Engineering	
Report number:	MME.2023.8819	
Thesis committee:	Dr. J. Jovanova,	TU Delft committee Chair, 3ME
	Dr. A. Grammatikopoulos,	TU Delft daily supervisor, 3ME
	Dr.ir. P.R. Wellens,	TU Delft committee member, 3ME
	ir. M. Stofregen,	Company Supervisor, Huisman (Huisman Equipment B.V.)
Project duration:	September 5, 2022 – June 22, 2023, 2023	

TU Delft

Preface

This report results from the final assignment fulfilling my master's degree in Mechanical Engineering at the Delft University of Technology, carried out in cooperation with Huisman Equipment in Schiedam.

When I was younger, I never exactly knew what I wanted to do, but I have always been fascinated by machines and technology. My decision to start mechanical engineering at the TU Delft was no surprise to the people around me, but there have been times I wondered if it was the right place for me. During my master, and especially during this project, I realised that I made the right decision to continue my studies at the university. This project and the activities of Huisman embody my interpretation of Mechanical Engineering, large equipment designed to perform tasks that will improve the world. I am very thankful to Huisman for allowing me to experience a more practical work environment and showing me how all learned theory is brought to practice. Special thanks go to my daily supervisors, Matthijs from Huisman and Apostolos from the TU Delft, their guidance and feedback have played a large role in the completion of this project.

I would also to thank the people close to me for their support during this project and my time spent in Delft. My parents and brother for always praising my determination and persistence throughout the duration of my studies. My girlfriend, Romy, for always supporting me in every way. And my friends for sharing the discussion on both this project and many other topics of common interest for a welcome distraction from time to time.

With my master's thesis now complete, I look forward to starting my career as an engineer.

J.J.A. Kortekaas
Schiedam, June 2023

Abstract

As the world's electricity consumption continues to rise, more countries realize the need for renewable energies. Not only to reduce carbon emissions but also to gain energy independence. Floating Offshore Wind (FOW) is seen as a solution to harvest wind energy in deeper oceans, reaching better wind speeds, and providing the option of installing wind energy in steep coastal areas. However, currently demonstrated installation methods are limited by their need for large fit-out ports, requiring large quay areas with strict requirements. Therefore, a way must be found to limit these motions to enable a safe, quick, and routine installation procedure.

Huisman has introduced the Windfarm Installation Vessel (WIV) as a complete solution to assemble and install offshore wind turbines at sea. Installing a floating wind turbine at sea brings two main challenges, the relative motions between the floating structures and the load transfer between the two floating structures. The proposed installation procedure considers a connection between the installation vessel and the floating support structure to reduce the relative motions and facilitate the load transfer. This research investigates how the connection's structural configuration affects the system's relative motions and loads. A two-dimensional multi-body model has been formulated considering a rigid link between the installation vessel and the floating support structure. The hydrodynamics of the floating structures and the regular wave loads on the structures are calculated using Ansys AQWA. A modular tool has been scripted using this model, which allows for a quick assessment of the structural configuration of the connection for the various wave loads. The tool includes options to change the system's parameters to vary the structural configuration of the connection. Other modelling elements that are included in the tool are ballast (transfer) and pre-tensions on the connection. The tool is used to investigate the performance of the connection between the installation vessel and a semi-submersible floating support structure during the offshore installation of the floating offshore wind turbine. The performance of the system during five discrete installation stages is investigated. The different installation stages cover varying amounts of ballast transfer, as well as the mating phase of the wind turbine. It has been shown that the ballast transfer mostly changes the static load on the connection, and the dynamic effects are minimal. A system analysis is performed considering the effect of adding stiffness in one direction of motion and the effect of adding coupled stiffnesses. The performance of different stiffness configurations is measured using the relative motions between the wind turbine mating point and the loads on the connection.

The free-floating relative response shows two peaks in the relative motions at 13 and 15 seconds. These peaks are caused by the pitch response of the floating support structure, also causing large relative surges and heave motions at the mating point. It is shown that the connection can subdue the dominant peak response at 13 seconds, but the peak in the pitch response at 15 seconds remains. The relative surge and heave motions can be minimized using the connection without excessive connection force. Overall, it can be concluded that a combination of stiffness in the different connection directions will provide the most favourable results. A different stiffness on both sides of the connection is also shown to improve the system's behaviour. However, further detailed analysis is required to find optimal stiffness values for the connection.

List of Figures

List of Tables

List of Abbreviations

CG Centre of Gravity. iii, 5, 6, 21, 23, 25–28, 30–34, 36–40, 42, 45, 46, 50, 55, 76, 77, 79
CPC Collective Pitch Control. 13

DOF Degrees-of-Freedom. iii, 5, 6, 21, 22, 25, 27, 29, 30, 34, 38, 40
DP Dynamic Positioning. 21, 39

EOM Equations of Motion. 28, 31–34, 45

FBD Free-Body Diagram. iii, 27, 30
FLNG Floating Liquefied Natural Gas. 20, 21
FOW Floating Offshore Wind. ii, 1–3, 7, 10, 11, 13, 14, 17, 18
FOWT Floating Offshore Wind Turbine. 1–5, 7, 10, 12–14, 16, 18, 19, 25
FWT Floating Wind Turbine. 2, 12, 13

GW gigawatt. 2

HAWT Horizontal Axis Wind Turbine. 10
HLV Heavy Lift Vessel. 16
HTV Heavy Transport Vessel. 14, 15

IPC Individual Pitch Control. 13

LCOE Levelised Cost of Energy. 15

MW megawatt. vi, 1, 2, 8, 10, 12, 13, 15, 16, 37, 38
MWh megawatt hour. 8

OWF Offshore Wind Farm. 7, 8, 10
OWT Offshore Wind Turbine. 1–3, 7–9, 17

RAO Response Amplitude Operator. iii, 23, 24, 39, 45
RLFB Rigid Link Flexible Boundaries. 25, 30, 31
RMFC Rigid Module Flexible Connector. 21, 30
RMS Root Mean Square. 76, 81
RNA Rotor-Nacelle Assembly. 17, 38

TLP Tension Leg Platform. 2, 11, 12, 14, 17, 83

VAWT Vertical Axis Wind Turbine. 10

VLFS Very Large Floating Structures. 20, 21

WIV Windfarm Installation Vessel. ii, 1, 3, 4, 6, 17, 20, 25, 35–41, 43, 81

WTG Wind Turbine Generator. 2–4, 8, 10, 13, 17

WTS Wind Turbine Shuttle. 3

Nomenclature

$\ddot{X}_i$	Acceleration state vector of body i.
$\ddot{x}_i$	Acceleration of mass i.
$\dot{X}_i$	Velocity state vector of body i.
$\dot{x}_i$	Velocity of mass i.
ω	Wave frequency.
ϕ	Phase shift.
$A_i(\omega)$	Added mass matrix of body i, dependent on wave frequency ω.
B_i	Damping matrix of body i.
$b_{i,ry}$	Damping constant of damping element i in pitch direction.
$b_{i,x}$	Damping constant of damping element i in surge direction.
$b_{i,z}$	Damping constant of damping element i in heave direction.
$b_{x,A}, b_{z,A}, b_{ry,A}$	Surge, Heave, and Pitch damping constant of connection side A.
$b_{x,B}, b_{z,B}, b_{ry,B}$	Surge, Heave, and Pitch damping constant of connection side B.
C_i	Stiffness/Restoring matrix of body i.
e	Spring elongation.
F	Force.
J_i	Inertia of body i.
k	Wave number.
$k_{i,ry}$	Stiffness constant of spring element i in pitch direction.
$k_{i,x}$	Stiffness constant of spring element i in surge direction.
$k_{i,z}$	Stiffness constant of spring element i in heave direction.
$k_{x,A}, k_{z,A}, k_{ry,A}$	Surge, Heave, and Pitch stiffness of connection side A.
$k_{x,B}, k_{z,B}, k_{ry,B}$	Surge, Heave, and Pitch stiffness of connection side B.
M_i	Mass matrix of body i.
m_i	Mass i.
t	Metric Ton (Tonne).
u_i	Displacement vector of body i.
X_i	Displacement state vector of body i.
x_i	Position of mass i.

Contents

1

Introduction

In the past decade, we have become increasingly aware of the necessity of replacing fossil fuels with renewable alternatives. The global movement towards the use of renewable energy is hindered mainly by the challenge of how to achieve enough capacity. Since the emergence of the first wind turbine generators, significant progress has been made. Wind energy is now seen as a serious contender for the generation of our increasing electricity demand. However, the growth rate is not nearly enough to meet the prospected targets. According to Global Wind Energy Council (2022), wind installations have to be scaled up four times this decade to get on track for a 1.5°C rise in global temperature. One of the contributing developments is Floating Offshore Wind (FOW), which has the potential to reach more constant wind resources in deeper waters and can be deployed at steep coastal areas, opening up at least four times the available ocean surface area compared to fixed-bottom offshore wind. Still, FOW is a relatively new technology of which only a few full-scale projects exist. Currently, demonstrated installation methods are restricted by their need for large quay areas with stringent requirements. To further commercialize floating offshore wind, a quick and reliable installation method must be realized to enable fast routine installations of Floating Offshore Wind Turbines (FOWT's). Huisman has presented the Windfarm Installation Vessel (WIV) as a solution to improve the installation of both fixed-bottom and floating Offshore Wind Turbines (OWT's). To overcome the existing challenges with the installation of FOWT's an in-situ installation method is proposed, meaning the wind turbine installation is performed at the wind farm location. Wind turbines will be assembled onboard, and installed with a single off-board lift, significantly reducing the complexity and the number of steps required to install an OWT. This thesis will describe the research done during a combined graduation assignment at the TU Delft and Huisman (Huisman Equipment B.V.). This research focuses on a connection between the installation vessel and a FOW support structure during the in-situ installation process of a FOWT. The following section will introduce the challenges of in-situ installation of FOW. Next, the problem will be discussed in more detail, and the research questions will be presented. This is followed by a brief description of the research methodology, and finally, the structure of the rest of the document will be explained.

1.1. In-Situ Installation of Floating Offshore Wind Turbines

The year 2009 marks the installation of the first full-scale FOWT, the Hywind Demo project consisted of a 2.3 MW turbine on a floating spar foundation. In 2017, Statoil's Hywind project had another world first, the Hywind Scotland floating wind farm was commissioned (Equinor, 2022a). Consisting of five 6 MW turbines, the wind farm has a total capacity of 30 MW, and since commissioning has been one of the best-performing wind farms in the UK (Equinor, 2021). The next floating wind farm to be commissioned was WindFloat Atlantic in 2019 (Principle Power, 2022c). This 25 MW wind farm consists of three 8.4 MW turbines on a semi-submersible support structure. The Hywind Scotland and WindFloat Atlantic wind farms are shown in Figure 1.1 a (Øyvind Gravås, 2017) and Figure 1.1 b (Principle Power, 2020) respectively. After these first projects, Principle Power and Equinor, have since expanded their portfolio and commissioned new wind farms. Currently, Equinor's Hywind Tampen is the largest wind farm in operation, consisting of 11 turbines with a total installed power of 88 MW (Equinor, 2022b). The successful operation of the first wind farms can be seen as a proof-of-concept and show that the tech-

(a) Hywind Scotland (Scotland) (b) Windfloat Atlantic (Portugal)

Figure 1.1: The Hywind Scotland (Øyvind Gravås, 2017) and Windfloat Atlantic (Principle Power, 2020) Floating Offshore Wind farms in operation.

nology has a promising future. However, it should be clear that FOW is still in its pre-commercial phase. This is reflected by the number of concepts still being published for floating support structures, indicating that industry standards have been set and possibilities remain open. Generally, these concepts can be divided into four main types: the spar, semi-submersible, barge, and the Tension Leg Platform (TLP) support structure. Of these, only the aforementioned spar and semi-submersible support structures are currently used in a commercial farm configuration. It is expected that the floating wind market will further develop and larger projects will start to emerge in the next decade (DNV, 2022). By 2050, floating offshore wind is projected to deliver around 250 gigawatt (GW) of wind energy (DNV, 2022). To put this number in perspective, around 250 Floating Wind Turbine (FWT) will have to be installed yearly, scaling up to around 600 15MW wind turbines each year to meet these projections. In contrast, currently, it took more than a year to install the eleven wind turbines of the Hywind Tampen wind farm. All demonstrated installation methods for FOWT's require the wind turbine to be installed at a quayside. However, there are certain limitations to the port-side assembly of floating offshore wind turbines. Since the Hywind Spar foundation has a draft of around 100m, suitable locations for the installation are hard to find and installations have only been carried out in deep water fjords in Norway. The WindFloat semi-submersible has a considerably lower draft of around 10-15m during installation, making it a more versatile option. Not only the draft, but other port requirements as well, such as load-bearing capacity, available equipment and staging area, are much more stringent than for use with typical cargo (Crowle and Thies, 2022). Currently, ports equipped with the right equipment and requirements are almost non-existent, and those that do exist (mainly in Europe) are mostly in use for the installation of fixed-bottom OWT's. A typical quayside floating wind turbine fit-out will take around ten days to complete (Crowle and Thies, 2021), and the limitations of wet-towing the completed assemblies (Ramachandran et al., 2022) restrict the allowable distance from the wind farm location. Considering these factors, huge investments are required to ready ports for the required installation capacity Since it is expected that floating wind will become a global market, many of these assembly ports will have to be constructed in various locations. Alternatively, in-situ installation methods, moving the installation of wind turbines away from assembly ports, could therefore prove to be a solution for further commercializing floating offshore wind. As is common with fixed-bottom offshore wind turbines, the support structure and wind turbine will be installed separately at the wind farm location. First, the floating support structure will be towed into place and connected to a mooring system. Next, an installation vessel will arrive with the wind turbine components or a completely assembled wind turbine. The wind turbine (components) will be lifted and mated with the floating support structure on open water. Various industry and research-based concepts have been presented, however, most lack advanced research and in-situ installation has not been demonstrated in practice yet. Since in-situ installation is a newly proposed installation method, various challenges can be identified for the in-situ installation of FOW. Similar to port-side installation, fabrication and transport of the support structures, mooring hook-up, electrical connections, and maintenance solutions are factors that still require further research. Due to the large size and weight, transportation of the support structures is a challenging operation. Installing the wind turbines at the wind farm location could, however, ease the process by only requiring a single transport from fabrication to the wind farm location. The main challenge of in-situ installation is the actual method of lifting the Wind Turbine Generator (WTG) (components) and the mating procedure to the floating support structure. Heavy lifting operations are common in the offshore domain. However, FOWT's pose unique challenges due to their shape and weight, and the repeatability of the operation. FOWT will have to be installed routinely every day, whereas most heavy lifting operations, in for example the oil and gas industry, are engineered single lifts with long preparation times. Therefore a robust solution has to be developed to ensure high workability of the installation procedure to enable operations in more severe weather conditions.

1.2. The Huisman Windfarm Installation Vessel (WIV)

The Huisman Windfarm Installation Vessel (WIV) has been introduced as a complete assembly and installation solution for OWT's. Huisman is a designer and manufacturer of large-scale equipment located in Schiedam, Netherlands. Established in 1929, Huisman has grown to be a leading manufacturer developing step-changing technical solutions with an extensive portfolio of cranes, offshore wind tools, pipelay and drilling equipment, as well as several special projects. Currently, a large focus is being put on the offshore wind market with projects covering large cranes for current generation jack-up vessels, motion-compensated pile grippers for the installation of monopile foundations and various other offshore wind tools. Other activities include concept designs for motion-compensated platforms, the Wind Turbine Shuttle (WTS) and its successor, the WIV. The WIV has been designed to be a versatile purpose-built vessel to improve the efficiency of offshore wind farm installation. Figure 1.2 shows a render of the Huisman WIV as envisioned during the installation of a FOWT onto a semi-submersible support structure.

Figure 1.2: Render showing the Huisman Windfarm Installation Vessel concept, pictured installing a wind turbine on a semi-submersible floating support structure

The semi-submersible installation vessel is designed with both fixed-bottom- and floating wind farms in mind, capable of assembling on board and installing WTG's in one piece as well as installing monopile foundations. The WTG's will be assembled onboard the vessel using multiple workstations to enable parallel assembly. By assembling the wind turbine on board, high workability can be achieved since there is no need to account for relative motions between the foundation and the vessel. The large installation tower can rotate around its base, making it possible to assemble a wind turbine on deck. At the same time, another is being installed onto a (floating) support structure using a full motion-compensated installation system. The vessel is capable of carrying ten mono-pile foundations and eight WTG's. An additional onboard crane allows using feeder vessels to supply additional components to the installation vessel, reducing logistics costs. The high versatility and usability make the WIV a viable and cost-effective installation method for FOW.

1.3. Problem Definition

The complete design of an installation vessel such as the Huisman WIV is an ambitious project with many challenging aspects. Since the span of a graduation project is only limited, the focus of this research will be on the system dynamics during the installation and mating procedure of the wind turbine. Even though years of experience exist in the field of offshore heavy lifting, wind turbines differ from typical offshore topsides being installed. Although the total mass might of a WTG be considered small compared to typical topsides, the shape and high centre of gravity make lifting operations considerably more challenging. Typical topside installations are highly engineered lifts, with ample preparation time and a potentially different approach for each project. The installation of FOWT's will have to be a routine operation, with minimal preparation time. It has been shown that the magnitude of the relative motion between the bottom of the wind turbine and the support structure is crucial for a successful mating of the wind turbine (Jiang et al., 2018a). Therefore, a way must be found to limit these motions to enable a safe, quick, and routine installation procedure. To achieve this, a mechanical connection between the installation vessel and the floating support structure is proposed to reduce the relative motions during the installation of the wind turbine. Since both the installation vessel as well as the support structure are floating, the coupled dynamics are complex. Multiple components are to be considered when looking at the system; a floating installation vessel (kept in position by a dynamic positioning system), the floating support structure (connected to a mooring system), the wind turbine to be installed, and a crane or installation tower that lifts the wind turbine. Another factor that is essential to the success of the mating procedure is the load transfer of the wind turbine between the installation vessel and the support structure. The weight of the wind turbine is significant enough to affect the hydrodynamic behaviour of the support structure highly. As a consequence, adjustments to the water ballast will have to be made to re-balance the support structure, an operation which can take up to several hours. Since the operation takes place in the open sea, with varying weather conditions, it is desired to minimize the time the wind turbine will be attached to both the installation vessel and the support structure. An installation procedure is proposed that will use the mechanical connection to transfer ballast forces between the installation vessel and the support structure. The installation vessel will make a connection with the support structure, and once connected, the water ballast will be transferred from the support structure to the installation vessel. This will result in a pre-tension on the connection, ideally keeping both structures at the same draft and rotation. Once the turbine is placed onto the support structure, the system's equilibrium changes and the pre-tension on the connection will be released. This means the wind turbine can be connected to the support structure and released by the installation vessel without having to wait on the re-balancing operation. The connection, therefore, serves two important functions, limiting the motions between the two floating structures, as well as providing a means to transfer ballast forces between the two floating structures. During the wind turbine installation, various stages of weight transfer and system connections exist. The connector should be able to deliver the desired behaviour in all of these situations. The goal of this study will be to create a tool that enables a quick assessment of the proposed connection, which can provide an understanding of how the structural configuration of the connection influences the system's performance during the various stages of installation. To date, limited research has been presented looking into the dynamic system behaviour during the in-situ installation process of FOWT. Recently presented studies are limited to the spar support structure and limited stages of the installation process (Hong et al., 2021, 2022; Liu et al., 2023). This work will contribute to existing research by combining and extending existing models to create a tool that enables fast assessment of two mechanically connected floating structures during the lifting and installation of a wind turbine assembly, considering the wind turbine assembly as a separate body, the ballast transfer between the bodies, and the mooring system of the structures.

1.4. Research Approach

As described in the problem definition, the installation process of an offshore wind turbine is a complex procedure, with coupled motions between the structures and changing situations during the installation process. This study will focus on how the interaction between the bodies in the system is affected by the structural configuration of the connection between the floating structures, in order to obtain a better understanding of the required structural configuration during the installation of the FOWT. The following main research question has been defined:

How does the structural configuration of a mechanical connection between an installation vessel and a floating support structure affect the relative motions and loads of the system during the various stages of the in-situ installation process of a floating offshore wind turbine?

The sub-questions below will help guide the project by dividing the research into smaller steps. To be able to answer the main research question a model has to be developed, covered by sub-questions one and two. Next, the model can be used to develop an understanding of the system to come to a final conclusion.

Developing the model

1. How to describe the motions of two connected floating bodies using a simplified multi-degree-of-freedom model?
2. How to extend the multi-degree-of-freedom model to include stiffness at the boundaries of the connector?

Understanding the system

3. What are the operational requirements and limitations of the system that need to be considered?
4. What is the effect of the different installation stages on the relative motions and loads of the system?
5. What is the effect of applying increasing stiffness to the boundaries of the connector on the relative motions and loads of the system?
6. What is the effect of coupled stiffness on the relative motions and loads of the system?

Following the research questions, the first step in the investigation of the system's behaviour during the installation of the wind turbine is to develop a mathematical formulation of the system. A simplified multi-body dynamic model of the system will be derived to obtain a better understanding of the structural configuration of the connection between the installation vessel and the support structure. The system will be abstracted into a two-dimensional representation of the system. Considering head waves, it is expected that the most dominant motions occur in the surge-heave plane of the system. The structures in the system will be assumed to be rigid bodies, each with three DOF, surge, heave, and pitch. For this study three main bodies will be considered, the installation vessel, the floating support structure and the wind turbine. Since the installation vessel and support structure are floating structures, the hydrodynamics of these bodies need to be taken into account. An Ansys AQWA model of the floating bodies will be used to calculate the linear hydrodynamic matrices of the system. The hydrodynamic interaction between the bodies will be taken into account and is included in the system matrices. The excitation wave loads on the CG of the bodies will be provided by Ansys AQWA as well. The mechanical interaction between the bodies will be described by various modelling components making use of spring and damper elements to couple the bodies. The most important interaction is the mechanical connection between the installation vessel and the floating support structure. To obtain a first understanding of the behaviour of a dynamic system, a frequency analysis provides a quick method to study the system's behaviour in various frequencies of excitation. Since the goal is to create a tool that allows for quick assessment of various system configurations, the frequency domain will be used to perform the system analysis. Time domain simulations will be used to visualize the motions of the system in certain configurations to more intuitively investigate the system's behaviour. To be able to create a frequency response of the system the equations of motion of the system are required to be linear. However, the motions between the bodies are a function of the translations and rotations of the CG, resulting in geometrically nonlinear equations of motion. The nonlinear equations of motion will be linearized using the small angle approximation. It is expected that the rotations of the bodies remain small enough to make use of the small angle approximation since it is also a limiting factor of the installation procedure on the open sea. The angle of the connection between the two bodies is however not only dependent on the rotations of the bodies but also on their relative heave displacement. Therefore, both a linear and nonlinear variant of the model will be scripted. The results of the linear and nonlinear system will be compared using a time-domain analysis, to determine whether the linear representation of the system can be considered accurate enough. The final scripted model will be a configurable MATLAB tool, which can be used to easily change the system configuration, the used parameters and which bodies are included. Finally, a parametric study will be conducted to obtain an understanding of how the motions and loads of the system are influenced by limiting motions and varying stiffness in the DOF of the connection, and the different installation stages. Based on the results of this system analysis the main research question will be answered.

1.5. Report structure

The remainder of the report is divided into the following chapters. Chapter 2 will provide a more detailed background of floating offshore wind energy, this chapter can be considered optional reading to become acquainted with the state-of-the-art of floating offshore wind. This chapter will also explain the reasoning behind the consideration of the Huisman WIV and the semi-submersible floating support structure for this study. Next, in Chapter 3 related works will be presented and discussed. Further theoretical background, to be used in the following chapters, will be introduced as well. Chapter 4 will describe the modelling approach and the mathematical formulation of the model is presented. Next, Chapter 5 describes how the mathematical equations are implemented to make the model represent the physical system. This is followed by a discussion on the performed system analysis in Chapter 6, where the approach for the system analysis will be explained. The results of the system analysis will be presented and discussed in Chapter 7. Finally, Chapter 8 will provide the final conclusions and recommendations of this research.

2

Introduction to Floating Offshore Wind

This chapter will provide background information on the emergence, developments, and components of FOWT's. First, the development of FOW will be discussed, followed by an overview of the main components of FOWT. Next, currently demonstrated installation methods will be shown. Finally, alternative installation methods and their challenges will be further elaborated on.

2.1. Development of Offshore Wind

This section will provide a brief look at the role of offshore wind in the energy transition, as well as an introduction to the history of offshore wind energy. Further developments in offshore wind and the move towards FOW will be discussed as well, followed by a brief overview of the current state of FOW.

2.1.1. Energy Transition

New reports indicate that the 2015 Paris agreement (COP21) goal to limit the global rise of temperature by 1.5°C will not be met. The latest projections are a rise of temperature of 2.3°C by the end of the century (DNV, 2021) or even 2.7°C with the current climate commitments for 2030 (United Nations Environment Programme, 2021). Even though these are not the brightest perspectives, there are some indicators of positive developments. Large economies are levelling-off or decreasing their use of coal as an energy source (bp, 2021), which is one of the most polluting forms of electricity generation. And while the latest climate commitments fall far short of achieving the necessary reduction in emissions, 49 countries and the EU have pledged a net-zero target for the future (United Nations Climate Change, 2021). An important development to achieve net-zero targets is electrification, which can already be witnessed by the increase in electric vehicles on the road. As indicated by European Environment Agency (2016), the emergence of electric vehicles will cause a further increase in electricity demand. Electric vehicles are not the only contributors to the rise in electricity use, other industries will adapt to use electrical energy as well, further increasing the world's electricity consumption. According to DNV (2021) the world grid-connected electricity production will almost double by 2050, as can be seen from Figure 2.1(a). While it might seem counter-intuitive, using more electricity will result in fewer emissions (Rosenow, 2021). Due to expected gains in efficiency, the world's primary energy use will stabilize around 2030 and gradually start to decrease, as shown in Figure 2.1(b) (DNV, 2021). While one part of the solution is to minimize the amount of energy being used, the second part is to ensure that the additional required electricity is being generated using clean renewable energy sources. Continuous research into renewable energy sources is making them an increasingly interesting alternative to fossil fuels. It is expected that (offshore) wind energy will play a large role in future electricity production. While this form of energy has been increasing in capacity over the last years, its rate of growth is not nearly enough to meet the prospected targets.

2.1.2. Developments of Offshore Wind Energy

In 1990 the first OWT was installed 300 meters off the coast of southern Sweden. A 220 kW turbine with a rotor diameter of 25 meters was installed in 7-meter deep water on a steel tripod foundation. The first commercially active wind farm was installed a year later in Denmark, the Vindeby Offshore Wind Farm

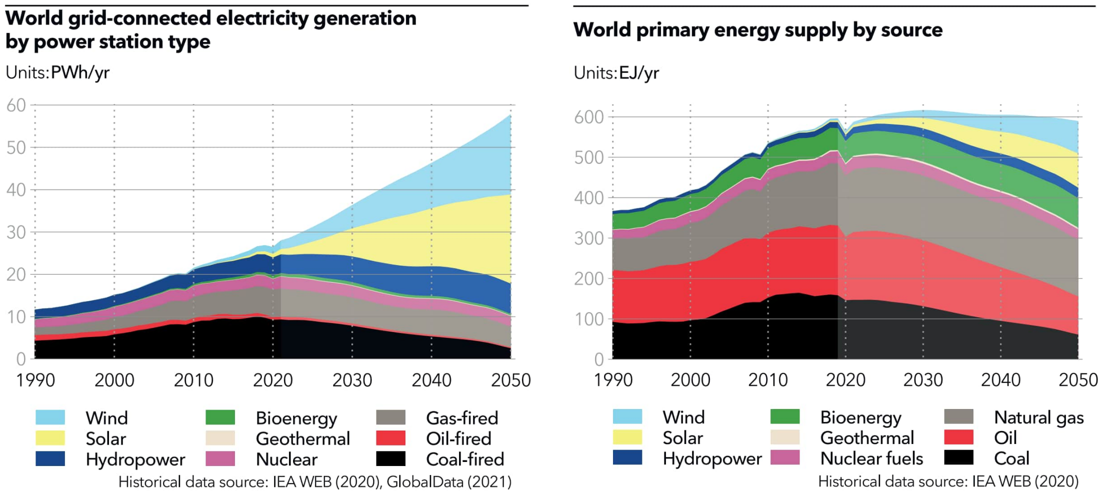

(a) (b)

Figure 2.1: The world grid-connected electricity generation by power station type (a) and the world primary energy supply by source (b). Adapted from the Energy Transition Outlook 2021 report(DNV, 2021)

(OWF), consisting of 11 450kW WTG's (Orsted, 2019). The next years showed a slow increase in the amount of wind energy, and only in the next decade did wind energy gain more momentum. Turbine sizes grew to a typical 3.6 MW and wind farms increased in size to an average of 100 MW. To accompany the larger turbines and wind farms, a dedicated industry started to develop and supply chains matured. The next focus of the industry was to drive down costs and accommodate higher demands. During the 2010's more countries started to invest in the wind industry, turbine sizes grew further, with 8 MW becoming not uncommon, and installation costs dropping as low as 61 euro per megawatt hour (MWh) (Orsted, 2019). Today, the total power of the first wind farm is easily generated by a single turbine, and the world's largest wind farm currently being installed is Hollandse Kust Zuid with a total installed power of 1540 MW (Vattenfall, 2022). Not only Europe is looking at offshore wind energy for its future demands, China and Taiwan are also investing heavily. This is also reflected in the total number of new installations in 2021. 15.7 GW of newly installed wind power brings up the global total of almost 50GW, with a large contribution of 12.7 MW from China (World Forum Offshore Wind, 2022). Global outlooks indicate a further rise of installed wind power in various global regions in the upcoming years, making offshore wind energy an important factor in the energy transition (DNV, 2021; United Nations Environment Programme, 2021; Global Wind Energy Council, 2022). Offshore wind still has relatively high installation costs compared to onshore wind. According to Guo et al. (2022), installation costs for onshore wind account for about 5% of the total costs, while for offshore wind this is between 20% and 30%. Offshore installation costs are higher due to difficult environmental conditions, often contractors have to wait for suitable weather windows to install the wind turbines. This makes the installation of wind turbines a time-consuming process. Since the year 2000 however, installation times for OWF's have reduced by 70% (Lacal-Arántegui et al., 2018). Following this reduction in installation times, the total cost reduction for wind farms can be as much as 75% for wind farms commissioned in 2024. Although these are impressive numbers, Lacal-Arántegui et al. (2018) also concludes that a large part of these improvements relates to the larger size of turbines that are being installed nowadays. Installation times of both monopile foundations and wind turbine generators were analysed. Over the discussed time period the installation time per turbine-foundation set decreased 22%, while installation time decreased 71% per MW. The decrease in installation time mostly contributed to the faster installation of the monopile foundations, which has improved by 87%, while the installation of the wind turbines only improved by 55%. Even though multiple types of fixed-bottom foundation types exist, the monopile foundation is the most common, and at the height of its popularity in 2014, 76.7% of the total installed OWT's used a monopile foundation (Sánchez et al., 2019). The main consideration when choosing a foundation type is the water depth at the location of the wind farm, soil and ocean conditions may also be deciding factors (Wang and Bai, 2010). After 2014 the accumulated share of monopile foundations started to decrease, mainly due to the upcoming Asian wind market using other foundation types, such as gravity base and jacked foundations. Overall, the main influences on the total installation costs are the learning rate, distance from the port to the farm location, and vessel deck area capacity. Even though incremental updates have been done to lower installation duration, the installation process for OWT's has not seen large disruptions over the last decade (Lacal-Arántegui et al., 2018).

2.1.3. Current State of Floating Offshore Wind

The installation methods that have been discussed so far are mainly used in water depths below 50 meters. As wind farm locations move to deeper water the installation process becomes more expensive and eventually economically or technically unfeasible. To overcome this problem floating wind turbines have been introduced as an alternative solution (Myhr et al., 2014). Reaching deeper waters and potentially providing easier installation, floating wind could be a game-changer in the offshore wind market. While floating wind is currently in its pre-commercial phase, still having significantly higher costs than fixed-bottom offshore wind, it has the potential to take over the offshore wind market (Landbo, 2017; DNV, 2020). The potential of floating wind is significant as it gives access to better wind resources further from the coast, as well as makes wind energy available for locations with steep costs. Figure 2.2 (Bosch et al., 2018) gives an overview of the available wind energy on the coast of different countries, separated by water depth. As can be seen from the figure the most significant energy production potential is found in deep waters, suitable for floating wind turbines.

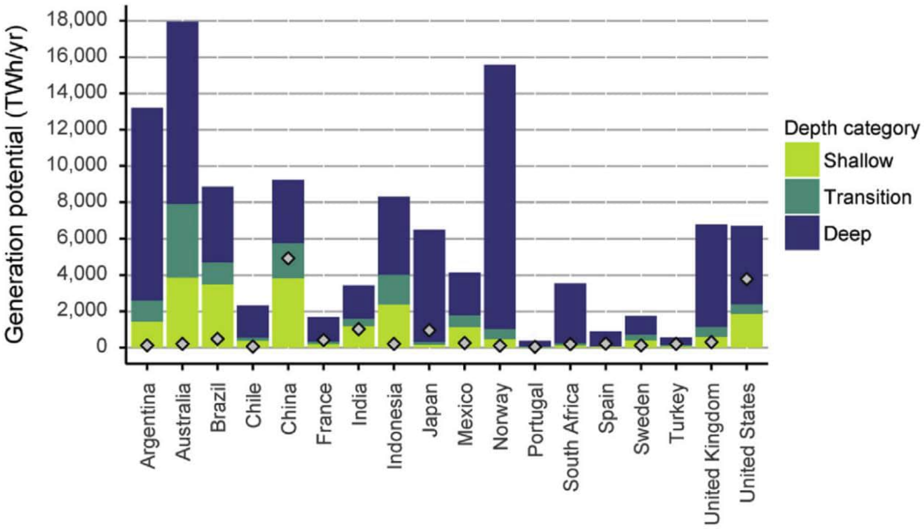

Figure 2.2: Annual average energy production potential of offshore wind farms for different water depths by country. (Adapted from Bosch et al. (2018))

As it becomes apparent that offshore floating wind has an important place in the world's future electricity production, interest from both industry and academics has increased. In addition to the full-scale wind farms that are currently in operation, many different concepts for floating wind turbines have been introduced. The four basic types are shown in Figure 2.3. The Hywind floating wind parks use a spar structure, which can be categorized as a ballast-stabilized support structure. Installation of these wind turbines has to take place in deep water because the spar has a very large draft. The wind turbine is fully assembled onshore and installed on the spar foundation with a single lift, requiring calm waters to perform the installation. In contrast, WindFloat Atlantic uses a buoyancy-stabilized support structure, the semi-submersible. The semi-submersible floating wind turbine can be installed in a port, using a quay crane to install the wind turbine components onto the support structure. Both types of floating wind turbines have to be towed to their wind farm location when the assembly is completed. According to Jiang et al. (2020), the spar floating wind turbines are the most technically mature The semi-submersible floating wind turbines have also shown to be a viable solution, as well as having a relatively mature installation process. Mooring-stabilized floating wind turbines are the least technically and commercially advanced. However, for all types of floating wind turbines installation methods are still open and foundation technologies are expected to further advance to enable easier installation.

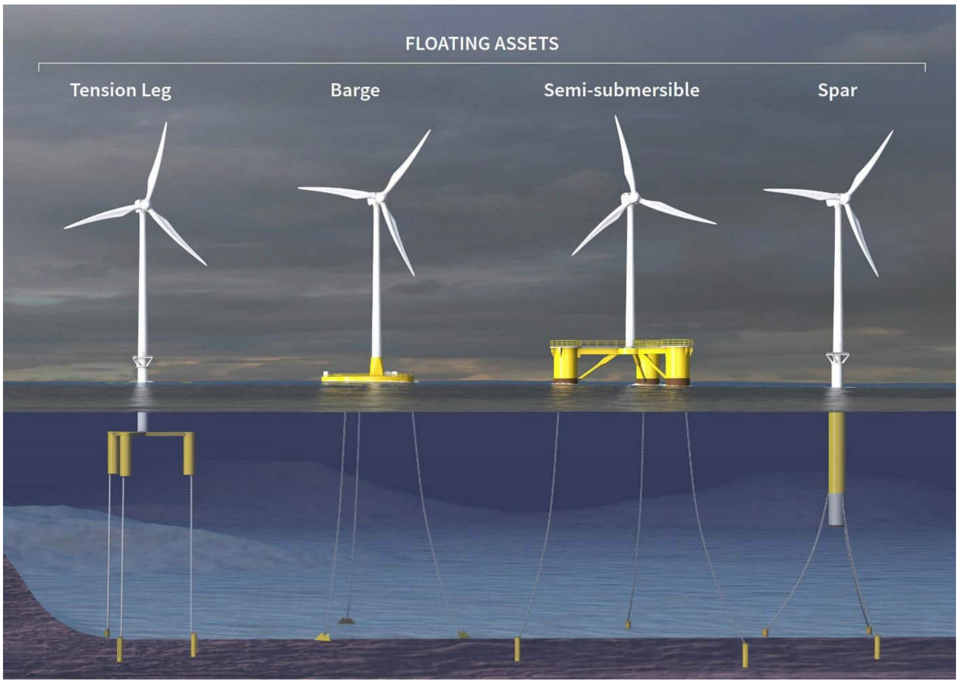

Figure 2.3: Four basic types of support structures. (Acteon, 2020)

2.2. Floating Offshore Wind Components

This section will discuss the various components of FOWT's. The two most important factors that influence the installation process of FOWT's are the turbine size and the type of floating support structure. The section will start with a brief description of current and future wind turbines. Different designs and concepts for FOWT support structures have been presented, various design considerations of support structures will be discussed and a comparison between the main types of support structures will be made. Finally, additional components of the FOWT, such as the mooring system and electrical connections, will be briefly discussed as well.

2.2.1. Wind Turbine Generator

While different approaches to harvesting wind have been proposed, the Horizontal Axis Wind Turbine (HAWT) is still the most used and researched type of wind turbine. Other designs include various types of Vertical Axis Wind Turbines (VAWT's), mostly used for smaller and urban applications (Kumar et al., 2018). For floating offshore wind applications the difference between HAWT's and VAWT's is analysed by Borg and Collu (2015). They conclude that due to highly oscillatory trust forces, with frequencies close to the range of wave excitation forces, VAWT's might be less suited for floating offshore wind applications, even though the absolute magnitude of the inclining moment might be slightly lower than HAWT. There is no particular design difference in WTG's used for offshore wind or FOW. The designs are mostly imposed by turbine manufacturers, with only slight changes to certain components to make them more suitable for the motions of floating support structures. WTG's have been increasing in size since the first installation, where the average of installed rated capacity in 2010 was around 3 MW, this has already grown to slightly more than 8 MW in 2020. Even larger 11 MW (SG 11.0-193 DD) turbines are being installed in OWF's that are currently under construction. The largest FOWT is part of the Kincardine wind farm (Principle Power, 2022b), also using a Vestas V164-9.5 MW WTG. The largest wind turbines in operation today are on-shore turbines built for testing purposes. At the end of 2021, Siemens Gamesa completed the installation of their SG 14-222 DD turbine, becoming the world's largest wind turbine with a maximum rated power of 15 MW (Durakovic, 2021b). Previously this record was held by the GE Haliade-X 14 MW turbine since 2019 (Durakovic, 2021a). This new generation of large turbines is being readied for mass production, expecting the first deliveries in 2024. As can be seen from these numbers, WTG's have not reached a maximum capacity yet, and larger turbine sizes are still demanded.

2.2.2. Floating Support Structures

Floating offshore structures are not newly invented by the offshore wind industry. Most designs are based upon proven concepts from the oil and gas industry, such as the semi-submersible, the spar and the TLP. The available knowledge on these types of platforms is an advantage for the offshore wind industry, and early concepts are directly based on these types of support structures. A comparison of floating oil and gas platforms with offshore wind turbines by Schneider and Senders (2010) shows the offshore wind market following a similar path to the oil and gas industry 50 to 60 years later. The offshore oil and gas industry started with fixed bottom constructions close to shore, evolving into larger structures in deeper water and eventually using floating structures for very large water depths of up to 2400 meters. However, a large difference between the oil and gas industry and the wind energy sector is the quantities of support structures required. Oil and gas rigs are usually produced as one-off designs, while the goal for floating wind will be wind farms using upwards of a hundred turbines. Therefore, more recently presented concepts show more focus on the fabrication aspect of the design and are more tailored for the use of wind turbines. Since the FOW market is still relatively new, many different concepts for floating support structures have been presented, and no industry standard has been set. The different concepts are mainly distinguished by their method of achieving stability, namely ballast, mooring, or buoyancy stabilised.

Design Considerations

Multiple design considerations determine what type of support structure is considered for an FOW farm. Design considerations include the operational draft of the support structure, the type of material used, and the turbine size. These three different aspects all influence each other, as turbine size determines overall size and stability requirements for the support structure, and material choice affects the weight and thus the draft of the structure as well. At most offshore wind locations closer to shore, the draft will be a limiting factor. The draft of the support structure is mainly determined by the stabilization mechanism, with spar foundations requiring the largest depth, as can be seen in Figure 2.3. The different methods of achieving stability can be captured within a stability triangle, as can be seen in Figure 2.4 (a) (Thiagarajan and Dagher, 2014). The three corners of the triangle indicate the main methods of achieving stability, namely ballast-, mooring-, or buoyancy stabilised. A ballast-stabilised support structure makes use of a heavy ballast on the bottom of the structure and achieves its buoyancy from the typically large cylindrical structure. Having the centre of mass below the centre of buoyancy of the complete structure results in a righting moment when the structure inclines. Buoyancy-stabilised support structures, also called water plane stabilised, use their water plane area to achieve stability. For a barge-type support structure, this is the most obvious, behaving similarly to ships. Semi-submersible support structures use smaller areas, moved further away from the centre of the structure. In this case, the multiple cylinders provide additional buoyancy, trying to maximize displaced water volume, while minimizing water plane area. In both cases, a large second moment of area achieves the restoring moment for the support structure. Mooring stabilized support structures are highly buoyant, secured to the sea bed with tensioned mooring lines. When the structure inclines, the tension in the mooring lines provides a righting moment. Most concepts can not fully be described by a single category, combining multiple principles to achieve stability. In Figure 2.4 the main types of floating support structures and their respective stabilization mechanisms are indicated.

Two materials are predominantly used to manufacture the floating support structures, namely steel and concrete. According to Matha et al. (2017) there are several advantages and challenges for both the use of steel or concrete support structures. The major benefit of the use of steel is that it is well-established in the offshore wind industry, meaning expertise is available. Assembly could be a relatively fast process if components are pre-fabricated. Furthermore, steel makes it possible to manufacture lighter support structures when compared to concrete. However, it is an expensive material and specialized equipment is required. It might be difficult to build large components or parts, as these need to be manufactured at shipyards as opposed to the construction site where the wind turbine is installed. Concrete, on the other hand, is a far cheaper material, without the necessity for specialized equipment. Since concrete is easier to source as a raw material it can be produced locally and less storage area for raw materials is required. Concrete does however increase the weight and possibly the size of the support structure, and concrete is not capable of handling tension loads, making the structural design more difficult. Fabrication of the support structures has to be kept in mind as well since the ability to be mass-produced is an important factor in supplying market needs and bringing down costs (Matha et al., 2017).

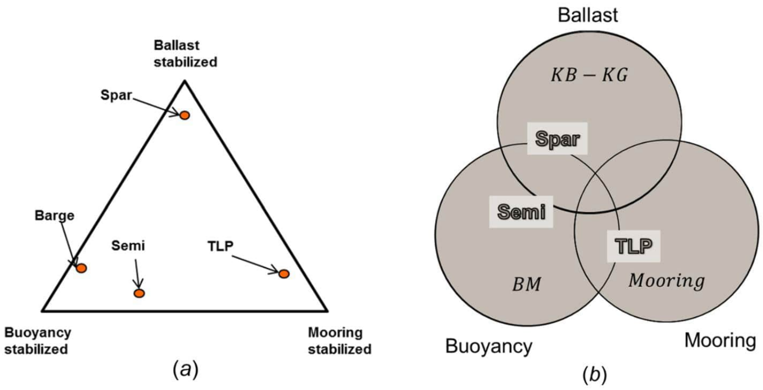

(*a*) (*b*)

Figure 2.4: (a) Stability triangle with annotation of common off-shore wind concepts and (b) Venn diagram showing sources of stability and generic offshore wind structures (Adapted from Thiagarajan and Dagher (2014)).

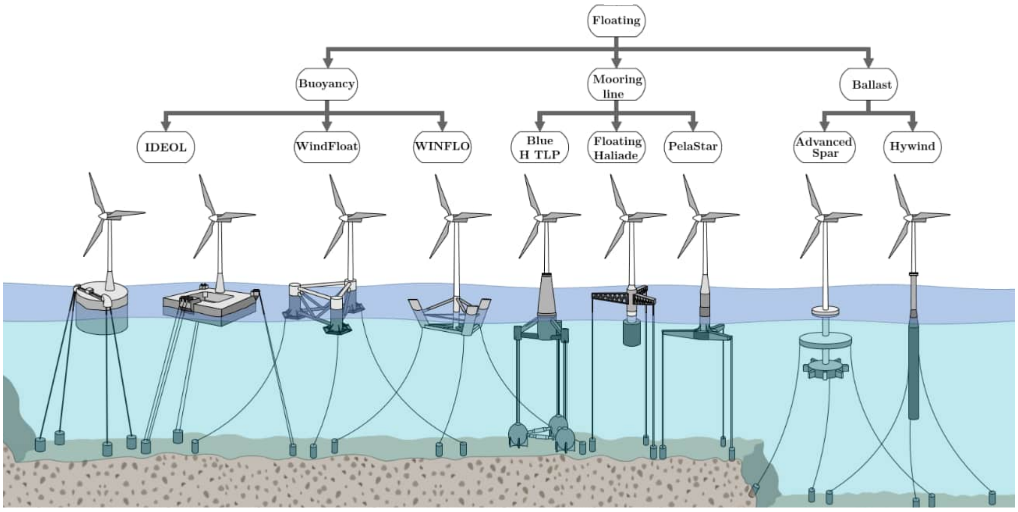

Figure 2.5: Overview of concepts for offshore wind floating support structures (Adapted from Rodrigues et al. (2016)).

Figure 2.5 shows a selection of FOWT concepts, divided into the main categories. Currently only two concepts have been proven in full scale wind farm layouts, namely the Hywind spar and the WindFloat semi-submersible. Other concepts are less advanced and development of several of these has halted or reconsidered, such as the WINFLO (offshoreWIND.biz, 2014) and Blue H TLP. BW Ideol has continued the development of their barge type support structures, with two functioning MW prototypes since 2018 (Floatgen and Hibiki), as well as a planned pre-commercial project of three 10 MW turbines to be constructed in 2022-2024 (BW Ideol, 2022). Concepts are not limited to those shown in this figure, many different concepts of semi-submersible, barge, spar and TLP support structures have been proposed with little variations between concepts. The Pelastar and floating Haliade TLP support structures are combined in a concept presented by GE and Glosten. Their design uses a 12 MW GE turbine combined with a redesigned Pelastar support structure for a light weight FWT with up to 35% less mass compared to current designs (Buljan, 2022). Academic research shows that design improvements are still possible, advancing existing designs, or combining designs into new concepts. It will depend on the industry whether or not these ideas will be adapted.

Comparison

As mentioned before, each type of support structure has various advantages and disadvantages. Many reviews have been written to discuss the performance, economic and manufacturing aspects of each support structure type. Of the many reviews comparing the different support structure types, an overview is shown in Appendix A. Various early studies comparing the dynamics of the main different types of support structures in more detail have been published as well (Li et al., 2011; Jonkman and Matha, 2011; Goupee et al., 2012).

2.2.3. Additional Components

Additional components are required for the operation of a FOWT. Control systems are used to actively stabilise the wind turbine. To keep the floating wind turbine at its desired location a mooring system is required. Additionally, to transport the generated power to the mainland electrical connections have to be made.

Control System

When in operation the FOWT has to be able to endure a range of different weather conditions. The control system is a vital component to ensure the safe and efficient operation of the turbine. As is common with fixed-bottom wind turbines, the control system adjusts the pitch of the rotor blades to achieve optimal efficiency in various wind speeds, known as Collective Pitch Control (CPC) control. However, an FOWT not only has to be able to control its blades to maximize efficiency, but it also has to counter the motions of the floating platform. For high-frequency variations, individual control of the blade's pitch (Individual Pitch Control (IPC)) is used to vary rotor thrust to achieve stability. The WindFloat support structure also features an active ballast system to be able to compensate for low-frequency changes in wind speed and direction (Principle Power, 2022a). According to Salic et al. (2019), conventional controller designs, such as PI or PID models are no longer appropriate, since more degrees of freedom must be controlled. Ha et al. (2021) conclude that each type of support structure has a different ideal control method. It is expected that improvements in control technologies will lower operations and maintenance costs while maximizing the performance of the WTG.

Mooring System

Mooring systems have readily been used in the offshore industry, therefore, mature knowledge is available of these complex systems. However, similar to the support structure, the use case of FOWT poses additional challenges. Important aspects of the mooring system for FOWT's are the mooring footprint, installation costs, and the resulting motions of the support structure. Installation and hookup of the mooring system cover around 10% of the costs of the FOWT according to Katsouris and Marina (2016). Mooring configurations specifically for FOWT are still being researched, both to bring down costs for the installation of mooring lines, as well as to optimize the performance. Fulton et al. (2022) investigate four mooring designs that will accommodate 15 MW FOWT's. Their comparison includes the station-keeping performance of the mooring systems, as well as an installation methodology and the supply chain to assess the economic feasibility of the designs. The four configurations tested all use a spread mooring configuration, for a semi-submersible support structure with three attached mooring lines. The investigated designs use a semi-taut polyester, catenary all chain, taut polyester and 4-taut nylon configuration. It is concluded that all configuration exhibit roughly the same motion characteristics, with no defined best configuration, differences are observed in the maximum tension forces in the mooring lines. From the tested configurations, the taut polyester and taut nylon variants show the lowest costs, with the semi-taut system being the most expensive. Other ideas to reduce the costs of larger commercial wind farms include the use of shared mooring and 'plug-and-play' connections. Shared mooring enables attaching multiple FOWT's to single anchor points, saving on installation time and material cost (Ocean Energy Resources, 2022). To make installation less time-consuming, "plug-and-play" connections have been introduced (Jon Dunstan, 2022). The system separates the installation and hookup of the mooring system, making it easier to schedule installation and commissioning. The system is also modular and has an integrated electrical cable, making it suitable for many different support structure types. An integrated electrical cable further simplifies the hook-up procedure.

Electrical Connections

To connect the wind farm to the mainland grid, electrical connections have to be made. While offshore cables have been used for a long time, with floating wind turbines a new challenge emerges. In a wind farm various types of cables are being used, inter array cables are used to connect the wind turbines to each other as well as to the substation, and export cables connect the substation to the mainland. Support structures of FWT have a certain degree of motion that has to be withstood by the electrical cable, therefore dynamic cables have to be used. Current installations are small and function without an offshore substation, however for large commercial farms floating substations will be required, research has been presented looking into the behaviour of floating substations as well (Frédéric Grizaud, 2022), (Raúl Rodríguez, 2022). Even though there are still challenges to overcome, it is expected that the electrical infrastructure will keep up with the further development of FOW.

2.3. Installation of Floating Offshore Wind Turbines

Installation procedures for FOWT's are still subject to continuous development. Unlike the installation of fixed-bottom wind turbines where a lot of industry experience exists and various installation methods have been identified (Guo et al., 2022), no industry standard has been identified yet. Recently, the Kincardine FOW farm has been installed using WindFloat semi-submersible support structures and the Hywind Tampen wind farm is currently nearing completion, making use of concrete spar support structures. Even though these are different types of floating support structures, the offshore installation process is very similar. The wind turbine is mated with the support structure at a fit-out port, and the completely assembled floating wind turbine is installed offshore. Additional seabed preparations and mooring pre-lay operations are required before the wind turbine is installed. Generally, the offshore installation process of a semi-submersible or spar support structure can be described by the following steps indicated by Matha et al. (2017).

I: Float Out; Tug boats hook up to the support structure and tow the wind turbine out of the harbour, if required the support structure is correctly ballasted.

II: Transit; Transit to the wind farm location, where the floating wind turbine is exactly positioned for installation.

III: Installation; The support structure is attached to the mooring lines, the operational draft is achieved by final ballasting, and the mooring lines are pre-tensioned.

IV: Cable Installation; The cable lay vessel will be positioned and the electrical connections are made.

V: Termination; All crew leaves the support structure and all additional equipment is removed.

VI: Return; Installation vessels return to the coast.

Since a TLP has less stability without being attached to a mooring system, a float-out installation as described above is not possible. A comparison between estimated estimation installation times for all support structure types has been made by Crowle and Thies (2021) and is shown in 2.1. This shows that due to the complex mooring installation the TLP has the longest total installation duration. Installation procedures for the TLP support structure have so far only been proposed by commercial and academic research. The fabrication and installation process for the Hywind Spar and WindFloat support structure will be discussed in more detail below.

Table 2.1: Typical installation duration for various support structures (in days) (Crowle and Thies, 2021)

Installation step	Barge	Semi-submersible	Spar	TLP
Anchor installation	12	6	6	18
Support structure loadout onto Heavy Transport Vessel (HTV)	2	2	2	2
Dry tow to outfit port	5	5	5	5
Float off from HTV to a sheltered harbour	2	2	4	2
Outfit turbine tower, nacelle and blades in a sheltered harbour	10	10	10	10
Tow to site	4	4	4	4
Connect moorings	12	6	6	18
Connect power cables	5	5	5	5
Total	52	40	42	64

2.3.1. Demonstrated Installation Methods

The approach during the installation of the Hywind Tampen wind farm has already evolved from experiences learned during the installation of the Hywind Scotland wind farm. The fabrication of the Hywind Scotland spar was done using steel, while the improved Hywind Tampen spar is constructed using concrete. Presumably, this decision was made because concrete fabrication could be completely done in Norway, eliminating the need to transport the support structures over long distnances. The fabrication was done in two stages, first, a ring of the main section was fabricated in a dry dock in Stord. Next, the sections were wet-towed to Dommersnes, where the rest of the spar structure was fabricated using slipforming in a deep water harbour. The completed support structures, more than 100 meters long, are then towed to Wergeland Base in Gulen, where they are moored to a deep water fit-out quay. Components of the 11 9.5 MW wind turbines are also shipped to Gulen, set to arrive at roughly the same time as the support structures. Contrary to the Hywind Scotland wind turbines, the turbines of Hywind Tampen are installed at the quayside. The various components are assembled onto the support structure using an onshore crane, omitting the challenging heavy lift operations used for the first Hywind farm. An image of the wind turbine installation can be seen in Figure 2.6(a). When the installation of the wind turbine is complete a float-out procedure follows and the turbine is wet-towed to the wind farm location.

The WindFloat Atlantic and Kincardine offshore wind farms are currently the only two operational wind farms using semi-submersible support structures. The installation process for both wind farms is very similar, differing only in the fabrication and fit-out locations and fabrication method. In both instances, the support structures were manufactured using steel with a very similar design. Fabrication of the WindFloat semi-submersibles took place in two different shipyards, located in Portugal and Spain. The first two platforms of WindFloat Atlantic were fabricated at the Lisnave shipyard in Portugal, built up in a dry-dock and wet-towed to the fit-out quay in Northern Spain. The Kincardine wind turbines followed a similar fabrication process as the final support structure of the WindFloat Atlantic farm. Fabrication was done onshore at the Navantia shipyard in Spain, after which the support structures were transported on an HTV to the fit-out location in Rotterdam. Similar to the Hywind Tampen project, the wind turbines were assembled onto the support structures using an onshore crane at the quayside. Assembly of the final blade of a Kincardine wind turbine at the fit-out quay in Rotterdam is shown in Figure 2.6(b). After the turbine is installed, a similar float-out process follows as described above.

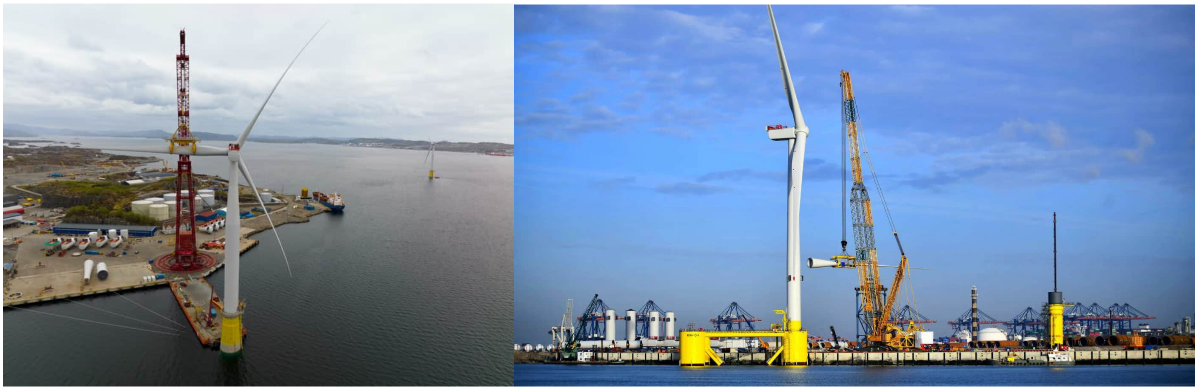
(a) (b)

Figure 2.6: (a) Installation of a Hywind Tampen wind turbine at the Wergeland Base fit-out quay (offshoreWIND.biz et al., 2022). (b) Kincardine wind turbine assembly at the fit-out quay in Rotterdam (Principle Power, 2022d).

2.3.2. Limitations of current installation methods

As is common with new technologies, there are still open challenges with the fabrication and installation of floating wind turbines. Looking at the described processes above, it can be noted that these are lengthy with many, sometimes difficult to perform, steps for each wind turbine. The floating wind industry has to further mature to be ready for full commercial-scale projects. Demonstrated projects show the potential of the technology, but proposed methods are only demonstrated for smaller projects. When thinking of the large number of wind turbines that will have to be installed, existing infrastructure and equipment are limited and installation times and Levelised Cost of Energy (LCOE) have to come down. Currently, all installations have been carried out on a project-to-project basis. For each installation, custom solutions have been found that made use of mostly existing infrastructure and ports. As a result differences in installation processes can be observed between the projects, for example between Hywind Scotland and Hywind Tampen. Their methods changed from using a Heavy Lift Vessel (HLV) to using an onshore crane for the assembly of the wind turbine, and a manufacturing method was chosen that enabled fabrication closer to the fit-out port. Experience from the earlier demo projects helps to improve the process and further ready the industry for mass production. It can also be used to give an estimation of the requirements for a dedicated floating wind infrastructure capable of supporting the installation of commercial floating wind farms. To limit the required transportation operations, the potential development of large floating wind hubs has been discussed (Eatough, 2021; Ramirez et al., 2020). The requirements of these hubs vary for each type of support structure, the main difference between the various types is the required draft at the fit-out quay. An overview of the requirements of a hub to be used for 5 MW wind turbines is given by Crowle and Philipp (2021); Crowle and Thies (2022) and is shown in table 2.2. While, especially for the spar support structure, the draft is the most specific requirement, location, quayside, and equipment requirements are also more stringent for floating wind structures. To be able to transport the support structures to and from the quayside, not only the draft should be sufficient, but the width of the navigation channels should be enough for the support structure and supporting vessels. Another location requirement is the air draft, no bridges should restrict the passage of the completely assembled wind turbines. Furthermore, road and rail connections are preferred for the delivery of components. Onshore staging areas are required as well for the storage of the wind turbine components. A large sheltered harbour is required for the wet storage of the completed support structures. Next, ample quay length is required for the mooring of the support structures followed by the assembly of the wind turbine. Cranes with large lifting capacities and adequate height are required for the installation of the wind turbine components. Depending on the installation method the nacelle is the heaviest component that needs to be lifted. Since onshore cranes are used the bearing capacity of the quay should be large enough to support the crane, which for heavy lifting areas can reach 15 t/m2.

Table 2.2: Minimum assembly port requirements for different types of support structures based on six 5MW wind turbines (Crowle and Philipp, 2021; Crowle and Thies, 2022).

Primary criteria	Semi-submersible	Barge	Spar
Material	Steel	Steel	Steel
Water depth	12-14 m	10-12 m	90 m
FOWT width	90 m	30 m	20 m
Channel width	140 m	110 m	90m
Air draft	Unrestricted	Unrestricted	Unrestricted
Shipyard	6 hec.	4 hec.	5 hec.
Area fit out	6 hec.	6 hec.	6 hec.
Quay length	120m	60m	80m
Fit out quay capacity	15t/m2	15t/m2	15t/m2
Shipyard capacity	10t/m2	10t/m2	10t/m2
Crane for 5 MW turbine	1000 tonne	1000 tonne	1000 tonne

However, none of these facilities exists, even for the established fixed-bottom wind sector, and it seems unlikely that these will emerge in the upcoming future. Since wet-towing operations are difficult, these hubs should be located within a reasonable distance from the wind farms to be installed. This leads to the conclusion that many assembly ports with stringent requirements have to be developed, requiring huge investments. Once the wind farms are operational and the area surrounding the port has no further plans for floating wind, these expensive ports are left without work. While it is commonly mentioned that quay-side assembly is a large benefit of floating wind turbines, it is probably unfeasible to realize the required infrastructure to assemble the required number of wind turbines. Therefore the development of more time and resource-efficient installation methods should be considered. Moving away from ports, alternative installation methods for floating wind turbines will be discussed in the next section.

2.4. In-Situ Installation

The main requirement of the proposed procedures is that the mating procedure of the wind turbine and support structure does not require port facilities. Currently, different methods can be divided based on their basic approach. Near-shore installation methods use sheltered or shallow waters near shore to install the wind turbine onto the floating support structure. This does mean that the assembled floating wind turbine still has to be towed to the wind farm location. An example of this is a floating dock that is designed for the installation of a spar-type floating offshore wind turbine (Jiang et al., 2020). The floating dock is designed to shield the support structure from the environment during the installation of the wind turbine components. Alternatively, the wind turbine will be installed at the wind farm location, this installation method will be referred to as in-situ installation. Various approaches exist, with presented designs considering integrated installation methods, such as Sensewind and Windcrete, as well as concepts making use of purpose build installation vessels. The Windcrete (Windcrete, 2022) foundation, is a monolithic support structure from concrete which can be horizontally fabricated in a dry dock. The wind turbine tower is integrated into the design of the support structure, enabling easier installation of the WTG at sea. SENSEWind presents a Rotor-Nacelle Assembly (RNA) carriage that can be attached to a customized wind turbine tower. The nacelle and blades can be installed onto the carriage at a low height. Once the RNA is complete the carriage will lift itself along the tower and tilts the RNA into place. Figure 2.7(a) shows the SENSEWind device on a TLP support structure mid-installation. Installing the wind turbine using an installation vessel is more equivalent to the installation method for fixed-bottom OWT. First, the support structure will be installed at the wind farm location, after which the installation vessel arrives to perform the wind turbine installation. Next, an installation vessel arrives to install the wind turbine components onto the floating support structure. The most advanced concept currently found in academic literature is a catamaran installation vessel, as proposed by SFI MOVE project 5: Innovative Installation of Offshore Wind Power Systems (SFI MOVE, 2021). The most recent concept of the project is shown in Figure 2.7(b). During installation, the wind turbine will be lifted using wires connected to the bottom of the tower and the assembly is stabilized by additional wires connected to the tower. Mechanical coupling between the spar foundation and vessel is realized using a fender and tension wires. The aforementioned Huisman WIV also can be seen as a concept proposing in-situ installation using a purpose build installation vessel. Comparing the Huisman WIV to the SFI MOVE catamaran vessel, many similarities can be observed. However, the WIV is designed to be more flexible, capable of installation onto various types of support structures and having the possibility of assembling the wind turbines onboard the vessel. Considering the discussed challenges with current installation methods and the versatility of the concept, the WIV is a promising solution for the future installation of FOW farms.

(a) (b) (c)

Figure 2.7: (a) Self-installation option from Sensewind, the rotor-nacelle assembly is transported along the tower of the wind turbine and is tilted in place. (SENSEWind, 2022). (b) NTNU SFI MOVE catamaran installation vessel (SFI MOVE, 2021). (c) The Windfarm Installation Vessel (WIV) concept from Huisman (Huisman, 2022).

3

Related Literature and Theoretical Background

This chapter will provide an overview of scientific works that have contributed to the advancements of this research, as well as to supply the theoretical background required for the modelling and analysis of the system. A brief overview of recently published literature related to the proposed research will be presented. Since FOW still is an emerging technology, limited research has been presented to this date. Research has mostly focused on the design and operation of the FOWT, whereas the installation of the wind turbines has only more recently gained attention. Therefore not only literature directly related to the installation of FOW will be considered, but works describing other relevant offshore operations will be considered as well. This chapter will also provide the required theoretical knowledge used in the remainder of this report, describing basic theory on system dynamics and floating offshore structures.

3.1. Related Literature

As mentioned before, little research directly related to the in-situ installation of FOWT's has been presented. The focus of academic research has been on the design and operation of FOWT, much less on the installation procedure for the structures. This is also reflected in currently demonstrated installation methods, which are being done on a project-to-project basis. Now that the proof of concept has been shown it is important that effective installation methods will be developed. Section 3.1.1 will provide an overview of the most relevant literature found on the in-situ installation for FOWT. Even though further research into possible installation options is limited, research into offshore operations and structures has existed for longer, and various other topics are potentially relevant to this study. Section 3.1.2 will provide an overview of relevant models describing offshore structures and operations.

3.1.1. In-situ installation

The SFI-Move marine operations centre at the NTNU in Norway is one of the main contributors to FOW installation research. One of their projects, 'Project 5: Innovative Installation of Offshore Wind Power Systems', is an ongoing research project into the optimization of the installation efficiency of floating offshore wind. Currently, their focus is on installing wind turbines on spar foundations, as these are mostly demonstrated in Norway, and are difficult to install at the shore due to their large draft. Various papers have been presented describing a catamaran installation vessel concept and various aspects of it. Hatledal et al. (2017) describe the catamaran gripper-monopile mechanism for the first time. The considered concept is shown in Figure 3.1, in this version of the concept grippers were used to lift and install the wind turbine, as well as to make a connection to the spar foundation. In Figure 3.1(a) the connection between the vessel and the spar is made, followed by the positioning phase shown in Figure 3.1(b). Next, the wind turbine is mated to the support structure as seen in Figure 3.1(c), and finally the support structure is released by the installation vessel (Figure 3.1(d)). Hatledal et al. (2017) investigate contact forces between the spar and the installation vessel's grippers during the connection phase. Various vessel headings were compared and it has been shown that the vessel should be aligned with the direction of the waves to keep the forces to a minimum. It was concluded that the contact forces involved in the operation were substantial and the effect of these forces on actual equipment should be further investigated, as well as the coupled behaviour of the entire system. Further research should also include irregular waves and wind and underwater current forces.

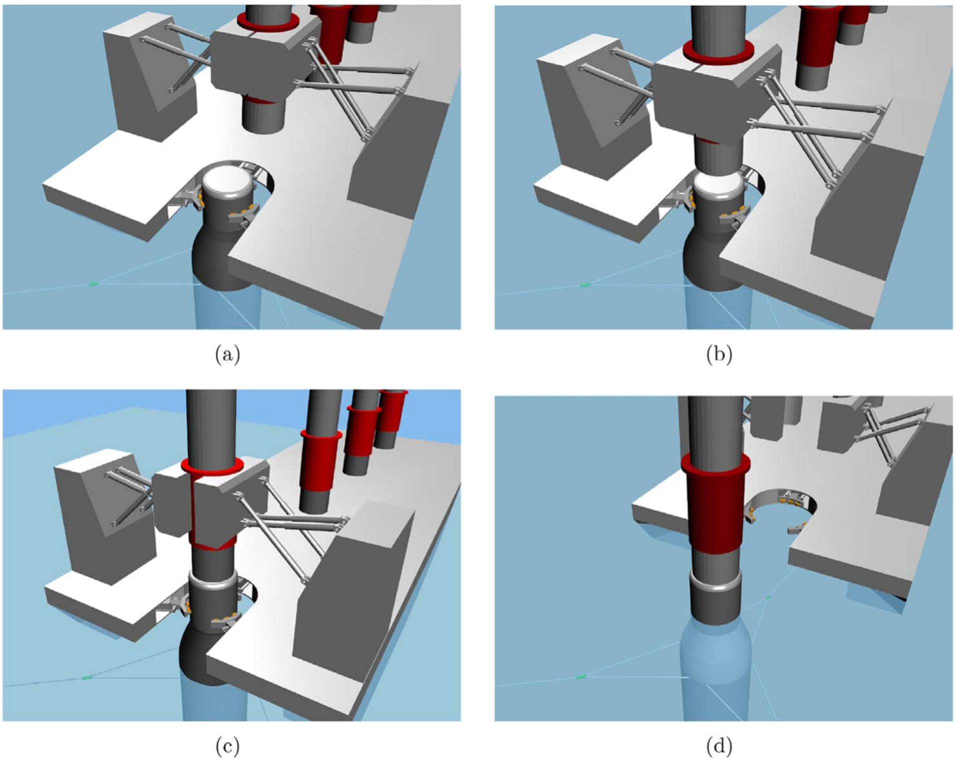
(a) (b) (c) (d)

Figure 3.1: Catamaran using lifting grippers (Hatledal et al., 2017),(Jiang et al., 2018a).

The behaviour of the wind turbine during the mating phase is studied by Jin et al. (Jin et al., 2018) and Jiang et al. (Jiang et al., 2018b). Jin et al. investigate the relative motions between the wind turbine and a fixed-bottom foundation after the wind turbine has been placed above the foundation, and before the wind turbine is lowered onto the spar support structure. A numerical simulation was carried out to investigate the effect of an external force to control the vertical motion of the assembly. Their results show that when a proper controller is used the wind turbine motions can be controlled with reasonably large external forces. This is further examined by Jiang et al. (2018b), carrying out a time domain simulation of the mating phase including irregular waves and active heave compensation. It is shown that an active heave compensator can reduce the relative motions between the wind turbine and the floating support structure. The dynamic response analysis of the coupled system is further investigated by Jiang et al. (2018a). Looking at the steady state prior to the mating process, the effect of wind loads and wave conditions on the motion response of the catamaran and spar as well as gripper forces and mooring forces are discussed. The relative motions at the mating point are less sensitive to the orientation of the wind turbine blades and are largely influenced by wave conditions. The following modelling challenges for the installation of FOWT's using the SFI MOVE catamaran concept are presented (Jiang et al., 2018a), this can be further applied to in-situ installations using purpose build installation vessels.

- **Structural dynamics.** As mentioned before, multiple bodies are connected during the installation operation. These bodies form a large coupled mechanical system, which has several eigenmodes. It is, therefore, important to model the mechanical couplings and understand the effect on the dynamics of the complete system.
- **Hydrodynamics.** The hydrodynamics of the two floating bodies should be considered during the modelling. Both the vessel and the support structure exhibit hydrodynamic effects that should be included in the complete model. This varies for different types of vessels and support structures,

in the case of the research by Jiang et al. the sloshing modes between the hulls of the catamaran should be considered, the spar might exhibit different behaviour in shallow water. Additionally, viscous effects on both bodies should be considered.

- **Automatic control.** During the different stages of the installation process, various components of the system require automatic control. For example, during the initial connecting stage, the vessel has a dynamic positioning system to keep the vessel's translations to a minimum. During the mating stage, the wind turbine has to be motion-compensated to reduce relative motions between the tower of the wind turbine and the support structure. In addition, the ballast of the support structure could be controlled to simplify the load transfer of the wind turbine between the installation vessel and the support structure.

The most recently presented research by the SFI Move project, Hong et al. (2021), Hong et al. (2022), and Liu et al. (2023), looks into a connection between the spar foundation and the installation vessel. A mechanical connection using fenders and connection wires is used to limit the relative motions between the spar foundation and the installation vessel. Their conclusions show that the relative motions are smaller when both systems are coupled, various pretensions in the wires were tested, and different tensions showed favourable results for the various degrees of freedom. For future research, it is recommended to look into more complex environmental loads, as well as extend the analysis with the dynamics of the lifted wind turbine. Further optimization of the floating bodies and mechanical coupling systems is mentioned to shift the natural periods of the system outside of the linear wave excitation range. As can be seen from the various publications the catamaran wind turbine installation concept from SFI MOVE is still under development, with research still being presented on the various components of the system and steps of the installation process. The proposed method of connecting the spar foundation and the installation vessel is different from the proposed connection between the Huisman WIV and a semi-submersible support structure. However, their research provides insight into what to consider during the dynamic analysis of the connected floating structures.

3.1.2. Modelling Offshore Structures and Operations

As described in Chapter 1 the system will be abstracted into a multi-body system. The modelling of offshore lifting operations is often carried out using multi-body systems as well, and the interaction of floating structures and suspended cargo has to be described for these types of operations as well. Connections between floating structures have also been studied, with the main purpose of investigating the behaviour of Very Large Floating Structures (VLFS). VLFS are used to create large floating areas from multiple modules, using flexible connections. Even though these fields do not consider the installation of floating offshore wind turbines, the approach used to form the presented models is applicable to the proposed system and will be considered during the formulation of the model in Chapter 4.

Offshore Lifting Operations

Lifting and installation of large and heavy objects have been studied as well, for example for the installation of large topside constructions for the oil and gas industry. Different methods of installation exist, such as float-over installation, as well as installations using heavy lifting vessels. The various stages of load transfer during a float-over installation have been studied by Choi et al. (2014) and Jung et al. (2018). However, during these installations, the load is placed on a stationary jacket construction. Ha et al. (2018) presents a numerical model of the lifting of a topside by a large crane vessel, onto an Floating Liquefied Natural Gas (FLNG) facility. In this model, no connection is required between the two floating bodies, due to the much calmer environmental conditions, but the presented equations of motion describe the interaction between the heavy topside module and the FLNG facility. A combination of the hydrodynamics of the floating structures (3.1) and applied forces (3.2) is used to describe the motions of the bodies in the model.

$$\begin{bmatrix} M_1 + A_{11} & A_{12} & 0 \\ A_{21} & M_2 + A_{22} & 0 \\ 0 & 0 & M_3 \end{bmatrix} \begin{bmatrix} \ddot{X}_1 \\ \ddot{X}_2 \\ \ddot{X}_3 \end{bmatrix} + \begin{bmatrix} R_{11} & R_{12} & 0 \\ R_{21} & R_{22} & 0 \\ 0 & 0 & 0 \end{bmatrix} \begin{bmatrix} \dot{X}_1 \\ \dot{X}_2 \\ \dot{X}_3 \end{bmatrix} + \begin{bmatrix} C_{11} & 0 & 0 \\ 0 & C_{22} & 0 \\ 0 & 0 & 0 \end{bmatrix} \begin{bmatrix} X_1 \\ X_2 \\ X_3 \end{bmatrix} = \tag{3.1}$$

$$\begin{bmatrix} F_1^{wire} \\ 0 \\ F_3^{wire} \end{bmatrix} + \begin{bmatrix} 0 \\ F_2^{LMU} \\ F_3^{LMU} \end{bmatrix} + \begin{bmatrix} F_1^{thruster} \\ 0 \\ 0 \end{bmatrix} + \begin{bmatrix} 0 \\ F_2^{mooring} \\ 0 \end{bmatrix} + \begin{bmatrix} F_1^{exciting} \\ F_2^{exciting} \\ 0 \end{bmatrix} + \begin{bmatrix} F_1^{drift} \\ F_2^{drift} \\ 0 \end{bmatrix} + \begin{bmatrix} F_1^{others} \\ F_2^{others} \\ F_3^{others} \end{bmatrix} \tag{3.2}$$

Here, M_i is the mass matrix of the i^{th} body and $A_{i,j}$ is the added-mass matrix of the floating bodies. The displacements, velocities and accelerations of the bodies are described with X_i, $\dot{X}_i$, and $\ddot{X}_i$, respectively. R_{ij} is the retardation matrix, and C_{ij} is the hydrostatic restoring matrix. The Dynamic Positioning (DP) system of the crane vessel applies force $F_i^{thruster}$, and the mooring system of the FLNG is included by force $F_i^{mooring}$. The interactions between the crane vessel and cargo are included by the F_i^{wire} and F_i^{LMU} (Mounting interface) forces. Wave force are capture by $F_i^{exciting}$ and F_i^{drift} and F_i^{other} describes other potential external forces.

Very Large Floating Structures (VLFS)

Connections between floating structures are an important aspect of studies looking into VLFS. Jiang et al. (2021) present a review of the most recent research into connectors for VLFS systems. Various types of connections and their relative positive and negative properties are discussed. In more detail, Lu et al. (2021), Zhao et al. (2019) are Shi et al. (2018) present different numerical models looking into connector stiffness of various designs. Even though these are different types of structures, and interactions vary, the studies present a helpful look into modelling the connected floating bodies and analyzing connector loads. The Rigid Module Flexible Connector (RMFC) model presented by Riggs and Ertekin (1993), forms the base of these studies and provides a linearized formulation for a flexible connection between two directly coupled rigid floating structures. The model presents the interaction between the modules as a linear structural stiffness matrix, which is formed by the different connections in the model. The connections are modelled with discrete, zero-length springs. Each connection has a stiffness matrix $\overline{k_c}$, which is a diagonal matrix with the stiffness of the connection in the various DOF. The spring force-deformation relationship is given by Equation 3.3.

$$F = k_c u \tag{3.3}$$

Where F is the spring force matrix, k_c is the stiffness matrix and u is the deformation vector. For a connection between modules i and j the structural stiffness matrix is determined as follows. The displacements of each connector can be transformed to the modules CG by transformation matrix T_c, as shown in Equations 3.4 and 3.5.

$$\overline{u} = T_c u_{i-j}, \text{ where } u_{i-j} = [u_i^T u_j^T]^T \tag{3.4}$$

Where u_i^T is the 6x1 displacement vector for module i and the tranformation matrix T_c is defined as below:

$$T_c = \begin{bmatrix} 1 & 0 & 0 & 0 & x_3^i & -x_2^j & -1 & 0 & 0 & 0 & -x_3^j & x_2^j \\ 0 & 1 & 0 & -x_3^i & 0 & x_1^j & 0 & -1 & 0 & x_3^j & 0 & -x_1^j \\ 0 & 0 & 1 & x_2^j & -x_1^j & 0 & 0 & 0 & -1 & -x_2^j & x_1^j & 0 \\ 0 & 0 & 0 & 1 & 0 & 0 & 0 & 0 & 0 & -1 & 0 & 0 \\ 0 & 0 & 0 & 0 & 1 & 0 & 0 & 0 & 0 & 0 & -1 & 0 \\ 0 & 0 & 0 & 0 & 0 & 1 & 0 & 0 & 0 & 0 & 0 & -1 \end{bmatrix} \tag{3.5}$$

Here, x_1^i,x_2^i and x_3^i are the x, y and z distance of the connector to the CG of body i. The resulting structural stiffness matrix K_C describing the coupling between body i and j is calculated by Equation 3.6.

$$K_C = T_c^T k_c T_c \tag{3.6}$$

3.2. Theoretical Background

The main objective of this research is to focus on the dynamics of the connection. The system can be seen as a combination of multiple bodies with elements that couple them, which is a typical example of multi-body dynamics. The floating structures are excited by waves, and their behaviour is largely influenced by the water, so a basic understanding of hydrodynamics is required as well. Below a brief explanation of the required rigid body dynamics and the incorporation of hydrodynamics will be given.

3.2.1. Multi Body Dynamics

The investigated system can be abstracted into a combination of interconnected bodies. The bodies in the model are assumed to be rigid and do not deform when subjected to external forces. A well-used approach to studying the dynamic behaviour of a system of rigid bodies is multi-body dynamics. Multi-body dynamics is a method to derive the mathematical description of coupled systems of (rigid) bodies. The motions of a rigid body are described in six DOF, three translations and three rotations, by the Newton-Euler equations of motion. The Newton-Euler equations are derived using Newton's second law of motion and Euler's equations of rotational motion. The equations of motion can be separated into the translational (3.7) and rotational (3.8) equations.

$$F = Ma = M\ddot{x} \tag{3.7}$$

Where F is the sum of the external force, M is the mass, and a is the linear acceleration of the body. The acceleration can also be written as the second derivative of the position of the body $\ddot{x}$.

$$M = J\alpha = J\ddot{\theta} \tag{3.8}$$

Where M is the sum of applied moments, J is the body's inertia, and α is the angular acceleration of the body. The angular acceleration can also be written as the second derivative of the rotation of the body $\ddot{\theta}$.

A well-known example of a dynamic system is a mass-spring-damper system moving in one dimension, as shown in Figure 3.2.

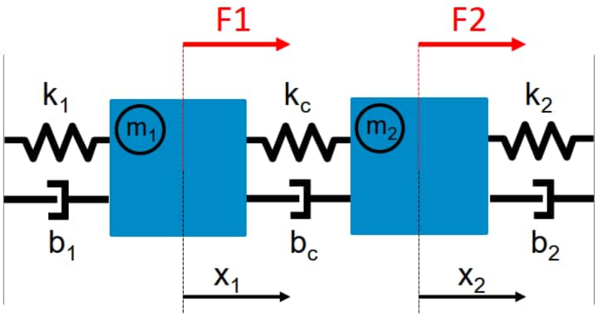

Figure 3.2: One-Dimensional Mass-Spring-Damper system with two interconnected point masses.

Here, two masses are connected to each other and the fixed world using spring and damper elements. Each point mass has a displacement x, a mass m and is subjected to force F. The masses are connected to the fixed world and each other with spring elements with stiffness constants k and damper elements with damping constants b. The interactions between the masses are described by the equations of motion shown in Equation 3.9.

$$\begin{bmatrix} m_1 & 0 \\ 0 & m_2 \end{bmatrix}\begin{bmatrix} \ddot{x}_1 \\ \ddot{x}_2 \end{bmatrix} = \begin{bmatrix} F_1 \\ F_2 \end{bmatrix} + \begin{bmatrix} -k_1 - k_c & k_c \\ k_c & -k_2 - k_c \end{bmatrix}\begin{bmatrix} x_1 \\ x_2 \end{bmatrix} + \begin{bmatrix} -b_1 - b_c & b_c \\ b_c & -b_2 - b_c \end{bmatrix}\begin{bmatrix} \dot{x}_1 \\ \dot{x}_2 \end{bmatrix} \tag{3.9}$$

This equation can be written in matrix form as shown in Equation 3.10. Where M is the system's mass matrix, B the system's damping matrix, C the system's stiffness matrix and X, $\dot{X}$, and $\ddot{X}$ the position, velocity and acceleration of masses in the system respectively. For multibody systems the equations of motion have a similar form, however, for each body, more degrees of freedom are used to fully describe their motions.

$$F = M\ddot{X} + B\dot{X} + CX \tag{3.10}$$

3.2.2. Floating Structures

The motions of a floating structure are described in six degrees of freedom, three translations, surge, sway and heave, and three rotations, roll, pitch and yaw. For this research, a two-dimensional approach is taken, only the translations in the surge-heave plane will be considered. The stability of a floating structure is based on the interaction between the centre of gravity, the centre of buoyancy and the metacentre of the structure. The buoyancy and gravity force will always find a balance, determining the draft of the structure. When the structure starts moving, the displacement of water creates a restoring force. Additionally, when the angle of a floating structure changes, the buoyancy force and the gravity force are not in equilibrium anymore and will create a moment. For a stable vessel design, this moment will restore the angle of the vessel. Considering linear hydrodynamics, these restoring forces can be captured within the stiffness matrix of the body. Similarly, hydrodynamic damping can be added as a damping matrix. Additionally, an added mass term is added to the mass matrix of the structure, which is due to the added forces of having to accelerate the water around the structure. The damping and added mass matrices are frequency dependent. The typical equations of motion for a floating structure can therefore be written as Equation 3.11. Where $F_{exc}(\omega)$ is the excitation force based on a certain wave frequency, M is the structural mass matrix, $A(\omega)$ is the added mass matrix, $B(\omega)$ is the frequency-dependent damping matrix, C is the restoring matrix, and X are the states of the structure.

$$F_{exc}(\omega) = [M + A(\omega)]\ddot{X} + B(\omega)\dot{X} + CX \tag{3.11}$$

A simplified interpretation of hydrodynamic interaction is used for the first creation of the model. A body coupled with spring and damper elements in the surge, heave and pitch direction will be used to approach the interaction with water. For each body, the forces and moments are a result of the springs and dampers connected to the CG of the bodies and the fixed world. This is a very simple approach, but the resulting stiffness and damping matrices will later be replaced by the linear hydrodynamic restoring and damping matrices acquired from an Ansys AQWA analysis. The force F_w is an external oscillatory force, which will later be replaced by the wave excitation force. The simplified two-dimensional (surge, heave and pitch) motions of floating body i can be described by Equations 3.12-3.14.

$$m_i\ddot{x}_i = F_{i,wx} - k_{i,x}x_i - b_{i,x}\dot{x}_i \tag{3.12}$$

$$m_i\ddot{z}_i = F_{i,wz} - k_{i,z}z_i - b_{i,z}\dot{z}_i \tag{3.13}$$

$$J_i\ddot{\theta}_i = M_{i,w} - k_{i,ry}\theta_i - b_{i,ry}\dot{\theta}_i \tag{3.14}$$

3.2.3. Ansys AQWA

Ansys AQWA is a commercially available computational software to assess the effects of wave, wind and current on floating and fixed offshore structures. A three-dimensional linear radiation and diffraction analysis can be used to determine the linear hydrodynamics for multiple structures. The hydrodynamic interaction effects between the structures are hereby taken into account. Since this project is a first analysis of the dynamic system, this approach yields accurate enough results to investigate the influence of a connection between the floating structures. The hydrodynamic matrices and forces acting on the CG of the structures can be calculated for various regular wave frequencies and wave headings. The excitation force provided by Ansys AQWA includes Froude-Krylov and diffraction wave forces. The force RAOs are described at the CG of the structures. This means the phase difference of the force and the distance between the structures must be considered. The definition for the wave force RAOs provided by Ansys AQWA is as follows:

$$Q = Q_0 cos(-\omega t + \phi) \tag{3.15}$$

Where Q_0 is the amplitude, ω the frequency and ϕ the phase shift. The definition of the force includes a negative sign for the frequency This must be accounted for when determining the RAOs of the structures.

3.2.4. System Analysis

The equations of motion will be solved numerically, both in the frequency domain using RAOs, as well as in the time domain. In the time domain, the motions of a system are calculated for each discrete time step. To solve the equations of motion numerically, the equations will have to be written as a system of first-order differential equations. A combination of states is chosen that can represent the system's motions as a first-order equation. Typically the states chosen are the position and velocity of the bodies. Combined with the acceleration, which is now a first-order derivative, the states fully describe the motions of the system. This research will use the Runge-Kutta solver chosen for a good combination of accuracy and speed. The first-order initial value problem is defined as follows, where y_0 is the system's initial condition.

$$\frac{dy}{dt} = f(t, y), y(t_0) = y_0 \tag{3.16}$$

The Runge-Kutta algorithm calculates the states of the system at the next time step y_{n+1} using Equations 3.17 and 3.18.

$$y_{n+1} = y_n + \frac{1}{6}(k_1 + 2k_2 + 2k_3 + k_4)h, \tag{3.17}$$

$$t_{n+1} = t_n + h \tag{3.18}$$

Where y_n is the current system state, t_n is the current time step, h is the size of each time step, and k_1 to k_4 are four increments

$$\begin{aligned} k_1 &= f(t_n, y_n), \\ k_2 &= f(t_n + \frac{h}{2}, y_n + \frac{k_1}{2}), \\ k_3 &= f(t_n + \frac{h}{2}, y_n + \frac{k_2}{2}), \\ k_4 &= f(t_n + h, y_n + hk_3) \end{aligned}$$

A potential downside of numerical time-domain solvers is the potential for errors. The smaller the time step is chosen, the more accurate the results will be, however, solving the equations becomes more computationally intensive. This is mostly noted when very large changes occur during each time step, this will therefore be a limitation of the used method. The Runge Kutta method is considered one of the more precise methods compared to other iterative solvers such as Euler or Euler forward.

The frequency domain analysis requires the system to be written as a combination of linear equations. Using regular waves for the analysis, the excitation of the bodies is harmonic. Since the excitation is harmonic, the floating structure is expected to reach a harmonic oscillation as well. The frequency response for floating structures is typically calculated using RAOs, which can be seen as a transfer function of the wave excitation and the structure's motions. The amplitude and phase of the motion are calculated using Equation 3.19. The output is normalized giving the response of the structure per meter wave height.

$$RAO(\omega) = \frac{F_{exc}}{C - (M + A(\omega))\omega^2 + iB(\omega)\omega} \tag{3.19}$$

4

Model Formulation

The first step in the investigation of the system's behaviour during the installation of the wind turbine is to develop a mathematical formulation of the system. The complete system model will consist of various elements, each mathematically describing a way of interaction between the different bodies present in the model. A modular MATLAB tool will be scripted that can be used to easily adapt the configuration of the studied system. First, the modelling approach will be discussed in section 4.1, describing how the physical system is abstracted and what elements are required to be able to describe the system by a two-dimensional multi-body model. The goal of this study is to investigate the influence of the configuration of this connector on the relative motions and loads of the system, to achieve this a versatile connection model must be formalized. The focus of Section 4.2 will be on the mathematical description of this connection, describing the modelling process leading to the Rigid Link Flexible Boundaries (RLFB) model for the connection between the floating structures. Next, in Section 4.3 a description will be provided of the additionally required elements that are available in the modular MATLAB tool. The next chapter will further elaborate on the practical background and implementation of the various modelling elements. The next chapter will discuss how these elements are combined and which parameters are used to formulate a complete mathematical description of the system.

4.1. System Abstraction and Modelling Approach

The Huisman WIV is chosen as the basis for the modelling of the in-situ installation procedure of a FOWT. However, this modelling approach can also be applied to a combination of other vessels or floating support structures. The system will be abstracted into a dynamical model by considering the installation vessel, the floating support structure, and the wind turbine, as separate rigid bodies. A rigid-body approach is chosen since it is expected that the stiffness of the connection is much smaller than the stiffness of the bodies, therefore the impact on the motions of the system caused by the connection will be the most dominant. It is expected that the most dominant motions and forces will occur in the longitudinal plane of the installation vessel and support structure. Therefore, a two-dimensional representation of the system will be analysed in the surge-heave plane. A two-dimensional model will provide more comprehensible results focused on the dominant motions of the system. For each body in the model the three DOF, surge, heave, and pitch, will be considered as the set of generalized coordinates. The hydrodynamics of the floating structures are analysed using Ansys AQWA. The model considers the dimensions and behaviour of both bodies and the hydrodynamic interaction between the structures. This data will be integrated into the model using the linear hydrodynamic matrices calculated by Ansys AQWA, which can be added to the system matrices. The wave-excitations forces will are applied at the CG of the floating structures and will be considered external excitation forces in the model. The mechanical coupling between the various bodies in the model will be integrated using a combination of springs and dampers. The MATLAB tool will provide various elements that can be used to define the interaction between the rigid bodies. The most important one is the connection between the installation vessel and the floating support structure. Additionally, various other elements are required to describe the installation procedure of the FOWT. The installation process requires to transfer the weight of the turbine from the installation vessel onto the floating support structure. During offshore lifting operations, it is typical that (water) ballast is used to maintain the draft and balance of the floating structures. Therefore, the model needs to be capable of capturing this varying ballast on the various components. When ballast is transferred between the connected floating structures, the equilibrium of the system may change. It is envisioned the connection between the installation vessel and the floating support structure will make use of cylinders to provide the required stiffness during the operation. In practice, a pre-tension can be applied with the cylinders to subject a 'static' force on the connection. Instead of requiring a very high overall stiffness to keep the system balanced, a higher static load can be absorbed while keeping the dynamic stiffness lower so the system is still free to move. The pre-tension force on the cylinder will be included in the model as well. Since the goal is to have a fast-solving tool, the preference is to get a linear model to describe the motions of the system. During the installation procedure, it is expected that the angles of the bodies remain small (less than 6 degrees). Typically, the limits for offshore operations are restrictive since it becomes too dangerous for the crew and equipment to continue working in rougher sea states. Even though it is expected the relative angles of the bodies remain small (less than three degrees) it is important to investigate the difference between the linear and nonlinear descriptions of the model, especially since the relative angles between bodies might become larger. Therefore, in the sections below both linear and nonlinear system equations will be presented.

4.2. The Connection Model

A start of the model is made by considering the system as a very simple coupled mass-spring-damper system. One-dimensional coupled mass-spring-damper systems have been readily described and can be seen as 'textbook' examples of multi-degree-of-freedom systems. This very simple abstraction describes the interaction between two masses, which represent the installation vessel and floating support structure. Each mass is connected to the fixed world with a spring and damper, which can be seen as the interaction of the masses with the water, and the applied force F_{exc} as the wave excitation force. A linear spring between the masses is used to represent the flexible connection as is shown in Figure 4.1. In this example, the spring forces on each mass can be easily determined as a function of the displacement of the bodies $(x_2 - x_1)$ and the spring constant k_c. However, this representation is limited to a one-dimensional motion only, and the spring connecting the bodies can only exert a force on the centre of the masses. As mentioned before, more degrees of freedom are required to capture the essential motions of the system. The next step in the modelling process is to replace the two masses with 2-D rigid bodies, and the connecting spring is now attached to points on the bodies with a distance from the CG, this step is shown in Figure 4.1 as well. This system is considered the first simplified multi-degree-of-freedom model that describes the motions of two connected floating bodies. The next section will further detail the mathematical formulation of the modelling element describing the connection between two floating bodies.

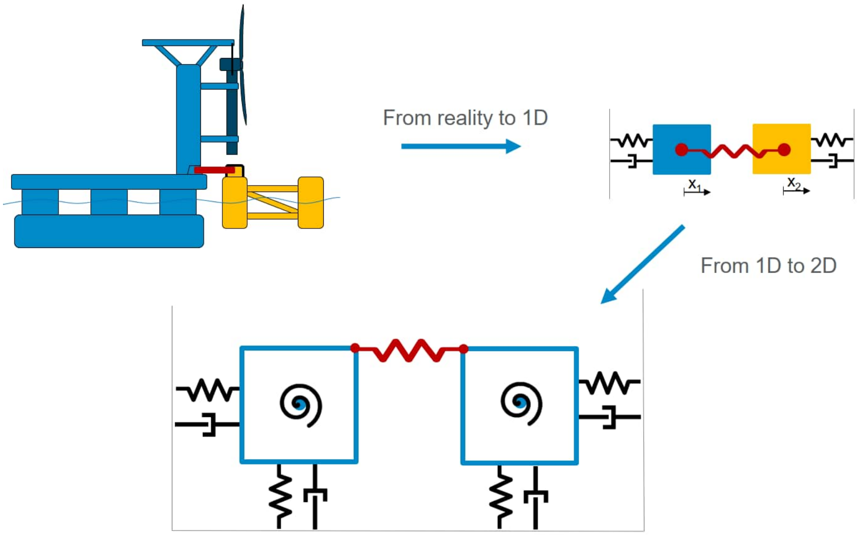

Figure 4.1: Figure showing the first steps of the modelling process.

4.2.1. Flexible Connection between Rigid Bodies

During the initial modelling phase, the hydrodynamic matrices of the structures are left out and are replaced by a simplified system of springs and dampers. The springs and dampers connect the bodies to the fixed world and will be formulated following the approach in Section 3.2.2. The system matrices M, C, and B can later be replaced by the hydrodynamic matrices from Ansys AQWA. The focus of this section will be the description of the body's interaction with the connecting spring. In the one-dimensional example, the spring force is only dependent on the translation in the horizontal direction of the CG of the masses. Now that more DOF will be considered the displacements of the attachment points of the spring are not as simple to describe. Figure 4.2 shows a Free-Body Diagram (FBD) indicating the system variables and the spring forces. The mathematical description of a linear spring connected between rigid body i and j will be presented below.

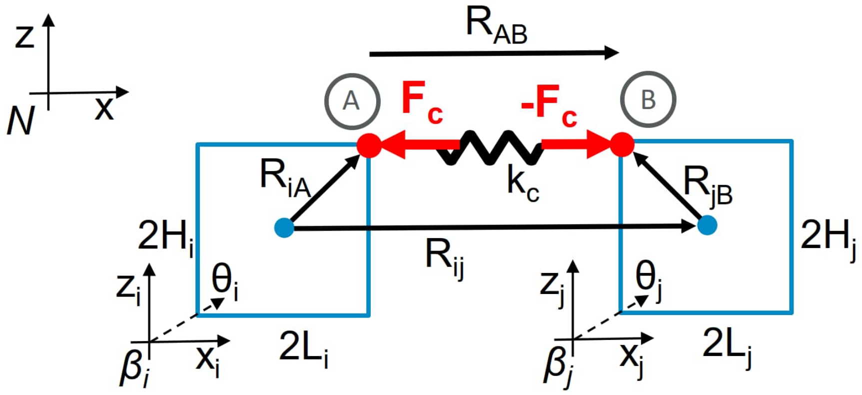

Figure 4.2: Free-Body Diagram (FBD) showing the connector forces and positions of the application point.

The motions of the bodies are expressed in inertial frame N in the general x (surge) and z (heave) direction. Each body has three degrees of freedom, $X_i = [x_i, y_i, \theta_i]^T$. The motion of body i is defined by X_i, $\dot{X}_i$, $\ddot{X}_i$, representing the displacement, velocity, and acceleration vector respectively. The body-attached frames β_i and β_j, are used to express points attached to the rigid bodies. The angles θ_i and θ_j are the angles of the bodies with respect to the inertial frame. Each body has a mass m, inertia J, a length $2L$ and height $2H$. The connecting spring is attached at point A on body i and point B on body j. The position vectors R_{iA} and R_{jB} from the CG to points A and B are expressed in body-fixed frames β_i and β_j respectively. The distance between the CG of the bodies is given by vector R_{ij}. The total spring force of the connection is a function of the change in spring length and the stiffness coefficient k_c. The current spring length is given by vector R_{AB}, and the elongation can be calculated using initial spring length L_0. The spring force F_c can be described by Equation 4.1.

$$F_c = \underbrace{k_c(|R_{AB}| - L_0)}_{\text{Magnitude}} \times \underbrace{\frac{R_{AB}}{|R_{AB}|}}_{\text{Direction}} \tag{4.1}$$

The first part of the equation defines the magnitude of the spring force and the second part the direction. Spring length vector R_{AB} is dependent on the position and the angle of the rigid bodies and can be written as the addition of the vectors R_{iA}, R_{ij}, R_{jB}. To express the spring length vector as a function of the displacements of the bodies, all vectors have to be expressed in the inertial frame as shown in Equation 4.2

$${}^{N}R_{AB} = -\,{}^{N}R_{iA} + {}^{N}R_{ij} + {}^{N}R_{jB} \tag{4.2}$$

Vector R_{ij} is a function of the postition of the CG of the two bodies, as expressed in Equation 4.3.

$${}^{N}R_{ij} = \begin{bmatrix} x_j - x_i \\ z_j - z_i \end{bmatrix} \tag{4.3}$$

To express vector R_{iA} and R_{jB} in the inertial frame, rotation matrix ${}^{N}C_{\beta i}$ from body frame βi to the inertial frame is used, as shown by Equations 4.4 and 4.5.

$$ {}^{N}R_{iA} = {}^{N}C_{\beta_i}\, {}^{\beta_i}R_{iA} = \begin{bmatrix} cos(\theta_i) & sin(\theta_i) \\ -sin(\theta_i) & cos(\theta_i) \end{bmatrix} \begin{bmatrix} L_i \\ H_i \end{bmatrix} = \begin{bmatrix} L_i cos(\theta_i) + H_i sin(\theta_i) \\ H_i cos(\theta_i) - L_i sin(\theta_i) \end{bmatrix} \tag{4.4} $$

$$ {}^{N}R_{jB} = {}^{N}C_{\beta_j}\, {}^{\beta_j}R_{jB} = \begin{bmatrix} cos(\theta_j) & sin(\theta_j) \\ -sin(\theta_j) & cos(\theta_j) \end{bmatrix} \begin{bmatrix} -L_j \\ H_j \end{bmatrix} = \begin{bmatrix} -L_j cos(\theta_j) + H_j sin(\theta_j) \\ H_j cos(\theta_j) + L_j sin(\theta_j) \end{bmatrix} \tag{4.5} $$

The contribution of the spring force to the Equations of Motion (EOM) of the system is shown in Equations 4.6-4.11. The x and z component of the force contributes to the total force in each respective direction. Since the force is applied at a distance from the CG of the bodies, a moment will also be applied by the spring force. When three dimensions are considered, the magnitude of this moment is calculated using the cross-product of the position and force vector. Since only two dimensions are considered, the moment is always perpendicular to the plane and can therefore be calculated by Equations 4.8 and 4.11.

$$ m_i \ddot{x}_i = -F_{c,x} \tag{4.6} $$

$$ m_i \ddot{z}_i = -F_{c,z} \tag{4.7} $$

$$ J_i \ddot{\theta}_i = (F_{c,x}\, {}^{N}R_{iA,z} - F_{c,z}\, {}^{N}R_{iA,x}) \tag{4.8} $$

$$ m_j \ddot{x}_j = F_{c,x} \tag{4.9} $$

$$ m_j \ddot{z}_j = F_{c,z} \tag{4.10} $$

$$ J_j \ddot{\theta}_j = -(F_{c,x}\, {}^{N}R_{jB,z} + F_{c,z}\, {}^{N}R_{jB,x}) \tag{4.11} $$

Looking at the equations, it should be noted that due to the rotation of the bodies, the spring force is geometrically nonlinear. Since a linear model is preferred, the spring force will be linearized using the approach presented in Appendix B, this approach is only valid for small rotations of the bodies. Using this approach, the spring can be linearized by assuming the angle of the spring does not change much from its initial angle α. The linearized spring force is described by Equation 4.12. Similar to Equation 4.1, the first part of the equation describes the magnitude of the spring force, and the second part describes the direction.

$$ F_c = \begin{bmatrix} k_c\ e\ cos(\alpha) \\ k_c\ e\ sin(\alpha) \end{bmatrix} \tag{4.12} $$

The spring elongation e is a function of the displacement of the two attachment points A and B and the initial spring angle α. The linearized displacement of the points is given by Equations 4.14-4.17, using the small-angle approximation.

$$ e = (u_{B,x} - u_{A,x}) cos(\alpha) + (u_{B,z} - u_{A,z}) sin(\alpha) \tag{4.13} $$

$$ u_{A,x} = x_i + \theta_i H_i \tag{4.14} $$

$$ u_{A,z} = z_i - \theta_i L_i \tag{4.15} $$

$$ u_{B,x} = x_j + \theta_j H_j \tag{4.16} $$

$$ u_{B,z} = z_j + \theta_j L_j \tag{4.17} $$

The calculation of the applied moment is also affected by the use of the small-angle approximation, resulting in a change in the equations of the rotation of the bodies, as shown in Equations 4.18,4.19.

$$J_i\ddot{\theta}_i = (F_{c,x}H_i - F_{c,z}L_i) \tag{4.18}$$

$$J_j\ddot{\theta}_j = (-F_{c,x}H_j + F_{c,z}L_j) \tag{4.19}$$

Considering the system as shown in Figure 4.2, the initial angle of the spring is zero degrees. Since the equations of motion are now linearized, the system of equations can be written in matrix form, as shown in Equation 4.20. The resulting stiffness matrix K_s will be referred to as the structural stiffness matrix, caused by the mechanical coupling between the different bodies in the model.

$$\underbrace{\begin{bmatrix} m_i & 0 & 0 & 0 & 0 & 0 \\ 0 & m_i & 0 & 0 & 0 & 0 \\ 0 & 0 & J_i & 0 & 0 & 0 \\ 0 & 0 & 0 & m_j & 0 & 0 \\ 0 & 0 & 0 & 0 & m_j & 0 \\ 0 & 0 & 0 & 0 & 0 & J_j \end{bmatrix}}_{\text{Mass matrix } M} \begin{bmatrix} \ddot{x}_i \\ \ddot{z}_i \\ \ddot{\theta}_i \\ \ddot{x}_j \\ \ddot{z}_j \\ \ddot{\theta}_j \end{bmatrix} = \underbrace{\begin{bmatrix} -k_c & 0 & -H_ik_c & k_c & 0 & H_jk_c \\ 0 & 0 & 0 & 0 & 0 & 0 \\ -H_ik_c/2 & 0 & -H_i^2k_c & H_ik_c & 0 & H_iH_jk_c \\ k_c & 0 & H_ik_c & -k_c & 0 & -H_jk_c \\ 0 & 0 & 0 & 0 & 0 & 0 \\ -H_jk_c/2 & 0 & -H_iH_jk_c & H_jk_c & 0 & H_j^2k_c \end{bmatrix}}_{\text{Structural stiffness matrix } K_s} \begin{bmatrix} x_i \\ z_i \\ \theta_i \\ x_j \\ z_j \\ \theta_j \end{bmatrix} \tag{4.20}$$

The presented model gives a first simplified model for the connection between two rigid bodies. However, the linearization approach used for the spring force has some limitations. This works for the particles as described in Appendix B, or when the motions of the bodies are primarily in the direction of the initially assumed spring angle. However, since the modelled structures are floating, motions in both the surge and heave directions are expected. Even though the angles of the individual floating structures may be assumed small (pitch angles) there is a possibility that a connection angle occurs due to the relative heave displacement between the bodies. Therefore it is important that the angle of the connection is not a fixed assumed angle.

4.2.2. Rigid Link with Flexible Boundaries

To be able to take the connection angle into account, the connection will be added as an additional rigid body to the model, which allows the position and rotation of the connection to be captured by the model. The single linear spring connecting the bodies is replaced by a rigid body, as shown in Figure 4.3. The body will act as a link between bodies i and j and will be referred to as the rigid link element.

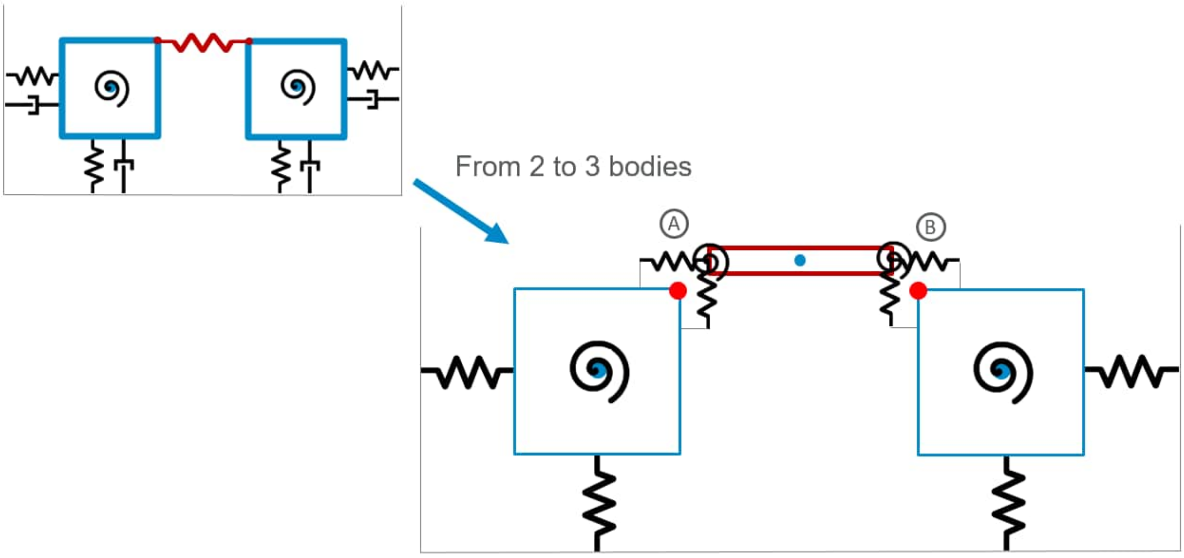

Figure 4.3: Second step in the modelling process, considering the connection between the bodies as a separate rigid body connected with springs and dampers in all DOF. Each spring element in the diagram also includes a damper, even though not shown.

The rigid link element is connected to the bodies at connection sides A and B with zero-length linear springs and a rotational spring. This results in a rigid connection with flexible boundaries at sides A and B. For the three DOF of each connection point a different stiffness can be used, providing a highly adaptable model of the connection. The RMFC model mentioned in Chapter 3 assumes a flexible connection between rigid floating bodies. For the connection between the installation vessel and a floating support structure, however, a mechanical connector attached to the installation vessel is used to make a temporary connection. Even though the RMFC model is used to describe the interaction between directly connected floating structures, the model does provide the linearized equations for a flexible connection. However, does not include rotational stiffness or damping in the connection. The mathematical description of the RMFC is expanded to describe the linearized interaction between the connection and bodies i and j. Subsequently, the geometric nonlinearities will be included in this description to generate a nonlinear version of the model to be able to assess the effects of linearizing. This results in the creation of the RLFB connection model. A FBD of the rigid link element, showing the relevant parameters and connection forces, is depicted in Figure 4.4. The mathematical description of the rigid link element will be presented below.

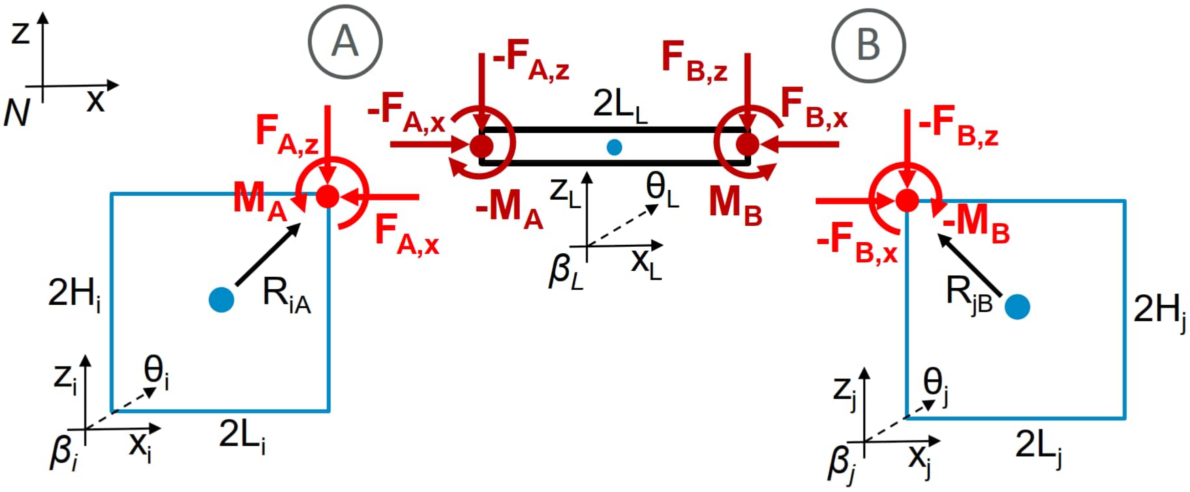

Figure 4.4: Free-body diagram showing the resulting connection forces between the link and bodies i and j as considered by the rigid link element.

Since the link is added as an additional body, the considered system now has a total of nine DOF, described by X_i, X_j, and X_L. The parameters for bodies i and j have remained similar, the link has length $2L_L$ and has an attached body frame β_L. The connection point of the link is in line with the CG of the body. The zero-length springs connecting the link to the bodies restrict the translations of the bodies in the horizontal and vertical directions, resulting in spring forces F_A and F_B. Additionally, torsion springs restrict the rotations between the bodies, resulting in moments M_A and M_B. The spring force in each DOF can be seen as a function of the displacement of the attachment points and the spring constant in the respective direction. Connection sides A and B now each has a stiffness matrix K_A and K_B, which is a diagonal matrix with the translational and rotational stiffnesses of the springs, as shown in Equation 4.21. Therefore, the stiffness of the connection can be influenced in six DOF.

$$K_A = \begin{bmatrix} k_{Ax} & 0 & 0 \\ 0 & k_{Az} & 0 \\ 0 & 0 & k_{Ary} \end{bmatrix} \qquad K_B = \begin{bmatrix} k_{Bx} & 0 & 0 \\ 0 & k_{Bz} & 0 \\ 0 & 0 & k_{Bry} \end{bmatrix} \tag{4.21}$$

The spring force is a relation between the elongation and the stiffness constant of the springs. Below the mathematical formulation will be provided for the interaction at connection side A, the derivation for side B is analogues. Similar to the approach described in Section 4.2.1, the displacements of the connection points will have to be derived to determine the change in spring length. Equations 4.14-4.17 can be written in matrix form, following a similar approach as shown for the RMFC model. The displacement vectors $u_{A,i}$ and $u_{A,L}$ of the connection points of side A on body i and L in the inertial frame can be determined by the linearized displacement transformation matrices N_{iA} and N_{AL} as shown in Equations 4.22, where X_i and X_L are the displacement vectors of the CG of body i and the link respectively.

$$u_{A,i} = N_{iA}X_i \qquad u_{A,L} = N_{LA}X_L \tag{4.22}$$

$$N_{iA} = \begin{bmatrix} 1 & 0 & R_{iA,z} \\ 0 & 1 & -R_{iA,x} \\ 0 & 0 & 1 \end{bmatrix} = \begin{bmatrix} 1 & 0 & H_i \\ 0 & 1 & -L_i \\ 0 & 0 & 1 \end{bmatrix} \tag{4.23}$$

$$N_{AL} = \begin{bmatrix} 1 & 0 & R_{LA,z} \\ 0 & 1 & -R_{LA,x} \\ 0 & 0 & 1 \end{bmatrix} = \begin{bmatrix} 1 & 0 & 0 \\ 0 & 1 & L_L \\ 0 & 0 & 1 \end{bmatrix} \tag{4.24}$$

Combining the linearized displacement transformation matrices N_{iA} and N_{AL}, leads to the expression of the transformation matrix T_A for connection side A, shown in Equation 4.25. This matrix describes the transformation of the displacement points to the CG for both bodies on side A of the connector.

$$T_A = \begin{bmatrix} N_{iA} & -N_{LA} \end{bmatrix} = \begin{bmatrix} 1 & 0 & H_i & -1 & 0 & 0 \\ 0 & 1 & -L_i & 0 & -1 & -L_L \\ 0 & 0 & 1 & 0 & 0 & -1 \end{bmatrix} \tag{4.25}$$

Using the transformation matrix, the structural stiffness matrix $K_{S,A}$ of side A of the connection can be described by Equation 4.26.

$$K_{S,A} = T_A^T\ K_A\ T_A = \begin{bmatrix} k_{Ax} & 0 & H_i k_{Ax} & -k_{Ax} & 0 & 0 \\ 0 & k_{Az} & -L_i k_{Az} & 0 & -k_{Az} & -L_L k_{Az} \\ H_i k_{Ax} & -L_i k_{Az} & k_{Ar} + H_i^2 k_{Ax} + L_i^2 k_{Az} & -H_i k_{Ax} & L_i k_{Az} & L_i L_L k_{Az} - k_{Ar} \\ -k_{Ax} & 0 & -H_i k_{Ax} & k_{Ax} & 0 & 0 \\ 0 & -k_{Az} & L_i k_{Az} & 0 & k_{Az} & -L_L k_{Az} \\ 0 & -L_L k_{Az} & L_i L_L k_{Az} - k_{Ar} & 0 & L_L k_{Az} & L_L^2 k_{Az} + k_{Ar} \end{bmatrix} \tag{4.26}$$

The 9x9 structural stiffness matrix of the rigid link element is a sum of the contributions of the stiffness matrices of sides A and B. Each quadrant of the structural stiffness matrices of connection sides A and B is added to the equations of the respective bodies. The contributions to the system's linear EOM for the link element are defined by Equation 4.27. Where M_i,M_j, and M_L are the mass matrices of the bodies, and X_i,X_j, and X_L the displacement vectors of the bodies and the link.

$$\begin{bmatrix} M_i & 0 & 0 \\ 0 & M_L & 0 \\ 0 & 0 & M_j \end{bmatrix} \begin{bmatrix} \ddot{X}_i \\ \ddot{X}_L \\ \ddot{X}_j \end{bmatrix} = \begin{bmatrix} K_{S,A[ii]} & K_{S,A[iL]} & 0 \\ K_{S,A[Li]} & K_{S,A[LL]} + K_{S,B[LL]} & K_{S,B[Lj]} \\ 0 & K_{S,B[jL]} & K_{S,B[jj]} \end{bmatrix} \begin{bmatrix} X_i \\ X_L \\ X_j \end{bmatrix} \tag{4.27}$$

The linear version of the model is now able to deal with limited rotations of the connection. It is however important to investigate the impact of the linearization of the equations, so a nonlinear version will be formulated as well. Replacing the linearized displacements with the geometrically nonlinear equations presented in the Section above, a nonlinear formulation of the RLFB can be made. Since there is no initial spring length, the displacements of the connection points directly relate to the elongation of the springs. The spring force vector F_A is comprised of the spring force in the horizontal and vertical direction, as well as the moment around the y-axis, which is calculated using the stiffness K_A and the displacement of the points on body i and L on side A of the connection (Equation 4.28). The formulation for the force on side B of the connection is analogues.

$$F_A = K_A(u_{A,i} - u_{A,L}) \tag{4.28}$$

The displacements $u_{A,i}$ and $u_{A,L}$ of side A of the connection can be calculated using the displacements of the CG of the bodies and the displacement caused by the rotation of the bodies, as shown in Equation 4.29 for body i.

$$u_{A,i} = \begin{bmatrix} x_i \\ z_i \\ \theta_i \end{bmatrix} + \begin{bmatrix} cos(\theta_i) & sin(\theta_i) & 0 \\ -sin(\theta_i) & cos(\theta_i) & 0 \\ 0 & 0 & 1 \end{bmatrix} \begin{bmatrix} R_{iA,x} \\ R_{iA,z} \\ 0 \end{bmatrix} \tag{4.29}$$

The resulting spring force acts on a point of the body and can be translated to the CG of the body using transformation matrix $T_{A,i}$. Please note the transformation matrix uses the position of the application point in the inertial frame to determine the moment around the CG caused by the spring force and is, therefore, dependent on the rotation of the body.

$$F_{c,i} = [T_{A,i} F_A] \tag{4.30}$$

$$T_{A,i} = \begin{bmatrix} 1 & 0 & 0 \\ 0 & 1 & 0 \\ {}^N R_{iA,z} & -{}^N R_{iA,x} & 1 \end{bmatrix} \tag{4.31}$$

A similar derivation is used to formulate the damping forces at the connection boundaries. The damping force is a function of the damping coefficient and the velocity between the bodies. The relative velocity at a point on the rigid body is a combination of the linear velocity of the CG of the body and the additional effect of the angular velocity of the body. The linearized formulation for the velocity of the connection point on body i of side A of the connection is shown in Equation 4.32.

$$v_{A,i} = \begin{bmatrix} \dot{x}_i \\ \dot{z}_i \\ \dot{\theta}_i \end{bmatrix} + \begin{bmatrix} \dot{\theta}_i R_{iA,z} \\ -\dot{\theta}_i R_{iA,x} \\ 0 \end{bmatrix} \tag{4.32}$$

Finally, the damping matrix can be calculated using the difference in velocity between the two bodies. The contribution to the linear EOM of the damping force is shown in Equation 4.33, where B_S is the structural damping matrix. Again, for the nonlinear formulation of the force, the geometric nonlinearities are taken into account.

$$\begin{bmatrix} M_i & 0 & 0 \\ 0 & M_L & 0 \\ 0 & 0 & M_j \end{bmatrix} \begin{bmatrix} \ddot{X}_i \\ \ddot{X}_L \\ \ddot{X}_j \end{bmatrix} = \begin{bmatrix} B_{S,A[ii]} & B_{S,A[iL]} & 0 \\ B_{S,A[Li]} & B_{S,A[LL]} + B_{S,B[LL]} & B_{S,B[Lj]} \\ 0 & B_{S,B[jL]} & B_{S,B[jj]} \end{bmatrix} \begin{bmatrix} \dot{X}_i \\ \dot{X}_L \\ \dot{X}_j \end{bmatrix} \tag{4.33}$$

4.3. Governing Equations of Motion

Now that the rigid link between the installation vessel and the floating support structure can be described, the next step is to add the additionally required modelling elements to capture the physical system. The additional elements allow for the addition of lift wires, connections, water ballast, and pre-tension on the connection. The model always contains three main bodies, the vessel, the floater and the wind turbine. The mass matrix M of each body is comprised of the mass and inertia of the bodies, for floating bodies, the added mass M_a is considered as well. The hydrodynamics of floating bodies are described by the hydrodynamic stiffness and damping matrices C and B. Suspended bodies, such as the wind turbine, have an applied gravity force F_G to the CG. These bodies interact in different ways based on the elements that are added. If required, multiple links, connections, ballasts and pre-tensions can be added to the system. Depending on which elements are included, a conditional script adds the respective body matrices and forces the system's EOM. The script is written to only require the basic parameters of the elements that need to be added and it will calculate the resulting EOM based on what is added. The effect of the interaction forces on the CG of the bodies is calculated and added to the EOM. Below is a description of the model elements, elaborating on the required parameters, the mathematical formulation and their contributions to the governing EOM. An overview of the required parameters for each element can be found in Table 4.1.

4.3.1. Model Elements

Rigid Link

The rigid link element uses the above mathematical formulation to add a rigid connection between two bodies in the model. In order to be added to the model the desired position on structures A and B should be provided, as well as between which structures the link should be added. The physical properties of the link are required to calculate the inertia of the link and assemble the mass matrix M_L. Its length is calculated based on the initial positions of the attachment points on the bodies, and the height is an additional input parameter. For each side of the connection, the stiffness and damping coefficients should be provided to form the K_A, K_B, B_A and B_B matrices. For the nonlinear model, the force F_L is added to the EOM, whereas for the linear model, the relevant entries are added to the K_S and B_S matrices.

Connection

The connection element is used to directly couple two bodies together. It makes use of a similar mathematical formulation as the link element, but only one side will be used. For the connection, the two bodies to be connected should be specified, as well as the position of the connection on each body. It is, however, important that the connection points on the two bodies have similar coordinates in the global coordinate system, to prevent initial errors in the model. The connection element can both have stiffness as well as damping. Therefore, the stiffness and damping coefficients in the three directions should be specified as well. For the nonlinear model, the force F_C is added to the EOM, whereas for the linear model, the relevant entries are added to the K_S and B_S matrices.

Lift Wire

The lift wire element is used to suspend the wind turbine from the installation vessel. For the linear model, the spring linearization as described in B is applied and the spring will only be able to exert forces in the initial (vertical) direction of the spring. The input parameters include both structures to which the wire attaches and the attachment location on each body. The wire stiffness will also have to be provided. The initial length is calculated using the initial position of the bodies. In the nonlinear model, the spring force will be calculated using the formulation of Section 4.2.1, and the force F_W will be added to the EOM, for the linear model the relevant entries are added to the K_S matrix.

Water Ballast

The water ballast will be added as an additional point mass on the rigid bodies. To add the ballast forces to the model, the application point on the structure and the mass of the ballast need to be specified. The mass of the ballast will be added to the mass matrix M of the bodies. Using the Parallel Axes Theorem the inertia is calculated based on the distance from the CG of the body and it will be added to the mass matrix of the body. Additionally, the point mass will introduce a gravitational force acting on a specified position on the body. The force can be translated to the CG of the body using Equation 4.30. For the linear model, it is assumed that due to the small angle assumption and the vertical direction of the force, the force on the CG of the body does not significantly change with a small rotation of the body. The nonlinear model does take into account the rotations of the attachment point. The applied forces do not change over time and are added as a separate force vector F_B.

Pre-tension Forces

When the ballast is changed on the floating structures, the system's static equilibrium will change. If there is no stiffness in the connection in the direction to counteract this force, it could be that a pre-tension at this location is required to rebalance the system. The application point of the pre-tension should be similar to the position of the connection between the bodies. The force and moment should be calculated and can be applied individually. Similar to the ballast force the pre-tension force will be translated to a force on the CG of the bodies and will be added as a separate applied force F_P.

Mooring System

Mooring stiffness is an additional stiffness action on the CG of the floating to simulate the mooring systems. The separate stiffness matrix K_m will be added to the model, a diagonal matrix with the stiffness in various DOF.

Table 4.1: Overview of required input parameters for the model elements.

Rigid Link	Connection	Lift Wire	Water Ballast	Pretension
Structure A	Structure A	Structure A	Structure	Structure
Structure B	Structure B	Structure B	Position Structure	Position Structure
Position Structure A	Position Structure A	Position Structure A	Mass	Force
Position Structure B	Position Structure B	Position Structure B		Moment
Stiffness (6DOF)	Stiffness (3DOF)	Stiffness (1DOF)		
Damping (6DOF)	Damping (3DOF)			
Mass				
Inertia				
Height				

4.3.2. Equations of Motion

The nonlinear equations of motion are a combination of the interaction forces in the system and the linear hydrodynamic matrices. Equation 4.34 shows the nonlinear EOM for the system. The states of the bodies in the model are given by X, $\dot{X}$, $\ddot{X}$ which are the displacement, velocity and acceleration vectors respectively.

$$(M+M_A)\,\ddot{X}+B\dot{X}+(C+K_M)X = F_G+F_{wave}(t)+F_L(X_i,\dot{X}_i)+F_C(X_i,\dot{X}_i)+F_W(X_i)+F_B(X_i)+F_P(X_i) \quad (4.34)$$

The left side of the equation describes the hydrodynamics of the model, and the influence of the mooring system K_M is added to the stiffness matrix. Gravity force F_G and wave force F_{wave} and the gravity force are applied to the CG of the bodies and do not change based on the motions of the bodies. The forces F_L (link forces), F_C (connection forces), F_W (wire forces), F_B (ballast forces), F_P (pre-tension forces) are results of the additional elements that are added to the model and are affected by the translations and rotations of the bodies. The linear EOM of the whole system can be described by the following Equation:

$$M\ddot{X} + (C + K_M + K_S)X + (B + B_S)\dot{X} = F_{wave} + F_G + F_B + F_P \quad (4.35)$$

The linear hydrodynamics remain unchanged, however, following the formulation in Section 4.2.2, the interaction of the added elements will be added as linear matrices as well. The matrices K_S and B_S are the structural stiffness and damping matrices added by the rigid-link, connection and wire elements. The ballast and pre-tension forces are linearized as well, therefore, the magnitude of these are now considered statically applied forces. The interaction between the various bodies in the model is now fully defined. In the next chapter, the equations will be used to formulate the model of the considered system.

5

Model Parameters and Implementation

This chapter will explain the implementation of the various presented modelling elements that will be used to investigate the dynamics of the wind turbine installation procedure considering the Huisman WIV and a semi-submersible floating support structure. Until now, the system has been abstracted to be able to formulate the mathematical model of the connection. However, it is important to implement the right parameters and allow for the required situations to be investigated. First, the installation procedure will be described in more detail, and five discrete installation stages will be identified in Section 5.1. Next, the parameters and dimensions of the main structures in the system will be presented in Section 5.2, as well as a general overview of the system. This section will also detail the integration of the hydrodynamic data from Ansys AQWA, and the model response will be validated against the results from Ansys AQWA. Section 5.3 will detail the implementation of the modelling elements as required to describe the interaction between the bodies in the system. A detailed explanation of the implementation of the various modelling elements will be given as well as a further elaboration on how the parameters are adapted for the different installation stages. Finally, the total system model will be presented, and the outcome of the time-domain and frequency-domain models will be compared and validated.

5.1. Installation Procedure

As mentioned in the introduction, the installation of a floating wind turbine is a complex procedure. In reality, the installation is a continuous process with system states constantly changing. Both under the influence of environmental conditions, as well as the interaction of various control inputs and motion compensation systems. The focus of this project is on the dynamics of the connection between the installation vessel and the floating support structure under various environmental loads. Therefore, the installation procedure has been divided into five discretized installation stages which allow the change in the system's behaviour to be studied. The installation vessel and the floating support structure are coupled with the connection during all five installation stages, the different stages consider the ballast transfer and the mating of the wind turbine as explained below. Installation stages 1 to 3 consider the ballast transfer between the floating support structure and the installation vessel, to investigate the influence of the change in mass on the dynamic behaviour of the system. During the first stage, the connection between the installation vessel and the floating support structure has been made, and no ballast has been transferred yet. Installation stage two considers 50 per cent of the mass of the turbine to be transferred from the first column of the floating support structure into the last column of the installation vessel. At installation stage three, all ballast has been transferred from the floating support structure to the installation vessel. During the first three stages, the wind turbine is suspended from the installation tower of the WIV. Once the ballast is transferred, the wind turbine will be lowered and mated to the support structure, as is shown in the figure at stage 4. During this stage, the whole system is connected since the turbine is still attached to the installation tower. Finally, the wind turbine is released at stage five of the installation process, while the floating support structure remains connected to the installation vessel. The five different stages of the installation procedure are shown in the simplified system diagrams in Figure 5.1.

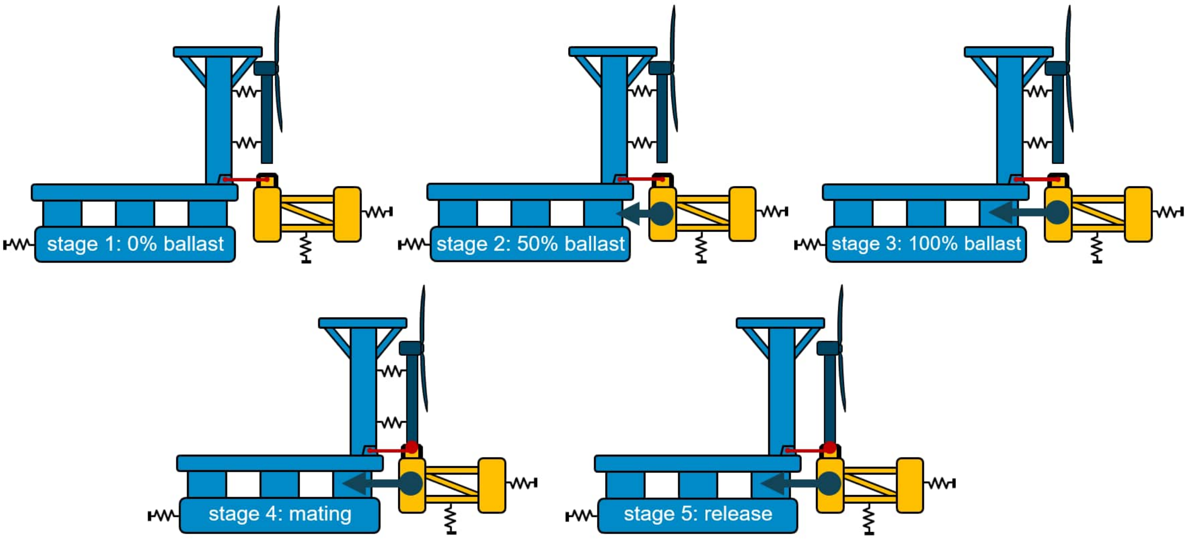

Figure 5.1: Overview of the five installation stages.

5.2. Structure Properties

The first step in the implementation of the model is to add the physical properties of the three main structures, the installation vessel, the floating support structure, and the wind turbine, to the bodies in the model. The chosen structure dimensions and properties are based on the Huisman WIV design and a current study using the WIV and a semi-submersible support structure carried out by Huisman. The dimensions of the wind turbine are based on the 15MW reference turbine as described by IEA (Gaertner et al., 2020). Figure 5.2 shows an overview of the body's main dimensions and CG locations.

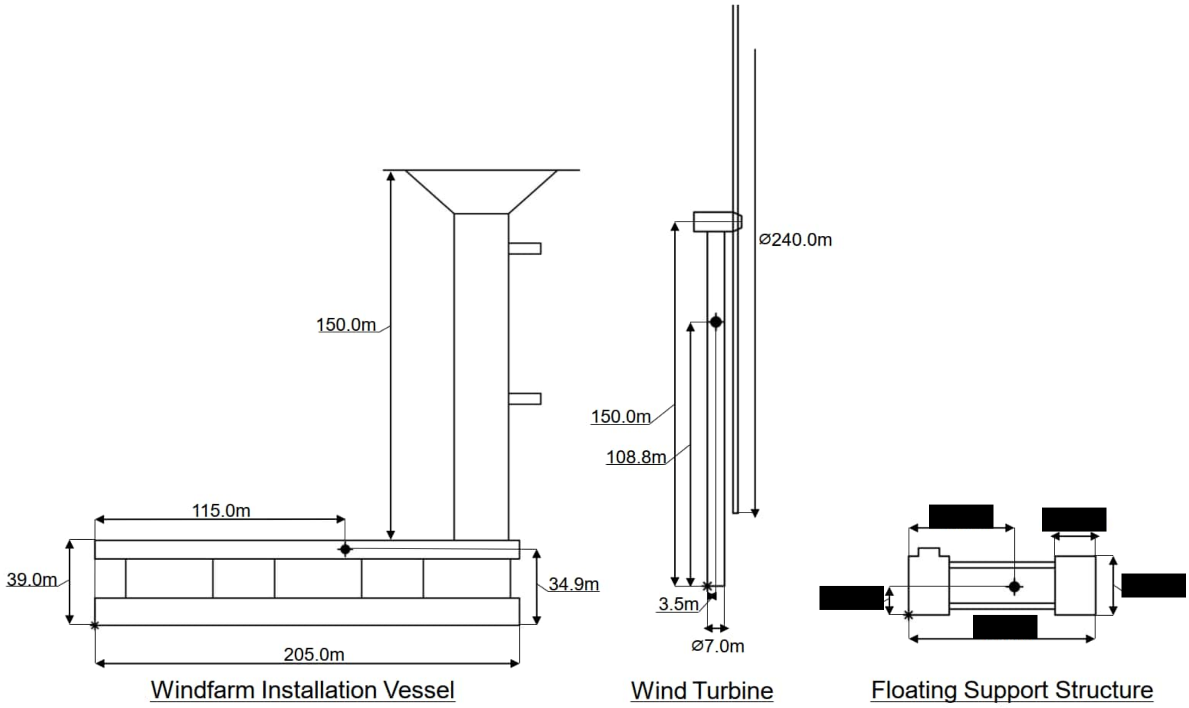

Figure 5.2: Overview of main structure dimensions and CG locations in the respective body frames.

The structure's mass and inertia are the most important physical properties of the structures to correctly include in the dynamic model of the system. These were obtained from an Ansys AQWA model containing the installation vessel and the floating support structure. The model of the installation vessel used in the Ansys AQWA analysis already includes a 15 MW wind turbine. To be able to add the wind turbine as a separate body to the model, the structural mass matrix of the installation vessel should be adapted by subtracting the mass and inertia of the wind turbine. Gaertner et al. (2020) provide the mass and inertia of the different components of the 15 MW IEA wind turbine. The total mass and inertia are determined by combining the values for the different components, the combined CG of the wind turbine is determined from presented mass distributions. Using the Parallel Axis Theorem, the added inertia of the wind turbine body is calculated and subtracted from the structural mass matrix of the installation vessel. To be able to use the provided hydrodynamic data from the Ansys AQWA analysis, the draft and position of the installation vessel should remain similar to the Ansys AQWA model. Since the mass of the wind turbine was originally included in the model, the draft and balance of the installation vessel should not change when added separately to the dynamic model. A gravity force, using a gravitational acceleration of 9.81 m/s^2, acts on the body of the wind turbine. This results in the weight of the wind turbine also being applied as a force on the attachment point on the vessel. To keep the draft of the vessel the same, an additional force is applied to the attachment point on the vessel to balance the effect of the wind turbine. This means the addition of the wind turbine as a separate body does not affect the static equilibrium of the installation vessel. It is assumed that, in practice, this can be seen as adding or removing water ballast to keep the installation vessel balanced and at the same draft, regardless of the stage of the operation. The inertial frame for the system model is chosen to be similar to the coordinate system in the Ansys AQWA model, to ensure the values obtained from the Ansys AQWA analysis can be used. The relative positions of the WIV and the floating support structure are shown in Figure 5.3, and the locations of the CGs of the structures are equal to the Ansys AQWA model. The wind turbine is positioned 10 meters above the floating support structure and centred above the front column during the first three installation stages. During installation stages 4 and 5, the wind turbine will be mated to the support structure, lowering the initial position of the CG of the wind turbine by 10 meters. The general arrangement of the total system is shown in Figure 5.3. An overview of the main parameters of the structures can be found in Table 5.1.

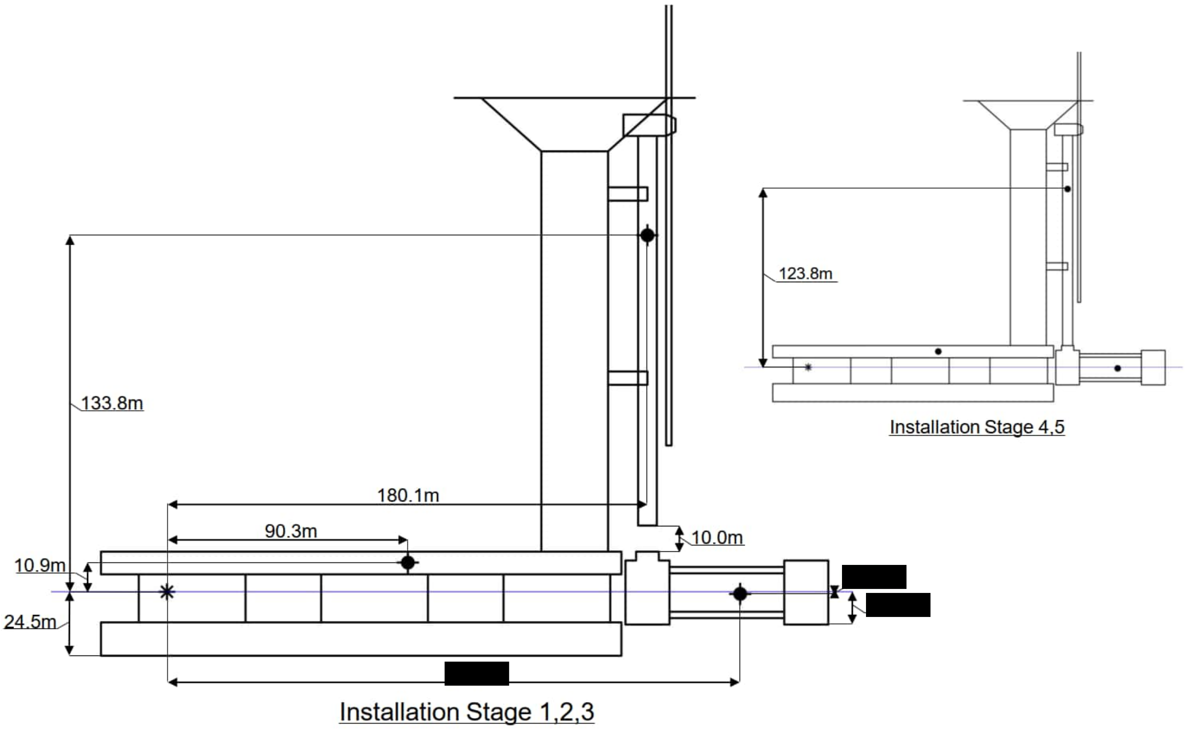

Figure 5.3: General arrangement of the system, indicating the positions of the installation vessel, wind turbine, and support structure in the inertial frame. For installation stages 4 and 5 only the position of the wind turbine is changed.

Table 5.1: Overview of main structure parameters.

Huisman WIV			Semi-submersible support structure		15 MW Reference Wind Turbine (Gaertner et al., 2020)		
Length Overall	205.0	m	Length (Side View)	[redacted]	Hub Height	150.0	m
Hull Depth	39.0	m	Column Diameter	[redacted]	Tower Diameter	7.0	m
Tower Height	150.0	m	Column Height	[redacted]	Rotor Diameter	240.0	m
Operational Draft	24.5	m	Operational Draft	[redacted]			
					Tower Mass	860	t
					RNA Mass	1017	t
Total Mass	153686	t	Total Mass	[redacted]	Total Mass	1877	t
(Pitch) Inertia	5.24E+11	$kg{\cdot}m^2$	(Pitch) Inertia	[redacted]	(Pitch) Inertia	5.33E+9	$kg{\cdot}m^2$
CG (body frame)	[115.0,34.9]	m	CG (body frame)	[redacted]	CG (body frame)	[3.5,108.8]	m
CG (inertial frame)	[90.3,10.9]	m	CG (inertial frame)	[redacted]	CG (inertial frame) *Installation stage 1,2,3*	[180.1,133.8]	m
					CG (inertial frame) *Installation stage 4,5*	[180.1,123.8]	m

5.2.1. Hydrodynamics

The hydrodynamics of the floating structures are implemented using the linear hydrodynamic matrices, which result from the Ansys AQWA analysis. The Ansys AQWA model includes three-dimensional models of the structures, only the surge, heave and pitch data will be considered to generate the matrices for the proposed model. The analysis carried out considers a water depth of 1000 meters, and the behaviour of the system for various wave headings and wave periods is investigated. Regular wave excitation is considered with 50 discrete wave periods determined based on the eigenfrequencies of the structures in the model, ranging from 3.49 to 62.83 seconds. All wave periods are analyzed for wave headings ranging from 180 to -180 degrees, with 15-degree intervals. During this study, the main wave heading considered will be head waves, or 0 degrees, along the longitudinal direction of the system. The output of the analysis provides the required linear system matrices, M, C, B_v, $A$and B for both the installation vessel and the floating support structure. The structural mass matrix M includes the mass and inertia values as shown in Table 5.1 and are obtained from the physical properties of the structures. The hydrostatic stiffness matrix C and additional viscous damping term B_v, are frequency independent. Added mass matrix A and damping matrix B are frequency dependent and change for the different wave excitation periods. The wave forces the structures experience for each wave period are also provided by Ansys AQWA. The wave excitation force is given as a single harmonic excitation force for each DOF, as mentioned in Section 3.2.2. The forces are described at the CG of the structures, giving the amplitude per meter wave height in Newton and the phase shift with respect to the harmonic wave. For both structures, the crest of the wave will occur at a different time because of the distance between the CG of the structures. This means the phase of the force experienced at the CG of the structures and the phase shift due to the distance between the structures have to be taken into account when applying the excitation force to the structures. Equation 5.1 shows how to determine the phase difference between the CG of the body and the origin of the inertial frame.

$$\phi = kxcos(\theta) + kysin(\theta) \tag{5.1}$$

Where ϕ is the phase shift, k is the wave number, $[x, y]$ is the location of the structure, and θ is the wave heading.

This results in the following equation for the excitation force on a structure.

$$F_{exc} = F_{amplitude} \cdot cos(-\omega t + F_{phase} + \phi) \tag{5.2}$$

Where F_{exc} is the excitation force, $F_{amplitude}$ is the amplitude of the given wave force, ω is the wave frequency, t the time step, F_{phase} is the phase of the given wave force, and ϕ is the phase shift due to the location in the inertial frame.

For both structures, the phase difference is added to the phase of the resulting wave force from Ansys AQWA. In the time domain simulation, this results in a shifted harmonic excitation. In the frequency domain, the additional phase shift is accounted for when determining the relative motions between the structures. After the hydrodynamic data is implemented, the response of the model is compared to the resulting RAOs provided by Ansys AQWA. The comparison of the magnitude and phase of the response for a wave heading of zero degrees is shown in Figure 5.4. Here, the response at the CG of the structures is shown, not considering phase differences due to the distance between the structures. As can be seen from the graph, the responses are very similar, therefore, the hydrodynamic response of the model is deemed to be sufficient.

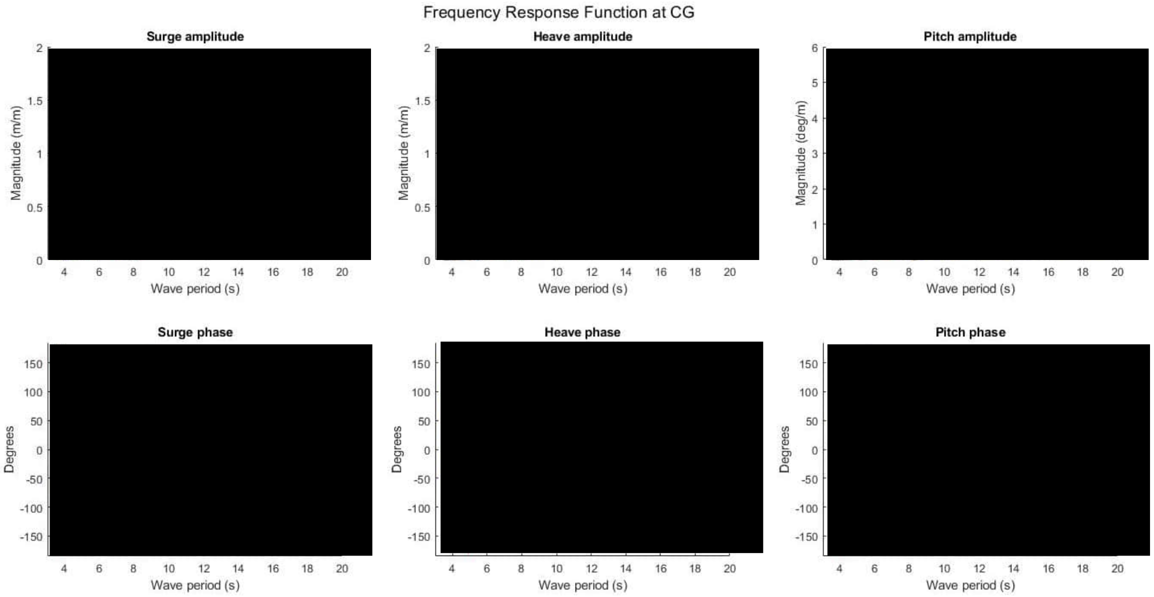

Figure 5.4: Comparison between the RAOs provided by Ansys AQWA and the 2-D linear hydrodynamic model showing the response at the CG of the floating bodies.

Mooring stiffness is not included in the Ansys AQWA analysis. Therefore this will be added separately to the model. During early time-domain simulations, it was observed that the addition of the mooring and DP system is required to keep the floating structures from drifting. The installation vessel is not connected to a fixed mooring system but uses a DP system to remain in position. The mooring system of the floating support structure is very complex. However, the mooring is not very stiff due to its long length and use of polyester material and will therefore have a small effect on the behaviour of the support structure. Since this research focuses on the connection between the structures, it is only essential to consider a potential change in dynamic behaviour. The implementation of the mooring system during this study is kept simple. Based on practical experience, it is chosen to tune the mooring stiffness of both structures to a natural surge period of around 105 seconds. This results in a DP stiffness of 5.93*10^5 N/m for the WIV and a mooring stiffness of [redacted] N/m for the floating support structure. The mooring stiffness will be added as a separate matrix K_m to the stiffness matrix C of the floating structures.

5.3. Structure Interaction

The next step is to implement the modelling elements presented in Chapter 4 to describe the interaction between the structures. The various installation stages require different combinations of parameters for the modelling elements. Below, the implementation of the connection model, the coupling of the wind turbine, and the implementation of the ballast and pretension will be described.

5.3.1. Connection

Three different methods of adding a connection between the installation vessel and the floating support structure will be implemented, using two different modelling elements. The three different connection types differ in the number and positions of the flexible sides of the connection, as shown in Figure 5.5. Connection type 1 is fixed at the side of the vessel and has a flexible connection on the side of the support structure, as indicated by the blue bar in the figure. Instead of the link element, this connection type uses the connection element with three DOF on the support structure side. Conversely, connection type 2 is fixed at the side of the support structure and is flexible at the side of the installation vessel, as indicated by the yellow bar in the figure. Connection type 3 is the most versatile, making use of the rigid link element, which adds a flexible connection on both sides of the link, as indicated by the red connection element in the figure.

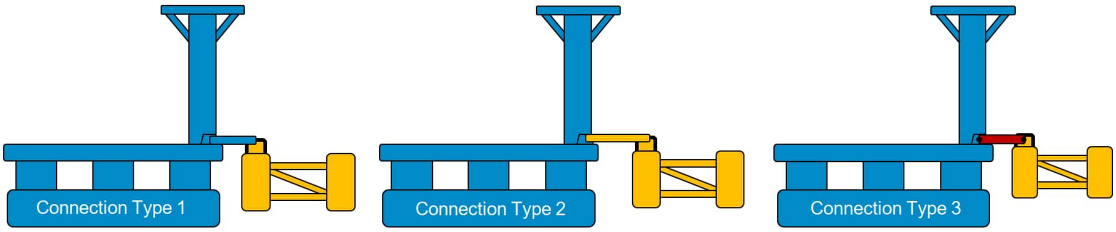

Figure 5.5: Overview of the three considered connection types.

Using the rigid link element, a fixed connection will be approached using a high finite stiffness since, in practice, a fixed connection will probably be required on at least one side of the connection. The behaviour of the three different connection types will be compared to validate the link element's implementation and investigate the effect of using a finite stiffness to approach a fixed connection. It should be noted that the inertia of the rigid link is not added to the bodies when using connection types 1 and 2. An overview of the connection locations from the body's CG for the different connection types and the rigid link parameters are shown in Table 5.2. The mass and dimensions of the rigid link are determined in consultation with Huisman, the weight is chosen to be 6000 t and the height of the connection is 3 meters. For now, gravity forces acting on the link are neglected, since it is assumed that the link is supported by the installation vessel. The mass and inertia effects on the accelerations of the link are included since these will affect the dynamic behaviour of the system. Different values for the stiffness and damping coefficients for each side of the connection can be applied, where k and b indicate the stiffness and damping coefficients and the direction and side of the connection are indicated by x, z, ry and A, B respectively. These values will be varied in the system Analysis and are specified in the next Chapter. Figure 5.6 shows a schematic indicating the location of the rigid link element connecting the installation vessel and the floating support structure.

Table 5.2: Overview of the model elements used for the different connection types.

	Connection Type 1	Connection Type 2	Connection Type 3
Element	Connection	Connection	Rigid Link
Structure A	WIV	WIV	WIV
Position on A	[89.8,4.1] m	[75,4.1]m	[75,4.1] m
Structure B	Support Structure	Support Structure	Support Structure
Position on B	[redacted] m	[redacted] m	[redacted] m
Stiffness A	fixed	$[k_{xA}, k_{zA}, k_{ryA}]$ N/m	$[k_{xA}, k_{zA}, k_{ryA}]$ N/m
Damping A	fixed	$[b_{xA}, k_{zA}, b_{ryA}]$ Ns/m	$[b_{xA}, k_{zA}, b_{ryA}]$ Ns/m
Stiffness B	$[k_{xB}, k_{zB}, k_{ryB}]$ N/m	fixed	$[k_{xB}, k_{zB}, k_{ryB}]$ N/m
Damping B	$[b_{xB}, b_{zB}, b_{ryB}]$ Ns/m	fixed	$[b_{xB}, b_{zB}, b_{ryB}]$ Ns/m
Mass	-	-	6000 t
Height	-	-	3 m
Inertia	-	-	1.14E+8 $kg{\cdot}m^2$

5.3.2. Wind Turbine

The wind turbine is coupled to the rest of the system using the modelling elements described in Table 5.3. During the first three installation stages, the wind turbine is suspended from the installation vessel and held in place by the two motion-compensated grippers. To represent this in the model, the turbine will be coupled to the installation vessel with a lift wire element and is connected to the installation tower using two connection elements which can be seen as the grippers. The stiffness of the grippers is determined based on the design eigenfrequency of a mechanical system this size, which is around 1 second in practice. The initial position of the turbine is changed to account for the elongation of the lift wire. Not changing the position results in oscillations since there is no damping in the wire. This results in an offset of -0.23 meters of the initial heave position of the wind turbine, effectively pre-stretching the lift wire and moving the wind turbine to its static equilibrium position. At stages 4 and 5, the wind turbine is mated to the support structure, which is achieved using a connection element, coupling the wind turbine tower to the floating support structure. The stiffness of the connection element is chosen to be very high in all three directions, effectively fixing the two bodies together. During the fourth installation stage, the whole system is coupled since the wind turbine is still in the gripper of the installation vessel. In practice, the grippers will be motion-compensated during this stage. Therefore, the grippers will behave as a more flexible system. The gripper stiffness is lowered to 2 per cent of the original stiffness during stage 4 to prevent very large gripper forces and to prevent the grippers from influencing the relative motions. The lift wire still supports the weight of the turbine during this stage. The wind turbine is released from the tower during the fifth installation stage and is only connected to the floating support structure. Figure 5.6 shows a schematic indicating the locations of the wire element and the top and bottom grippers.

Table 5.3: Overview of used elements to couple the wind turbine body.

	Lift-Wire	Connection 1 Top Gripper	Connection 2 Bottom Gripper	Connection 3 Mating Point
Stage	Stage 1-4	Stage 1-4	Stage 1-4	Stage 4-5
Structure A	WIV	WIV	WIV	Support Structure
Structure B	Wind Turbine	Wind Turbine	Wind Turbine	Wind Turbine
Position on A	[89.8,174.1] m	[89.8,138.1]m	[89.8,69.1] m	[redacted] m
Position on B	[0,37.2] m	[0,15.2]m	[0,-53.8] m	[0,-108.8] m
Stiffness	8E+4 kN/m	[4E+4,0,0] kN/m	[4E+4,0,0] kN/m	[1E+5,1E+7,1E+9] kN/m
Damping	-	[5E+4,0,0] kNs/m	[5E+4,0,0] kNs/m	[1E+2,1E+2,1E+2] kNs/m

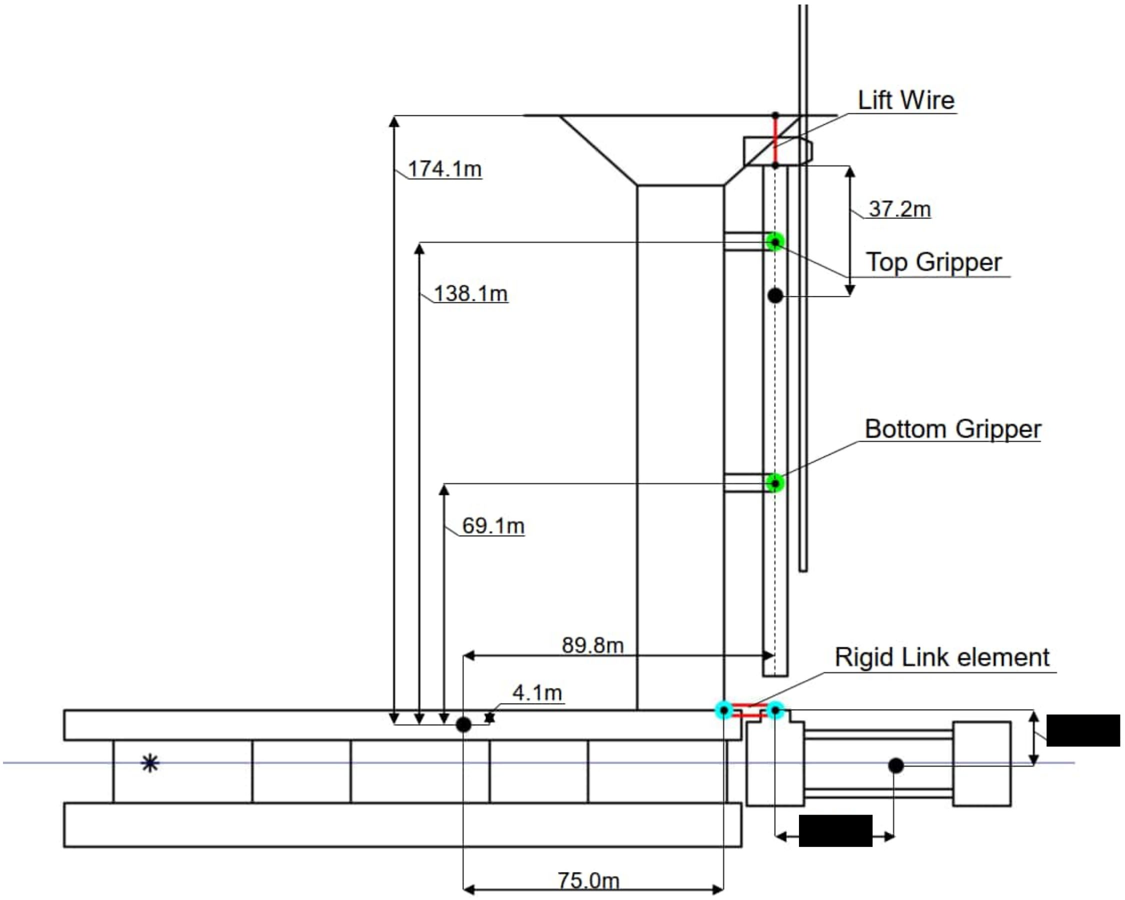

Figure 5.6: Schematic showing the positions of the various coupling elements in the system.

5.3.3. Ballast

During the installation procedure, ballast is moved from the floating support structure to the installation vessel to account for the mass of the wind turbine being placed onto the support structure. For this research, it is assumed that the total amount of ballast being removed from the support structure is equal to the mass of the wind turbine since the ballast is moved from the column on which the wind turbine will be mated. Removing a similar mass from a similar distance from the CG as the wind turbine when placed means the draft and balance of the support structure remain equal. When the wind turbine is released from the installation vessel, the balance and draft of the installation vessel should also remain similar. Since, for the installation vessel, it is not possible to house the water ballast at the same distance from the CG as the wind turbine is suspended, additional ballast is required to keep the vessel balanced. As mentioned before, the draft of the vessel must remain similar to be able to use the hydrodynamic data. The wind turbine is suspended at a distance of 89.8 meters from the CG of the installation vessel, and the ballast is located at 56 meters from the CG. Since the distance from the CG for the two masses is different, the installation vessel will experience a moment causing it to pitch. This means that additional ballast from the front of the vessel will have to be pumped to the rear to rebalance the vessel. In doing so, no additional ballast is required, and the draft of the vessel will remain similar. During installation stages 1 to 3, the ballast is increased from 0 to 50 to 100 per cent of the total ballast mass. An overview of the mass and position of the ballast elements for each structure is shown in Table 5.4.

Table 5.4: Overview of ballast elements in the model.

	Ballast 1 (turbine mass + rebalancing ballast)	Ballast 2 (rebalance the installation vessel)	Ballast 3 (turbine mass removed from support structure)
Structure	WIV	WIV	Support Structure
Position on S.	[56.2,-4.4] m	[-56.2,-4.4] m	[redacted] m
Mass	2443 t (1877+566 t)	-566 t	-1877 t

5.3.4. Pretension

The ballast transfer procedure changes the balance of the system. When no opposing force is present, the floating support structure will start to obtain a positive pitch angle and the front column will start to rise due to the decreased mass. During early time domain simulations, it was observed that the pitch angles of the bodies can reach as much as 8 degrees without wave excitation. Therefore, the proposed installation procedure's success depends on the forces due to ballast transfer to be supported by the connection. Simultaneously, the connection model should be as versatile as possible, and ideally, the system should remain in equilibrium without the addition of stiffness in the connection. A pre-tension will therefore be applied at the connection boundaries to maintain a balanced system, regardless of the stiffness of the connection. The behaviour resulting from different connection stiffnesses will then only be dependent on the motions of the system due to the wave excitations and can be more easily compared for different configurations. In practice, pretension can be applied to hydraulic cylinders to 'carry' the main part of the load. On top of that, an additional dynamic stiffness can be introduced to limit the system's motions due to wave excitation. The pre-tension values are determined by calculating the static equilibrium for the applied ballast loads. An equal amount of force is applied to each body not to offset the overall equilibrium of forces in the system. During the different installation stages, the pretension scales with the change in ballast. Table 5.5 shows the applied pre-tension for the different connection types. Figure 5.7 shows a schematic indicating the location of the ballast and pre-tension forces.

Table 5.5: Overview of pretension elements in the model for the various connection types.

	Connection Type 1	Connection Type 2	Connection Type 3
Structure	WIV	WIV	WIV
Position on S.	[89.8,4.1] m	[75,4.1]m	[75,4.1] m
Force	18413 kN	18413 kN	18413 kN
Moment	-	-272021 kNm	-272021 kNm
Structure	Support Structure	Support Structure	Link side A
Position on S.	[redacted] m	[redacted] m	[-7.4,0] m
Force	-18413 kN	-18413 kN	-18413 kN
Moment	-	272021 kNm	272021 kNm
Structure			Link side B
Position on S.			[7.4,0] m
Force			18413 kN
Moment			0 kNm
Structure			Support Structure
Position on S.			[redacted] m
Force			-18413 kN
Moment			0 kNm

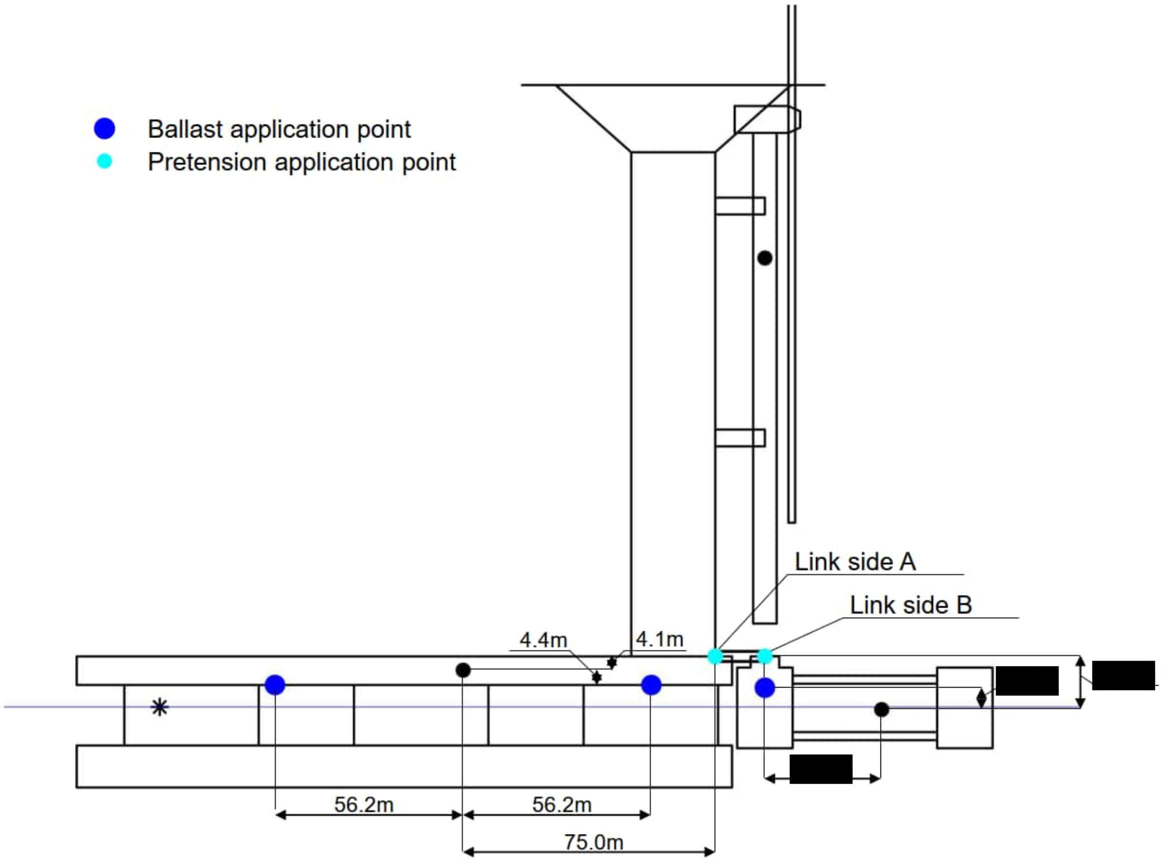

Figure 5.7: Schematic showing the positions of ballast and pretension application points on the bodies in the model.

5.4. The System Model

The system model is now fully defined. Combining the mathematical formulation of the used elements, the model's linear EOM, using connection type 3 including the rigid link as a fourth body, are shown in Equations 5.3. For the different installation stages, the general structure of the equation does not change. Certain matrices do change depending on the coupling of the bodies.

$$\begin{aligned}
&\begin{bmatrix} M_v + A_v & 0 & 0 & 0 \\ 0 & M_f + A_f & 0 & 0 \\ 0 & 0 & M_t & 0 \\ 0 & 0 & 0 & M_L \end{bmatrix} \begin{bmatrix} \ddot{X}_v \\ \ddot{X}_f \\ \ddot{X}_t \\ \ddot{X}_L \end{bmatrix} + \begin{bmatrix} (B_v + B + B_S)_v + & 0 & 0 & 0 \\ 0 & (B_v + B + B_S)_f & 0 & 0 \\ 0 & 0 & (B_S)_t & 0 \\ 0 & 0 & 0 & (B_S)_L \end{bmatrix} \begin{bmatrix} \dot{X}_v \\ \dot{X}_f \\ \dot{X}_t \\ \dot{X}_L \end{bmatrix} \\
&\quad + \begin{bmatrix} (C + K_m + K_S)_v & 0 & 0 & 0 \\ 0 & (C + K_m + K_S)_f & 0 & 0 \\ 0 & 0 & (K_S)_t & 0 \\ 0 & 0 & 0 & (K_S)_L \end{bmatrix} \begin{bmatrix} X_v \\ X_f \\ X_t \\ X_L \end{bmatrix} \\
&\quad = \begin{bmatrix} F_v^{wave} \\ F_f^{wave} \\ 0 \\ 0 \end{bmatrix} + \begin{bmatrix} 0 \\ 0 \\ F_t^{gravity} \\ 0 \end{bmatrix} + \begin{bmatrix} F_v^{ballast} \\ F_f^{ballast} \\ 0 \\ 0 \end{bmatrix} + \begin{bmatrix} F_v^{pretension} \\ F_f^{pretension} \\ 0 \\ F_L^{pretension} \end{bmatrix}
\end{aligned} \tag{5.3}$$

A MATLAB tool has been scripted, which generates the equations of motions based on the input parameters for the different system configurations and different wave excitation forces. Both frequency-domain and time-domain simulations can be run with the tool, and the results for each run can be saved. The frequency domain behaviour is evaluated using RAOs, and the time-domain results are calculated using the numerical Runge Kutta 4 approach, as explained in Section 3.2.1. The system's frequency response is plotted, and for time-domain simulations, an animation can be created showing the system's motions for the simulated time. To avoid erratic behaviour in the time domain simulations, a wave ramp-up period can be specified during which the wave force is slowly built up. For the time-domain simulation, linear and nonlinear model versions can be created and evaluated. The computation time for the nonlinear model is significantly higher, around ten times, due to the more complex equations that must be evaluated for each time step. Calculating the system's frequency response is the quickest method of analysing the system, taking less than a second for a certain configuration. The output parameters for the models are the chosen system states, the positions and velocities of the CGs of the structures. The relative motions and forces between points on the bodies are required to determine the system's performance. The next chapter will cover which points are considered and how the relative motions are calculated. A figure of a time-domain animation output of the MATLAB tool is shown in Figure 5.8. The plotted body's dimensions are based on the specifications, and the location of the CG of each body is indicated with a black dot. Here, the red line indicates the wire element, the green dots show the system coupling using the connection element, and the red body connected with cyan dots is the rigid-link element. The angles of the bodies are updated for each time step to indicate the current state of the system.

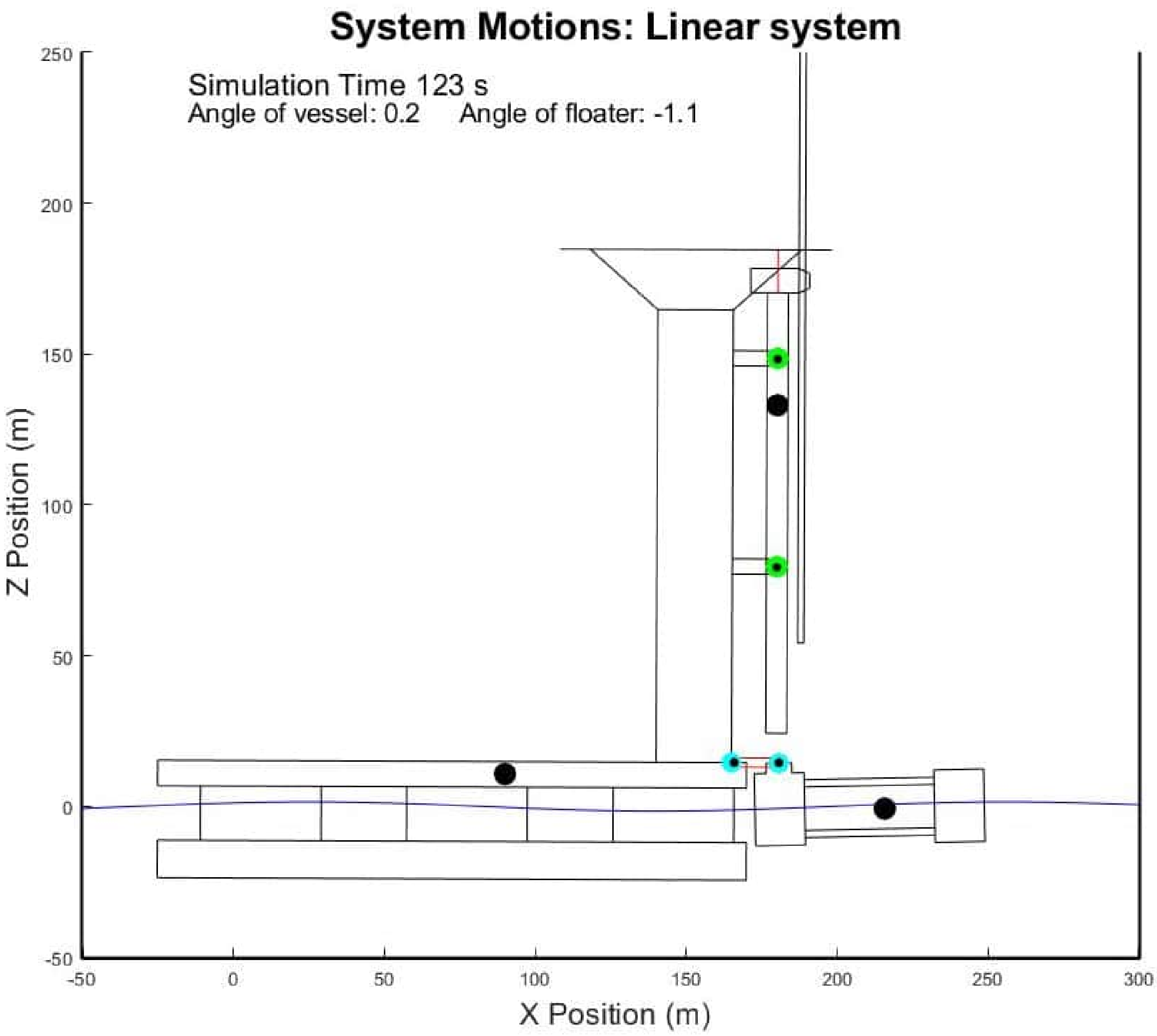

Figure 5.8: The animation output of a time-domain simulation created by the MATLAB tool

Validation

The behaviour of the model will be compared between the time domain and the frequency domain. Considering regular waves with an amplitude of 2 meters, the steady state displacements of the time-domain results should reach a similar amplitude as the frequency response. Figure 5.9 compares the response of the CG of the bodies for a wave period of 12.1689 seconds. The time-domain graph shows that after around 200 seconds, the steady state is reached. The amplitude of the time domain closely matches the amplitude calculated from the system's frequency-domain analysis with a similar configuration (shown with dashed lines). This indicates that the model behaves as expected.

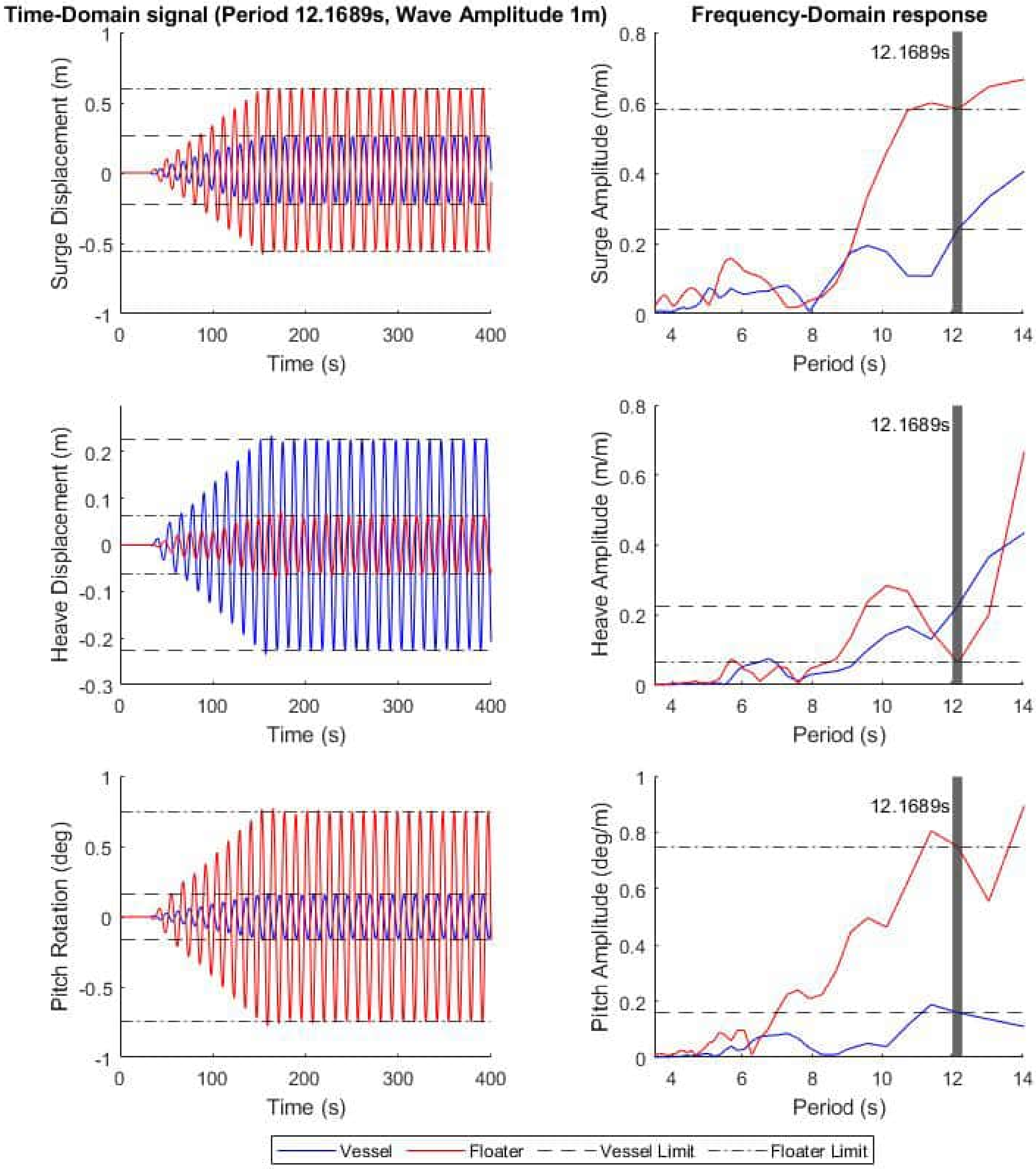

Figure 5.9: Comparison between the Time-domain and Frequency domain results of the linear model.

Next, the difference in behaviour between the three connector types is investigated. Figure 5.10 compares connection types with similar stiffness characteristics. In the comparison between connection types 1 and 3, the vessel side of the connection is fixed. Whereas for connection types 2 and 3, the fixed side is at the floater. This comparison compares three different configurations of each connection type. One side of the connection is fixed, and on the other side, a high stiffness will be added in one direction of motion. The red lines indicate a high stiffness in the surge direction, the green lines in the heave direction, and the blue lines in the pitch direction. The other directions are free at the flexible side of the connection. The performance of the connection types is compared by looking at the relative motion at the mating point. A further explanation of how the relative motion is derived will be given in the next chapter. The solid lines indicate the performance of connection type 3, using a rigid link element, and the dashed lines are the model's response using connection types 1 and 2. Overall, the behaviour of the system using connection types 1 and 3 is comparable. However, larger differences are observed when the connection is fixed at the support structure side. The missing inertia of the link most likely explains this. Since the mass of the installation vessel is large compared to the mass of the link, neglecting it has less impact on the result. Contrary, when adding the mass and inertia of the link to the support structure, the difference in behaviour is much more significant.

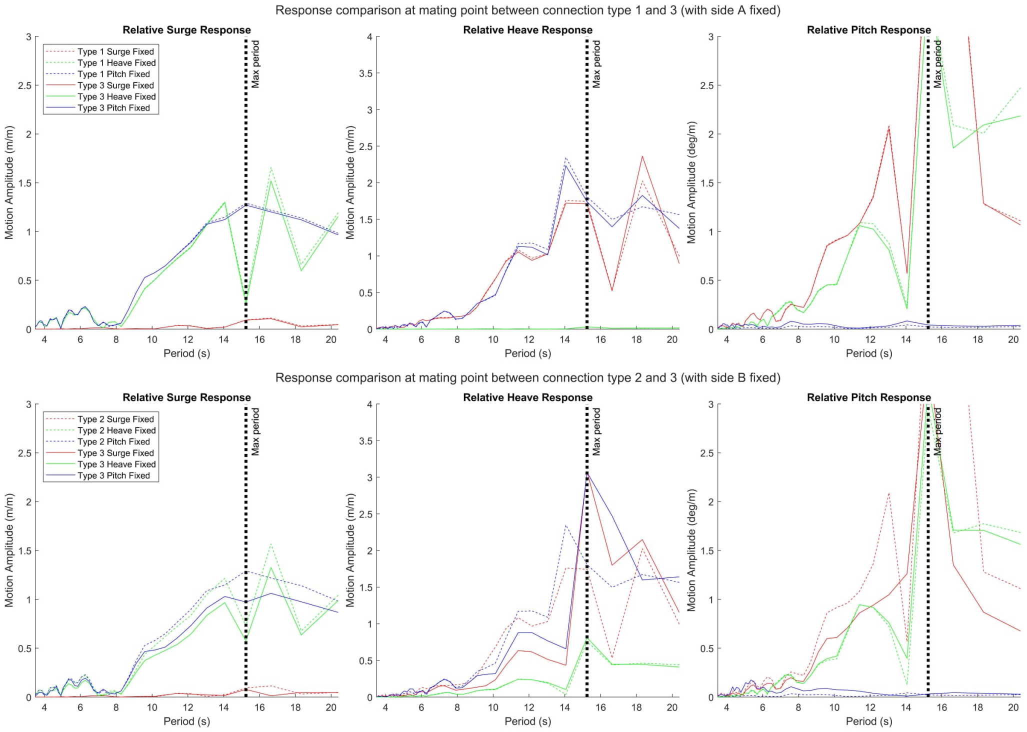

Figure 5.10: Graph comparing the motions between connection types 1 and 3, and 2 and 3 for different connection stiffness configurations.

Not only the relative displacements of the different connector types are of interest, the forces on the connection points should also be compared. Similar to the motions, comparing the forces between connection types 2 and 3 shows large deviations. Therefore, the implementation of connection type 2 is deemed inadequate and will not be considered. The comparison between connection types 1 and 3, is shown in Figure 5.11. The forces experienced by the flexible side of the connection are very similar. Since there is only a stiffness in one direction of the connection, only forces in one direction for each configuration are shown.

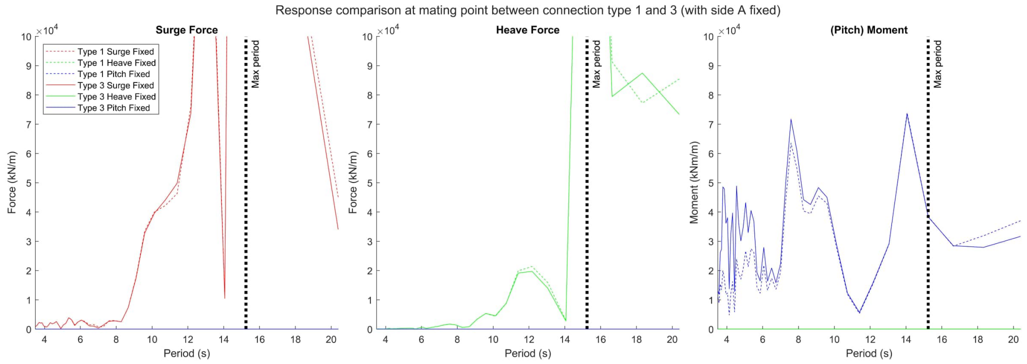

Figure 5.11: Graph comparing the connection forces of the flexible side of the connection between connection types 1 and 3.

These results show that the different connection types behave similarly. Connection type 3 also seems to be able to simulate fixed connections using a high finite stiffness. Therefore, it is decided that for further system analysis connection, only connection type 3 will be considered. In the next chapter, the stiffness of both sides of the connection will be varied.

6

System Analysis

Even though the model is a simplification of reality, the system contains many variables of interest. It is therefore vital that specific parameters are investigated which are essential at this early stage of the design process. This chapter details the system analysis that has been performed to better understand how the system's performance is influenced by its structural configuration. The parameter study focuses on varying the stiffness of the link between the installation vessel and the floating support structure in various directions, to investigate how the stiffness influences the motions and loads of the system. First, the performance metrics and operational limits of the system will be described. The performance metrics will detail which motions and loads are considered to assess the performance of the system. This is followed by a description of the operational limits that have been defined to limit the scope of the analysis and to be able to quantify the result data. Next, the setup of the frequency domain parameter study will be detailed. Starting with a description of the various stiffness values that will be considered. The effect of the different installation stages on the behaviour of the system will be briefly discussed, after which a number of parameter groups will be defined to further investigate the behaviour of the system. Finally, the results of running the different parameter groups will be presented and discussed.

6.1. Performance Metrics and Operational Limits

The presented model describes a complex dynamic system, of which two translations and one rotation per body are used to describe the total system motions. Many variables can be obtained from the model output, and it is important to find those relevant to the investigated system's performance. As mentioned in the introduction, the relation between the motions and loads of the system is being investigated. Therefore, the motions of the connection point on both the floater and the vessel will be considered potential performance metrics. Using the relative displacement and velocity between the connection point on the vessel and the link and between the floating support structure and the link, the total expected connection forces can be derived. The goal of the system is to be able to connect the wind turbine to the floating support structure successfully. The relative motions between the bottom of the wind turbine tower and the mating point on the floating support structure are very important for the successful mating procedure. Since the wind turbine is motion compensated, it is also important to consider the wind turbine's motions relative to the installation tower. The displacement will be the largest at the top gripper location. Therefore, the location of the top gripper on the vessel and on the wind turbine are identified as points of interest as well. During the initial installation stages, the wind turbine is still connected to the installation vessel, and the relative motions between the vessel and the wind turbine will be small. Motion compensation is not included in the model, but the required range of motion can be approximated by looking at the motions of the floating support structure. Once the turbine is installed, it will have a fixed connection to the floating support structure, and the wind turbine will have to follow the motions of the floating support structure. This means that right before connecting, the gripper should be able to follow the translations and rotations of the wind turbine relative to the floating support structure. The relative displacement between the top gripper and the wind turbine is a function of the pitch angle of the floater and the relative surge motion at the mating point. Figure 6.1

shows the locations of the identified points of interest in the system.

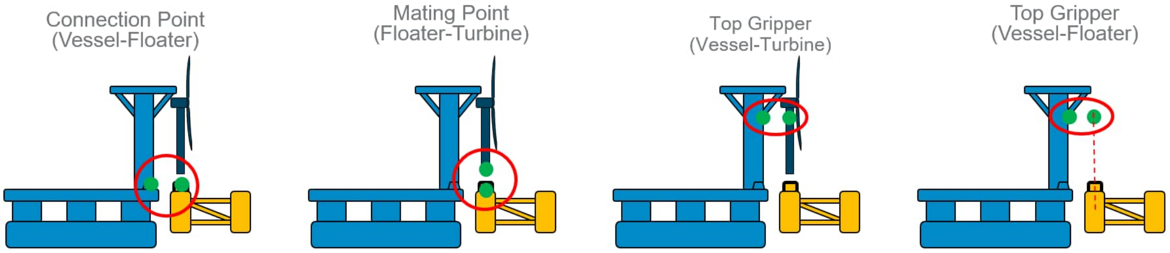

Figure 6.1: Figure identifying the points-of-interest of the system.

6.1.1. System Motions

The success of the mating procedure is mostly influenced by the relative motions between the bottom of the wind turbine tower and the mating point on the floating support structure. Therefore the performance metrics for the motions of the system will be limited to the relative pitch angle between the wind turbine and the floating support structure, as well as the two translations of the mating point. The direct outputs of the time-domain model are the state variables, providing the motions and velocities of the CG of the various bodies. To determine the relative displacement and velocity between the two considered points, the motions of the points relative to the CG of the bodies will have to be determined first. This is a function of the rotation of the CG, the location of the point on the body, and the translations of the CG. Next, the motions of these points can be compared between the bodies to find the relative motions between the chosen points of interest. Since both bodies have different locations in the inertial frame and different responses, their motions will be out-of-phase. The phase difference between the motions must therefore be taken into account. In the time domain, this is already included in the displacement or velocity signal since the position at a certain time in the simulation is given. In the frequency domain, however, the response amplitude provides the amplitudes and associated phase of the displacement. The phase difference between the displacement amplitudes of both bodies needs to be taken into account to determine the relative motion amplitude between the two bodies. The motion performance metric will be the resulting relative motion amplitudes of the mating point between the floating support structure and the wind turbine.

6.1.2. System Loads

The considered performance metrics to investigate the loads on the connection will be the connection forces on side A and side B of the connection. Various aspects of the system influence the loads on the connection points The total system loads are a combination of the applied pretension forces and the dynamic forces due to the motions of the connection. The force as a result of the stiffness of the connection is a function of the elongation of the springs and the stiffness constant. Since zero-length springs are used, the elongation of these springs is directly related to the relative displacement between the two connection points. The relative displacement between the connection point on the vessel and the link, and the connection point on the floating support structure and the link provide the stiffness forces of side A and side B of the connection. The velocities of the points are required to calculate the relevant damping forces. The velocity in the frequency domain is calculated by taking the derivative of the displacement amplitude response in the frequency domain, as shown in Section 3.2.2. If only stiffness or damping were considered, the maximum force would occur at the maximum displacement or maximum velocity amplitude, respectively. However, since both are included in the connection model, the maximum dynamic force amplitude can be found by finding the maximum value of the complex stiffness and damping response signal. Due to the dynamic nature of the model, the connection forces on sides A and B are not equal, which would be expected of a system in static equilibrium. The maximum force on side A or side B in the given direction will be considered as the performance metric for the load on the connection. In certain configurations, a high finite stiffness is applied to approximate a fixed connection. While comparing the maximum forces between connection types 1 and 3, large forces were observed for connection type three at the fixed side of the connection, not present in the response of connection type one. The fixed connection is approximated with a very high finite stiffness, resulting in high reaction forces on that side of the connection. Therefore, only the force on the flexible side of the connection will be considered in these cases to avoid unrealistically high loads.

6.1.3. Operational Limits

In order to be able to assess the performance of the system, various operational limits will be defined. In practice, these limits will be seen more as design targets. If the system's performance for a specific period is less than desired, the workability of the equipment will be adjusted. However, due to the many possible combinations and considered variables, the limits will help guide the assessment of the results. The hydrodynamic data from Ansys Aqwa contains response data for regular waves with periods of 3.49s to 62.83s, as shown in Section 5.2. In practice, the expected workability of the installation vessel will have an upper limit of around 15-18 seconds, with decreasing allowable wave height at higher periods. For this system analysis, it is chosen to investigate the performance of the system in regular waves with a wave amplitude of one meter. Based on the available data from the Ansys AQWA analysis and the upper workability limit of the installation vessel, a period range of 3.49-15.24s will be investigated. The periods correspond to the available periods provided by the Ansys AQWA analysis. For the considered environmental conditions, motion and load amplitude limits have been defined to serve as a way to interpret the results. Based on the expected performance of the motion-compensation systems, operational limits of two meters, three meters and three degrees are defined for the relative surge, heave, and pitch motion amplitudes, respectively. The relative pitch angle between the wind turbine and the floating support structure is important for the mating procedure, as this largely influences the required gripper motions. Three degrees should be considered the upper limit since this results in an amplitude of roughly six meters at the top gripper. However, the relative pitch angle is also the most difficult to reduce due to the pitch response of the floater. In practice, the maximum considered operational wave height might be decreased for certain peak response periods. Similarly, force limits on the connection points have been defined as well. In the surge and heave direction, a maximum of 5000kN will be considered the limit, roughly 500 metric tons, which is not uncommon for offshore structures. The limit on the moment of the connection is harder to define since this might be more difficult to absorb structurally. Based on the heave force limits and the length of the link, a limit of 10 times the heave limit (50000kNm) is chosen for the pitch moment.

Since many connector configurations will be investigated, a way has to be found to compare the results for varying stiffness. For this reason, only the peak response of the relative motion and force amplitudes of the system between 3.49 and 15.24 seconds will be considered. The peak response is the maximum value of the response in the selected wave period range. Using this as a single value to represent the performance of a configuration, many different combinations of varying stiffness can be shown and compared in one graph.

6.2. Parameter Combinations

The model was used to evaluate many different configurations, with varying combinations of stiffness in the multiple directions of motion of the system. This section will further detail the considered configurations and the creation of parameter groups to investigate the performance of the system.

6.2.1. Stiffness Range

The first step will be to determine the effective stiffness range for each degree of freedom of the connection. Figure 6.2 shows the behaviour of the system for a range of varying stiffness in all three directions. Each row in the graph shows the system's surge, heave, and pitch response for an increase of stiffness in one direction of motion (the first row shows a varying surge stiffness, the second a varying heave stiffness, and the third a varying pitch stiffness). The dotted black lines in the graph indicate the peak response limits of the system, as described in the section above. The lines in the graph show the maximum peak response below 15 seconds for a varying stiffness, with a range of 250 points logarithmically distributed between 1N or 1Nm/rad and 10000MN or 10000MN/rad. For all results presented in the next chapter, the damping coefficient of the connection is equal to the stiffness. The coloured regions in the graph indicate the selected stiffness region that will be used to create the various parameter groups. Based on the overall response graph, these values are chosen since the largest variations happen within these regions. For each direction, 20 different stiffnesses are chosen, also logarithmically dis-

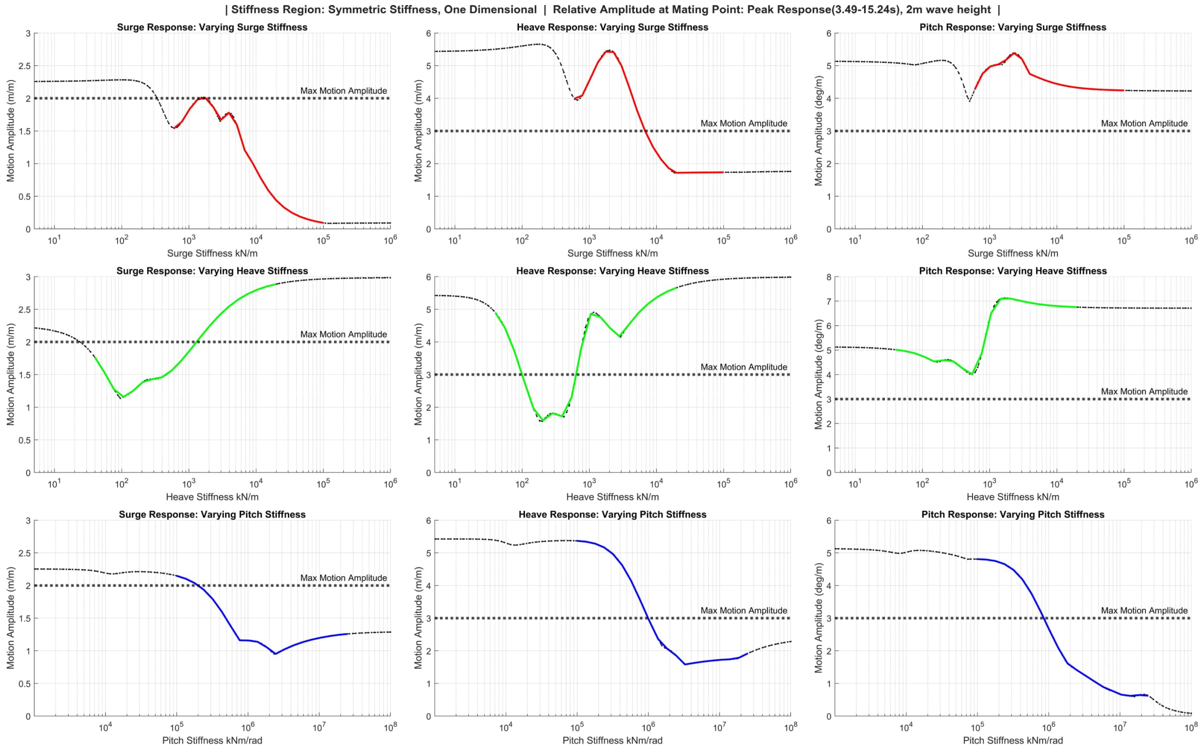

Figure 6.2: Graphs showing the selected stiffness variation regions for the surge, heave and pitch stiffness of the connection. Each row shows a variation of stiffness in one direction of motion. The coloured sections indicate the considered stiffness ranges for the system analysis.

tributed across the selected regions. The surge stiffness ranges from 600 - 100000 kN/m, the heave stiffness from 40 - 20000 kN/m and the pitch stiffness from 100000 - 25000000 kNm/rad. Also added to the stiffness range values are a stiffness of 0, making the connection unrestricted, and a high stiffness of 10^{10} kN/m for surge and heave and 10^{11} kNm/rad for pitch, making the connection ’fixed’. In the next sections, a free connection indicates a stiffness of 0 kN/m, a variable stiffness indicates the defined stiffness range, and a fixed connection indicates the highest stiffness value.

6.2.2. Effect of Installation Stages

Using the aforementioned stiffness range, the behaviour of the different installation stages is compared for increasing stiffness values. Figure 6.3 shows a set of graphs comparing the response of the system for the various installation stages. The top row shows the motion response in the surge, heave, and pitch direction. The motion response trend is very similar for installation stages 1, 2 and 3, meaning that the ballast transfer does not significantly change the system’s overall response. It can be seen, however, that overall the response decreases for lower stiffnesses when more ballast is transferred. As expected, the response for installation stages 4 and 5 is zero since the wind turbine is mated to the floater. Looking at the middle and bottom rows, showing the total and dynamic force response, the pretension required to balance the system during the ballast transfer causes the most significant change in connection forces. The bottom row of the graphs shows the differences in the stiffness and damping forces on the connection points. Overall a similar trend is shown for all installation stages. The response for installation stages 4 and 5 also does not significantly change the response of the system, with an exception for the higher stiffness values, where the response of installation stage 4 decreases. Based on this graph, a decision has been made to focus on the first installation stage for the system analysis.

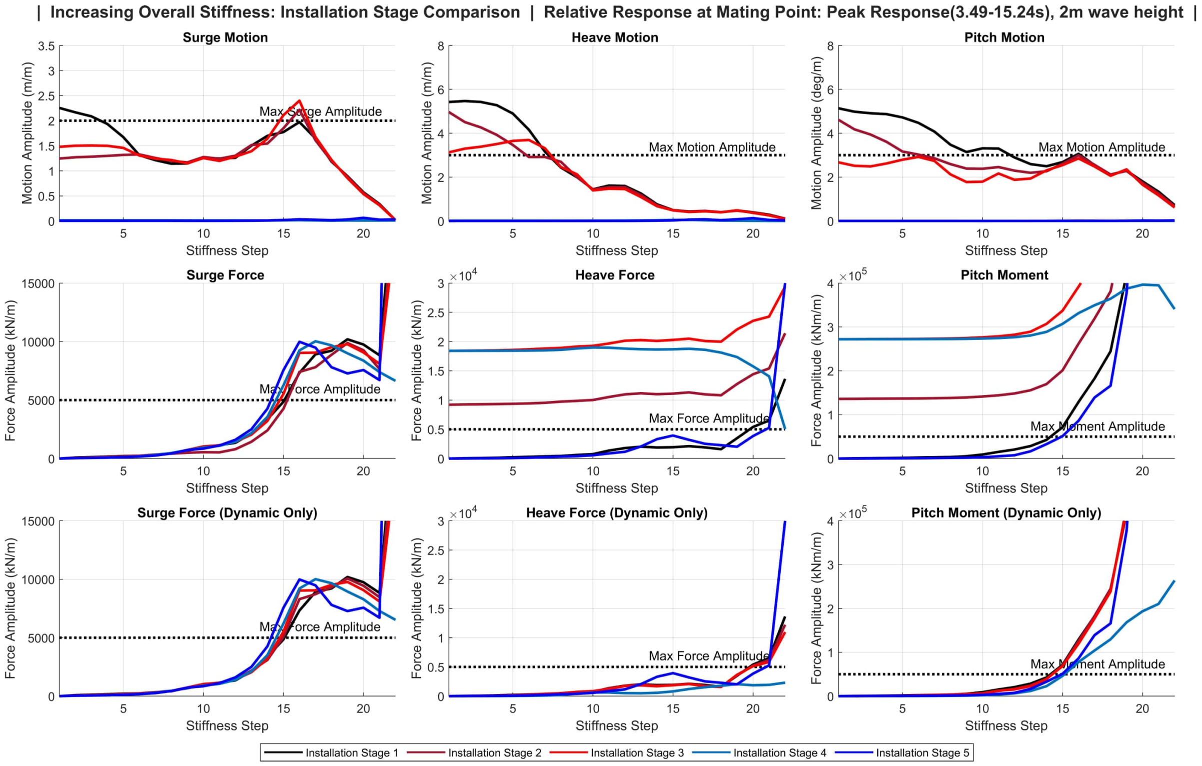

Figure 6.3: Graphs showing the peak-response comparison between the five installation stages for overall increasing connection stiffness.

6.2.3. Parameter Groups

Two-parameter groups will be tested to investigate the influence of varying stiffness in the multiple directions of motion. One will vary the stiffness equally on side A and side B of the connection, the symmetric stiffness variation group. The second will investigate the behaviour change when the stiffness on both sides of the connection is unequal, the asymmetric stiffness variation group. The coupling effect of adding stiffness in different directions is also investigated for each group. Tables 6.1 and 6.2 show an overview of the stiffness combinations in parameter groups 1 and 2. Parameter group 1 is divided into four subgroups A-D. Group 1A consists of a variation of the stiffness range of 22 different stiffness steps (the stiffness range defined above), each in one direction of motion. Next, the coupling between stiffnesses is investigated in Group 1B, investigating the difference in behaviour for six selected stiffnesses in one direction. In contrast, the other stiffness is varied using the stiffness range. This is further extended by group 1C, where the stiffness in two directions is varied using the stiffness range. Group 1D adds the third degree of freedom to the variation resulting in the highest number of instances. For analysis group 2, a distinction is made between the stiffness on sides A and B. The stiffness for both sides, A and B, are varied to capture as many variations as possible. A similar approach is taken for parameter group 2, increasing the coupling of directions for each group. A combination of free, varied and fixed connections for side A and side B results in 88 combinations per direction (Side A fixed-Side B varied, Side A free-Side B varied, Side A varied-Side B fixed, and Side A varied-side B free). For groups 2C and 2D, this is further extended with the additional degrees of freedom. In group 2D, the third direction is only considered free, with side A or side B fixed. The three different stiffness variations in the table indicate this for the third direction.

Table 6.1: Overview of parameter Group 1 (Symmetric stiffness variation).

	Total Instances	Coupling	Surge Stiffness Variations	Heave Stiffness Variations	Pitch Stiffness Variations
Group 1A	66	One-Dimensional	22	22	22
Group 1B	792	Surge-Heave Coupling	22	6	0
		Surge-Pitch Coupling	22	0	6
		Heave-Surge Coupling	6	22	0
		Heave-Pitch Coupling	0	22	6
		Pitch-Surge Coupling	6	0	22
		Pitch-Heave Coupling	0	6	22
Group 1C	1454	Surge-Heave Coupling	22	22	0
		Surge-Pich Coupling	22	0	22
		Heave-Pitch Coupling	0	22	22
Group 1D	31944	S-H Coupling (Pitch)	22	22	16
		S-P Coupling (Heave)	22	16	22
		H-P Coupling (Surge)	16	22	22

Table 6.2: Overview of parameter Group 2 (Asymmetric stiffness variation).

	Total Instances	Coupling	Surge Stiffness Variations		Heave Stiffness Variations		Pitch Stiffness Variations	
			A	B	A	B	A	B
Group 2A,B	1452	Surge One-Dimensional	22	22	0	0	0	0
		Heave One-Dimensional	0	0	22	22	0	0
		Pitch One-Dimensional	0	0	0	0	22	22
Group 2C	23234	Surge-Heave Coupling	22	22	22	22	0	0
		Surge-Pitch Coupling	22	22	0	0	22	22
		Pitch-Heave Coupling	0	0	22	22	22	22
Group 2D	69696	S-H Coupling (pitch A/B)	22	22	22	22	3	3
		S-P Coupling (heave A/B)	22	22	3	3	22	22
		P-H Coupling (surge A/B)	3	3	22	22	22	22

6.3. Sensitivity Analysis

A brief sensitivity analysis will be performed to investigate the influence of the assumed structural system parameters. The effect of increasing the set of operational limits will also be tested. For the presented parameter variations above, the damping constants of the connection are chosen to be similar to the stiffness constants. First, the sensitivity analysis will look into the effect damping has on the connection by considering two variations in damping. The default damping value will be compared to the system without damping (0%) and the system with damping constants 2.5 times bigger than the stiffness constant (250%). Secondly, the link mass and gripper stiffness are two structural parameters potentially influencing the system's behaviour. Therefore, these values will be varied as well. The link mass will be increased and decreased by 50 per cent compared to the default mass used for the other configurations. The stiffness of the grippers will be decreased by 20 and 50 per cent to investigate how additional motions of the wind turbine affect the rest of the system. Thirdly, the effect of increasing the set operational limits is also investigated. A wave period limit of 15 seconds is considered for the system analysis. Typically, larger wave periods result in larger motions. Therefore, the effect of decreasing this limit to 14 seconds and 13 seconds is considered. Finally, the linear vs nonlinear system behaviour is considered to investigate the effects of linearization of the equations of motion. The values of the compared configurations will be based on the results of the system analysis and will therefore be presented in the next chapter.

7

Results and Discussion

This chapter presents the results from running the model in the different configurations from the parameter groups. All results show the peak response of the relative motion between the wind turbine and the floating support structure at the mating point. The forces shown in the graphs are the maximum connection forces calculated according to the description in the previous chapter. Next, the results of the sensitivity analysis are presented as well. This chapter will discuss a selection of the most interesting results. Additionally, all results for the different parameter groups are attached in Appendix C and D. Finally, a brief discussion of the system analysis is presented at the end of the chapter.

7.1. Free Floating Response

A baseline will be established by running the model without stiffness in any connection direction. The relative response of the wind turbine mating point is shown in Figure 7.1. The set limits for the wave period and system motions are indicated in the graph as well. Also shown in the graph are the responses of the mating point on the wind turbine and the floating support structure, as well as the response of the CG of the floating structures. As can be seen, the response of the CG of the floating support structure is much smaller than the response of the turbine mating point at the peak at around 13 seconds. The high peak in the pitch response also causes a high peak in both the surge and heave directions. Contrary, the response of the installation vessel shows much less motion and is less influenced by the waves due to its larger size and higher mass. At 15 seconds, a clear low point is shown in the surge response. This is caused by the coupled heave and pitch motions of both structures, resulting in a very low relative amplitude. The motions of the floating support structure are the biggest contributor to the large relative motions and will therefore be the limiting factor of the system. As mentioned in the previous chapter, the peak response for each configuration will be used to compare the performance of the different configurations. For example, if this is a tested configuration, the motion amplitude values to compare will correspond to the peaks left of the period limit. For the surge and heave response, the value is taken at the peak around 13 seconds of 2.3 and 5.5 meters, respectively, and for the pitch response, the value of 5.1 degrees at the peak around 15 seconds.

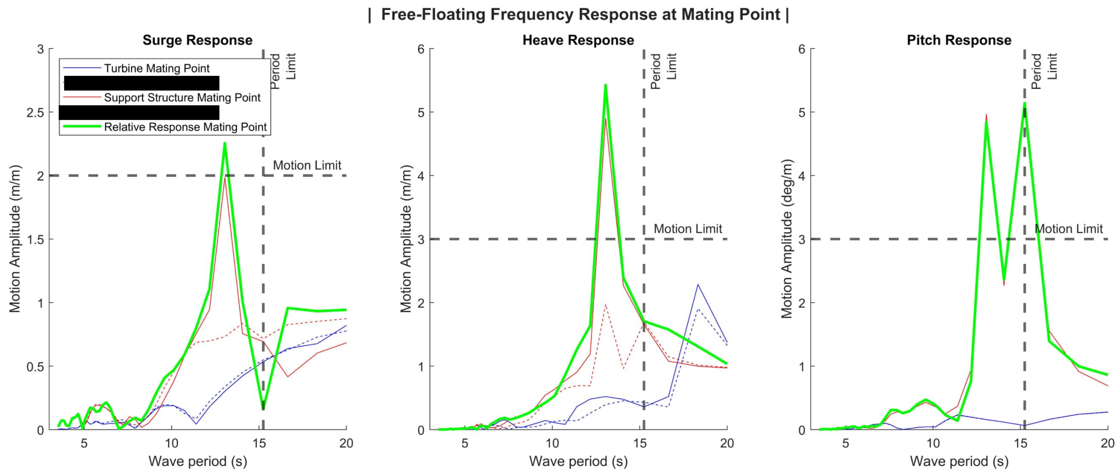

Figure 7.1: Relative Free Floating response at wind turbine mating point.

7.2. Symmetric Stiffness Variations

Below, the results of the symmetric stiffness groups will be discussed. Starting with the results of the configurations without any coupling, followed by the results investigating coupled stiffness in two and three directions.

7.2.1. Group 1A: One Directional

Figure 7.2 shows the results of the first parameter group. The stiffness is varied in one direction of motion of the connection. The figure shows three rows of graphs, each row showing the response for stiffness varying in the surge, heave and pitch direction, respectively. The connection forces are shown in the graph as well. Since the stiffness varies in one direction, only a force in the direction with stiffness is shown, the forces in the other directions remain zero. The x-axis shows an increasing stiffness value for each direction of motion. On the left y-axis, the peak motion amplitude response in meter per meter wave height. The right y-axis indicates the peak force amplitude response per meter wave height. For each configuration, the graph shows the peak response occurring for wave periods between 3.49 and 15.24 seconds. The wave period belonging to the peak response is indicated in the graphs with the coloured markers. Looking at the top left graph, a trend is shown where a higher stiffness in the surge direction leads to decreased motions and increased forces. The period of the first few stiffness points corresponds to the free-floating peak response period in the surge direction of 13 seconds. Increasing the stiffness changes the peak response period, reaching 14 seconds for the highest stiffness values. Although the surge peak response periods change when the stiffness is varied, the period remains in the range of the response peaks of the floating support structure. Adding surge stiffness also affects the heave motions, reaching a constant peak value from a surge stiffness of 20000 kN/m onwards. The peak period for the heave motions also changes from the first large pitch response peak of the support structure response at 13 seconds to the second peak at 15 seconds. Finally, adding surge stiffness affects the pitch response peaks the least. However, at around 2000 kN/m, the response peak at 13 seconds becomes larger than the free-floating peak at 15 seconds. The effect of adding stiffness in the heave direction of the connection, shown in the middle row of graphs, results in unexpected changes in the system's behaviour. For higher stiffness in the heave direction, the relative motion response in each degree of freedom is increased above the free-floating response. Especially in the heave direction, a clear optimum can be identified in the graph between a stiffness of 2000 and 4000 kN/m. Even though the surge and heave responses are within limits for this range, the pitch response still is above the set limits. Further increasing the heave stiffness results in increased motions in each direction. When looking at the time-domain animation for this configuration, it becomes clear that the unrestrained rotation of the connection causes this. Figure 7.3 shows a still image from the time-domain simulation for this configuration. Even though the link is fixed in the heave direction, it will start rotating around the connection points, meaning a larger heave response is experienced by the mating point. The results for adding stiffness in the pitch direction of the connection are shown in the bottom row of the graph. An increased pitch stiffness affects the system's behaviour in all directions.

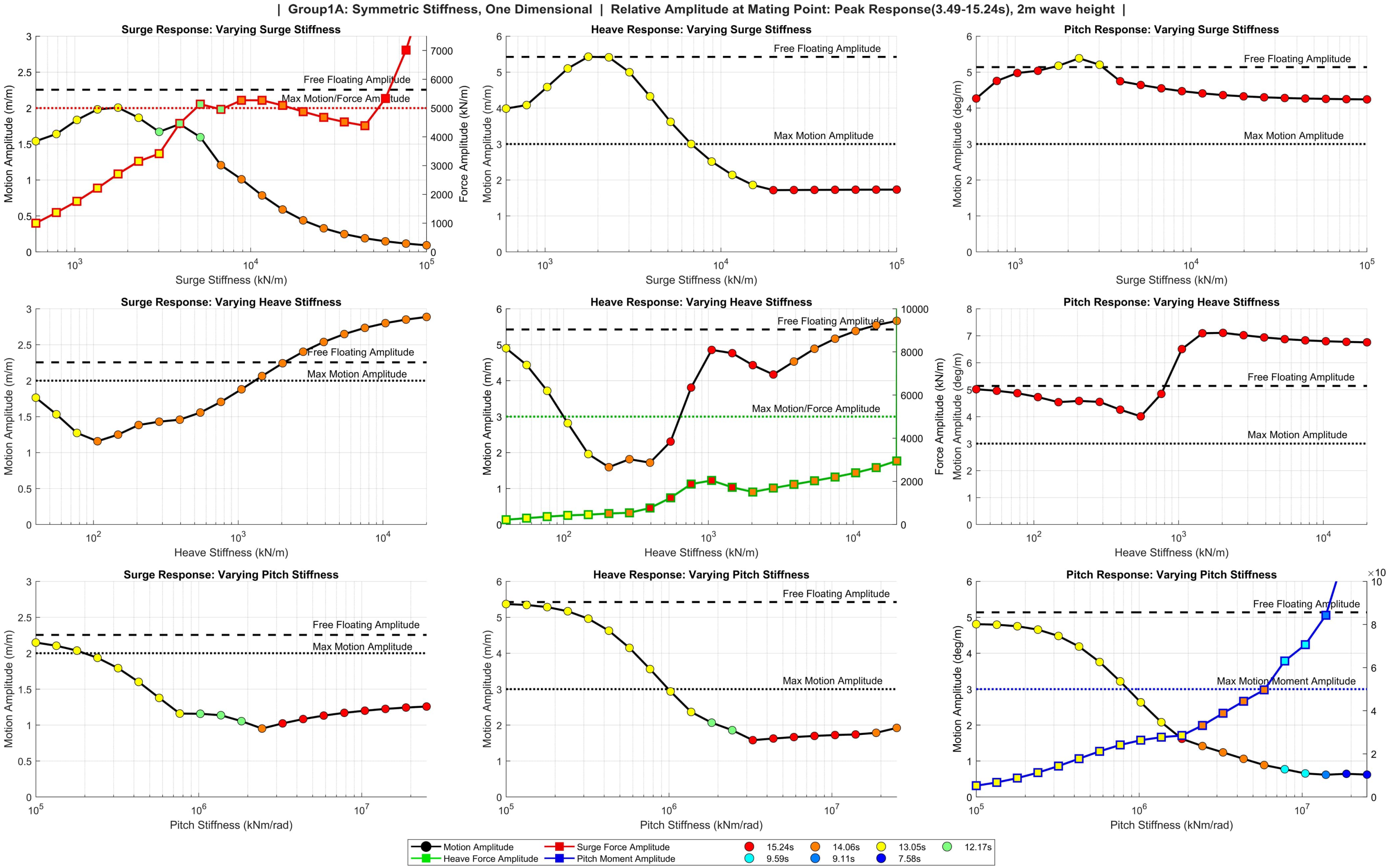

Figure 7.2: Group 1A: One-Directional variation

The motion response for each direction will drop below the set limits when a rotational stiffness of 1E+6 kNm/rad is reached. This is expected behaviour since the magnitude of the relative motions is largely affected by the pitch response of the support structure. The moment on the connection also behaves as expected, which increases for higher rotational stiffness. When a stiffness in the pitch direction is added, the peak response period for the pitch motion changes from 15 seconds when free-floating to 13 seconds with an added pitch stiffness. The peak period reduces to lower numbers for the highest stiffness configurations, indicating that the connection has suppressed the peak periods in the support structure's free-floating response. The effect of adding stiffness in any direction is difficult to predict, as is also shown by the heave response for a high stiffness being influenced by the pitch motions of the system. The pitch motions are the most difficult to suppress, adding stiffness in the pitch direction is the only option to keep the pitch motion within the set limits. The effect of adding heave stiffness resulted in unexpected behaviour, indicating that coupling between heave stiffness and another direction is required to make it more effective. Overall, these results show that it is difficult to stay within limits by adding stiffness in a single direction of motion. Therefore, the next section will look into coupling effects between two different directions of motion.

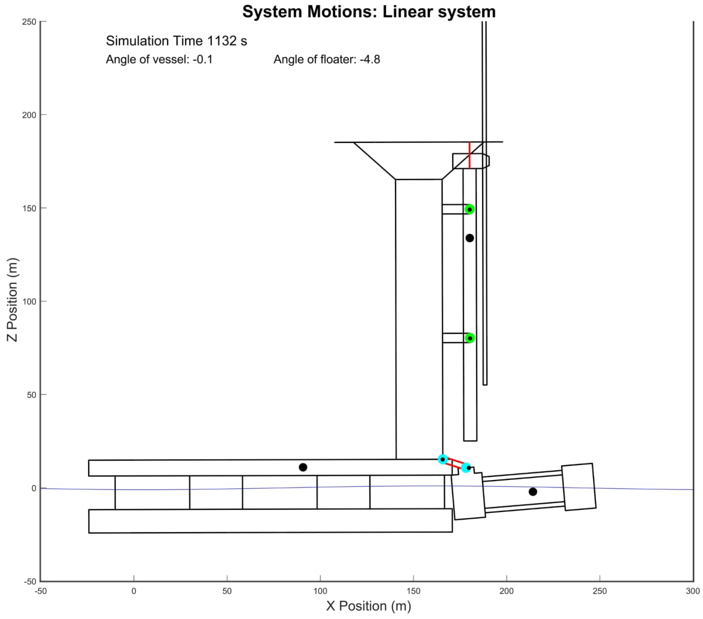

Figure 7.3: Figure showing the system's motions for a configuration with high heave stiffness (10000 kN/m). The free rotation of the link causes large relative heave motions.

7.2.2. Group 1B, 1C: Two Directional Coupling

Groups 1B and 1C investigate the motion response for a two-directional varying stiffness, i.e. the stiffness is varied in two directions, with the third direction being unrestricted. Three combinations, surge-heave, surge-pitch and heave-pitch stiffness variation, are investigated. The results for group 1B can be found in Appendix C and show the results for selected coupled stiffnesses in a line graph. Like Figure 7.2, the graph also indicates the peak periods to provide additional information on the system's behaviour. The results for group 1C show a better overview of all possible combination and is better suited to compare the different configurations. Figure 7.4 shows the motion response in these three combinations' surge, heave, and pitch directions. The two directions of varying stiffnesses are indicated on the x and y-axis of the graphs. Each square in the graph represents the results for a specific combination of two stiffnesses. The colour indicates the amplitude of the motion, forming a heatmap of the motion and force response of the system. The colour bars next to the figures indicate the magnitudes of the response. The defined motion and force limits are also indicated on the colour bars. Black areas on the graph are amplitudes that exceed the limits and should be avoided. The squares on the edges of the graph are slightly wider. These indicate the free and fixed connection stiffness in each direction, shown by the axis legend '0' and 'Fixed'.

Similar to the results shown in Figure 7.2, the surge and pitch stiffness influence the motions more directly than the heave stiffness, and the heave stiffness is only effective in combination with stiffness in at least one other direction. This is clearly shown by the vertical green area in the top left graph and the vertical blue area in the graph below. The surge stiffness is varied along the x-axis of both graphs, and the colours indicate that a low surge peak response is observed for a high surge stiffness. A similar, although less evident, trend is shown for the pitch response in the two graphs on the right side, showing the results for varying surge-pitch and heave-pitch stiffness. Here the horizontal blue and green areas indicating a small pitch response are found at the top of the graph in the range with high pitch stiffness. The heave responses for the different combinations, found in the middle column of graphs, show no clear horizontal or vertical areas of small motion responses. However, combining surge and heave stiffness can reduce the heave response, as shown by the yellow area in the graph. Similarly, by combining surge and pitch stiffness, the heave response can also be reduced, requiring either high surge or high pitch stiffness, indicated by the magenta areas. Finally, combining heave and pitch stiffness can also reduce the heave response. From this, it can be concluded that a combination of stiffnesses is required to reduce the heave response of the system. Whereas adding stiffness in a single direction can reduce the other two motion directions.

Not only are the relative motions of the system relevant but the connection forces should also be investigated. The connection forces of the coupled stiffness variations are shown in Figure 7.5. Comparing Figures 7.4 and 7.5, a relation between the motions and forces can be discovered, where smaller motions result in larger forces. Optimal system performance can most likely be identified by finding a balance between the reduction of relative motions and an increase in connection forces.

The motion and force results are combined into a single graph by taking the weighted average of these two performance metrics. The motions and forces are normalized using the determined operational limits, and the average of both is taken, considering an equal weight for both metrics. Figure 7.6 shows the weighted average of the motions and forces in the surge, heave and pitch direction. The maximum value shown in these graphs is 1, reached when the motions or the forces exceed the set limits or the weighted average exceeds the limit. Here, the average pitch response can be identified as the most critical direction, as either the motions or the moments of the connection exceed the set limits. The most promising results are shown by combining heave and pitch stiffness.

Further combining these results, Figure 7.7 shows the weighted average of the motions in all three directions, the weighted average of forces in all three directions and the overall average of the motions and forces. The last column of the graph indicates the system's combined performance, considering all of the mentioned performance metrics. The motion average graph comparing surge-heave stiffness combinations in the top left of the figure shows no possible combinations. This can be explained by looking at the results for the pitch response in Figure 7.6. Since the pitch motions are above the set limit, the average motion response reaches the limit of 1 for all combinations. The force average, on the other hand, does show combinations within the limits. Since the motion average exceeds the limits, no possible combinations are shown in the overall average graph. For the surge-pitch combination, the motion average graph shows more possibilities. Combining the motions and force graph, the overall average graph shows that low surge and relatively high pitch stiffness keep the system's response within the set limits. However, a more promising result is shown by combining heave and pitch stiffness. The motion average graph shows that pitch stiffness is required to stay within the set motion limits. Increasing heave stiffness results in a small improvement, with a lower pitch stiffness required to keep within limits. The opposite effect is observed in the force average graph, where adding heave stiffness results in higher forces and, thus, a smaller area of possible combinations. Looking at the overall average graph, this results in a similar range for the pitch stiffness, as seen in the surge-pitch stiffness combination. However, due to smaller heave forces and a more favourable motion response the area showing possible combination is larger.

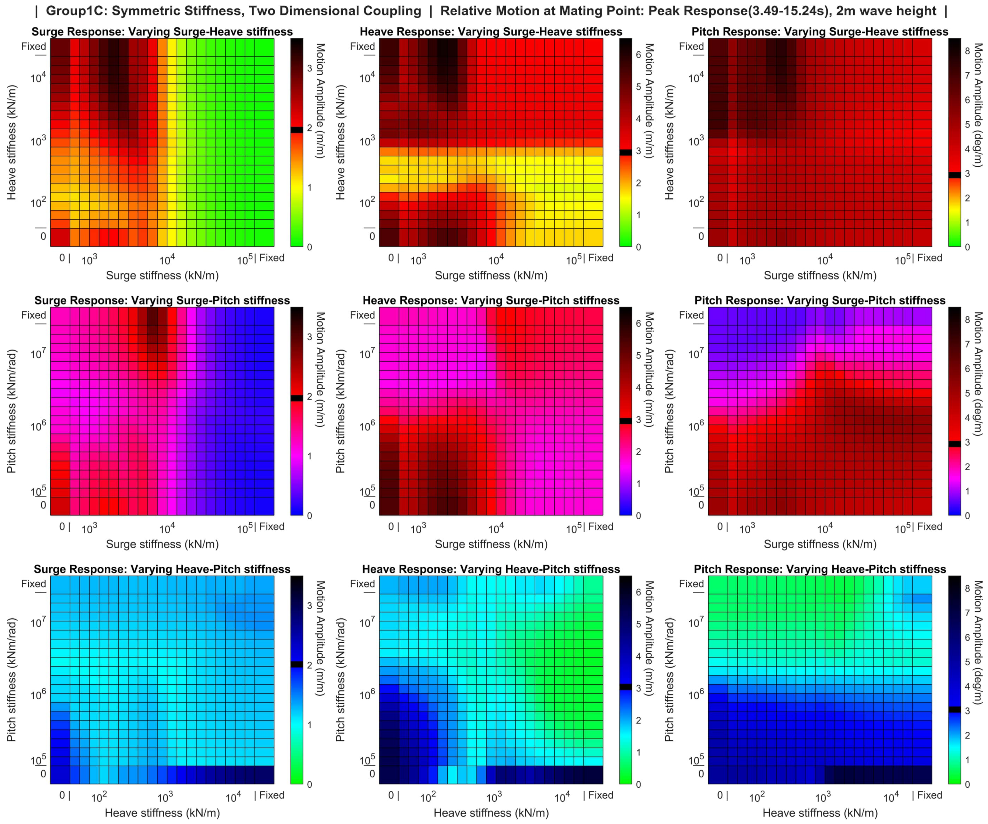

Figure 7.4: Group 1C: Relative Motions

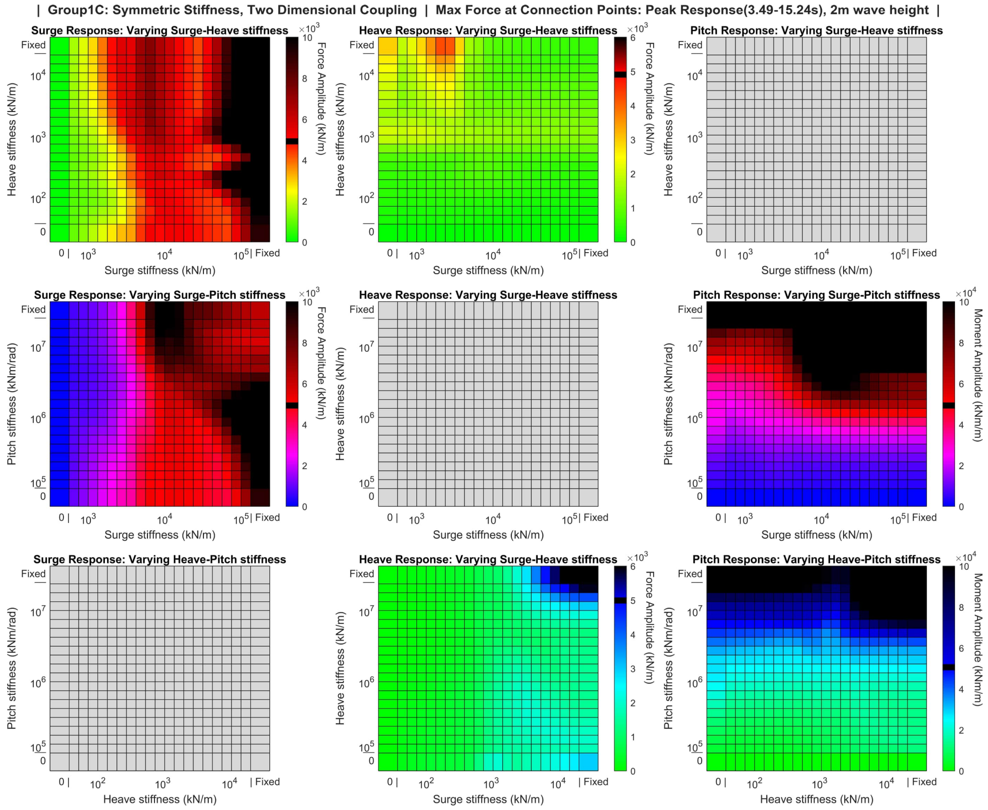

Figure 7.5: Group 1C: Connection Forces

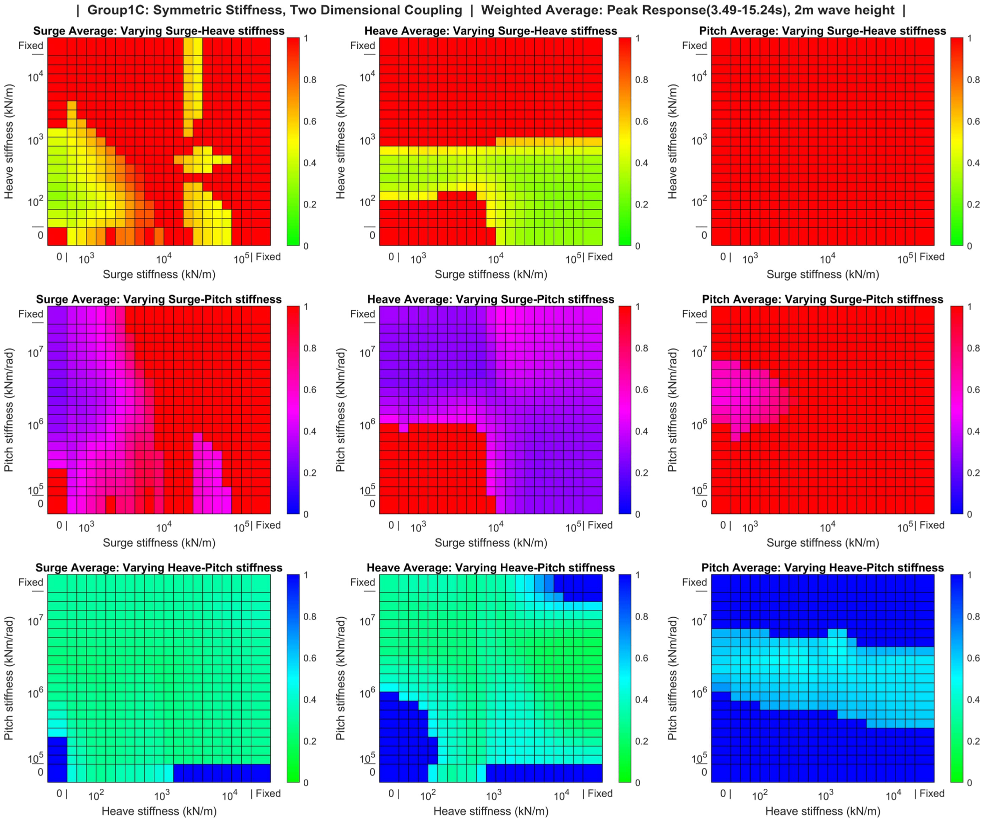

Figure 7.6: Group 1C: Weighted Average

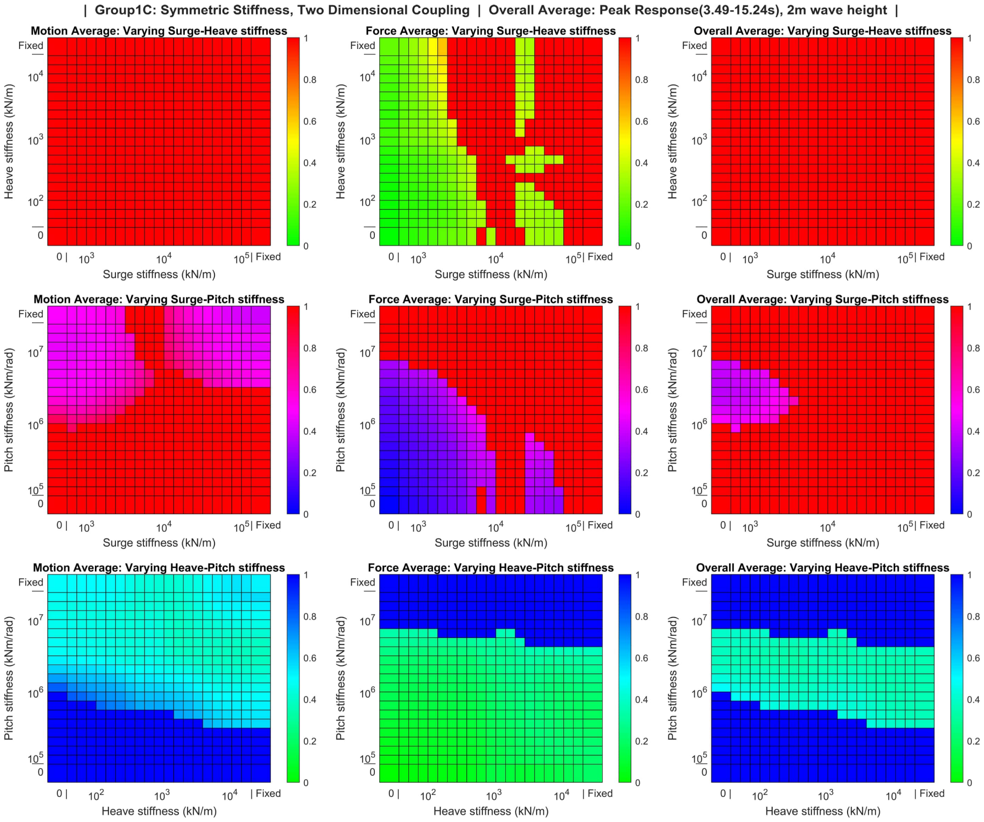

Figure 7.7: Group 1C: Overall Average

7.2.3. Group 1D: Three Directional Coupling

In practice, the connection is unlikely to be completely free to move in any direction. Group 1D aims to investigate the changes in behaviour when stiffness is added in the third direction of motion. A selection of six different stiffnesses in the third direction will be compared, shown in Figures 7.8-7.10. The six different stiffness values include free and fixed connection and four values of increasing stiffness showing the most interesting changes in the system's behaviour. Similar to the results of group 1C, the weighted average and overall average graphs will be used for the following parameter groups to investigate the system's performance considering the relative motions and connection loads. Figures 7.8-7.10 show the overall average values of the response of the three different coupling combinations. Appendix C includes the motion response, force response and weighted average graphs. As shown in Figure 7.8, adding pitch stiffness to the surge-heave combinations positively affects the possible combinations of surge and heave stiffnesses. A reduction in motion amplitudes for a combination of high heave and low surge stiffness mostly cause this. The forces on the connection for the lower surge stiffness values do not seem to increase. However, for larger surge stiffnesses, the forces exceed the limits. Further increasing the pitch stiffness results in a better relative motion response. However, fixing the motion in the pitch direction results in too high of connection forces. Another interesting observation is the range of surge stiffness in the middle of the graph, which still causes the motion response to exceed the limits. The results for combining surge and pitch stiffness do not seem to be affected by additional heave stiffness, as shown in Figure 7.9. Neither the average relative motions nor the average connection forces show a difference when heave stiffness is added to the system. Increasing the heave stiffness results in a marginally higher force, most noticed for a heave stiffness of 3897 kN/m. When the connection is fixed, the forces exceed the limits, but this also has little influence on the relative motions of the different combinations. Finally, Figure 7.10 shows the effect of adding surge stiffness when combining heave and pitch stiffness. Interestingly, this has a negative effect on the overall average performance of the system. The possible combinations achieving both acceptable motion and force responses decrease. When increasing the surge stiffness to 8862 kN/m and above, the resulting system motions start to decrease again, and the system's performance improves. For these stiffnesses, however, the forces in the connection are not within limits. Overall, combining stiffness in all directions of motion can have both a positive and a negative effect on the system's behaviour. The following sections will investigate this further by looking at asymmetric stiffness combinations.

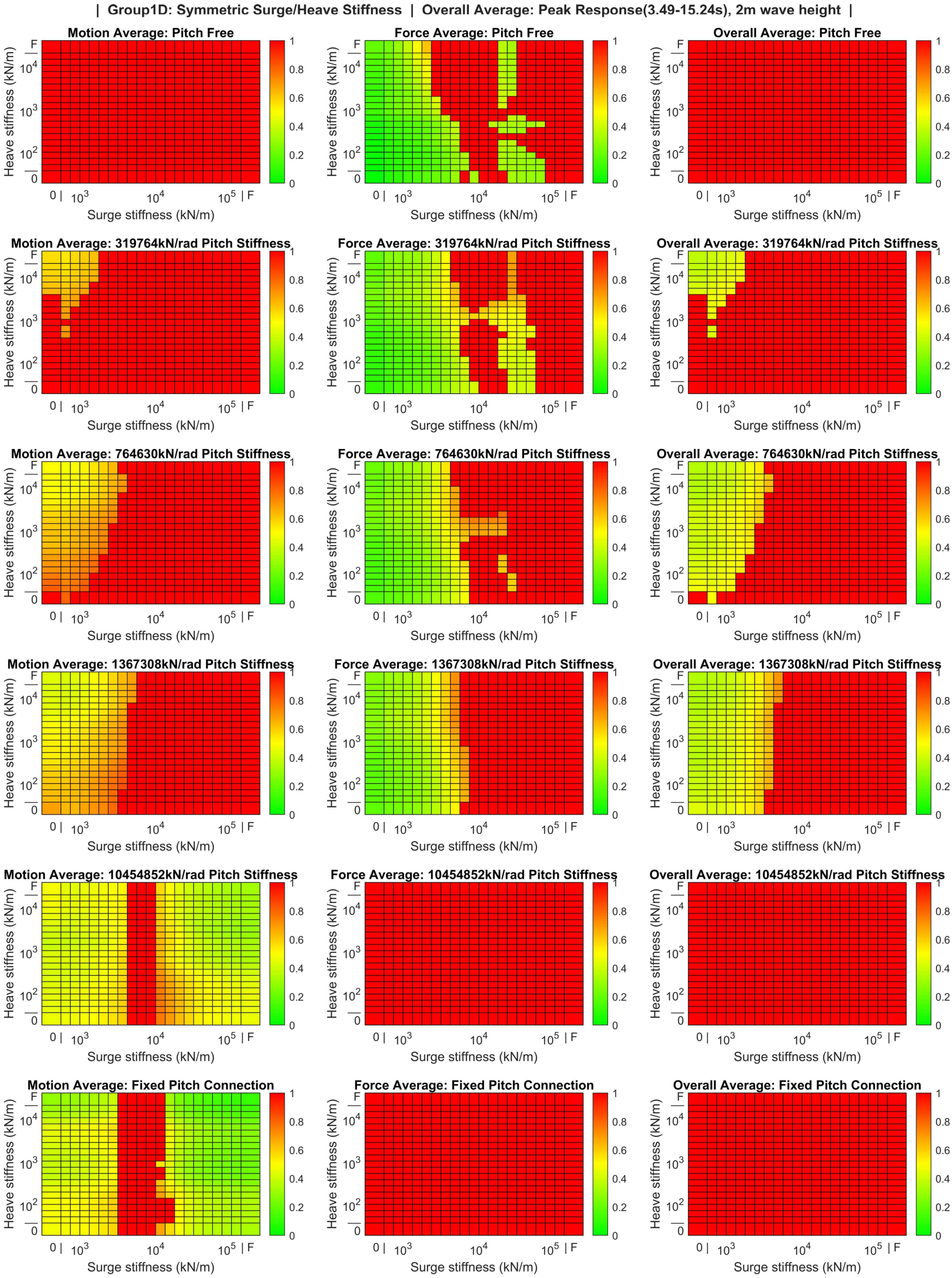

Figure 7.8: Group 1D: Surge-Heave Overall Average

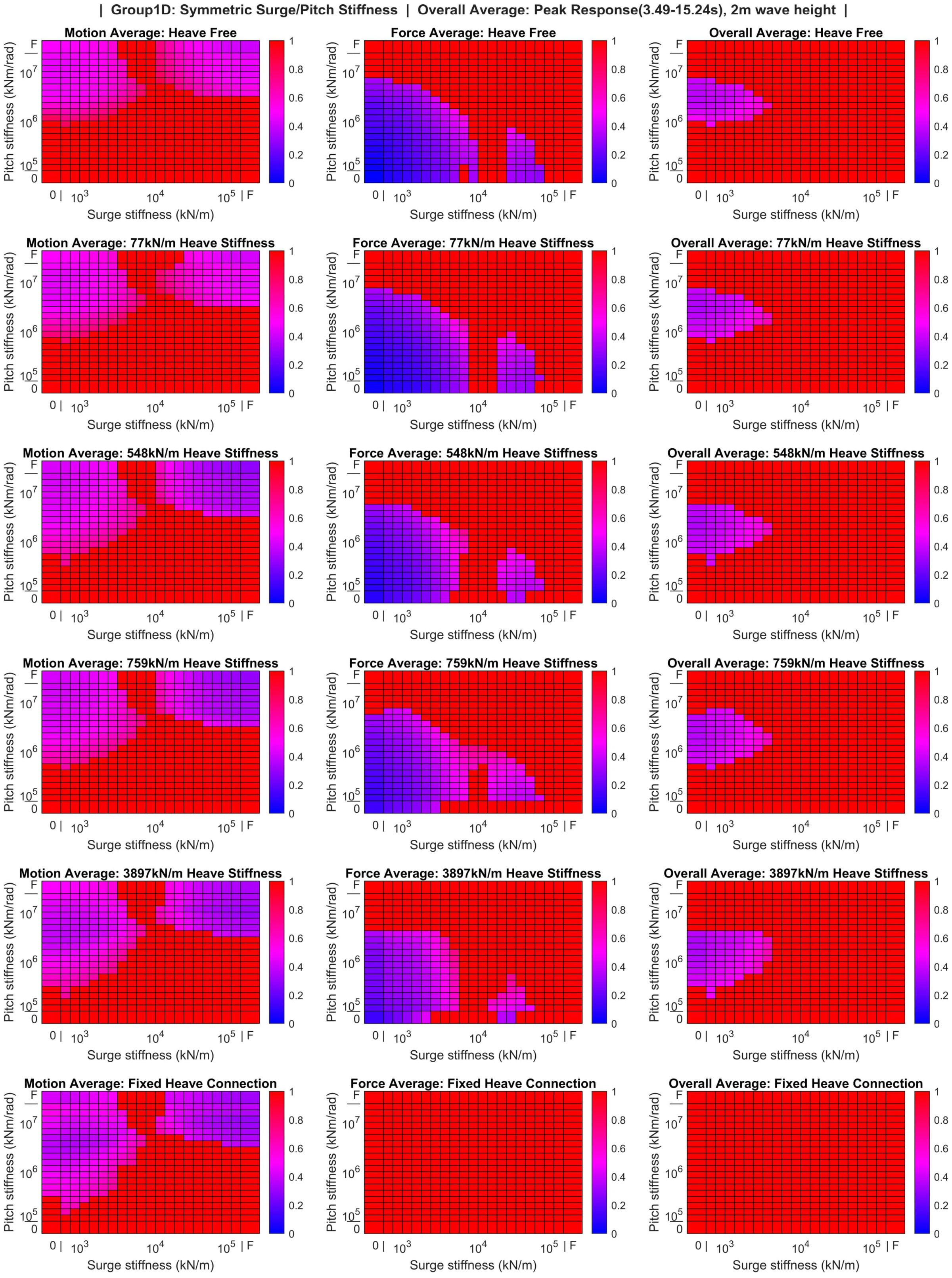
| Group1D: Symmetric Surge/Pitch Stiffness | Overall Average: Peak Response(3.49-15.24s), 2m wave height |

Motion Average: Heave Free
Force Average: Heave Free
Overall Average: Heave Free
Motion Average: 77kN/m Heave Stiffness
Force Average: 77kN/m Heave Stiffness
Overall Average: 77kN/m Heave Stiffness
Motion Average: 548kN/m Heave Stiffness
Force Average: 548kN/m Heave Stiffness
Overall Average: 548kN/m Heave Stiffness
Motion Average: 759kN/m Heave Stiffness
Force Average: 759kN/m Heave Stiffness
Overall Average: 759kN/m Heave Stiffness
Motion Average: 3897kN/m Heave Stiffness
Force Average: 3897kN/m Heave Stiffness
Overall Average: 3897kN/m Heave Stiffness
Motion Average: Fixed Heave Connection
Force Average: Fixed Heave Connection
Overall Average: Fixed Heave Connection

Figure 7.9: Group 1D: Surge-Pitch Overall Average

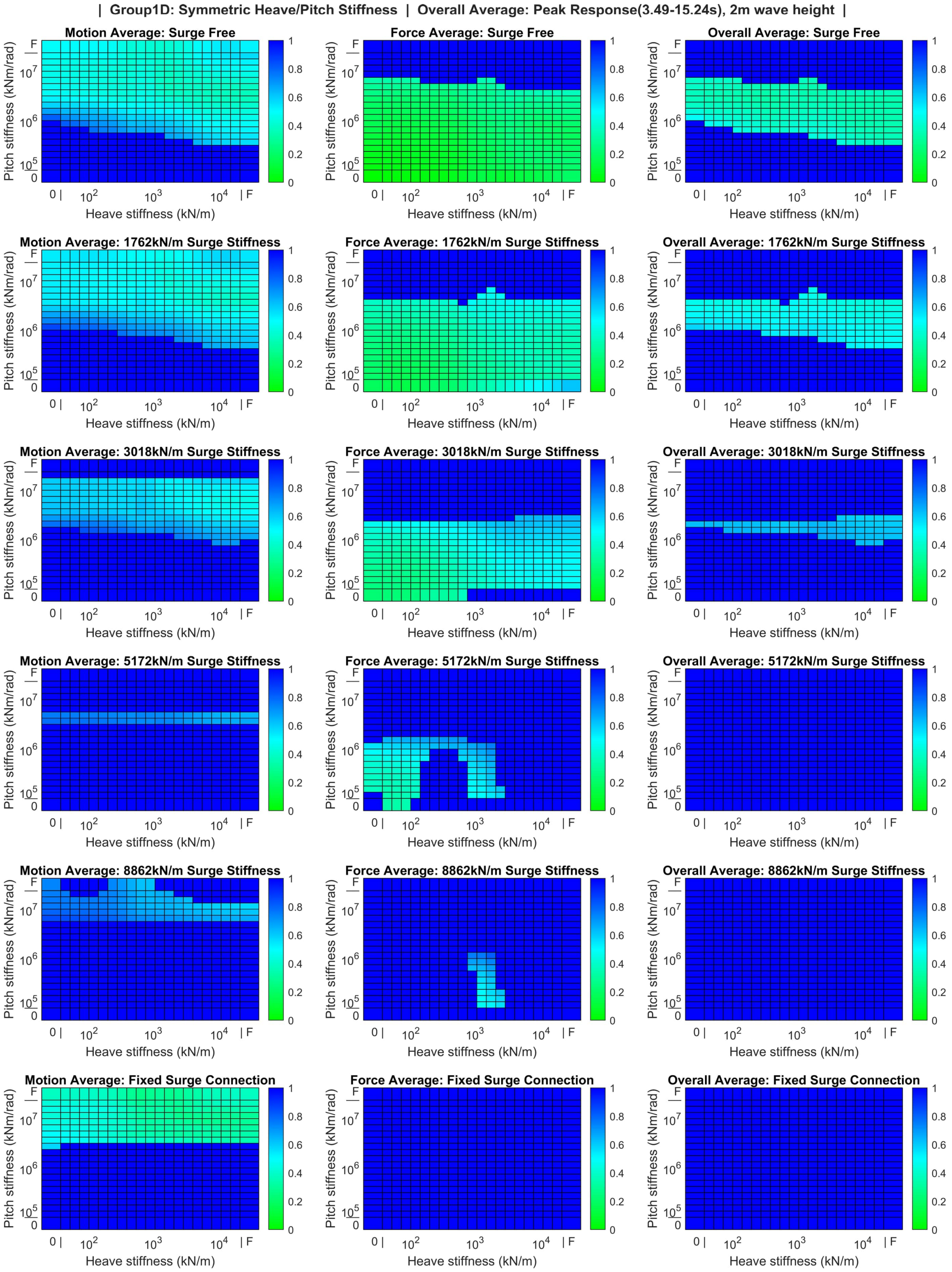

Figure 7.10: Group 1D: Heave-Pitch Overall Average

7.3. Asymmetric Stiffness Variations

Next, the results for the asymmetric stiffness groups will be discussed below. The stiffness of both sides of the connection varies independently, increasing the number of compared configurations. A similar course as with parameter group 1 is followed by increasing the complexity of the investigated combinations. Starting with the results of the configurations without any coupling, followed by the results investigating coupled stiffness in two and three directions of motion. Each graph investigating coupling will show more combinations due to the added variation between side A and side B of the connection.

7.3.1. Group 2A, 2B: One Directional

First, one-directional asymmetric stiffness is considered to see if there are any advantages to adding stiffness on side A or B of the connection. Figure 7.11 shows the motion and force response of the system combining stiffness in one direction on both sides of the connection. The x- and y-axis of these graphs show the surge stiffness of sides A and B of the connection, respectively. The magnitude of the response is indicated by the colour of the points in the graph, similar to previously shown graphs. In Figure 7.11, a difference can be observed when comparing the behaviour of the system when the connection is fixed on side A or side B. Especially the surge and heave motions are not symmetrical. The large difference between the vessel and the floating support structure in the free-floating response of the connection point can explain this. Since the motions of the support structure are much large when compared to the installation vessel. Fixing the connection on the side of the support structure will result in large forces at that connection point. The pitch stiffness shows a symmetrical response, indicating that adding stiffness to the pitch directions is less sensitive to one side of the connection. As seen before, high pitch stiffness is required to stay within the defined limits for the pitch motion response. Overall, it can be seen that varying the stiffness on each side of the connection can have both a positive and negative effect on the system's response. A similar conclusion to group 1A can be made, it remains difficult to intuitively predict what will happen to the motions of the system. The next section will investigate the coupling between the various motion directions and the influence of adding stiffness to each side of the connection.

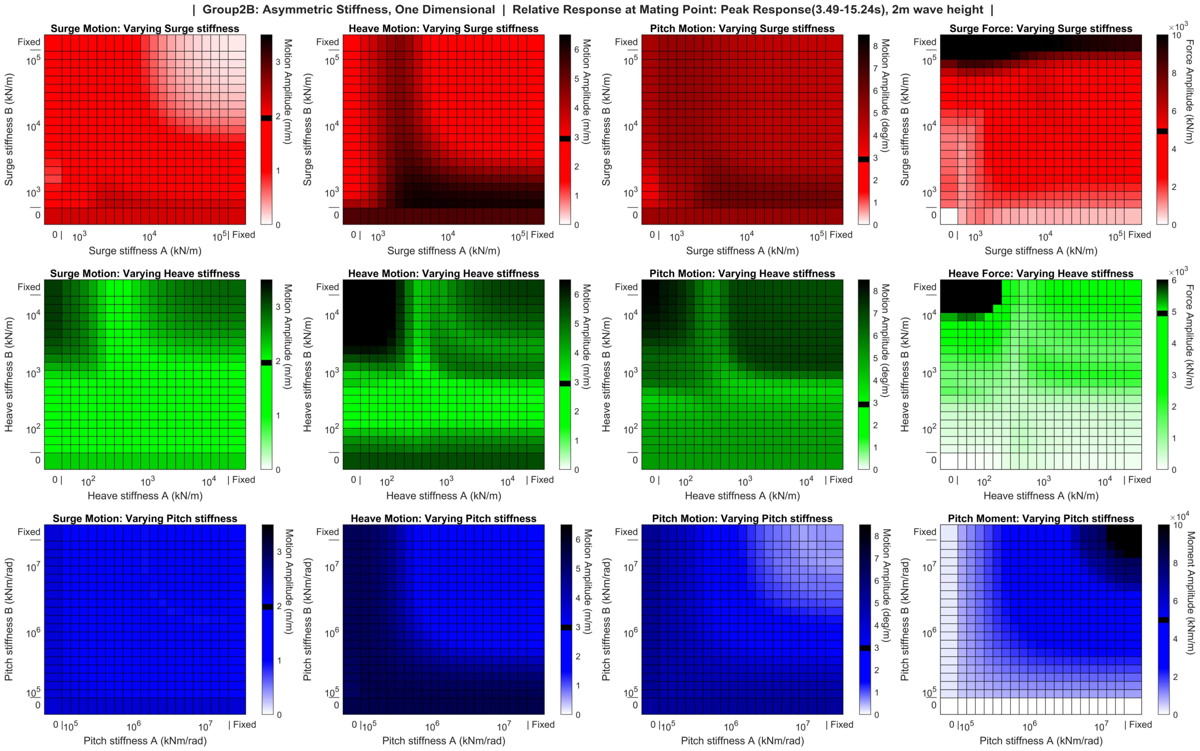

Figure 7.11: Group 2B: Asymmetric stiffness variation

7.3.2. Group 2C: Two Directional Coupling

Looking at the results for two-directional coupling, a similar trend is shown in the results of 1C. The motion response is shown in Figure 7.12. Similar to the results of group 1C, the x- and y-axis of the graphs indicate the two stiffnesses that are varied. The stiffness is now varied on both sides of the connection as well. The axis labels 'A Fixed' and 'A 0' indicate that the connection is fixed or free on side A. The arrows show an increasing or decreasing stiffness depending on the direction. The stiffness of connection side B is similarly labelled, and combining the two gives the combination of stiffnesses for each configuration. Looking at the surge motion response, it can be seen that fixing at least one side of the connection is beneficial. This is indicated by the large green and blue horizontal areas, respectively. It should be noted that stiffness on the other side is required to obtain and remain within the defined motion limits. Fixing the connection on one side without stiffness on the other side results in large motions. To limit the pitch motion response, very small areas in the surge and heave stiffness combination graph show potential combinations. These areas are better shown when looking at the weighted average graph shown in Figure 7.13. Looking at the average pitch response, it can be seen that certain combinations of stiffness exist that stay within the defined limits, which were not present in the symmetric stiffness results. Limiting the pitch motions when combining pitch stiffness with either surge or heave stiffness does show better results comparing the motion response graphs. The weighted average pitch response in Figure 7.13 shows that a combination of heave and pitch stiffness is still the most effective for staying within the defined motion limits. Overall, varying the stiffness on sides A and B of the connection shows more potential combinations than the symmetric stiffness variations. Investigating this further during the design of a connection is recommended.

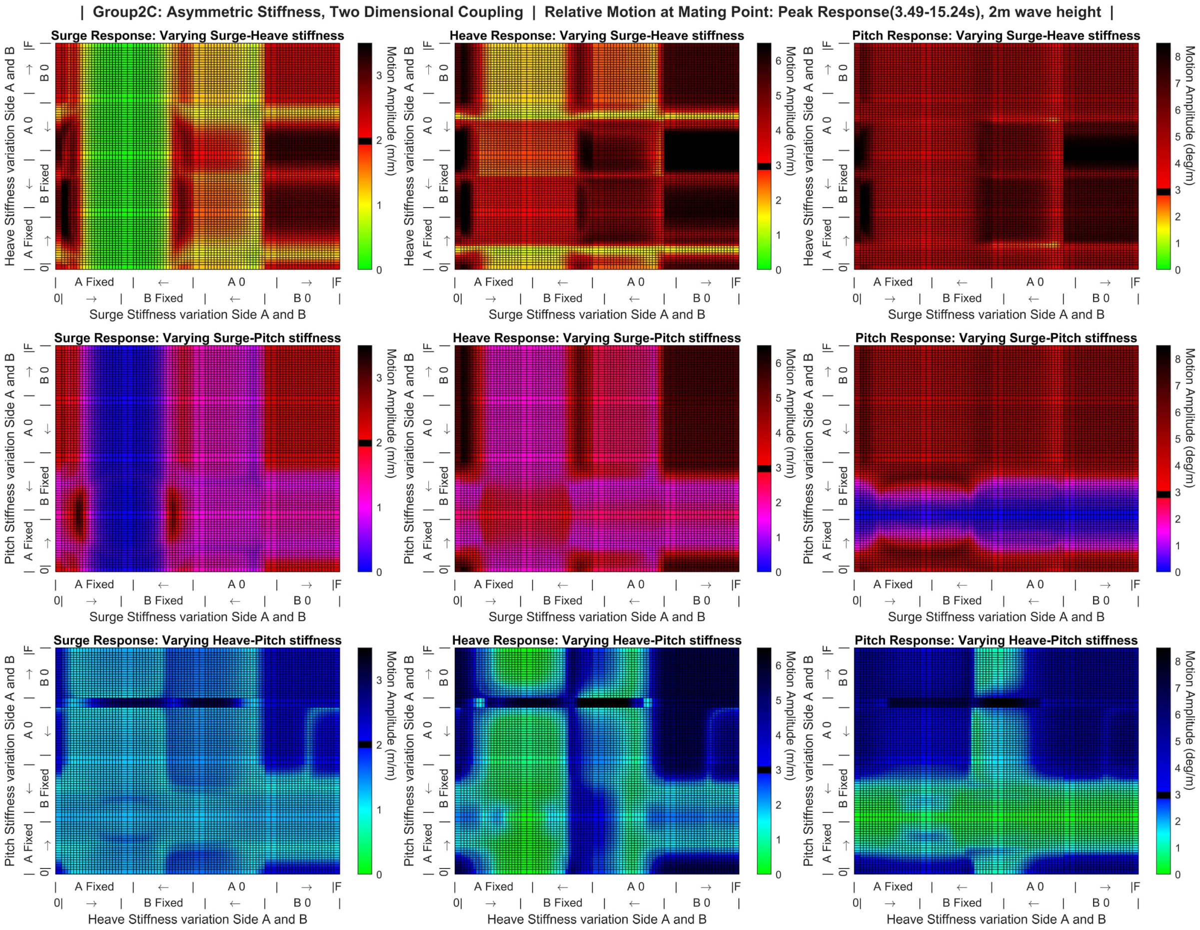

Figure 7.12: Group 2C: Motion Response

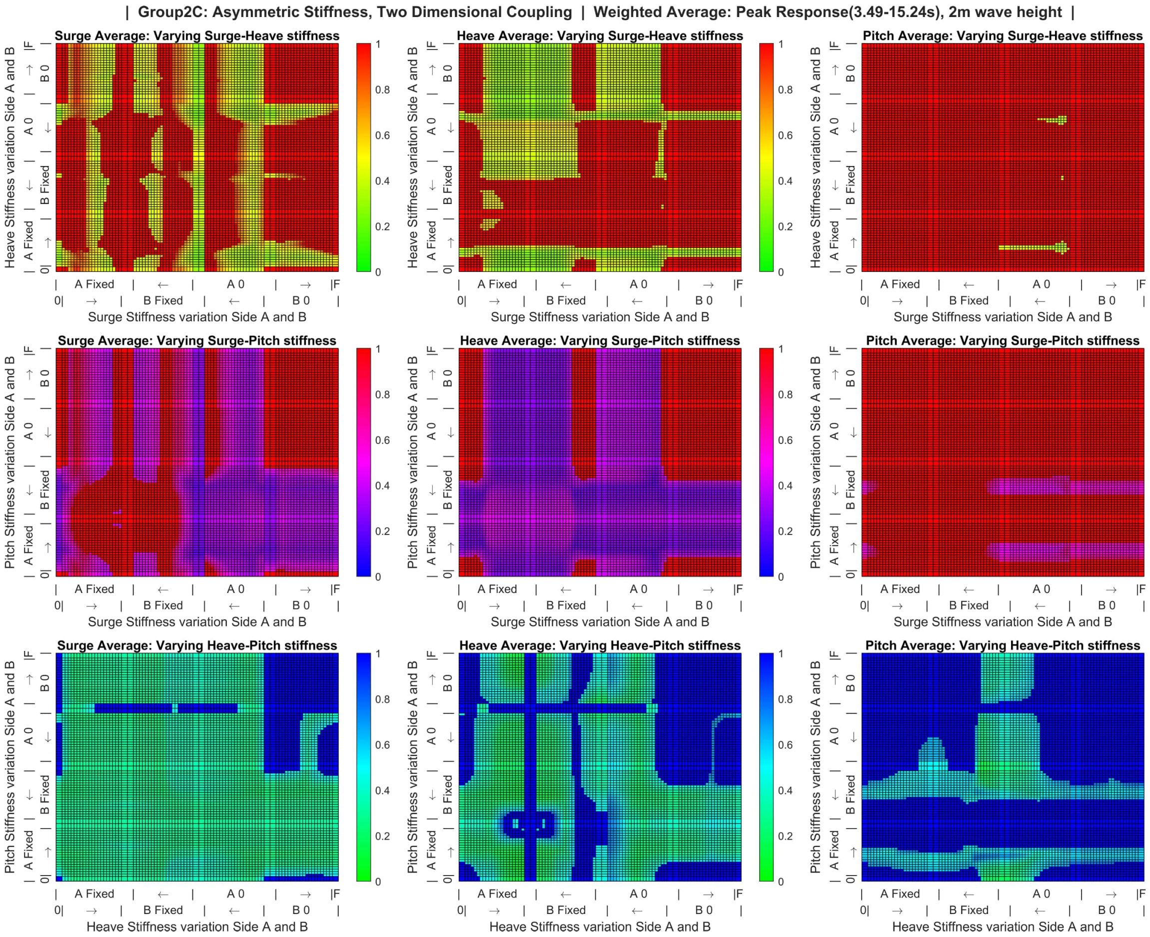

Figure 7.13: Group 2C: Weighted Average

7.3.3. Group 2D: Three Directional Coupling

Finally, looking at group 2D, it is investigated how the response changes when the third degree of freedom is fixed on one side of the connection. Since it is most likely that a combination of surge and heave stiffness will be used in practice, the effect of fixing the pitch motion on one side of the connection will be discussed here. The difference between having a connection with free pitch rotation or fixed on side A or side B is shown in Figure 7.14. The surge response is not affected much by fixing the pitch rotation on one side of the connection. Generally, the best response in the surge direction is when one side is fixed in the surge direction. The results show that by fixing the pitch motion on either side of the connection the heave and pitch motions will improve. In the heave direction, this results in a range of potential combinations for varying surge stiffness. The trend shown by the surge response is now also observed for the heave response, showing the best heave response when one side is fixed in the heave direction.

Considering the forces in the connection as well, Figure 7.15 shows the overall average response of the system. It is shown that fixing the connection on either side improves the potentially viable stiffness combinations, with a fixed connection on side B being slightly preferred. The large improvement in potential combinations mostly comes from the reduction in pitch motions caused by fixing the pitch rotation on one side of the connection. As mentioned, the floating support structure has the most dominant motion response in the considered wave period range. This is likely why fixing the connecting at the side of the support structure shows a decrease in relative motions. The added inertia of the link is much more substantial compared to the mass of the support structure. Fixing the link to the support structure effectively adds mass and inertia to the structure, decreasing its motions. Mechanically, it is difficult to fix the rotation of the connection at the side of the support structure, due to the high resulting moments. This is generally the trend shown by these results, better system behaviour might not always be the most practical to implement, and that has to be considered during the further design of the connection.

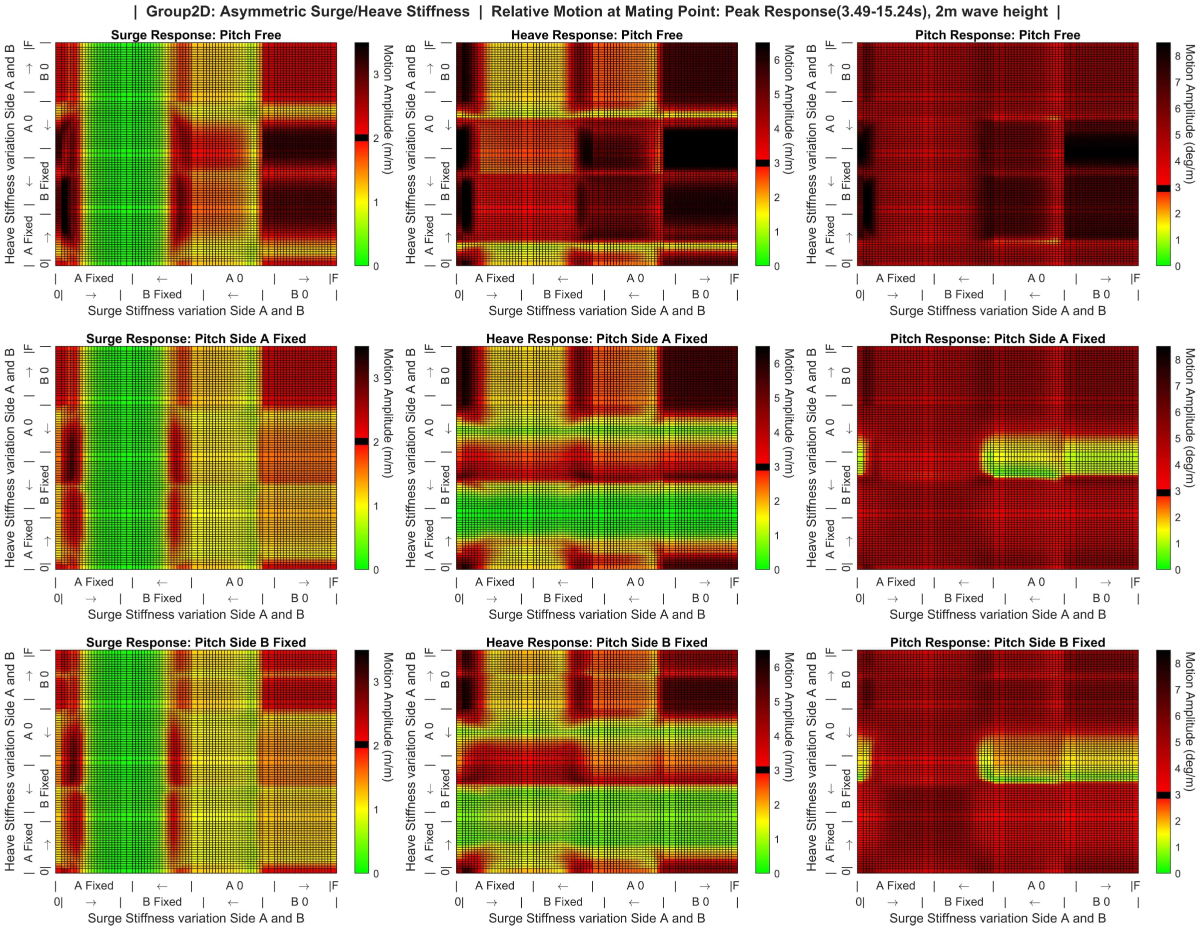

Figure 7.14: Group 2D: Surge-Heave Motions

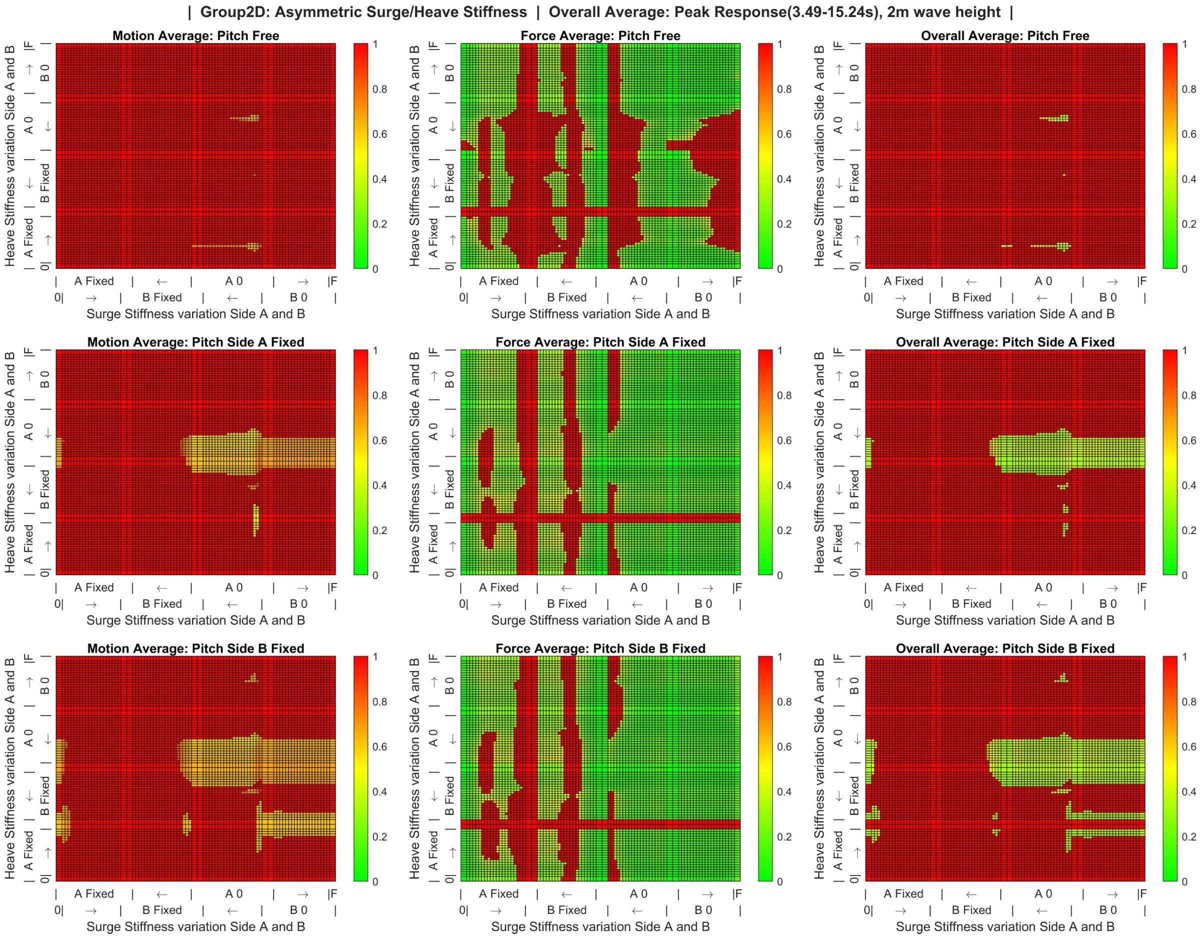

Figure 7.15: Group 2D: Surge-Heave Overall Average

7.4. Sensitivity Analysis

7.4.1. Damping

Figure 7.16 and 7.17 show the comparison of the motion and force response of the system for the three damping variations. Here, the results for a varying surge and heave coupling are shown, similar to analysis group 2C. The top row in the figures shows the surge, heave and pitch response for the system without damping, the second row shows the response for the default damping, and the bottom row shows the response with increased damping. The results indicate that damping has a favourable effect on the connection, decreasing the motion and the force response. Especially the motion response of the surge direction benefits from higher damping. Overall, the heave motion amplitude also decreases, but it increases slightly for the areas showing the lowest response with the default damping. Increasing the damping does decrease the loads on the connection for both the surge and heave directions. The effect of damping on the system is an interesting subject for future investigation.

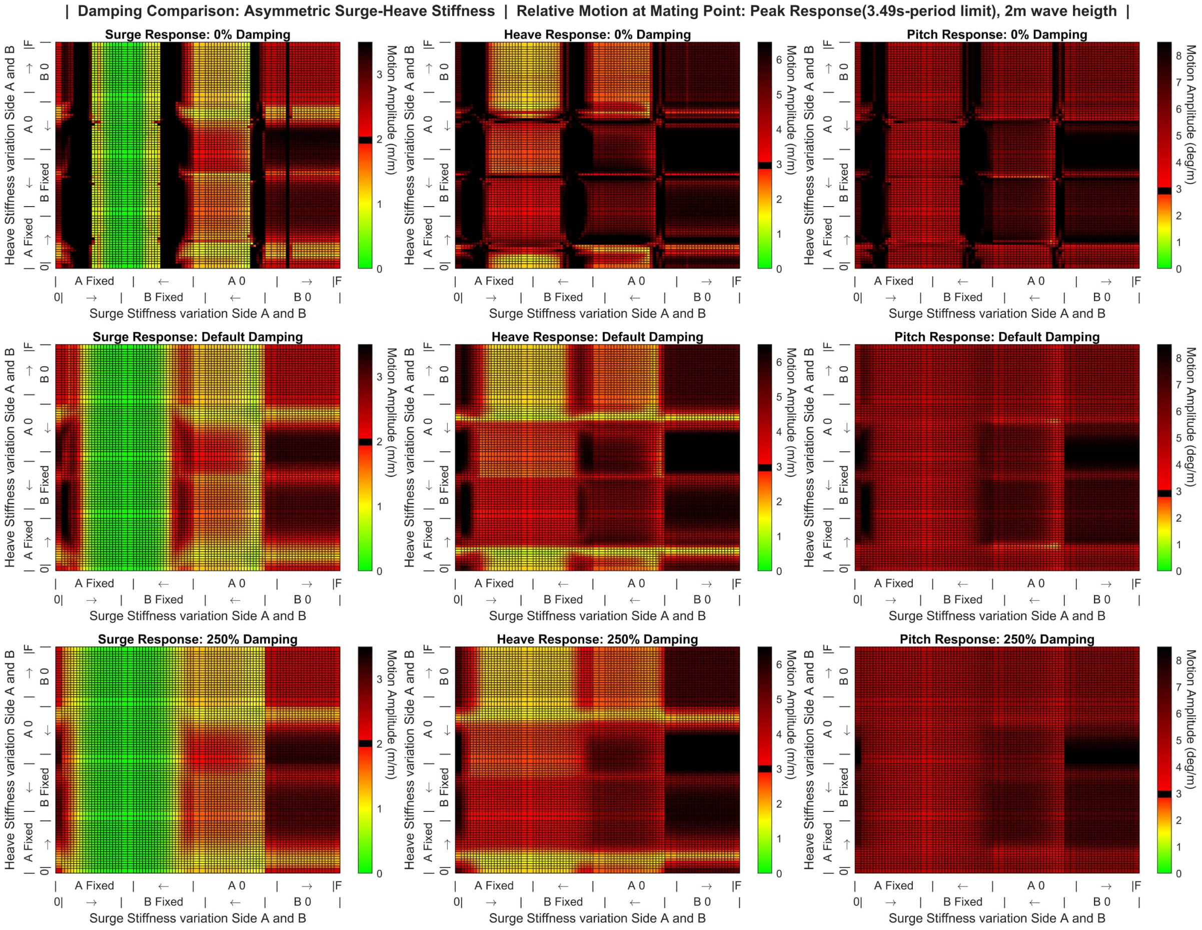

Figure 7.16: Comparison of the motion amplitudes for the damping variations.

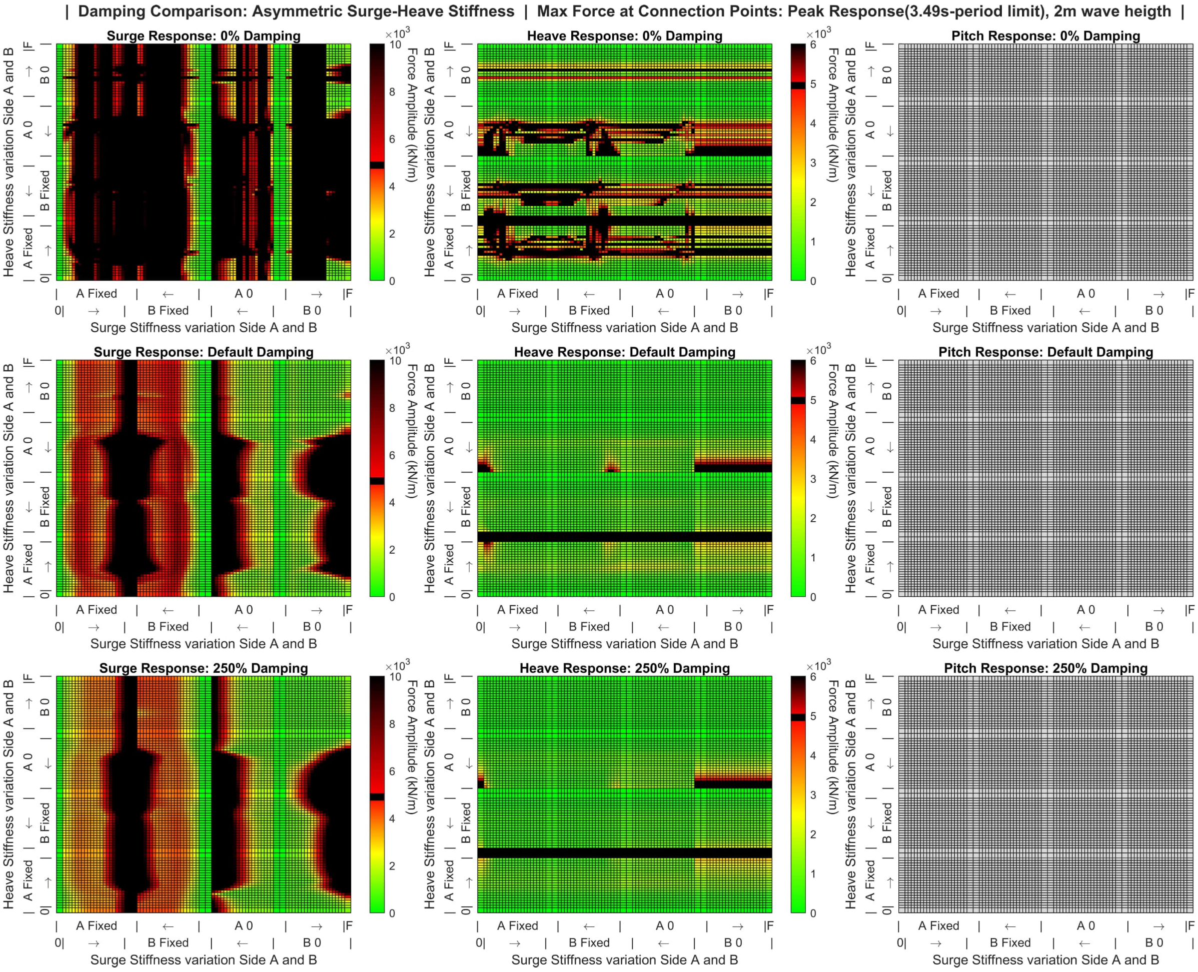

Figure 7.17: Comparison of the force amplitudes for the damping variations.

7.4.2. System Parameters

Figures 7.18 and 7.19 show the overall average results comparing the three different link mass and gripper stiffness variations, respectively. Looking at the response comparing the mass of the link it is generally shown that a lower mass increases the relative motions, and decreases the forces on the connection. Similarly, when increasing the mass of the link, the resulting motions are smaller, but the forces are higher. Most importantly it shows that the model is not sensitive to the mass of the link, and the behaviour of the system changes in an expected way.

The effect of the different gripper stiffnesses on the peak response of the system is negligible as well. This is mostly due to the small motions of the vessel, and a low response for smaller periods. Problems could arise when the eigenfrequency of the complete system is in the same range as the wave excitation. Based on the variations observed here, the model in its current state is not sensitive to the varied gripper stiffnesses.

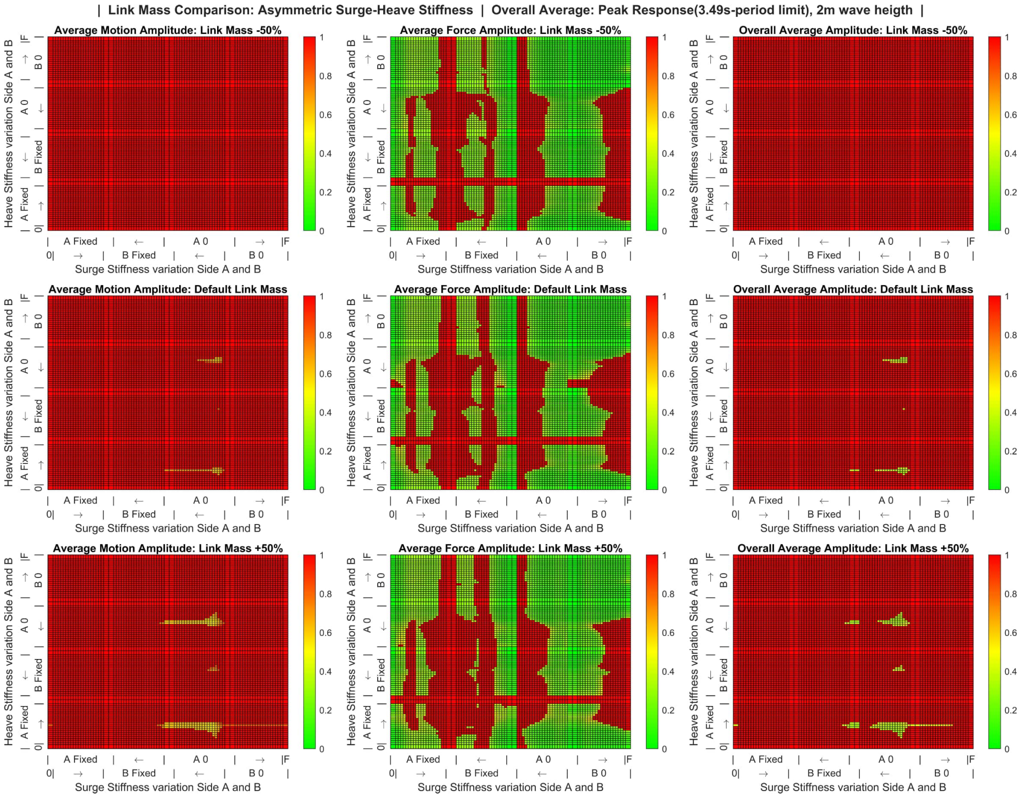

Figure 7.18: Comparison of the overall average for for the link mass variations.

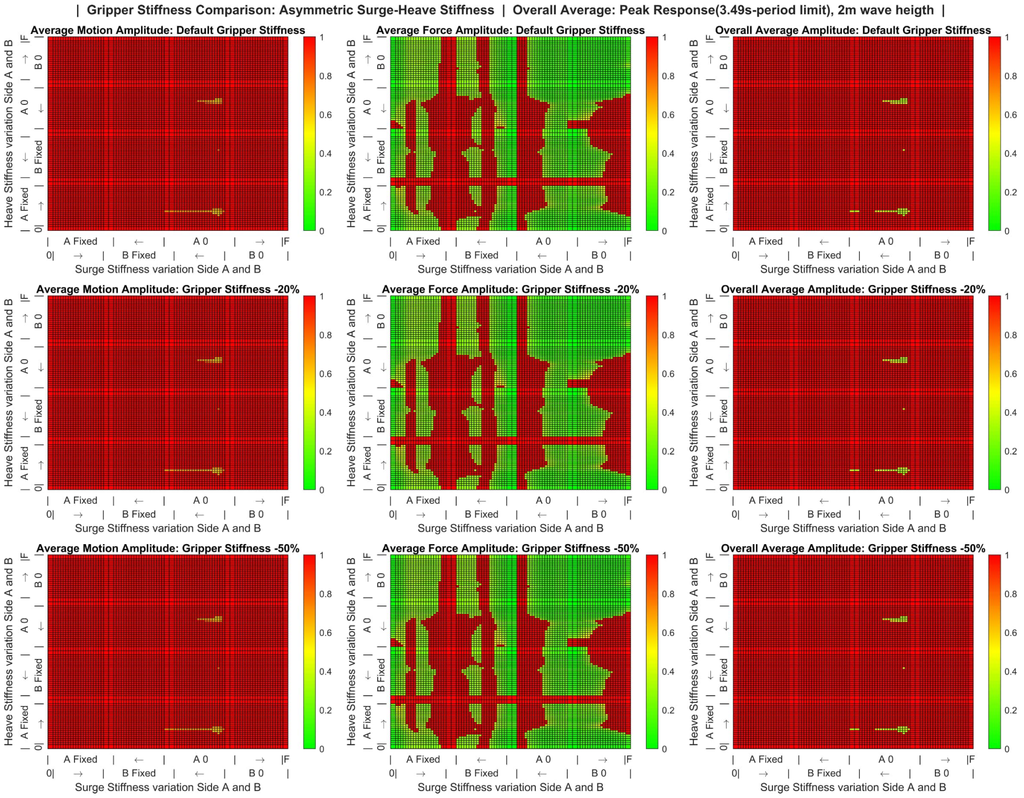

Figure 7.19: Comparison of the overall average for the gripper stiffness variations.

7.4.3. Operational Limits

The effect of lowering the considered wave periods on the overall average of the system's response is shown in Figure 7.20. This highlights that the system's peak responses occur at wave excitations with a period of 15 seconds, which is also observed in the results for parameter group 1A. Most peaks in the response occur at 15 degrees due to the large free-floating pitch response of the support structure at the period. Lowering the considered wave period range mostly improves the motion response of the system, as shown by the average motion results in the graph. The connection forces slightly decrease as well, as is expected when the resulting motions are smaller. Fixing both sides of the connections in the surge and heave direction still results in forces exceeding the set limits. Based on this the desired workability for larger wave periods will probably have to be lowered to remain within the design motion and load limits.

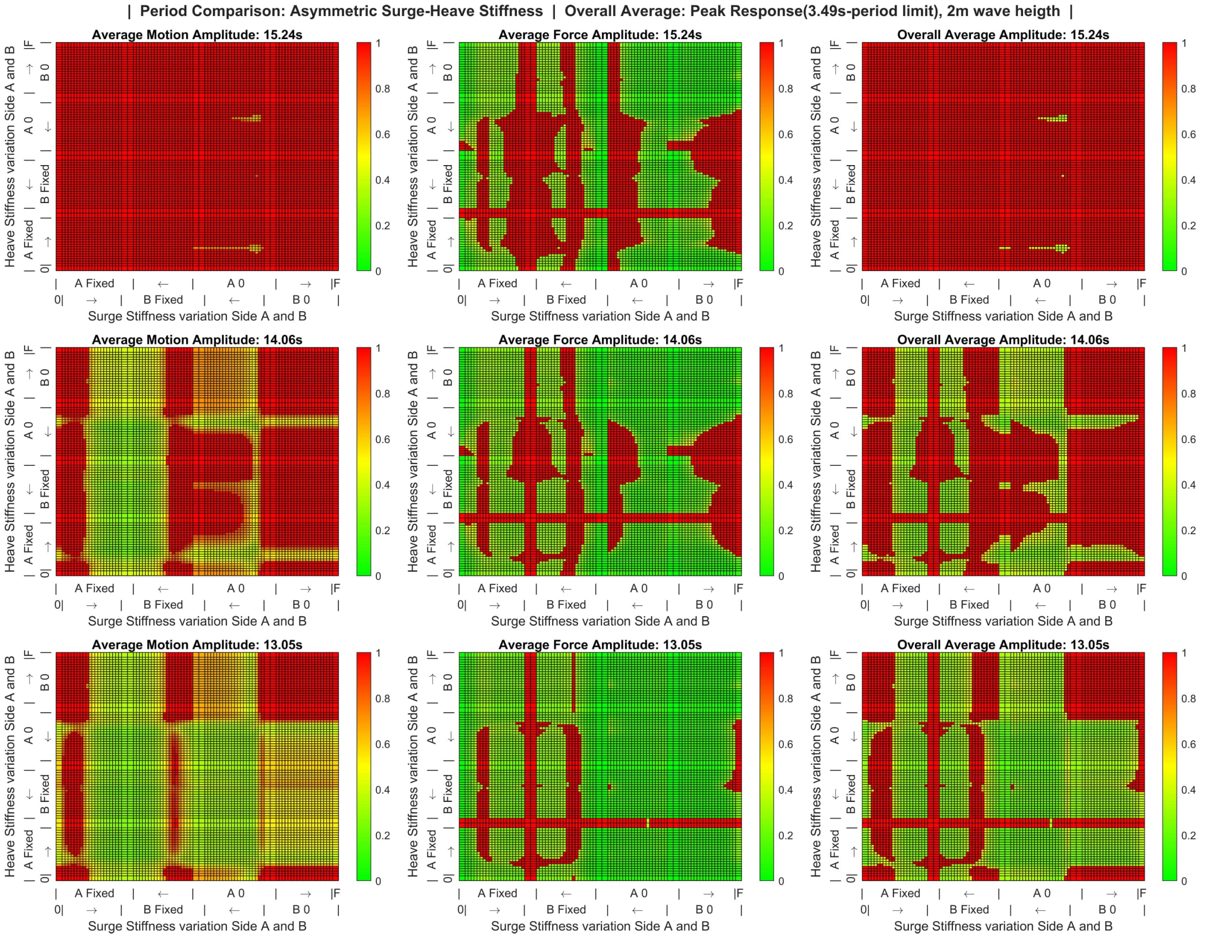

Figure 7.20: Comparison of the overall average for the wave period limit variations.

7.4.4. Linear vs Nonlinear Model

Two configurations are selected to investigate the difference between the linear and nonlinear versions of the model, one where the frequency analysis shows small displacements (configuration 1) and one where larger displacements are noticed (configuration 2). Table 7.1 shows the connection parameters of the two configurations.

Table 7.1: Connection stiffness and damping parameters for the two configurations used to compare the linear and nonlinear model.

	Stiffness Side A surge	 heave	 pitch	Stiffness Side B surge	 heave	 pitch
Configuration 1	2E+2 kN/m	7E+1 kN/m	1E+7 kNm/m	1E+5 kN/m	1E+5 kN/m	0 kNm/m
Configuration 2	1E+5 kN/m	1E+5 kN/m	1E+7 kNm/m	1E+2 kN/m	7E+1 kN/m	0 kNm/m

The environmental conditions for the time-domain simulation are a wave height of two meters and a wave period of 13 seconds. A settling time of 30 seconds and a wave build-up time of 270 seconds is used, and the simulation duration is 2400 seconds. The computation time for the linear variant of the model for this configuration is around 33 seconds, whereas the nonlinear variant requires 374 seconds to solve a single run. To compare the results of the linear and nonlinear model, both the maximum displacement and the RMS value of the signal will be used. The results of the time-domain simulations are shown in Table 7.2 The motion amplitudes for the CG of the installation vessel and floating support structure are shown, as well as the motion amplitudes of the mating point on the wind turbine and the floating support structure. The last three columns show the relative motion amplitude between the wind turbine mating points. The peak amplitude and the Root Mean Square (RMS) values of the time domain signal are compared, and the difference is shown as a percentage. As can be seen from the table, the linear model provides a good approximation of the nonlinear model, with the differences in values remaining smaller than 1% for the configuration with smaller displacements. The results for the second configuration with larger displacements show larger differences between the linear and nonlinear variants of the model. A maximum of 3.58% in the surge motion of the support structure is observed for a pitch motion amplitude of four degrees. Looking at the RMS values, the differences between the linear and nonlinear remain smaller than 1% for all displacements. Based on this comparison, it can be concluded that the linear approximation of the connection provides results accurate enough to analyse the system.

Table 7.2: Table showing the linear and nonlinear model comparison results.

Configuration 1 (Small disp.)	Vessel CG			Wind Turbine MP			Support Structure CG			Support Structure MP			Relative		
	surge [m]	heave [m]	pitch [deg]	surge [m]	heave [m]	pitch [deg]	surge [m]	heave [m]	pitch [deg]	surge [m]	heave [m]	pitch [deg]	surge [m]	heave [m]	pitch [deg]
Peak values															
Linear Disp.	0.3434	0.3964	0.1573	0.3074	0.5240	0.1588	0.5978	0.2410	0.3522	0.6529	0.2297	0.3522	0.9553	0.6904	0.3335
Nonlinear Disp.	0.3434	0.3964	0.1582	0.3075	0.5249	0.1601	0.5983	0.2410	0.3526	0.6528	0.2299	0.3526	0.9551	0.6918	0.3341
Difference (%)	0.00	0.00	0.57	0.03	0.17	0.81	0.08	0.00	0.11	0.02	0.09	0.11	0.02	0.20	0.18
RMS values															
Linear	0.2331	0.2692	0.1067	0.2087	0.3556	0.1078	0.4059	0.1636	0.2393	0.4432	0.1559	0.2393	0.6485	0.4685	0.2264
Nonlinear	0.2331	0.2692	0.1073	0.2086	0.3563	0.1086	0.4059	0.1636	0.2392	0.4432	0.1558	0.2392	0.6484	0.4694	0.2264
Difference (%)	0.01	0.01	0.56	0.04	0.21	0.79	0.00	0.00	0.01	0.00	0.02	0.01	0.01	0.19	0.01

Configuration 2 (Large disp.)	Vessel CG			Wind Turbine MP			Support Structure CG			Support Structure MP			Relative		
	surge [m]	heave [m]	pitch [deg]	surge [m]	heave [m]	pitch [deg]	surge [m]	heave [m]	pitch [deg]	surge [m]	heave [m]	pitch [deg]	surge [m]	heave [m]	pitch [deg]
Peak values															
Linear Disp.	0.3299	0.3838	0.1408	0.2974	0.4806	0.1420	0.7811	1.7440	4.0037	1.2900	4.2067	4.0037	1.4782	4.5946	4.0033
Nonlinear Disp.	0.3319	0.3838	0.1417	0.2991	0.4816	0.1433	0.8101	1.7446	4.0049	1.2617	4.2073	4.0049	1.4478	4.5952	4.0044
Difference (%)	0.60	0.00	0.64	0.57	0.21	0.91	3.58	0.03	0.03	2.24	0.01	0.03	2.10	0.01	0.03
RMS values															
Linear	0.2163	0.2516	0.0924	0.1949	0.3148	0.0933	0.5122	1.1081	2.5292	0.7975	2.6394	2.5292	0.9337	2.8943	2.5280
Nonlinear	0.2163	0.2516	0.0929	0.1949	0.3153	0.0940	0.5129	1.1084	2.5297	0.7971	2.6400	2.5297	0.9334	2.8951	2.5285
Difference (%)	0.00	0.00	0.53	0.02	0.17	0.76	0.13	0.03	0.02	0.06	0.02	0.02	0.04	0.03	0.02

Disp. = Displacements, MP = Mating Point, RMS = Root Mean Square

7.5. Discussion

The presented system analysis covers a wide range of configurations, which can mainly be used to discover overall trends in the system's behaviour. Considering only peak responses has certain drawbacks, but this method allows for quantifying the performance of the many configurations. Overall, it can be concluded that a combination of stiffness in the different connection directions will result in the most favourable results. A different stiffness on both sides of the connection is also shown to improve the system's behaviour. The motion response of the floating support structure contributes the most to the relative motions between the mating points. Especially the pitch response at a wave period of 15 seconds of the support structure is the main cause for large relative motions. In practice, the maximum allowable wave height for workability must be lowered for this period to maintain within the system's limits. A potential limitation of considering the peak response to determine system performance is shown by looking at the frequency response for a stiffness configuration chosen based on the system analysis results. The following configuration considers a fixed surge and heave connection on the side of the support structure and a fixed pitch connection at the side of the installation vessel. The heave and surge stiffness on the side of the installation vessel are 200 kN/m and 70 kN/m, respectively. On the side of the support structure, the connection is free in rotation. The frequency response of the relative motion is shown in Figure 7.22. As shown in the figure, the response remains within the set limits in each direction of motion. However, in the heave and pitch direction, the response rapidly peaks outside the considered wave period limits of 15 seconds.

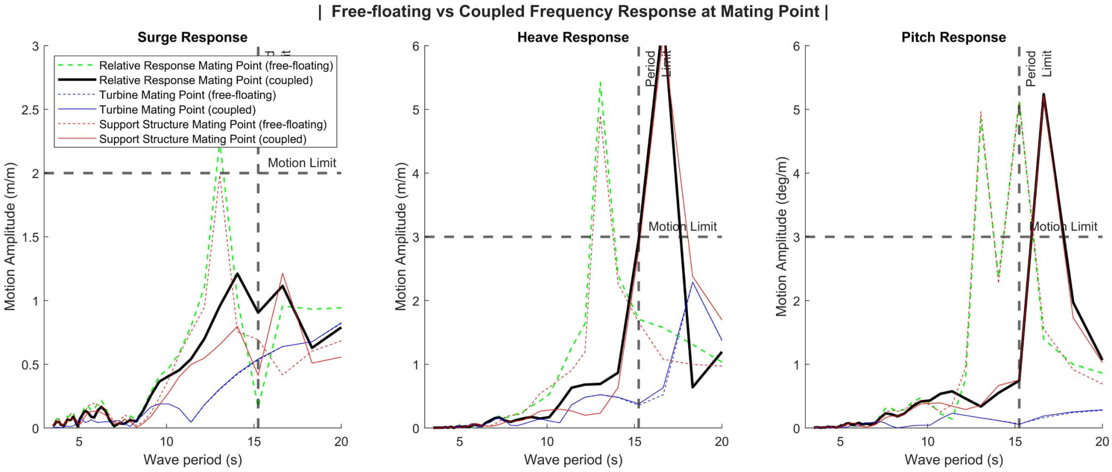

Figure 7.21: Relative motion response for a connection with stiffness of [2E+2 kN/m,7E+2 kN/m,1E+8 kNm/rad] at side A, and [1E+7 kN/m,1E+7 kN/m,0 kNm/rad] at side B.

The configuration above considers the connection to be fixed in the heave and surge direction at the side of the support structure and fixed in rotation on the installation vessel. Fixing the connection on one side in each direction of motion is favourable in practice since it reduces the required number of moving parts in the final construction. However, the configuration above might be difficult to construct since the connection must be able to move in both the surge and heave direction at the attachment point on the installation vessel. Overall, the system analysis results show that fixing the link on the side of the support structure is more favourable to the system's performance, considering the set limits. As mentioned, this is most likely due to the acceleration effects of the mass and inertia on the support structure. When the connection is completely fixed on the side of the support structure, the two bodies behave as a single body with a larger mass and inertia. Due to the increase in mass and inertia, the response of the support structure will become smaller. However, in this model, no gravity forces act on the connecting link, as it is assumed to be supported by the installation vessel. If gravity acts on the link, the support structure would not be able to support it if it was not attached to the installation vessel. Considering these practical implications, a similar configuration will be tested, changing the fixed sides of the connection. On the installation vessel, the heave and pitch direction will be fixed, and a similar surge stiffness of 200 kN/m will be added. On the side of the support structure, the connection is fixed in the surge direction, and a heave stiffness of 700 kN/m will be applied, the rotation is free. Figure

7.22 shows the frequency response graph of this configuration.

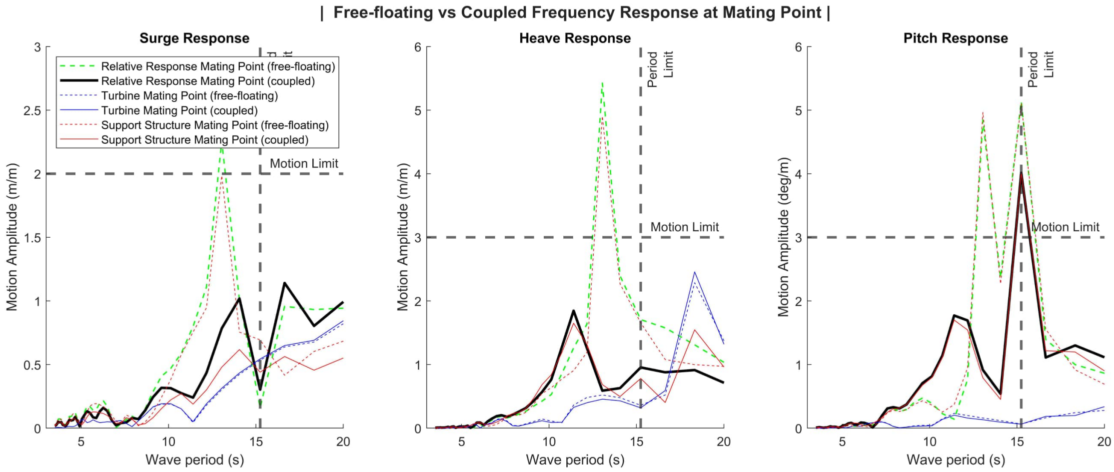

Figure 7.22: Relative motion response for a connection with stiffness of [2E+2 kN/m,1E+7 kN/m,1E+8 kNm/rad] at side A, and [1E+7 kN/m,7E+2 kN/m,0 kNm/rad] at side B.

In comparison, the overall surge and heave response is reduced, and the peak of the pitch response is smaller. The pitch response peak shifted to a wave period of 15 seconds, causing it to be just outside the set limits for the pitch motion. This configuration is rejected because of the set limits of the carried-out system analysis, even though, considering the practical limitations, it might be a better system configuration. Looking at this frequency response and analyzing this configuration using the time-domain simulation, it can be concluded that when fixing the rotation and heave motions at the vessel, it is beneficial to allow for some heave motion at the support structure's side. If the heave motion is also fixed, the support structure rotates around the connection, increasing its pitch response. Ideally, the connection point at the side of the floater follows the heave motion of the CG of the support structure to reduce pitch angles. In this regard, allowing for a rotation at the side of the support structure is more beneficial since the rotation point is closer to the support structure CG. Another option to achieve this would be to restrict the heave motion of the support structure by implementing a rotational stiffness on the side of the installation vessel. The connection would be fixed on the side of the support structure in surge and heave direction and can still rotate unrestricted. On the vessel's side, a similar surge stiffness is chosen, the heave direction is fixed, and the rotation has a stiffness of 10000 kNm/rad. Even though the connection can now rotate, the connecting link can still be supported from the vessel by implementing pre-tension on the cylinders. Figure 7.23 shows the frequency response graph of this configuration. As expected, a similar result is found compared to the second configuration. Both configurations achieve a similar result in the relative motions, using two different stiffness configurations. A comparison between the time-domain simulation of the two configurations is shown in Figure 7.24. Even though the response is still not within the set motion limits, the system's response has improved compared to the free-floating response.

Although overall trends have been identified by the carried out system analysis, it is recommended that for further design of the connection, a more concise approach is taken. The two configurations shown provide a good starting point for further optimization.

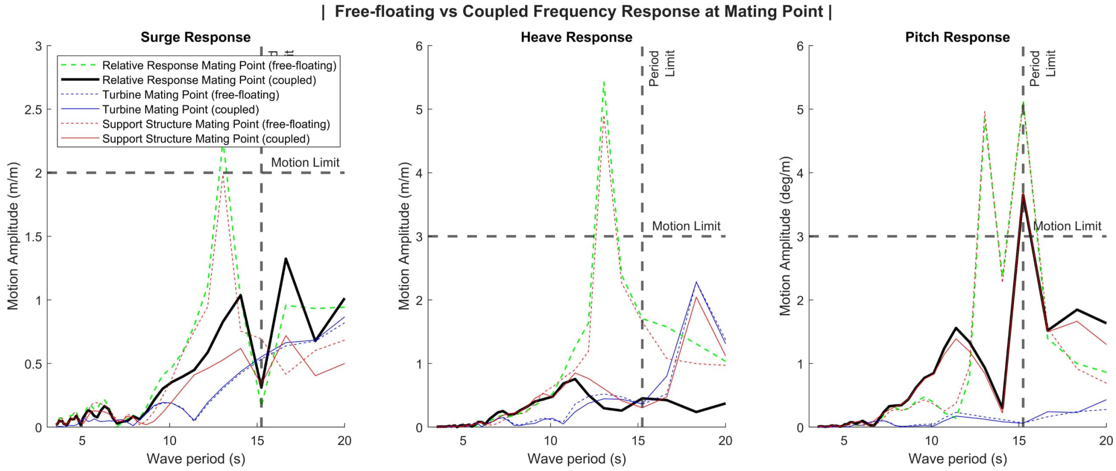

Figure 7.23: Relative motion response for a connection with stiffness of [2E+2 kN/m,1E+7 kN/m,1E+5 kNm/rad] at side A, and [1E+7 kN/m,1E+7 kN/m,0 kNm/rad] at side B.

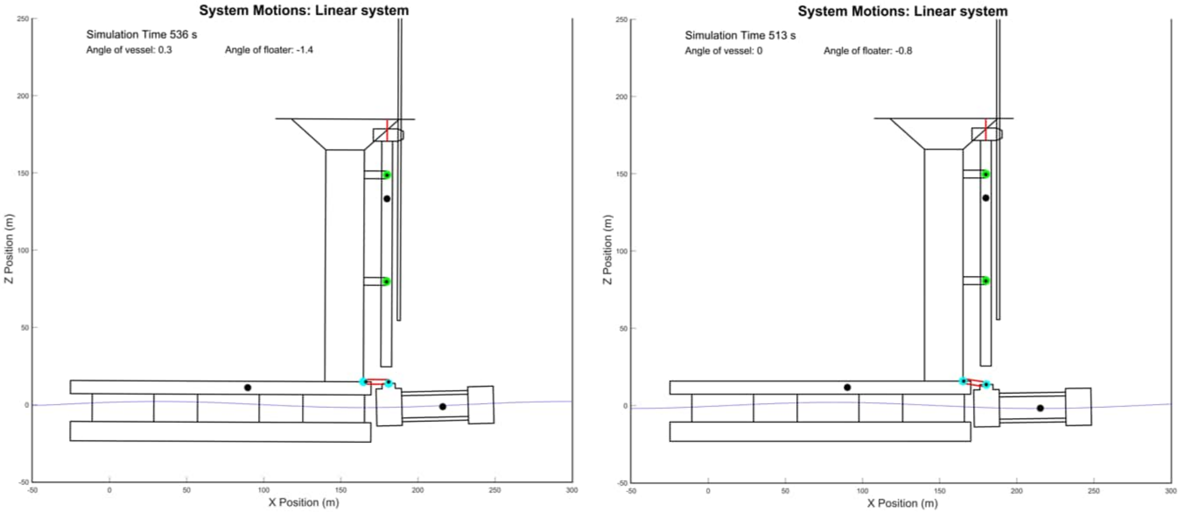

Figure 7.24: Time-domain comparison between the motions of the two selected connection configurations.

8

Conclusions and Recommendations

8.1. Conclusions

This project set out to develop a model to investigate the effect of the structural configuration of a connection between an installation vessel and a floating support structure during the installation of a floating offshore wind turbine. A two-dimensional dynamic model describing the motions of two bodies connected with a rigid link has been formalized, described as the Rigid Link Flexible Boundaries model. Due to the combined motions of the system, the equations of motion are geometrically nonlinear. To perform a frequency analysis of the system, the connection model is linearized. The time-domain response of the linear and nonlinear models have been compared and show a maximum error of 3.58% for the peak responses and an error smaller than 1% for the RMS values of the signal. It is therefore concluded that the linear model provides an accurate enough representation of the system.

The model is used to investigate the performance of the connection between an installation vessel and a semi-submersible floating support structure during the offshore installation of the floating offshore wind turbine. The installation procedure of a floating offshore wind turbine is a complicated operation. Huisman has introduced the Windfarm Installation Vessel (WIV) as a complete solution to assemble and install the wind turbine at the wind farm location. During installation, the wind turbine is suspended from the installation tower of the WIV and its position is controlled by two motion-compensated grippers. Installing a floating wind turbine at sea brings two main challenges, the relative motions between the floating structures and the load transfer between the two floating structures. The installation procedure has been divided into five discrete installation stages. During all stages, the installation vessel and floating support structure are coupled by the connection. A ballast transfer will be initiated between the support structure and the installation vessel, moving water ballast from the support structure to the installation vessel. At installation stage 1, zero per cent ballast has been transferred. Next, at installation 2, 50 per cent of the ballast is transferred, and the ballast transfer is complete at installation stage 3. During these stages, the connection load gradually increases since both floating structures should remain balanced. The connection should be able to carry the ballast's load since the system's equilibrium is changing. The ballast transfer is required to minimize the time of the mating operation of the wind turbine, during which the system is most vulnerable. The wind turbine can be released from the installation vessel without waiting for the ballast transfer to be complete while the system is connected. In the next stage, the wind will be lowered onto the support structure, connecting all bodies in the system. Finally, at stage 5, the wind turbine is released and attached to the floating support structure. A configurable MATLAB tool has been scripted to numerically assess the system's performance during the five installation stages, including the rigid link, ballast, pretension, and connection modelling elements. An Ansys AQWA analysis has been performed to obtain the hydrodynamic properties and loads for the two floating structures. The system's performance is analysed using regular waves with varying wave periods.

To assess the system's performance, the relative motions of the wind turbine mating point and the connection forces are considered. The effect of the different installation stages on the system's behaviour is investigated, and it was found that the main difference between the stages is the load on the connector due to the balance transfer. The dynamic loads due to wave excitation are similar for the first three installation stages. Only the fourth installation stage shows smaller motion responses due to the coupling between all bodies. An extensive system analysis focussing on the first installation stage has been performed. From the free-floating response of the relative motions, it can be concluded that the motion response of the support structure is limiting. Due to large peaks in the pitch response at 13 and 15 seconds, large responses in the surge and heave direction are also experienced at the mating point. Two parameter groups have been used to investigate the influence of the connection. Group 1 focuses on the effect of adding symmetric stiffness to the connection, meaning the stiffness on both sides of the connection is equal. Group 2 extends this by varying the stiffness on both sides of the connection separately. The effect of coupling between the different directions of motion has been investigated for both groups. Operational limits have been defined to quantify the system's performance for different stiffness combinations. The surge, heave and pitch motion amplitude limits have been set at 2 meters, 3 meters and 3 degrees, respectively, based on the expected performance of the motion-compensation systems. The peak of the relative motion response of wave periods below 15.24 seconds is chosen to capture the system's performance with a single value.

The proposed system analysis focussed on comparing many different configurations but was therefore limited in the depth of analysing system performance. This work has mostly shown trends in how the system responds to various stiffness values and coupling in multiple dimensions. When symmetrically varying the stiffness in a single direction, the effect of adding stiffness on the relative motions of the system is difficult to predict. The pitch motions are the most difficult to suppress. Adding stiffness in the pitch direction is the only option to keep the pitch motion within the set limits. The effect of adding heave stiffness resulted in unexpected behaviour, as a higher stiffness resulted in much higher system motions in all directions. Adding stiffness in a single direction of the connection does Overall, these results show that it is difficult to stay within the defined limits by adding stiffness in a single direction of motion. Coupling stiffness was shown to have a favourable effect on the response of the system. Combining heave and pitch stiffness resulted in a more expected heave response. When investigating the asymmetric stiffness it was found that when combining surge and heave stiffness, possible combinations within the defined limits for the pitch motion were present, which were not seen in the symmetric stiffness results. Finally, most asymmetric coupling results seem to favour fixing the connection on the side of the floating support structure. Fixing the link to the support structure effectively adds the mass and inertia of the link to the structure, decreasing its motions. Considering the practicality of the design, this might however be more difficult to achieve. Configurations fixing the connection on the side of the vessel are therefore investigated as well, and although these did not stay within the chosen motion limitations, the overall response indicated better overall performance. This shows a limitation of the approach taken for the system analysis.

In conclusion, a modular tool has been created that allows for a quick assessment of the structural configuration of the connection. The tool includes options to change the system's parameters to vary the structural configuration of the connection. A first system analysis has been carried out using this tool, showing the general trends of varying stiffness of the connection. Overall, it can be concluded that a combination of stiffness in the different connection directions will provide the most favourable results. It is also shown that a different stiffness on both sides of the connection can improve the system's behaviour. However, further analysis of the system is required to formalize a concrete design recommendation.

8.2. Recommendations

The connection behaviour is shown to be complex, not always behaving as expected, and is therefore well suited for follow-up academic research. The system analysis focussed on comparing different configurations but was therefore limited in the depth of analysing system performance. The results of a sensitivity analysis show that damping can positively influence the system's behaviour. Future research could further expand on this and investigate the behaviour of the system when the damping constants are separately varied in different directions of the connection. The proposed model can be used for further analysis, for example, to form the basis of an optimization study. Future work could further investigate design requirements and considerations to narrow down possible configurations, using an optimization algorithm. When a smaller selection of configurations is considered, the model could be extended to include different environmental conditions, including wave spectrum responses or irregular waves and the effect of wind. In reality, the wave heading will never be ideal, so it can also be interesting to look at the system in three dimensions, and investigate the effect of changing wave headings. More details on the structures involved can be added as well. The current version of the model assumes rigid bodies, due to the large mass of the structures, it might be interesting to consider flexible bodies. The influence of the support structure's mooring lines could be interesting as well, potentially, varying the tension could provide a more favourable frequency response of the support structure.

The system analysis also revealed some practical recommendations for the design of the connection. Comparing the different installation stages, the largest difference in the load of the connection is caused by the ballast transfer procedure. Minimizing the amount of ballast that is transferred will therefore decrease the loads on the connection. During the fourth installation stage, the whole system is connected causing the motions of the support structure to influence the load on the motion-compensated grippers. The force on motion-compensated grippers should be considered during this stage of the installation. Potentially, different configurations of the connection can be investigated as well. For example, adding additional links to the system. Looking at a four-bar mechanism the motion of the two vertical bars can be controlled by the length of the horizontal links. This could potentially improve the amount of control that can be had over the motions of the support structure. The effect of different types of floating support structures can be investigated as well, the behaviour of a spar or Tension Leg Platform (TLP) structure might influence the connection in a different way.

A

Research Paper

Dynamic Analysis of a Mechanical Connection Between An Installation Vessel and A Floating Support Structure to Limit the Relative Motions During the Installation of A Floating Offshore Wind Turbine

J.J.A. Kortekaas[a], Dr. A. Grammatikopoulos[a], Dr. J. Jovanova[a], ir. M. Stofregen[b]

[a]*Department of Maritime and Transport Technology, Faculty Mechanical, Maritime and Materials Engineering, Delft University of Technology, Delft, The Netherlands*
[b]*Huisman Equipment B.V., Admiraal Trompstraat 2, 3115 HH, Schiedam, The Netherlands*

Abstract

Huisman has introduced the Windfarm Installation Vessel as a complete solution to assemble and install offshore wind turbines at sea. Installing a floating wind turbine at sea brings two main challenges, the relative motions between the floating structures and the load transfer of the wind turbine. The proposed installation procedure considers a connection between the installation vessel and the floating support structure to reduce the relative motions and facilitate the load transfer. This research investigates how the connection's structural configuration affects the system's relative motions and loads.A two-dimensional multi-body model has been formulated considering a rigid link between the installation vessel and the floating support structure. The hydrodynamics of the floating structures and the regular wave loads on the structures are calculated using Ansys AQWA. A system analysis is performed to investigate the effect of adding stiffness in one or combined directions of motion of the connection. Overall, it can be concluded that a combination of stiffness in the different connection directions will provide the most favourable results. A different stiffness on both sides of the connection is also shown to improve the system's behaviour. Further analysis is required to find optimal stiffness values for the connection.

Keywords: Floating offshore wind, In-situ installation, Windfarm Installation Vessel, Semi-submersible wind turbine, Dynamic model, Numerical analysis

---

1. Introduction

As the world's electricity consumption continues to rise, more countries realize the need for renewable energies. Not only to reduce carbon emissions but also to gain energy independence. Floating Offshore Wind (FOW) is seen as a solution to harvest wind energy in deeper oceans, reaching better wind speeds and providing the option of installing wind energy in steep coastal areas. However, currently demonstrated installation methods are limited by their need for large fit-out ports, requiring large quay areas with strict requirements (Crowle and Philipp, 2021; Crowle and Thies, 2022). Therefore, a way must be found to enable safe, quick, and routine installation of Floating Offshore Wind Turbines (FOWT's). Huisman has introduced the Windfarm Installation Vessel (WIV) as a complete solution to assemble and install offshore wind turbines. An in-situ installation procedure is proposed whereby the mating operation of the wind turbine will take place at the wind farm location. Installing a floating wind turbine at sea brings two main challenges, the relative motions between the floating structures and the load transfer between the two floating structures. A mechanical connection between the installation vessel and the floating support structure is proposed as a potential solution for these challenges. Recently presented studies are limited to the spar support structure and limited stages of the installation process (Hong et al., 2021, 2022; Liu et al., 2023). It has been shown that the magnitude of the relative motion between the bottom of the wind turbine and the support structure is crucial for successfully mating the wind turbine (Jiang et al., 2018). This research aims to develop a two-dimensional multibody model which investigates the effect of the structural configuration of a connection between an installation vessel and a semi-submersible floating support structure during the installation of a floating offshore wind turbine. Connections between floating structures are an important aspect of studies looking into Very Large Floating Structures (VLFS). The Rigid Module Flexible Connector (RMFC) model (Riggs and Ertekin, 1993; Ding et al., 2020), which describes a flexible connection between two directly coupled rigid floating structures, will be extended to describe a rigid link with flexible boundaries connecting two floating structures. This work will contribute to existing research by creating a model that enables quick assessment of connector configuration between two floating structures during the lifting and installation of a wind turbine assembly, considering the wind turbine assembly as a separate body and the ballast transfer between the bodies.

2. Proposed Installation Procedure

The installation procedure has been divided into five discretized installation stages, allowing the change in the system's

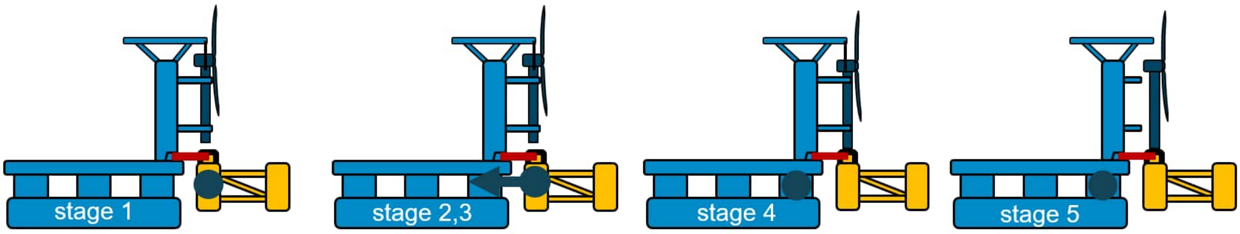

Figure 1: Schematics showing the five different installation stages. Installation stages 1-3 cover 0 %, 50 % and 100 % of ballast transfer from the support structure to the installation vessel. Next, the wind turbine is mated to the support structure at installation stage 4, coupling all bodies. At installation stage 5, the wind turbine is connected to the support structure.

behaviour to be studied. The installation vessel and the floating support structure are coupled with the connection during all five installation stages. The different stages consider the ballast transfer and the mating of the wind turbine. Installation stages 1 to 3 consider the ballast transfer between the floating support structure and the installation vessel to investigate the change in mass's influence on the system's dynamic behaviour. During the first stage, the connection between the installation vessel and the floating support structure has been made, and no ballast has been transferred yet. Installation stage two considers 50 per cent of the mass of the turbine to be transferred from the first column of the floating support structure into the last column of the installation vessel. At installation stage three, all ballast has been transferred from the floating support structure to the installation vessel. The connection load gradually increases during these stages since both floating structures should remain balanced. During the first three stages, the wind turbine is suspended from the installation tower of the WIV. Once the ballast is transferred, the wind turbine will be lowered and mated to the support structure, as shown in the figure at stage 4. All bodies in the system are connected during this stage since the turbine is still attached to the installation tower. At stage five, the wind turbine is released from the installation vessel while the floating support structure remains connected. The stages of the installation procedure are shown in the simplified system diagrams in Figure 1.

3. Numerical Analysis

Multiple components are to be considered when looking at the system; the WIV, the semi-submersible support structure, a 15 megawatt (MW) wind turbine, and the connection between the two floating structures. The wind turbine is suspended from the installation tower of the WIV, and its position is controlled with two motion-compensated grippers. A rigid-body approach is considered since the stiffness of the connection is expected to be much smaller than the stiffness of the bodies. The most dominant motions and forces are expected to occur in the longitudinal plane of the installation vessel and support structure. Therefore, a two-dimensional representation of the system will be analysed in the surge-heave plane. This results in three Degrees-of-Freedom (DOF) for each body, surge, heave and pitch. The hydrodynamic interaction between the floating structures is analysed using Ansys AQWA, and the resulting data will be implemented in the model. To allow for quick assessment of the system's response, a frequency domain analysis will be conducted, requiring linear Equations of Motion (EOM). The installation vessel and support structure are not directly coupled. Therefore, a rigid link body is added to the formulation to couple the motions of the two bodies, considering the distance between the two. Rotations of the floating bodies are assumed to remain small. The connection angle can also result from a difference in heave motion between the floating structures.

3.1. Dynamic Model

The coupled EOM shown in Equation 1 have been derived to describe the motions of the installation vessel, the support structure, the wind turbine, and the rigid link.

$$
\begin{aligned}
&\begin{bmatrix} M_v + A_v(\omega) & 0 & 0 & 0 \\ 0 & M_f + A_f(\omega) & 0 & 0 \\ 0 & 0 & M_t & 0 \\ 0 & 0 & 0 & M_L \end{bmatrix} \begin{bmatrix} \ddot{X}_v \\ \ddot{X}_f \\ \ddot{X}_t \\ \ddot{X}_L \end{bmatrix} \\
&+ \begin{bmatrix} (B_v + B(\omega) + B_S)_v & 0 & 0 & 0 \\ 0 & (B_v + B(\omega) + B_S)_f & 0 & 0 \\ 0 & 0 & (B_S)_t & 0 \\ 0 & 0 & 0 & (B_S)_L \end{bmatrix} \begin{bmatrix} \dot{X}_v \\ \dot{X}_f \\ \dot{X}_t \\ \dot{X}_L \end{bmatrix} \\
&+ \begin{bmatrix} (C + K_m + K_S)_v & 0 & 0 & 0 \\ 0 & (C + K_m + K_S)_f & 0 & 0 \\ 0 & 0 & (K_S)_t & 0 \\ 0 & 0 & 0 & (K_S)_L \end{bmatrix} \begin{bmatrix} X_v \\ X_f \\ X_t \\ X_L \end{bmatrix} \\
&= \begin{bmatrix} F_v^{wave} \\ F_f^{wave} \\ 0 \\ 0 \end{bmatrix} + \begin{bmatrix} 0 \\ 0 \\ F_t^{gravity} \\ 0 \end{bmatrix} + \begin{bmatrix} F_v^{ballast} \\ F_f^{ballast} \\ 0 \\ 0 \end{bmatrix} + \begin{bmatrix} F_v^{pretension} \\ F_f^{pretension} \\ 0 \\ F_L^{pretension} \end{bmatrix} \qquad (1)
\end{aligned}
$$

Where, the subscript indicates the respective bodies, v the installation vessel, f the support structure, t the wind turbine and L the rigid link. M_i is the mass matrix of body i and $A_i(\omega)$ is the frequency-dependent added-mass matrix of floating structure i. $(B_v)_i$ is the viscous damping term, and $(B(\omega))_i$ is the frequency-dependent hydrodynamic damping, and C_i the hydrostatic stiffness, of floating structure i. The linear hydrodynamic matrices, $A(\omega)$, C, B_v, $B(\omega)$ are aquired from Ansys AQWA. Wave, gravity, ballast and pre-tension loads are applied as external forces and moments, F^{wave}, $F^{gravity}$, $F^{ballast}$, $F^{pretension}$, on the system.

The structural stiffness and damping matrices K_S and B_S contain the coupling terms of the connected bodies. The connection of the rigid link is modelled using zero-length linear translational and rotational spring and damper elements. An independent stiffness and damping coefficient can be applied to sides A and B of the link. Describing the interaction of rigid link L between bodies i and j, the spring force deformation relation of the connection is described by Equation 2.

$$\begin{Bmatrix} F_i \\ F_L \\ F_j \end{Bmatrix} = \begin{bmatrix} K_S \end{bmatrix} \begin{Bmatrix} u_i \\ u_L \\ u_j \end{Bmatrix} \tag{2}$$

Where F_i, F_L, F_j are the connection spring force vectors containing the forces and moments for each displacement DOF. u_i, u_L, u_j are the displacements of the Centre of Gravity (CG) of the respective bodies. The displacement of the connection point on the body depends on the translation and rotation of the body. A linearized transformation matrix describes the displacements at the connection point. The spring forces are calculated using the relative displacement at the connection points in each direction. Using the linear transformation matrix, the structural stiffness matrix K_S can be described by Equation 3.

$$K_S = T^T \; K_L \; T, \qquad K_L = \begin{bmatrix} k_{xA} & 0 & 0 & 0 & 0 & 0 \\ 0 & k_{zA} & 0 & 0 & 0 & 0 \\ 0 & 0 & k_{ryA} & 0 & 0 & 0 \\ 0 & 0 & 0 & k_{xB} & 0 & 0 \\ 0 & 0 & 0 & 0 & k_{zB} & 0 \\ 0 & 0 & 0 & 0 & 0 & k_{ryB} \end{bmatrix} \tag{3}$$

where K_L is the 6x6 stiffness matrix of the rigid link, containing the translational and rotational stiffness of sides A and B on the diagonal. And T the combined linearized transformation matrix linking the displacements of the structures to the connection forces and moments at the CG, shown in Equation 4.

$$T = \begin{bmatrix} 1 & 0 & z_i & -1 & 0 & 0 & 0 & 0 & 0 \\ 0 & 1 & -x_i & 0 & -1 & x_{LA} & 0 & 0 & 0 \\ 0 & 0 & 1 & 0 & 0 & -1 & 0 & 0 & 0 \\ 0 & 0 & 0 & 1 & 0 & 0 & -1 & 0 & -z_j \\ 0 & 0 & 0 & 0 & 1 & -x_{LB} & 0 & -1 & x_j \\ 0 & 0 & 0 & 0 & 0 & 1 & 0 & 0 & -1 \end{bmatrix} \tag{4}$$

Here, x_i and z_i are the horizontal and vertical locations of the connection points on body i, x_{LA} and x_{LB} are the horizontal locations of connection points on the rigid link. No vertical distance is indicated, since it is assumed that the connection points are located at the centre of the link.

Similarly, the connection damping forces are derived based on the relative velocity between the bodies. The structural stiffness matrix also includes the lift wire of the turbine and the interaction with the motion-compensated grippers. The turbine lifting wire is approximated using a linear spring, assumed to remain under tension. The motion-compensated grippers subject a stiffness and damping force on the wind turbine in the surge direction. The resulting forces act on the connection point and have to be translated to the CG of the body. Since no geometric nonlinearities should happen, the position of the body is kept constant for all angles. Angles are small, so it can work A moment is then a function of the force and the position on the body. This method is also used to transform the ballast and pretension forces to a combined force and moment on the CG of the structures.

Ansys AQWA provides the magnitude and phase of the surge, heave, and pitch wave loads acting on the CG of the floating structures for each wave period. Considering the distance between the structures CG in the inertial frame, the wave's crest occurs at different times. An additional phase shift is applied to account for this. The wave excitation force can be described as a harmonic force using equation 5. Where ω is the wave period, and ϕ is the phase shift.

$$F_{exc} = F_{amplitude} \cdot cos(-\omega t + F_{phase} + \phi) \tag{5}$$

The two-dimensional model's motion Response Amplitude Operators (RAOs) are compared to the RAOs provided by Ansys AQWA. Figure 2 shows the results of the comparison. Small variations at certain wave periods can be observed, but both results correspond well overall. The implementation of the hydrodynamic data is considered similar enough to be used for further analysis.

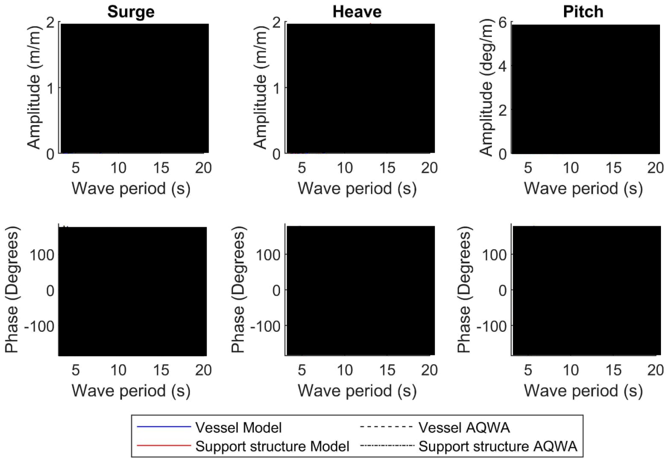

Figure 2: Comparison of motion RAOs of the installation vessel and floating support structure between Ansys AQWA and the numerical model.

3.1.1. Effect of geometric nonlinearities

Geometric nonlinearities exist due to the rotations of the bodies. The effect of linearizing the equations of motion has been investigated by carrying out time-domain simulations with the linear and nonlinear models for both small (<0.5 degrees) and large rotations (<4 degrees). Table 1 shows the percentage difference in the results between the two models for small and large rotations. Comparing the peak and Root Mean Square (RMS) values of both models, it is shown that the linearized model provides a sufficient approximation for the expected rotations.

3.2. Paramater Study

The model was used to evaluate many different configurations, with varying combinations of stiffness in the multiple directions of motion of the system. Table 2 shows the defined variations in each direction of motion of the connection. In total,

Table 1: Table showing the percentage difference between the results of the linear and nonlinear model variants. Configurations with small and large displacements are compared.

	Vessel CG [surge, heave, pitch]	Support Structure CG [surge, heave, pitch]
Small rotations (max. 0.5 degrees) (diff. in %)		
Diff. Peak val.	[0.00, 0.00, 0.57]	[0.08, 0.00, 0.11]
Diff. RMS val.	[0.01, 0.01, 0.56]	[0.00, 0.00, 0.01]
Large rotations (max. 4.0 degrees) (diff. in %)		
Diff. Peak val.	[0.60, 0.00, 0.64]	[3.58, 0.03, 0.03]
Diff. RMS val.	[0.00, 0.00, 0.53]	[0.13, 0.03, 0.02]

22 variations will be considered, including free and fixed connections. A free connection has a stiffness value of zero, and a fixed connection is approached using a high stiffness value, as indicated in the table. The flexible range considers 20 points which are logarithmically spaced in the range presented in the table. The damping constants of the connection are chosen to be equal to the stiffness values. Using these values, multiple connection configuration sets have been defined to investigate the influence of the connection on the system's response. Set 1 will evaluate the system's behaviour when a symmetric stiffness, equal on both sides of the connection, is added in either the connection's surge, heave, or pitch direction. The second set will investigate the symmetric coupling between the surge and heave direction. The third set extends this by varying the stiffness on both sides of the connection separately and investigating the effect of limiting rotations in the pitch direction. To compare the many configurations, each result will be evaluated using the peak relative motion response for a wave amplitude of 2m between a wave period range of 3.49-15.24s. Based on the expected performance of the motion-compensation systems, operational limits of 2 m, 3 m and 3 degrees are defined for the relative surge, heave, and pitch motion amplitudes, respectively. Similarly, the loads on the connection are limited to 5000 kN in the surge and heave direction and a rotational moment of 50000 kNm.

Table 2: Table showing the stiffness variations used for the system analysis. 22 different stiffness values are considered, including free and fixed connections. The flexible range contains 20 points logarithmically spaced between the indicated values.

Direction	Free	Flexible Logarithmic range	Fixed
Surge (kN/m)	0	6E+2 - 1E+5	1E+7
Heave (kN/m)	0	4E+1 - 2E+4	1E+7
Pitch (kN·m/rad)	0	1E+5 - 2.5E+7	1E+8

4. Results and Discussion

A baseline will be established by running the model without connection stiffness. The free-floating relative response of the system is shown in Figure 3. The peak in the support structure's pitch response at 13s is the main contributor to large relative motions in all directions and will be a limiting factor of the system's performance. The sections below will discuss how the connection will affect the system's behaviour.

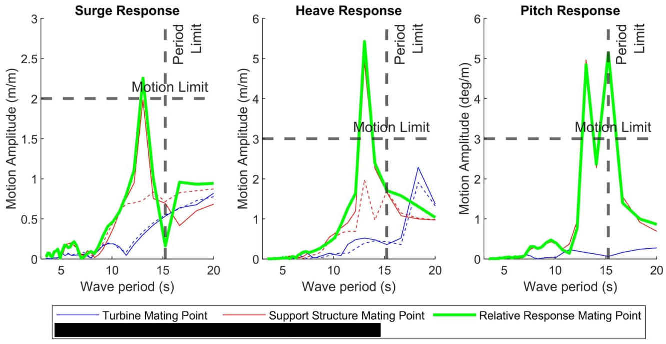

Figure 3: Free-floating relative motion response of the wind turbine mating point.

4.1. *Effect of installation stages*

To assess the effect of the different installation stages, the connection stiffness is combinedly increased in all connection directions for the 22 variations. The effect of the different installations on the system's dynamic behaviour is shown in Figure 7. The dynamic behaviour during the different stages follows very similar trends overall. During the first three stages, the motion response of the system shows a minimal change in the lower stiffness regions. The most significant change in connection forces is caused by the pretension required to balance the system during the ballast transfer. At installation stage 4, the forces for higher stiffness values are observed to be lower than the rest of the system. This can be attributed to the coupling between the wind turbine and the floating support structure while connected to the installation vessel. The heave forces at stage 5 are higher, caused by the added mass and inertia of the wind turbine to the support structure. The variation in dynamic force response between the installation stages is minimal. Since the dynamic variations are small, the rest of the system analysis will focus on installation stage 1.

4.2. *Effect of stiffness variations*

Figure 4 shows the results of the first parameter set. The effect of adding stiffness in any direction is difficult to predict, as is also shown by the heave response for a high stiffness being influenced by the pitch motions of the system. The pitch motions are the most difficult to suppress. Adding stiffness in the pitch direction is the only option to keep the pitch motion within the set limits. The effect of adding heave stiffness resulted in unexpected behaviour, indicating that coupling between heave stiffness and another direction is required to make it more effective. Overall, the results show that it is difficult to stay within limits by adding stiffness in a single direction of motion.

A heatmap graph showing the results for symmetric coupling is shown in Figure 5. The motion response in the surge, heave and pitch direction for different stiffness combinations are compared. The graph shows that a high surge stiffness reduces the

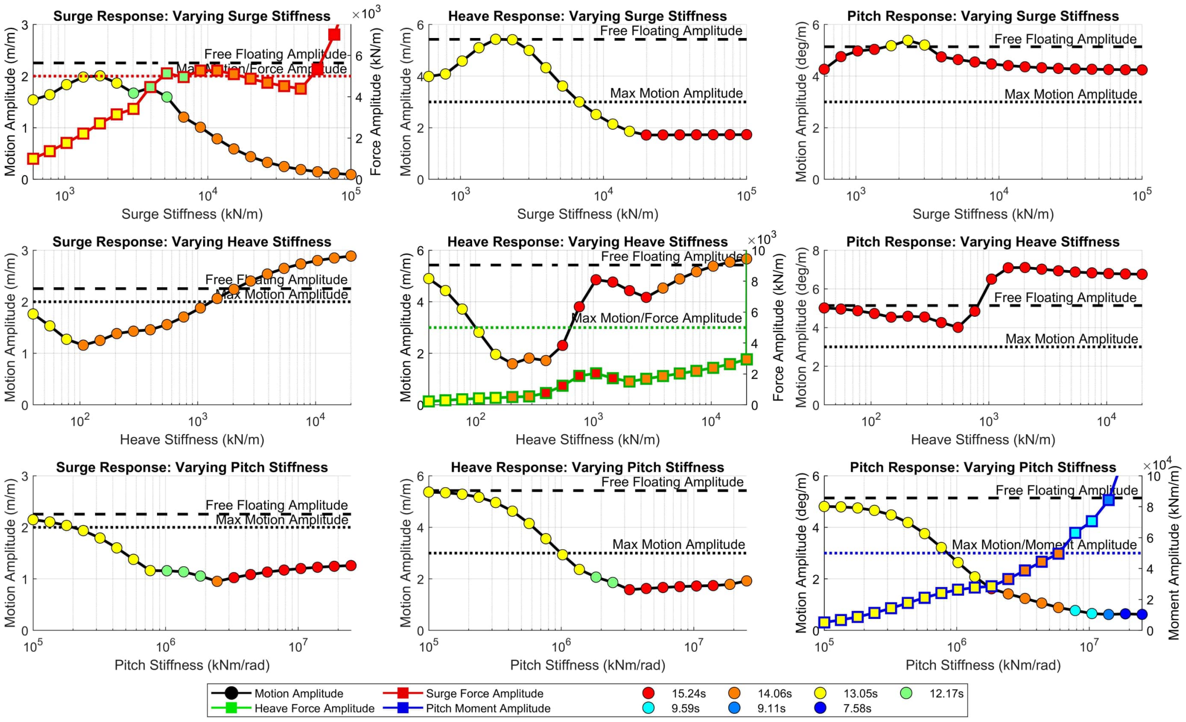

Figure 4: Graphs showing the peak relative motion response of the mating point for one-dimensional stiffness variation (for a wave amplitude of 2m between a wave period range of 3.49-15.24s). The connection force response is shown for each direction of stiffness variation. For each response point, the corresponding wave period is indicated by the coloured markers. To compare, the defined motion and load limits, as well as the free-floating relative motion amplitudes, are also included in the graphs.

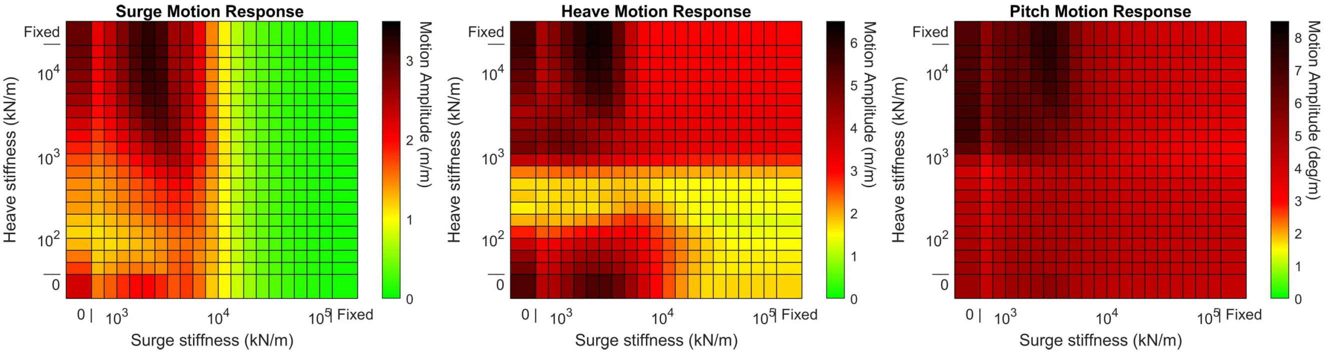

Figure 5: Heatmap graph showing the peak relative motion response (for a wave amplitude of 2m between a wave period range of 3.49-15.24s) of the mating point for combinations of surge and heave stiffness values. The colour bar indicates the magnitude of the peak response for each configuration.

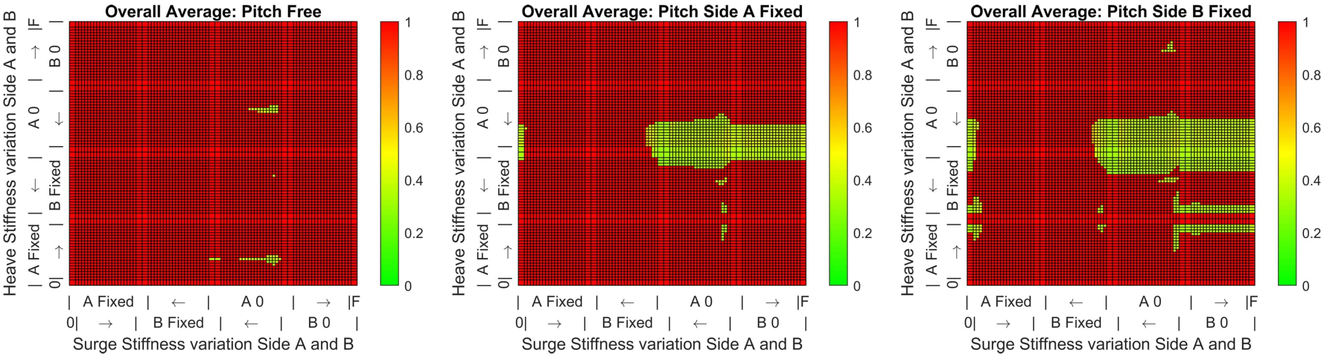

Figure 6: Heatmap graph showing the overall average response (for a wave amplitude of 2m between a wave period range of 3.49-15.24s) for different combinations of surge and heave stiffness values on side A and side B of the connection. The overall average value is a combination of the normalized average of the motion and connection force responses for all directions of motion. A value of 1 indicates the motion or load limits are exceeded. The response is compared for three different rotation stiffness values.

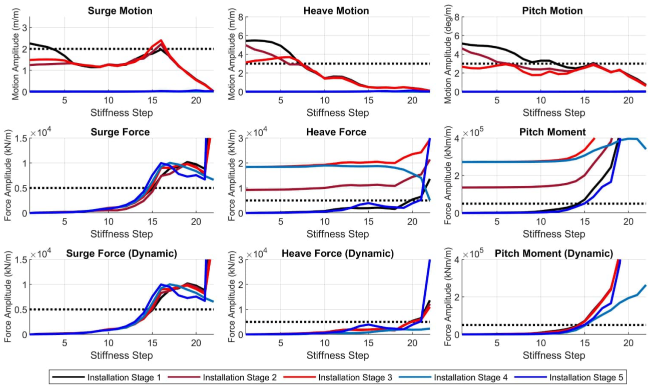

Figure 7: Graph comparing the peak response of the relative motions and forces for the different installation stages (for a wave amplitude of 2m between a wave period range of 3.49-15.24s). The horizontal axis indicates the variation in overall stiffness, each step corresponding to a combined increase in the surge, heave and pitch stiffness.

system's surge response. A higher surge response also contributes to a decrease in the heave motions. The pitch response is influenced the least by a combined surge and heave direction stiffness and is negatively impacted by high heave stiffness.

Figure 6 shows the results for parameter set 3. The overall average response of the system is shown for free rotation and for a fixed rotation on each side of the connection. The overall average response shows a combination of the normalized average of the motion and connection force responses for all directions of motion. The overall average response with a free pitch connection shows very limited combinations to stay within the defined limits due to the large pitch motion response, as also observed in Figure 5. However, small areas of possible combinations are now observed, which are not present in the symmetric coupling results. It is shown that fixing the rotational motion on either side improves the viable stiffness combinations. The large improvement in potential combinations can be attributed to the reduction in pitch motions caused by fixing the pitch rotation on one side of the connection. Adding stiffness in the heave direction is also more effective when the rotation is fixed on one side of the connection.

5. Summary and conclusions

A model has been proposed to describe the dynamics of a rigid connection between two floating structures. The model is used to investigate the performance of the connection between an installation vessel and a semi-submersible support structure during the offshore installation of the floating offshore wind turbine. Installing a floating wind turbine at sea brings two main challenges, the relative motions between the floating structures and the load transfer between the two floating structures. The installation procedure has been divided into five discrete installation stages. During all stages, the installation vessel and floating support structure are coupled by the connection. A ballast transfer will be initiated between the support structure and the installation vessel, moving water ballast from the support structure to the installation vessel. The connection load gradually increases during these stages since both floating structures should remain balanced. The ballast transfer is required to minimize the time the structures are connected during the mating operation of the wind turbine. An Ansys AQWA analysis has been performed to obtain the hydrodynamic properties and loads for the two floating structures. A configurable tool has been scripted to numerically assess the system's performance during the five installation stages, including the rigid link, ballast, pretension, and connection modelling elements. A system analysis has been carried out using this tool, showing the general trends of varying stiffness of the connection. The system's performance is analysed using regular waves with varying wave periods. The carried-out system analysis focussed on comparing many different configurations but was therefore limited in the depth of analysing system performance. This work has mostly identified trends in how the system responds to various stiffness values and coupling in multiple dimensions. Overall, it can be concluded that a combination of stiffness in the different connection directions will provide the most favourable results. Heave stiffness requires a coupled surge or pitch stiffness to limit the relative heave motions effectively. It is also shown that a different stiffness on both sides of the connection can improve the system's behaviour. Fixing the rotation of the connection on one side seems to be required to lower the relative pitch motions below the defined operational limit of 3 degrees. However, more research could be done to investigate favourable combinations of limiting motions on each side of the connection. The presented model could be used for a future optimization study to find optimal stiffness values for the connection.

References

Crowle, A., Philipp, R.T., 2021. Port and shipyard requirements for the installation of floating wind turbines [conference presentation]. RINA London Branch 21 Oct 2021, London, UK URL: `http://hdl.handle.net/10871/127588`.

Crowle, A.P., Thies, P.R., 2022. Floating offshore wind turbines port requirements for construction. Proceedings of the Institution of Mechanical Engineers Part M: Journal of Engineering for the Maritime Environment doi:10.1177/14750902221078425.

Ding, J., sheng Wu, Y., Zhou, Y., Ma, X.Z., Ling, H.J., Xie, Z., 2020. Investigation of connector loads of a 3-module vlfs using experimental and numerical methods. Ocean Engineering 195. doi:10.1016/j.oceaneng.2019.106684.

Hong, S., Vagnes, D., Halse, K.H., Nord, T.S., 2021. Mechanical coupling effect on the horizontal response of floating offshore wind turbine installation using a catamaran with a low height lifting system. Proceedings of the Thirty-first (2021) International Ocean and Polar Engineering Conference Rhodes, Greece, June 20 – 25 .

Hong, S., Zhang, H., Nord, T.S., Halse, K.H., 2022. Effect of fender system on the dynamic response of onsite installation of floating offshore wind turbines. Ocean Engineering 259. doi:10.1016/j.oceaneng.2022.111830.

Jiang, Z., Li, L., Gao, Z., Halse, K.H., Sandvik, P.C., 2018. Dynamic response analysis of a catamaran installation vessel during the positioning of a wind turbine assembly onto a spar foundation. Marine Structures 61, 1–24. doi:10.1016/j.marstruc.2018.04.010.

Liu, T., Halse, K.H., Leira, B.J., Jiang, Z., 2023. Comparative study of the mating process for a spar-type floating wind turbine using two alternative installation vessels. Applied Ocean Research 132, 103452. doi:10.1016/j.apor.2022.103452.

Riggs, H.R., Ertekin, R.C., 1993. Approximate methods for dynamic response of multi-module floating structures. Marine Structures 6. doi:10.1016/0951-8339(93)90016-V.

B

Spring Linearization

A Linear approximations of strains in kinematic elements

To describe the system of equations of motion for a two-dimensional lattice as a system of ordinary differential equations, the strains or elongations of the kinematic elements must be linearized. The way the strain or elongation of a kinematic element is derived depends for a large part on the definition of the displacements of the particles for which the considered element describes the kinematic relation. This appendix gives an overview of several linearizations of the elongation of kinematic elements for different magnitudes of the strains, including the definitions for the displacements of the particles involved.

A.1 Linearization for small strains

Let us consider Figure A.1a, showing the displacement of a particle $\mathbf{m_j,n_j}$ relative to the position of a particle **m,n** in two-dimensional space, where the kinematic relation between particles **m,n** **m,n** and $\mathbf{m_j,n_j}$ is described by a linear spring. The kinematic element between particles **m,n** and $\mathbf{m_j,n_j}$ initially has a length $\ell_j^{\mathbf{m,n}}$ and an angle $\alpha_j^{\mathbf{m,n}}$ with respect to the x-axis. Following the geometry depicted in Figure A.1a, we can express the elongation of the kinematic element between particles **m,n** and $\mathbf{m_j,n_j}$ as:

$$e_j^{\mathbf{m,n}} = \sqrt{\left(\ell_{x;j}^{\mathbf{m,n}} + e_{x;j}^{\mathbf{m,n}}\right)^2 + \left(\ell_{z;j}^{\mathbf{m,n}} + e_{z;j}^{\mathbf{m,n}}\right)^2} - \ell_j^{\mathbf{m,n}} \tag{A.1}$$

As the particles **m,n** and $\mathbf{m_j,n_j}$ move relative to each other, the elongation and the angle of the kinematic element in-between change continuously. Thus, while the horizontal and vertical components of the element length, respectively denoted as $\ell_{x;j}^{\mathbf{m,n}}$ and $\ell_{z;j}^{\mathbf{m,n}}$, can be described in terms of the element length through the initial angle $\alpha_j^{\mathbf{m,n}}$, the horizontal and vertical components of the elongation, respectively denoted as $e_{x;j}^{\mathbf{m,n}}$ and $e_{z;j}^{\mathbf{m,n}}$, cannot. Thus, using trigonometry to express the horizontal and vertical length components, as well as taking the element length out from under the square root, the elongation of the element between particles **m,n** and $\mathbf{m_j,n_j}$ becomes:

$$e_j^{\mathbf{m,n}} = \ell_j^{\mathbf{m,n}} \sqrt{1 + \frac{2}{\ell_j^{\mathbf{m,n}}}\left(e_{x;j}^{\mathbf{m,n}} \cos\alpha_j^{\mathbf{m,n}} + e_{z,j}^{\mathbf{m,n}} \sin\alpha_j^{\mathbf{m,n}}\right) + \left(\frac{e_{x;j}^{\mathbf{m,n}}}{\ell_j^{\mathbf{m,n}}}\right)^2 + \left(\frac{e_{z;j}^{\mathbf{m,n}}}{\ell_j^{\mathbf{m,n}}}\right)^2} - \ell_j^{\mathbf{m,n}} \tag{A.2}$$

Provided that the horizontal and vertical components of the elongation $e_{x;j}^{\mathbf{m,n}}$ and $e_{z;j}^{\mathbf{m,n}}$, and thus the strains, are significantly smaller than the initial element length, it follows that the quadratic terms under the square root are negligible. Additionally, given that $e_{x;j}^{\mathbf{m,n}}$ and $e_{z;j}^{\mathbf{m,n}}$ are small compared to the initial element length, it additionally follows that the second term under the square root must be significantly smaller than 1. Therefore, we approximate the elongation using a Taylor series, so that $\sqrt{1+a} = 1 + \frac{a}{2} + \ldots$. Rearranging the remainder of equation (A.2) then yields:

$$e_j^{\mathbf{m,n}} = e_{x;j}^{\mathbf{m,n}} \cos\alpha_j^{\mathbf{m,n}} + e_{z;j}^{\mathbf{m,n}} \sin\alpha_j^{\mathbf{m,n}} \tag{A.3}$$

Note here that the higher order terms of the involved Taylor series are neglected as they yield terms that are related to, or are of the same order as, the quadratic terms previously neglected.

The horizontal and vertical displacement of a particle **m,n** are defined as the total distance that the particle has travelled in respectively horizontal and vertical direction at time t compared to its initial position at time t_0. The horizontal and vertical displacements of a particle **m,n** may thus respectively be expressed as:

$$u_x^{\mathbf{m},\mathbf{n}} = x^{\mathbf{m},\mathbf{n}}(t) - x^{\mathbf{m},\mathbf{n}}(t_0) \tag{A.4}$$

$$u_z^{\mathbf{m},\mathbf{n}} = z^{\mathbf{m},\mathbf{n}}(t) - z^{\mathbf{m},\mathbf{n}}(t_0) \tag{A.5}$$

The displacements $u_x^{\mathbf{m}_j,\mathbf{n}_j}$ and $u_z^{\mathbf{m}_j,\mathbf{n}_j}$ of particle **m**$\mathbf{m}_j,\mathbf{n}_j$ may be described accordingly. Consequently, the horizontal and vertical components of the elongation may be expressed as:

$$e_{x;j}^{\mathbf{m},\mathbf{n}} = x^{\mathbf{m}_j,\mathbf{n}_j}(t) - x^{\mathbf{m},\mathbf{n}}(t) - \ell_{x;j}^{\mathbf{m},\mathbf{n}} = u_x^{\mathbf{m}_j,\mathbf{n}_j} - u_x^{\mathbf{m},\mathbf{n}} \tag{A.6}$$

$$e_{z;j}^{\mathbf{m},\mathbf{n}} = z^{\mathbf{m}_j,\mathbf{n}_j}(t) - z^{\mathbf{m},\mathbf{n}}(t) - \ell_{z;j}^{\mathbf{m},\mathbf{n}} = u_z^{\mathbf{m}_j,\mathbf{n}_j} - u_z^{\mathbf{m},\mathbf{n}} \tag{A.7}$$

Substituting equations (A.6) and (A.7) into equation (A.3), the elongation of the kinematic element between particles **m,n** and $\mathbf{m}_j,\mathbf{n}_j$ becomes:

$$e_j^{\mathbf{m},\mathbf{n}} = \left(u_x^{\mathbf{m}_j,\mathbf{n}_j} - u_x^{\mathbf{m},\mathbf{n}}\right)\cos\alpha_j^{\mathbf{m},\mathbf{n}} + \left(u_z^{\mathbf{m}_j,\mathbf{n}_j} - u_z^{\mathbf{m},\mathbf{n}}\right)\sin\alpha_j^{\mathbf{m},\mathbf{n}} \tag{A.8}$$

Let us emphasise here that the elongation of the kinematic element between particles **m,n** and $\mathbf{m}_j,\mathbf{n}_j$ may only be approximated by equation (A.8) when the displacements and elongations involved are small compared to the initial length of the kinematic element. In many cases and especially when

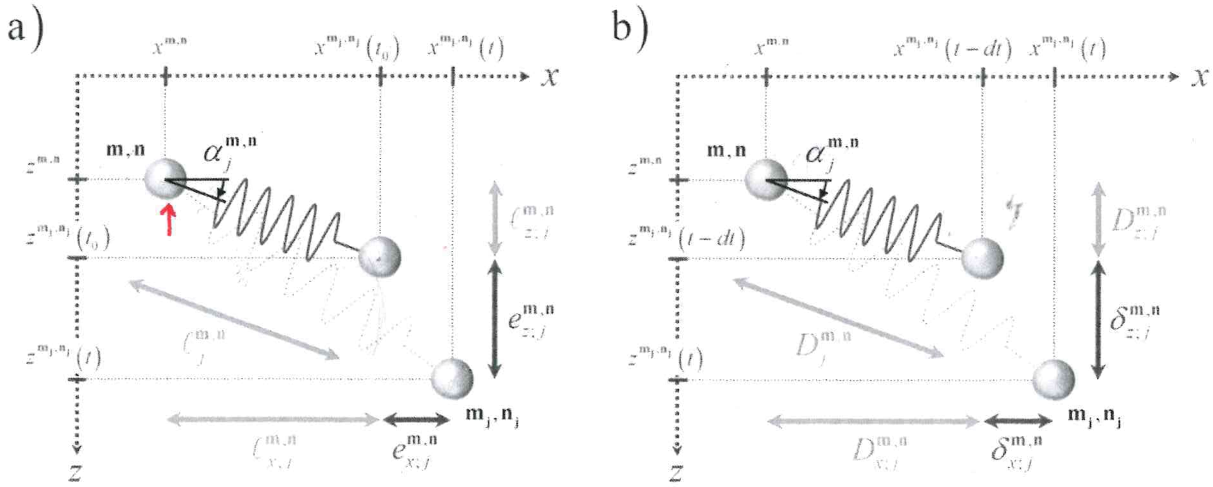

*Figure A.1: The elongation of a kinematic element between particles **m,n** and $\mathbf{m}_j,\mathbf{n}_j$ for:*
a) *small strains;* b) *large strains.*

consider nonlinear kinematic elements, we may not assume that the displacements and elongations in a lattice are small. We will therefore consider a more appropriate linearization for large strains in section A.2.

For the one-dimensional case, the angle of all kinematic elements is equal to zero at all times. Consequently, the expression for the elongation of a kinematic element between two adjacent particles **n** and **n+1**, may be derived directly and without any assumptions from equation (A.1) as:

$$e^{\mathbf{n,n+1}} = u^{\mathbf{n+1}} - u^{\mathbf{n}} \tag{A.9}$$

As the expression for the elongation of kinematic elements in a one-dimensional lattice according to equation (A.9) is obtained directly and without any assumptions, the one-dimensional lattice modelling does not require any linearization.

A.2 Linearization for large strains

To allow for large strains, and therefore to allow for large elongations of kinematic elements, i.e. elongations that are of the same order as the initial length of a kinematic element, we redefine the definition of the displacements of the particles in the lattice. Whereas previously the displacement of a particle was described as the distance between the position of that particle at time *t* versus its initial position at time t_0, we now define the displacement of a particle as the distance between its position at time *t* compared to its previous position at the time *t-dt*. The horizontal and vertical displacement of a particle **m,n** may thus respectively be expressed as:

$$u_x^{\mathbf{m,n}} = x^{\mathbf{m,n}}(t) - x^{\mathbf{m,n}}(t-dt) \tag{A.10}$$

$$u_z^{\mathbf{m,n}} = z^{\mathbf{m,n}}(t) - z^{\mathbf{m,n}}(t-dt) \tag{A.11}$$

Here, $x^{\mathbf{m,n}}(t)$ and $z^{\mathbf{m,n}}(t)$ respectively denote the horizontal and vertical coordinates of particle **m,n** at time *t*. The displacements $u_x^{\mathbf{m_j,n_j}}$ and $u_z^{\mathbf{m_j,n_j}}$ of particle $\mathbf{m_j,n_j}$ are derived accordingly. The corresponding displacement of a particle $\mathbf{m_j,n_j}$ relative to the position of a particle **m,n** in two-dimensional space is depicted in Figure A.1b. Here, $D_j^{\mathbf{m,n}}$ is the distance between particles **m,n** and $\mathbf{m_j,n_j}$ at time *t-dt* and $\alpha_j^{\mathbf{m,n}}$ now denotes the angle of the kinematic element with respect to the x-axis at time *t-dt*. Following the geometry depicted in Figure A.1b, we can then express the elongation $e_j^{\mathbf{m,n}}$ of the kinematic element between particles **m,n** and $\mathbf{m_j,n_j}$ as:

$$e_j^{\mathbf{m,n}} = \sqrt{\left(D_{x;j}^{\mathbf{m,n}} + \delta_{x;j}^{\mathbf{m,n}}\right)^2 + \left(D_{z;j}^{\mathbf{m,n}} + \delta_{z;j}^{\mathbf{m,n}}\right)^2} - \ell_j^{\mathbf{m,n}} \tag{A.12}$$

Here, $D_{x;j}^{\mathbf{m,n}}$ and $D_{z;j}^{\mathbf{m,n}}$ respectively denote the horizontal and vertical distance between particles **m,n** and $\mathbf{m_j,n_j}$ at time *t-dt*, which can expressed in terms of the distance $D_j^{\mathbf{m,n}}$ using the angle $\alpha_j^{\mathbf{m,n}}$, and $\ell_j^{\mathbf{m,n}}$ is the initial length of the kinematic element at time t_0. Furthermore, $\delta_{x;j}^{\mathbf{m,n}}$ and $\delta_{z;j}^{\mathbf{m,n}}$ respectively denote the change in horizontal and vertical distance between the particles during the last time step *dt* prior to time *t*.

Expressing $D_{x;j}^{\mathbf{m,n}}$ and $D_{z;j}^{\mathbf{m,n}}$ in terms of the distance $D_j^{\mathbf{m,n}}$, as well as taking $D_j^{\mathbf{m,n}}$ out from under the square root, the elongation of the kinematic element between particles **m,n** and **m$_j$,n$_j$** follows from equation (A.12) as:

$$e_j^{\mathbf{m,n}} = D_j^{\mathbf{m,n}}\sqrt{1+\frac{2}{D_j^{\mathbf{m,n}}}\left(\delta_{x;j}^{\mathbf{m,n}}\cos\alpha_j^{\mathbf{m,n}}+\delta_{z;j}^{\mathbf{m,n}}\sin\alpha_j^{\mathbf{m,n}}\right)+\left(\frac{\delta_{x;j}^{\mathbf{m,n}}}{D_j^{\mathbf{m,n}}}\right)^2+\left(\frac{\delta_{z;j}^{\mathbf{m,n}}}{D_j^{\mathbf{m,n}}}\right)^2} - \ell_j^{\mathbf{m,n}} \qquad (A.13)$$

According to the definition given by equations (A.10) and (A.11), we describe the displacements of a particle as the distance travelled by that particle during the last time step *dt* prior to time *t*. Consequently, the change in respectively the horizontal and vertical distance between the particles during this last time step *dt* can then be described in terms of the particle displacements as:

$$\delta_{x;j}^{\mathbf{m,n}} = x^{\mathbf{m_j,n_j}}(t) - x^{\mathbf{m,n}}(t) - D_{x;j}^{\mathbf{m,n}} = u_x^{\mathbf{m_j,n_j}} - u_x^{\mathbf{m,n}} \qquad (A.14)$$

$$\delta_{z;j}^{\mathbf{m,n}} = z^{\mathbf{m_j,n_j}}(t) - z^{\mathbf{m,n}}(t) - D_{z;j}^{\mathbf{m,n}} = u_z^{\mathbf{m_j,n_j}} - u_z^{\mathbf{m,n}} \qquad (A.15)$$

As $\delta_{x;j}^{\mathbf{m,n}}$ and $\delta_{z;j}^{\mathbf{m,n}}$ only describe the change in the horizontal and vertical distance between particles **m,n** and **m$_j$,n$_j$** during the last time step *dt*, their magnitudes are small compared to the interparticle distance $D_j^{\mathbf{m,n}}$ at time *t-dt*. That is, if the time step *dt* is chosen appropriately small. Consequently, the quadratic terms under the square root are negligible and the second term under the square root is significantly smaller than 1, allowing us to approximate the elongation using the Taylor series, so that $\sqrt{1+a} = 1+\frac{a}{2}+\dots$. This yields the elongation of the kinematic element between particles **m,n** and **m$_j$,n$_j$** as:

$$e_j^{\mathbf{m,n}} = \left(u_x^{\mathbf{m_j,n_j}} - u_x^{\mathbf{m,n}}\right)\cos\alpha_j^{\mathbf{m,n}} + \left(u_z^{\mathbf{m_j,n_j}} - u_z^{\mathbf{m,n}}\right)\sin\alpha_j^{\mathbf{m,n}} + \varepsilon_j^{\mathbf{m,n}} \qquad (A.16)$$

Here, $\varepsilon_j^{\mathbf{m,n}}$ is the elongation of the kinematic element between particles **m,n** and **m$_j$,n$_j$** at time *t-dt* that, during the last time step *dt*, is a constant that can be obtained as $\varepsilon_j^{\mathbf{m,n}} = D_j^{\mathbf{m,n}} - \ell_j^{\mathbf{m,n}}$. Expressing the elongation $e_j^{\mathbf{m,n}}$ according to equation (A.16) allows for significantly larger deformations in the lattice than equation (A.8), which is valid for small deformations.

For the one-dimensional case, the angle of all kinematic elements is equal to zero at all times and the expression for the elongation of a kinematic element between two adjacent particles **n** and **n+1**, can therefore be derived from equation (A.12) without any assumptions or linearization as:

$$e^{\mathbf{n,n+1}} = u^{\mathbf{n+1}} - u^{\mathbf{n}} + \varepsilon^{\mathbf{n,n+1}} \qquad (A.17)$$

Here, $\varepsilon^{\mathbf{n,n+1}}$ is the elongation of the kinematic element between particles **n** and **n+1** at time *t-dt*, which may be obtained as $\varepsilon^{\mathbf{n,n+1}} = D^{\mathbf{n,n+1}} - \ell^{\mathbf{n,n+1}}$.

C

Analysis Group 1 Extended Results

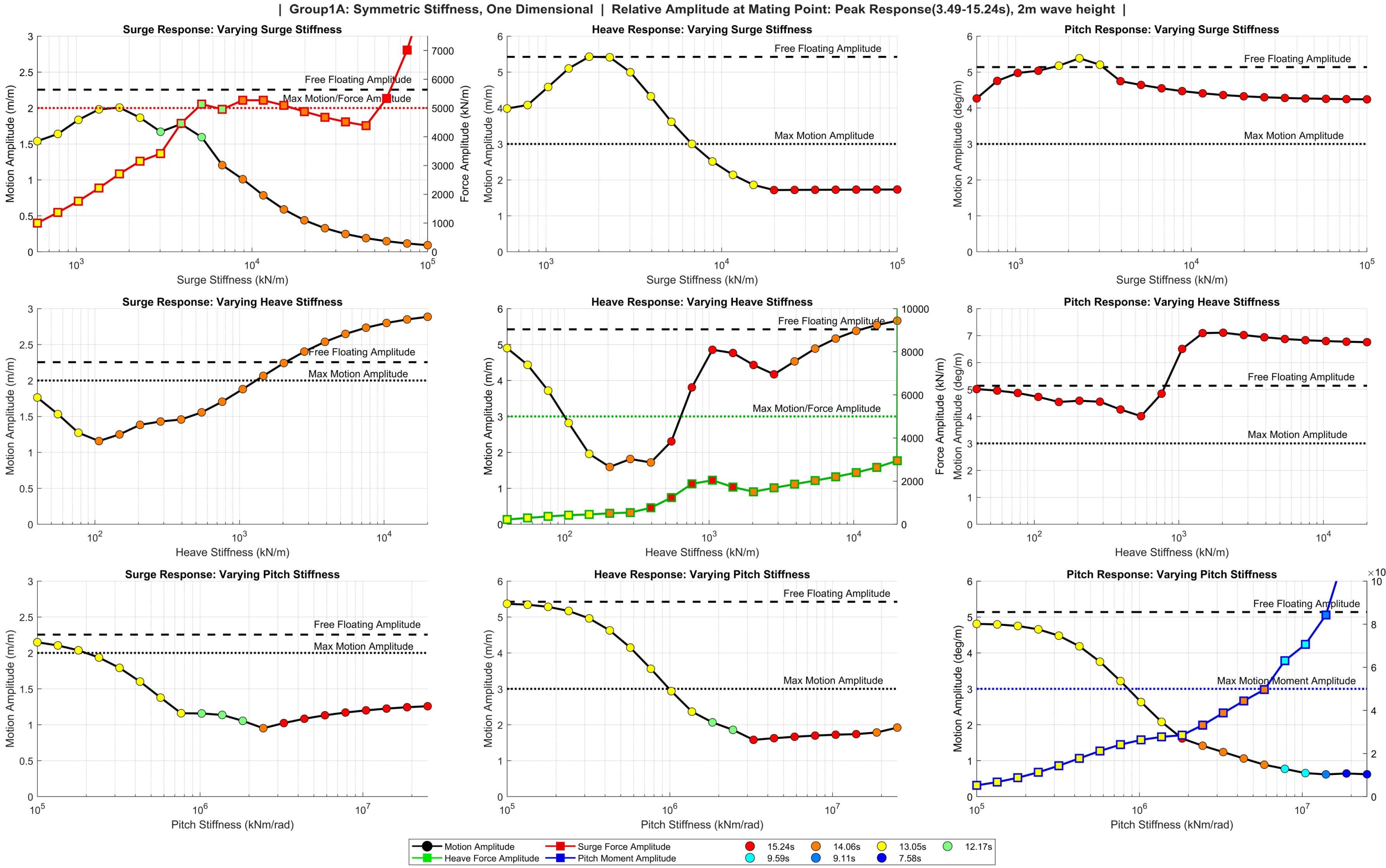

Figure C.1: Group 1A: One-Dimensional variation

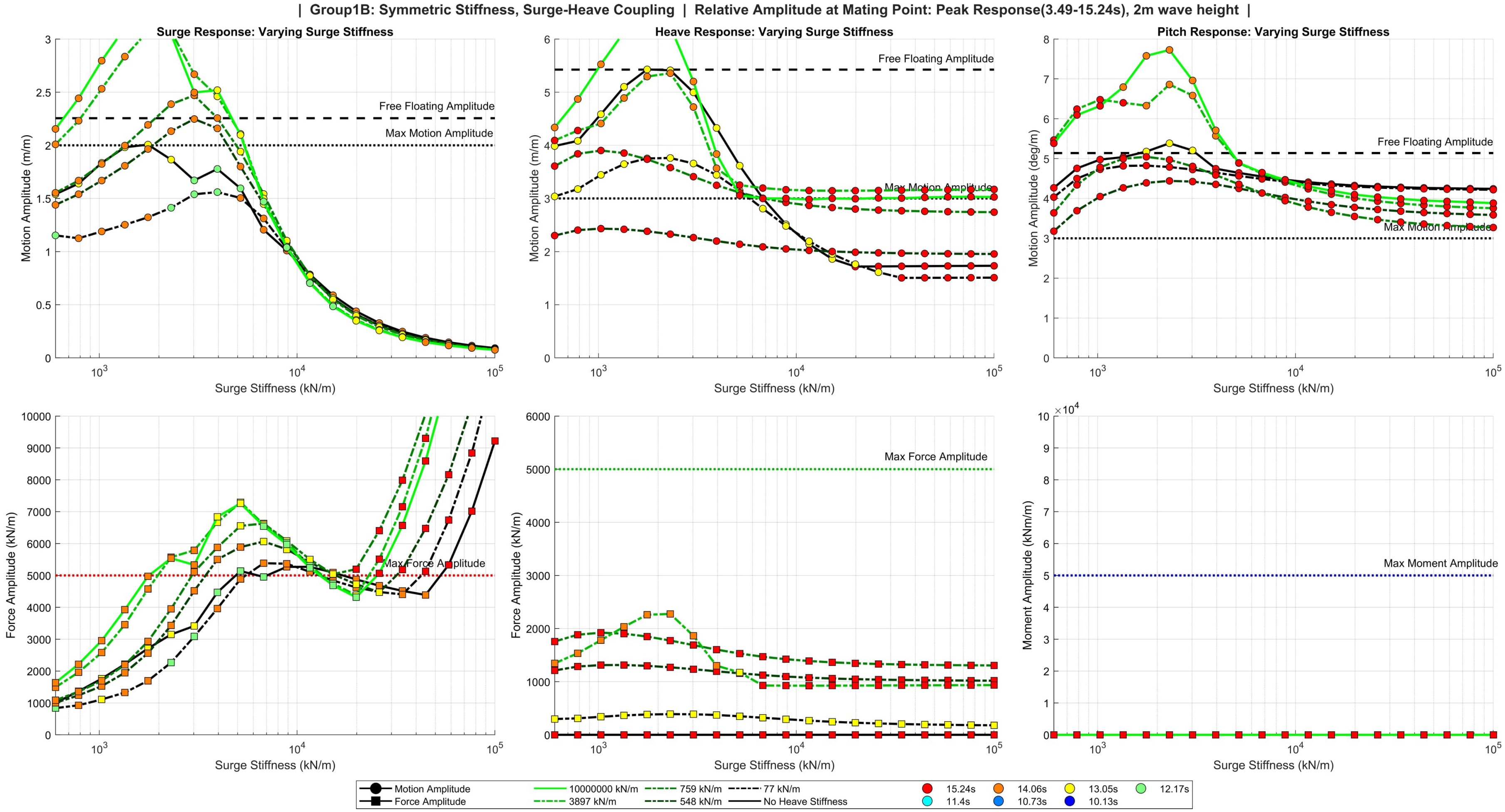

Figure C.2: Group 1B: Surge Heave Coupling

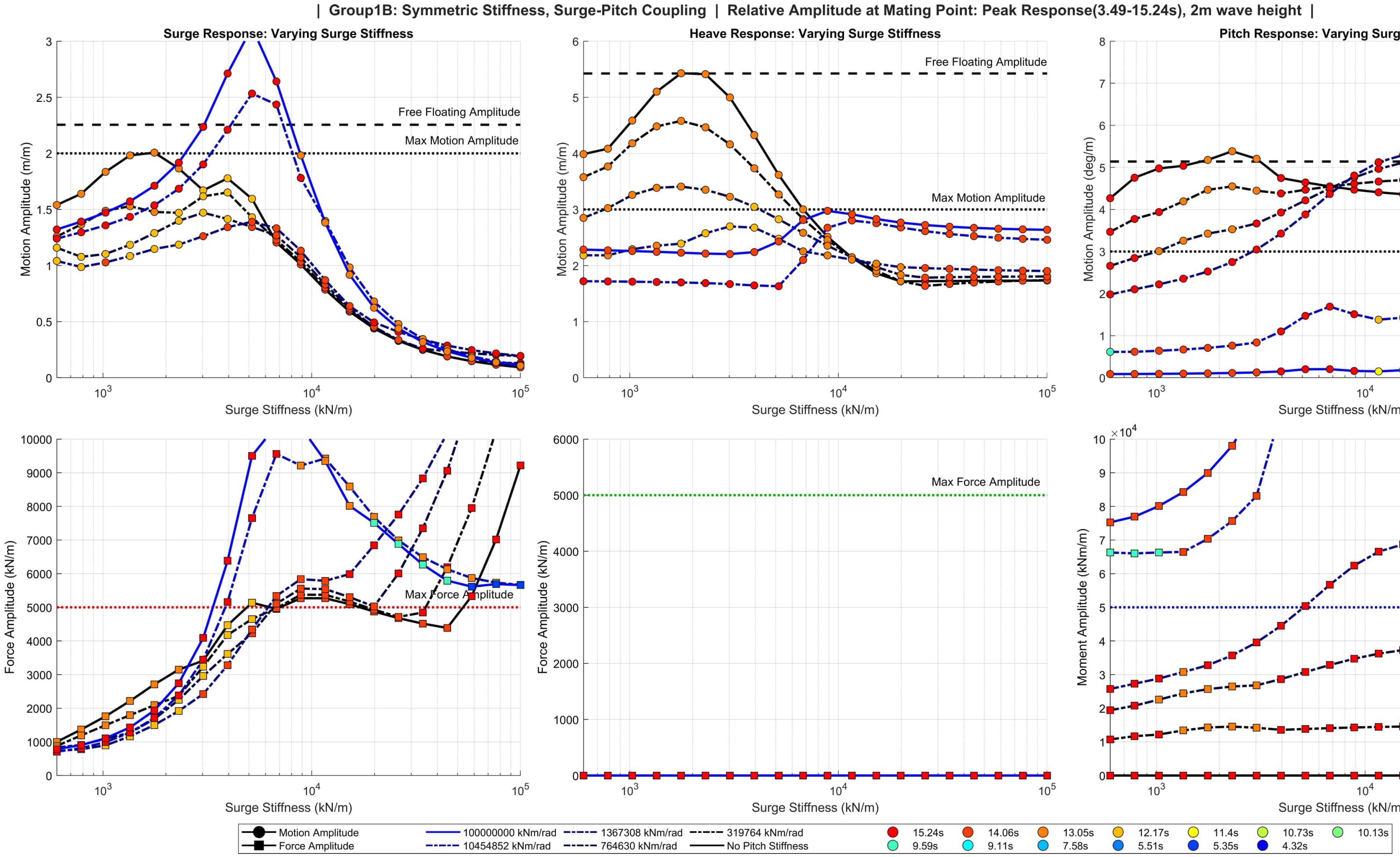

Figure C.3: Group 1B: Surge Pitch Coupling

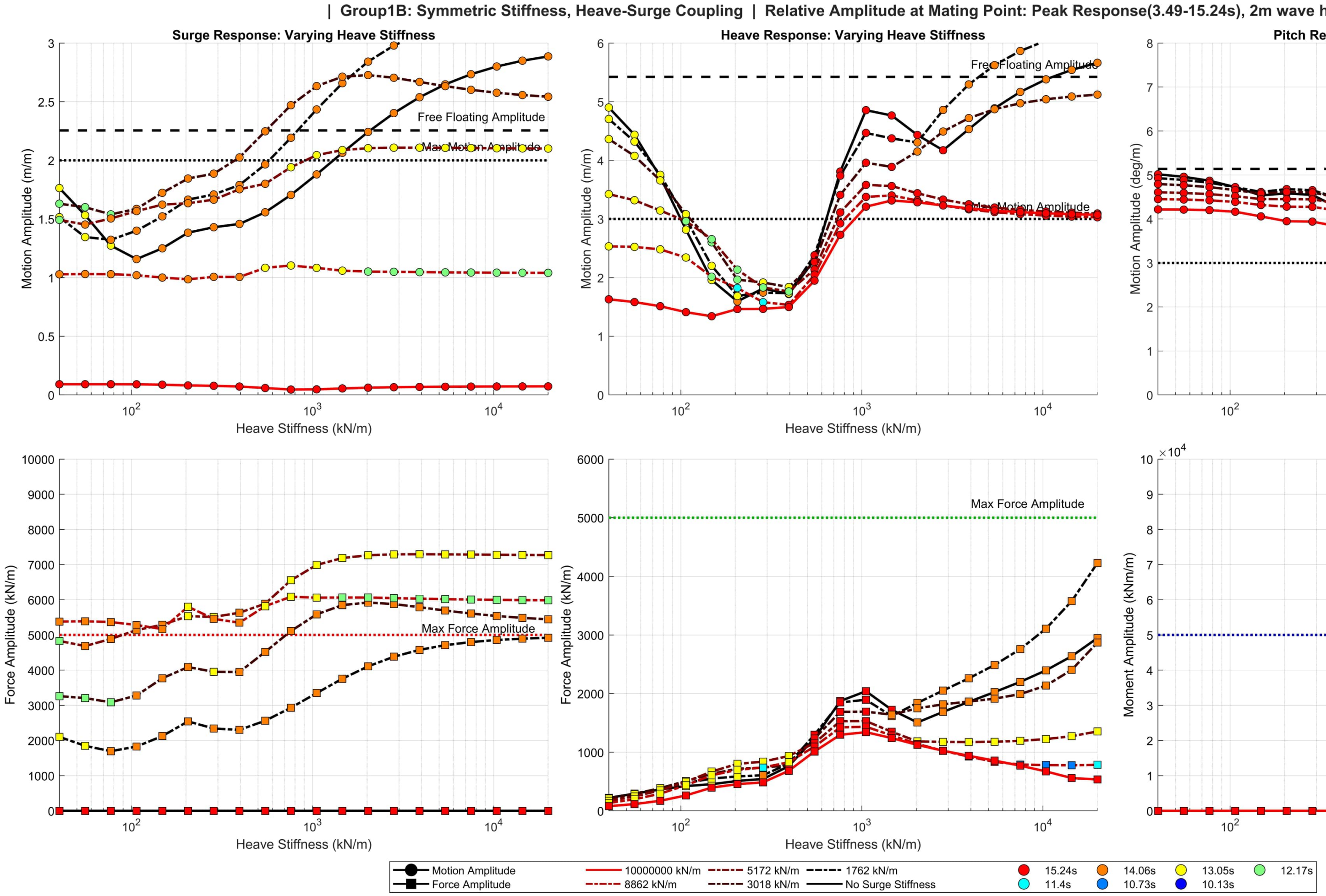

Figure C.4: Group 1B: Heave Surge Coupling

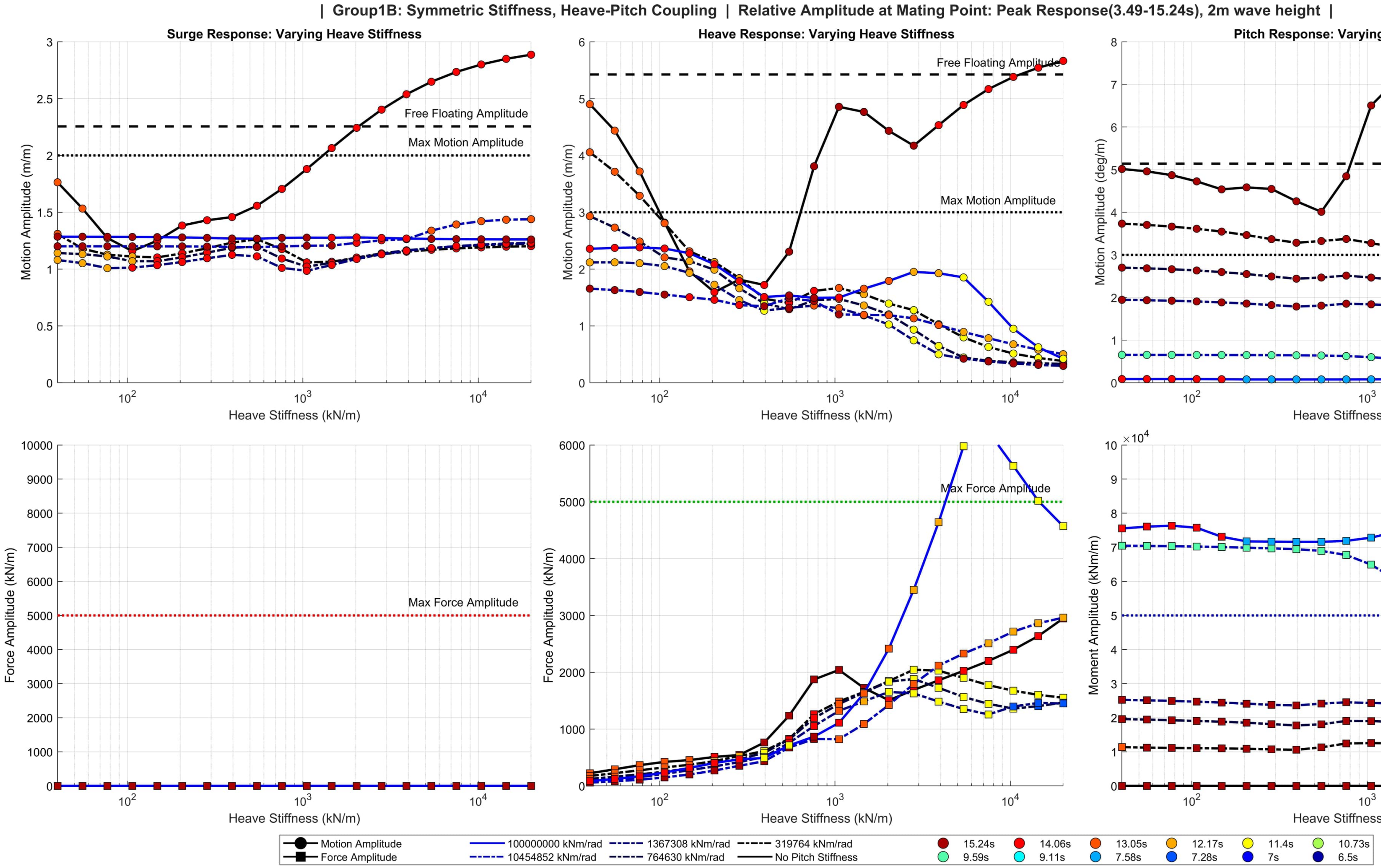

Figure C.5: Group 1B: Heave Pitch Coupling

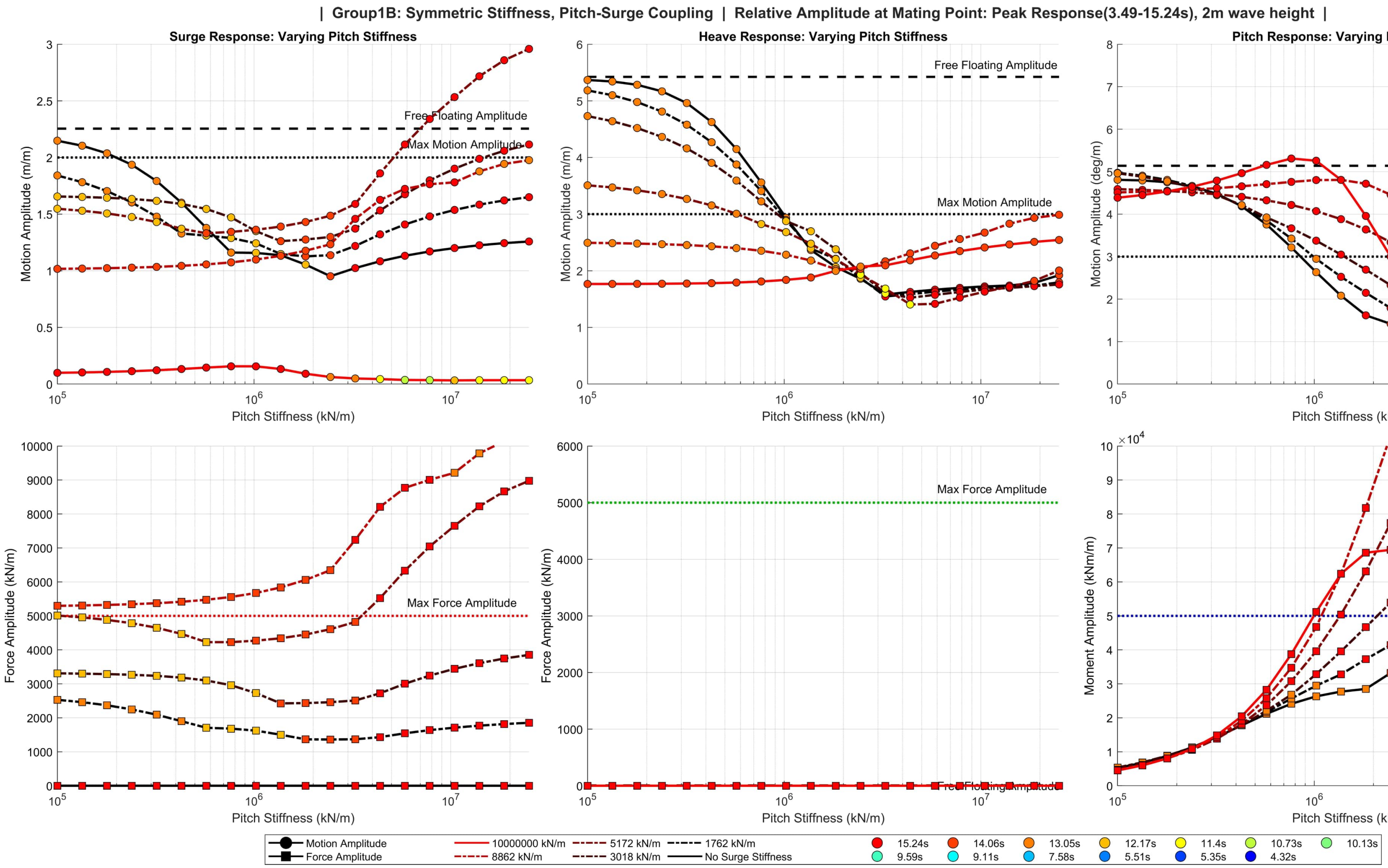

Figure C.6: Group 1B: Pitch Surge Coupling

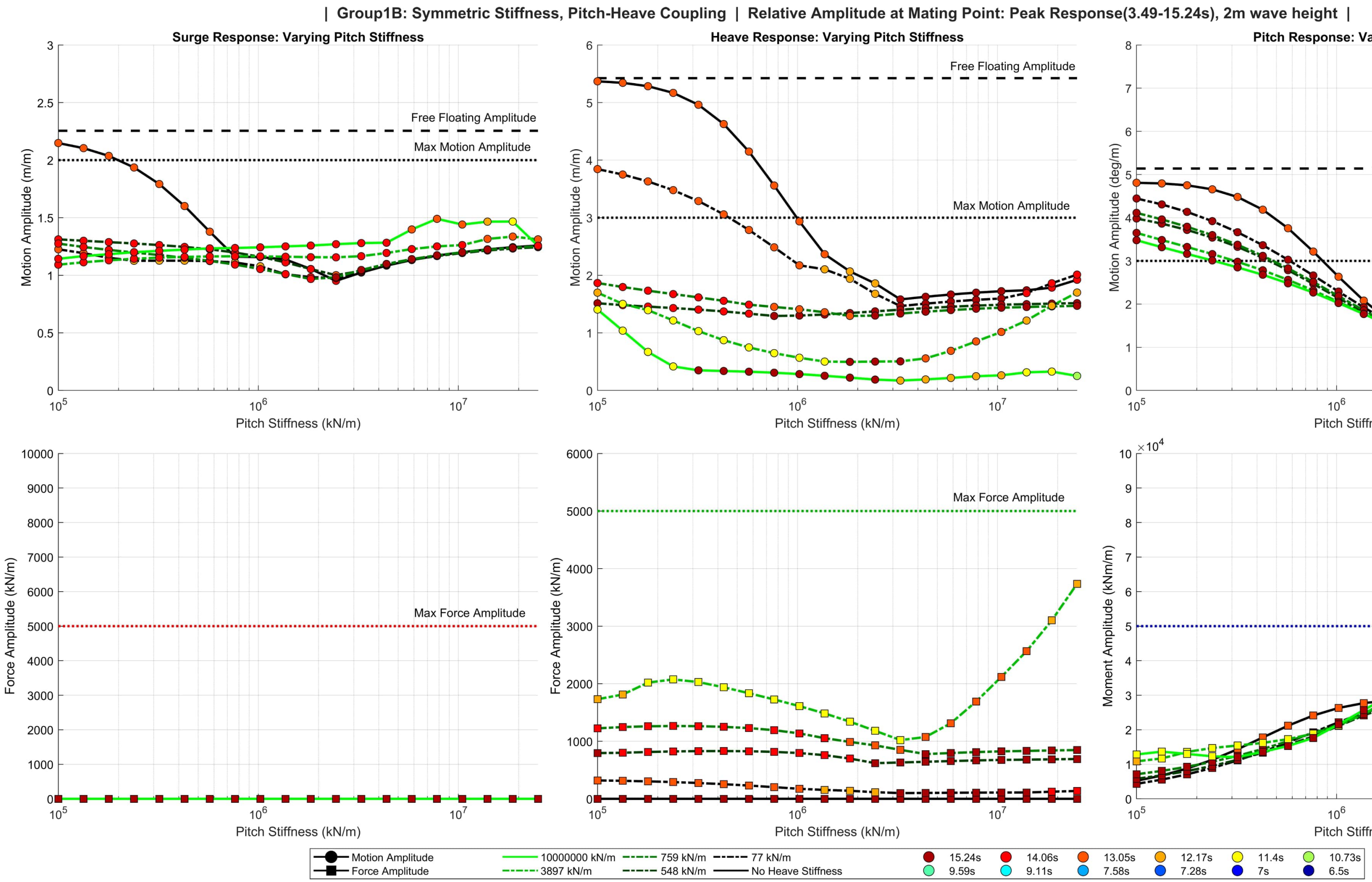

Figure C.7: Group 1B: Pitch Heave Coupling

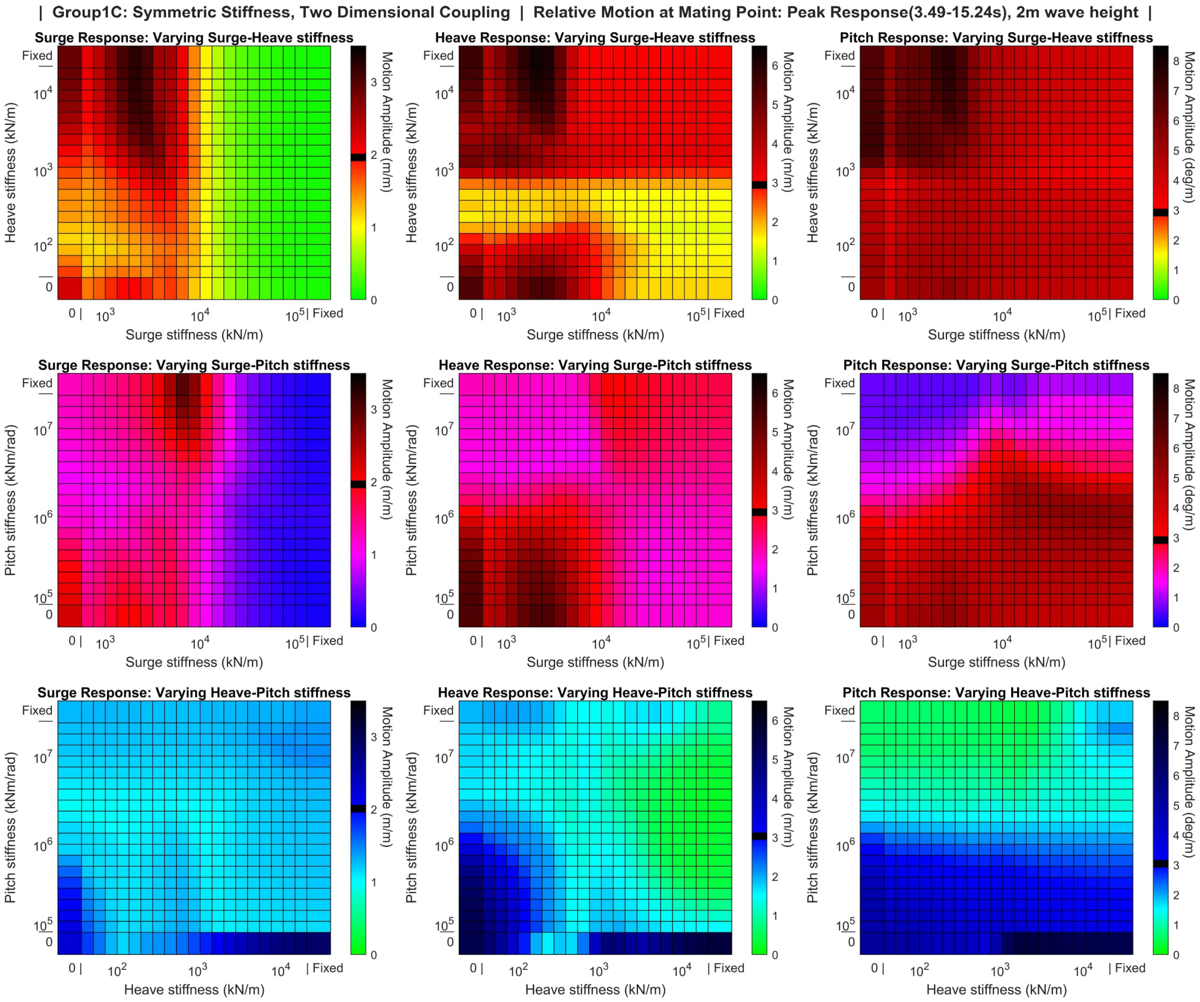

| Group1C: Symmetric Stiffness, Two Dimensional Coupling | Relative Motion at Mating Point: Peak Response(3.49-15.24s), 2m wave height |

Surge Response: Varying Surge-Heave stiffness

Heave Response: Varying Surge-Heave stiffness

Pitch Response: Varying Surge-Heave stiffness

Surge Response: Varying Surge-Pitch stiffness

Heave Response: Varying Surge-Pitch stiffness

Pitch Response: Varying Surge-Pitch stiffness

Surge Response: Varying Heave-Pitch stiffness

Heave Response: Varying Heave-Pitch stiffness

Pitch Response: Varying Heave-Pitch stiffness

Figure C.8: Group 1C: Relative Motions

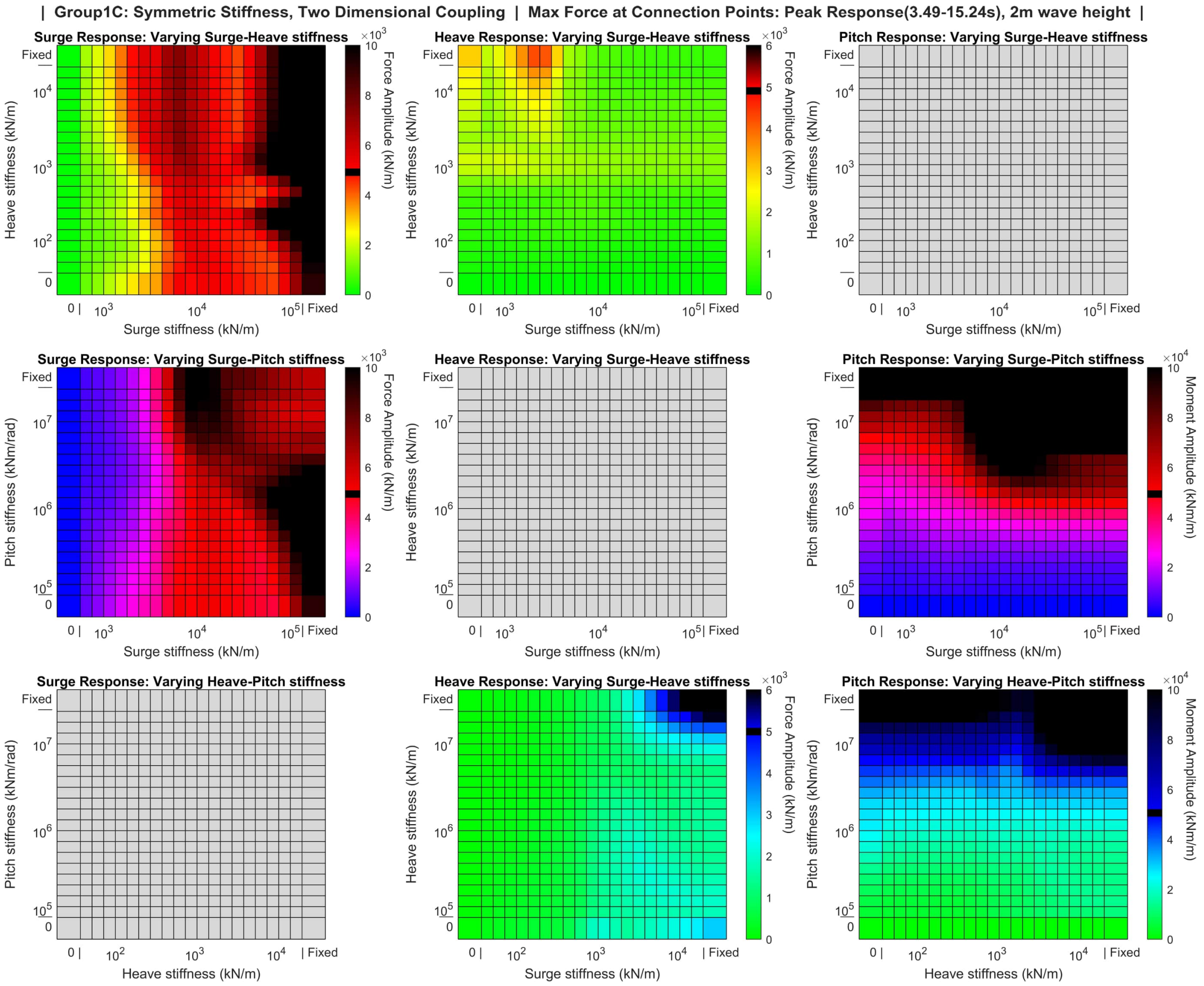

Figure C.9: Group 1C: Connection Forces

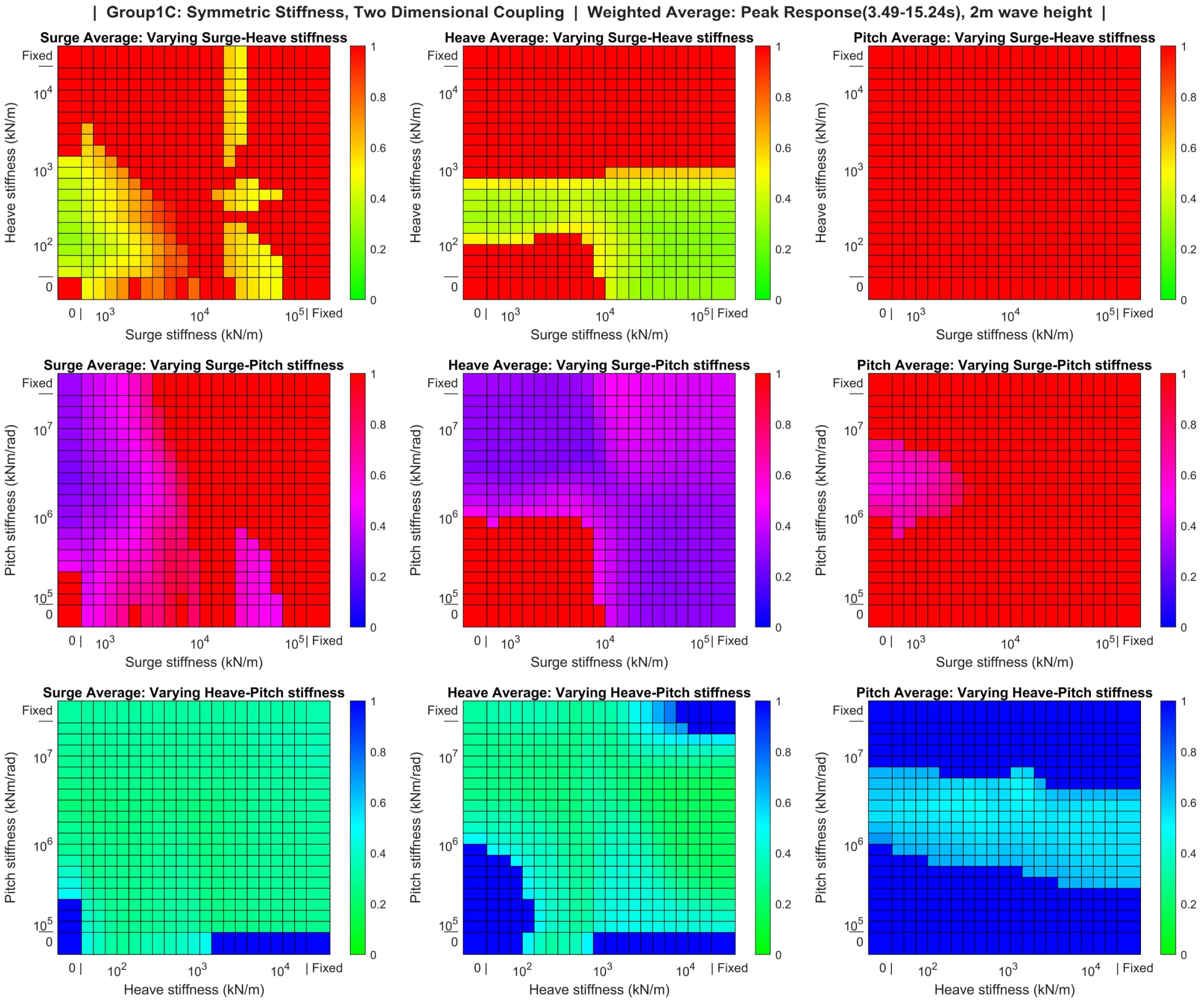

Figure C.10: Group 1C: Weighted Average

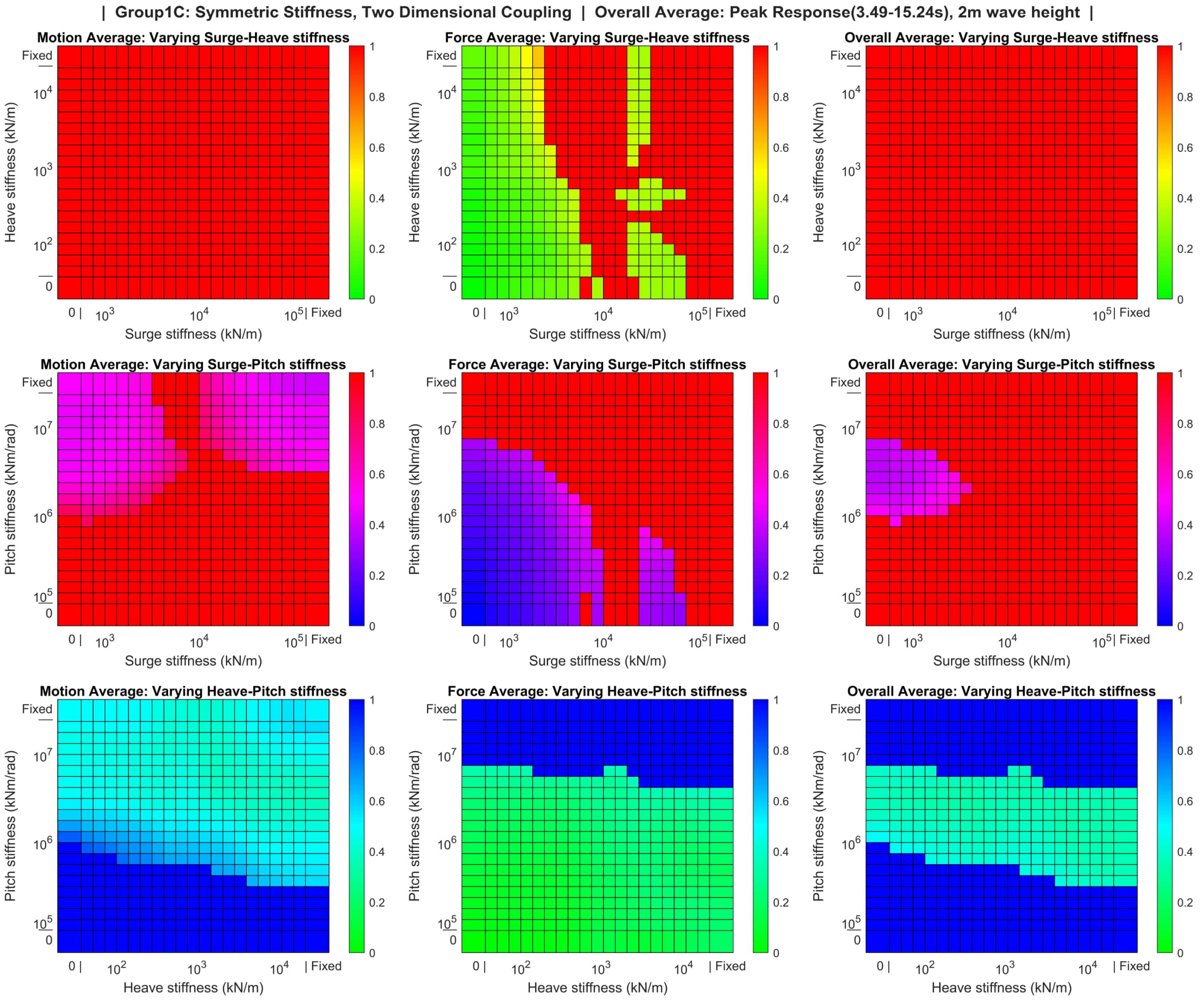

Figure C.11: Group 1C: Overall Average

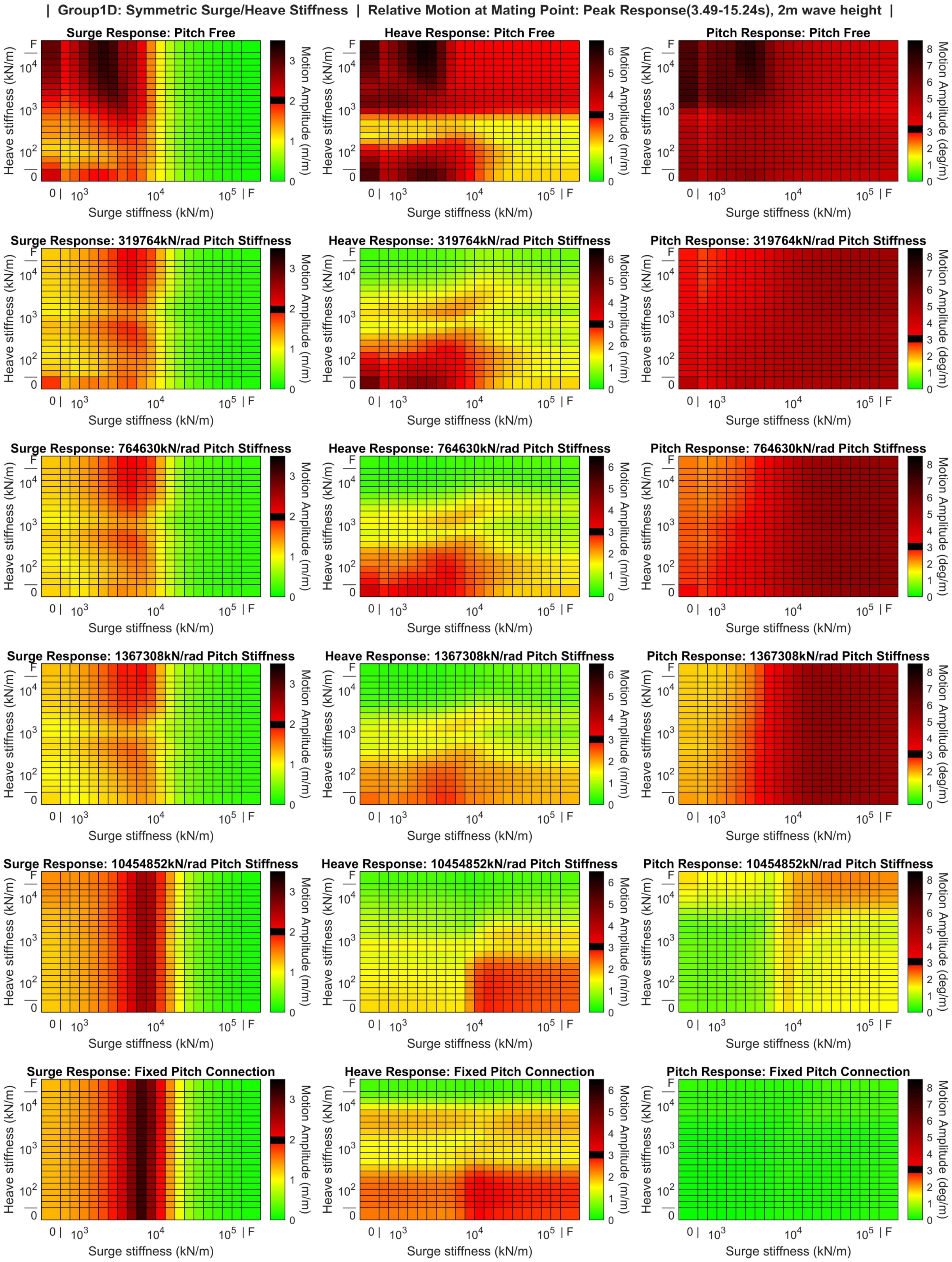

Figure C.12: Group 1D: Surge Heave Coupling Motions

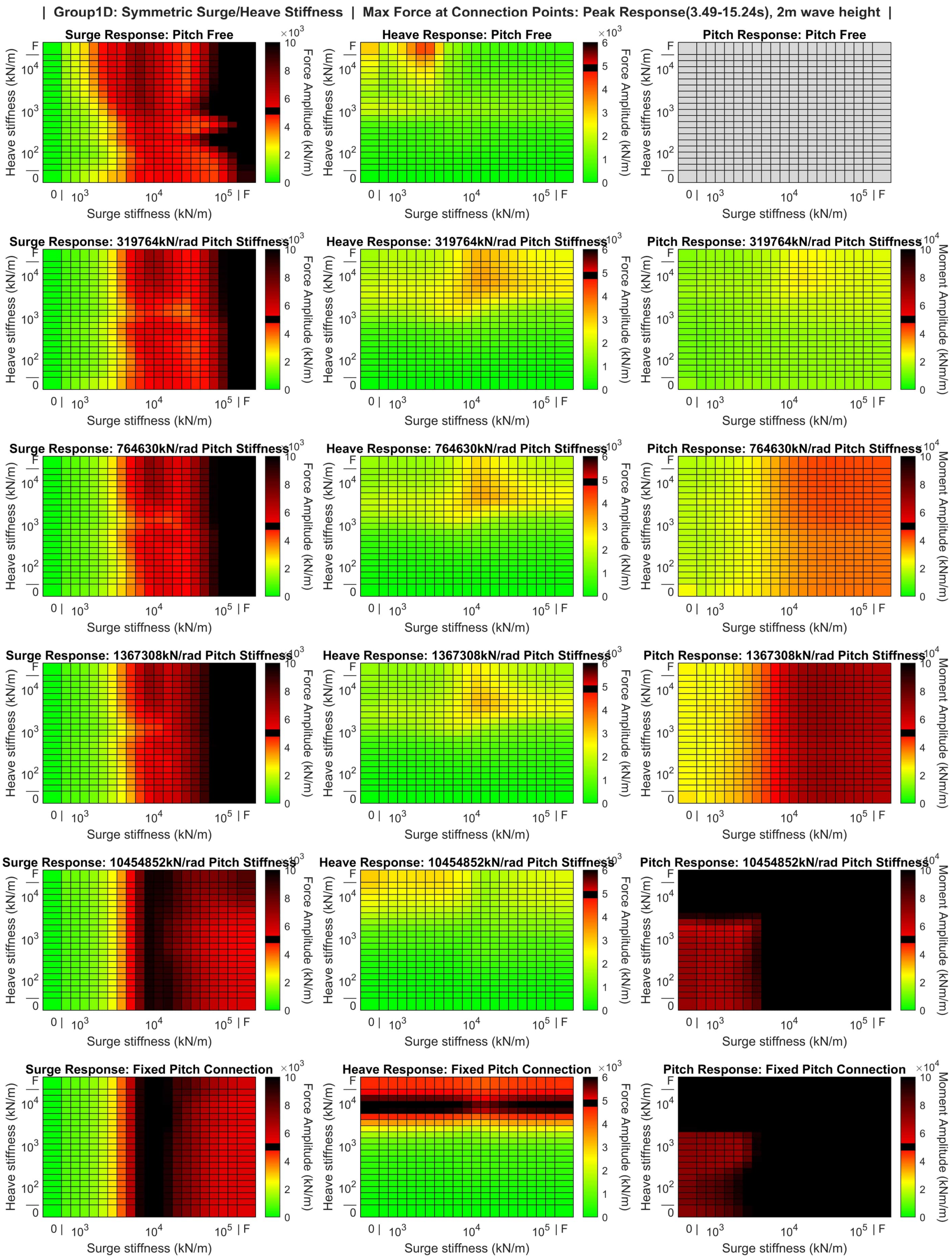

Figure C.13: Group 1D: Surge Heave Coupling Force

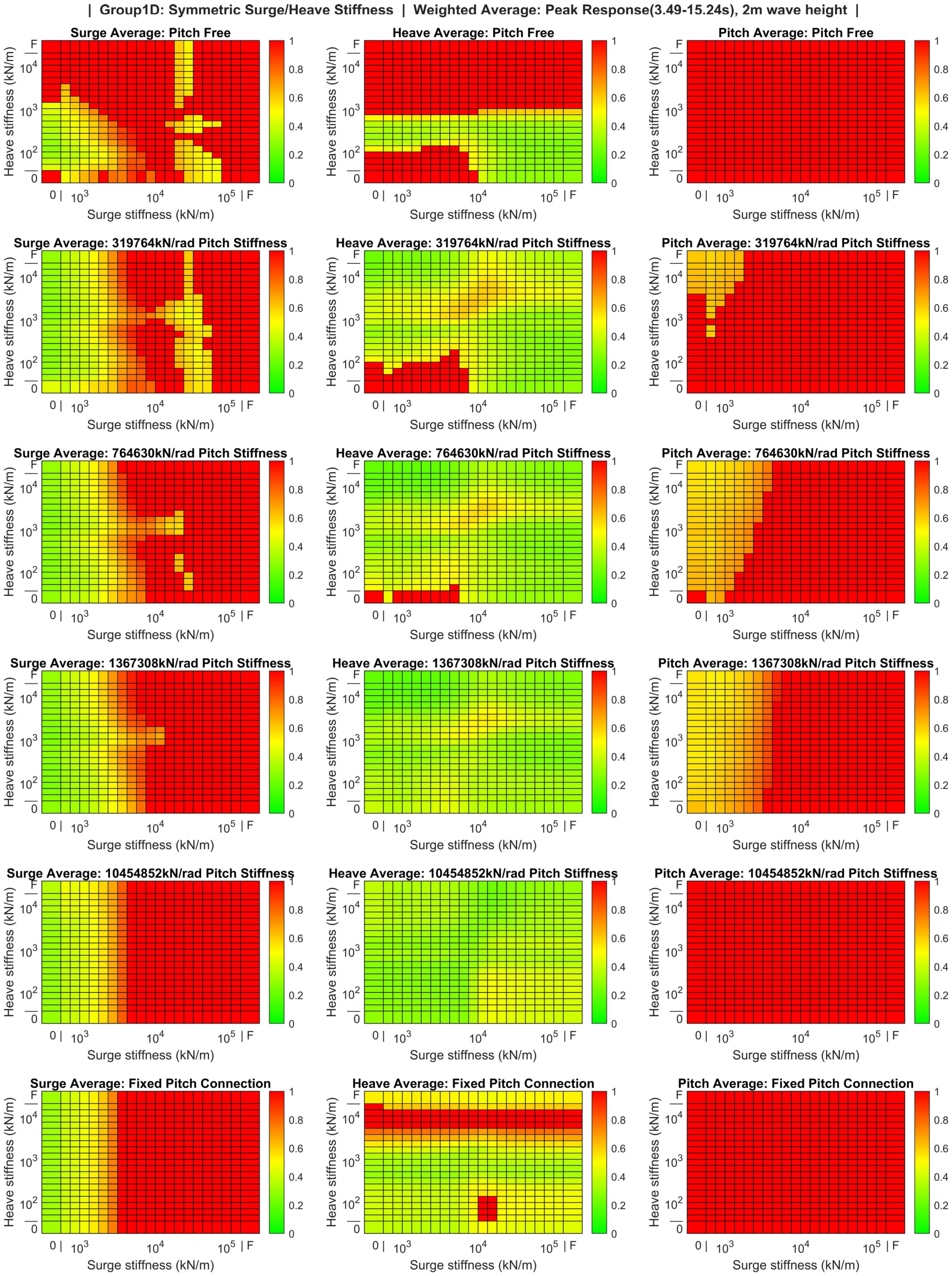

Figure C.14: Group 1D: Surge Heave Coupling Weighted Average

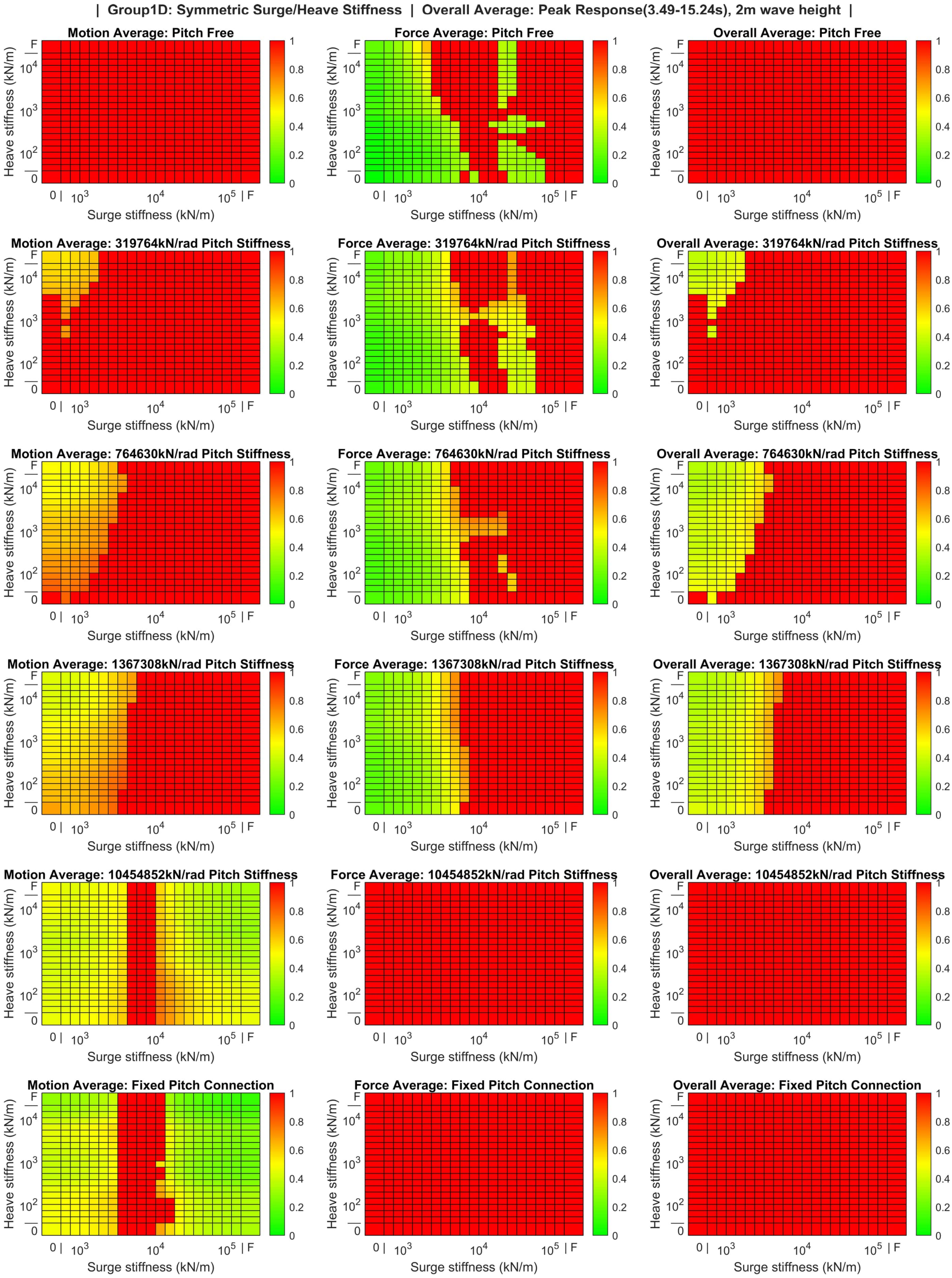

Figure C.15: Group 1D: Surge Heave Coupling Overall Average

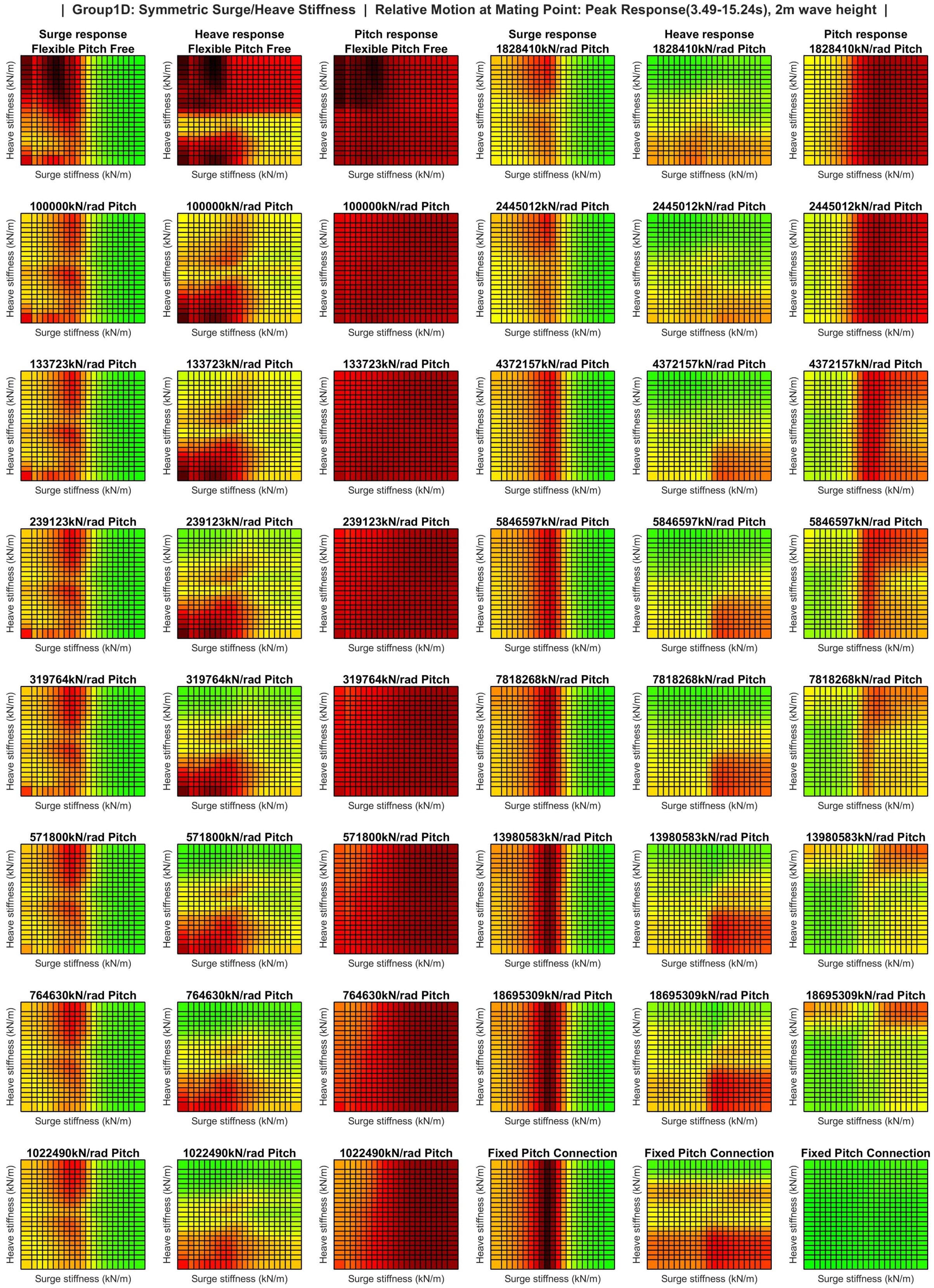

Figure C.16: Group 1D: Surge Heave Coupling Motions (16 variations)

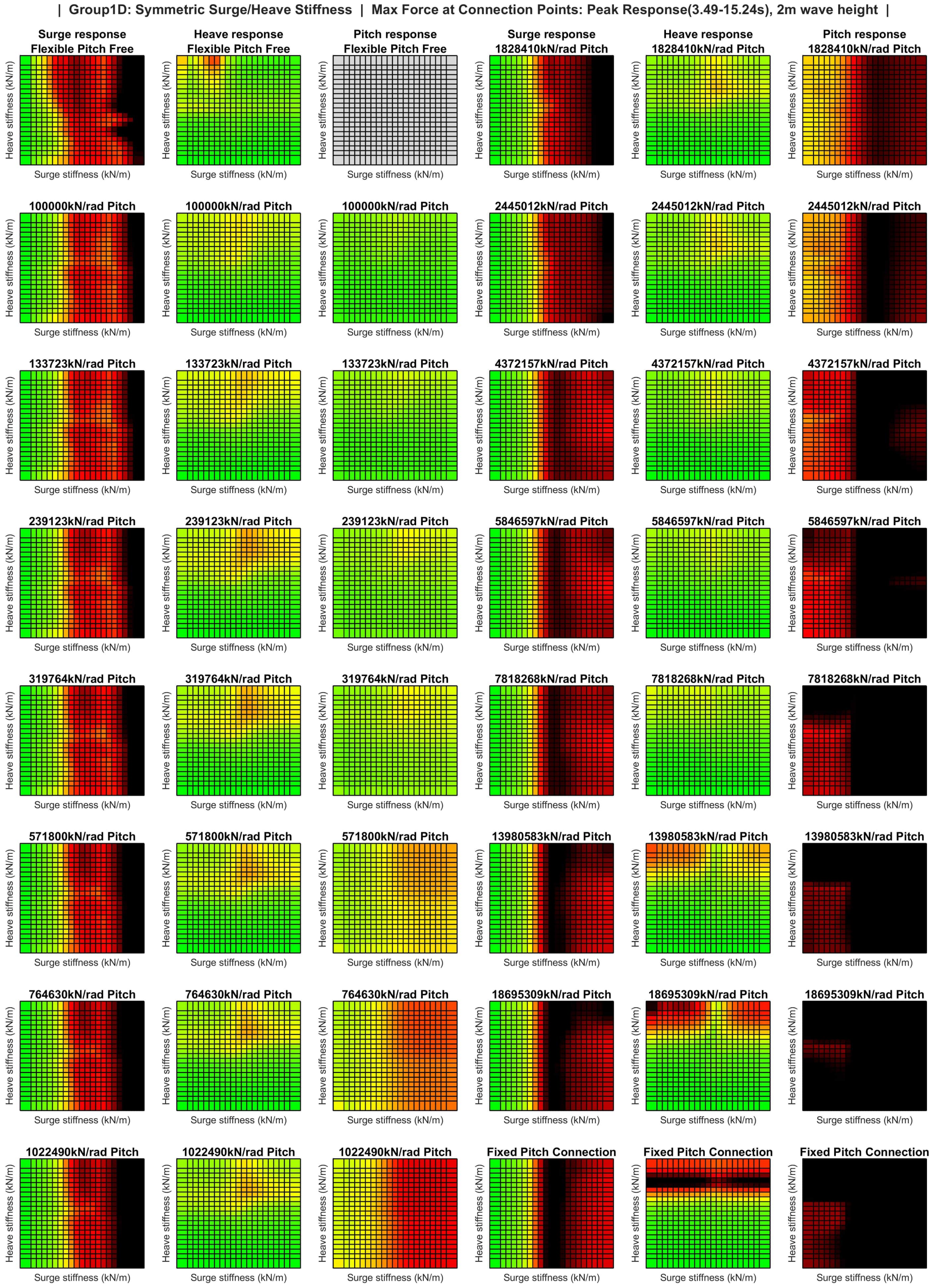

Figure C.17: Group 1D: Surge Heave Coupling Force (16 variations)

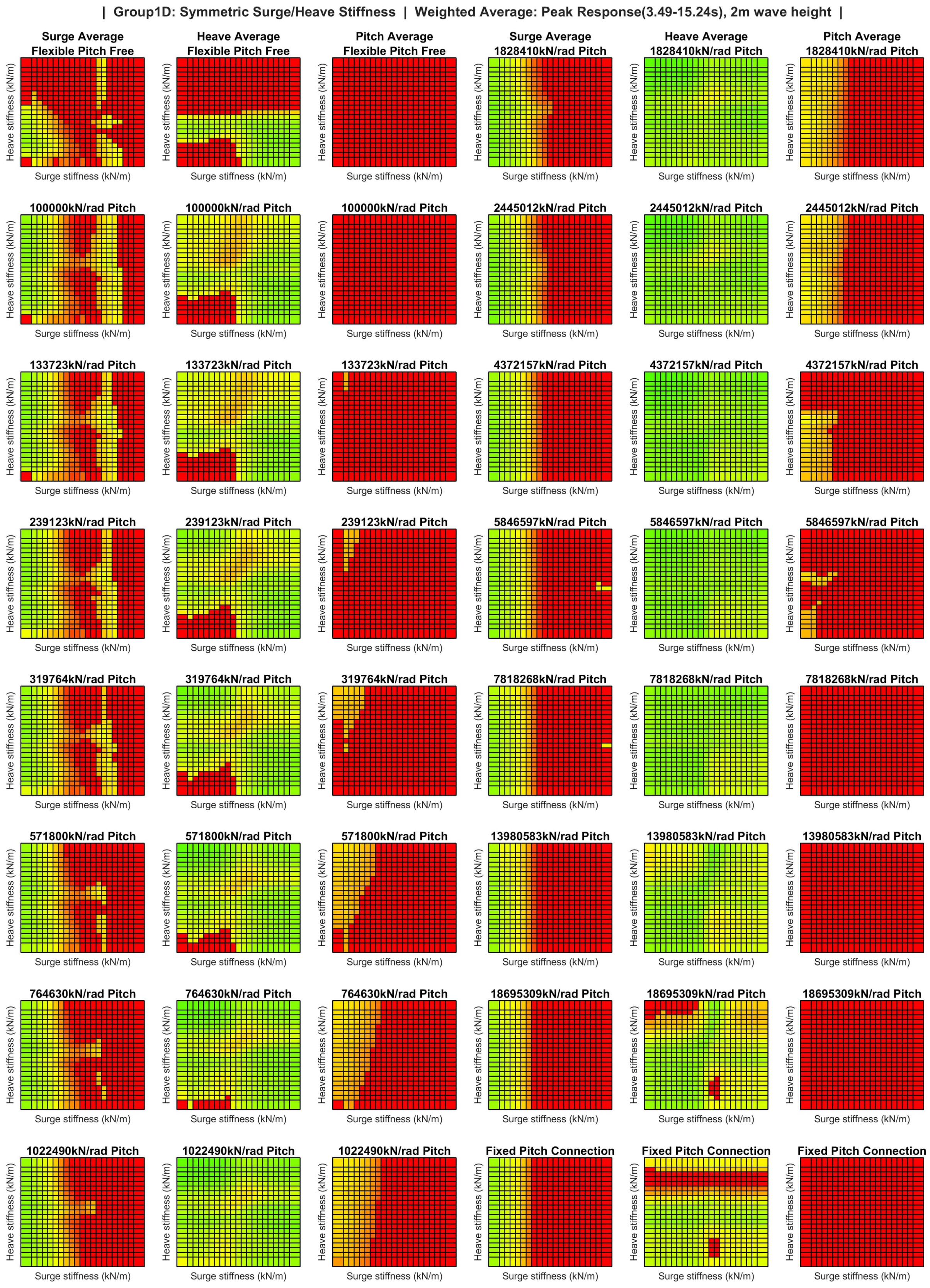

Figure C.18: Group 1D: Surge Heave Coupling Weighted Average (16 variations)
]

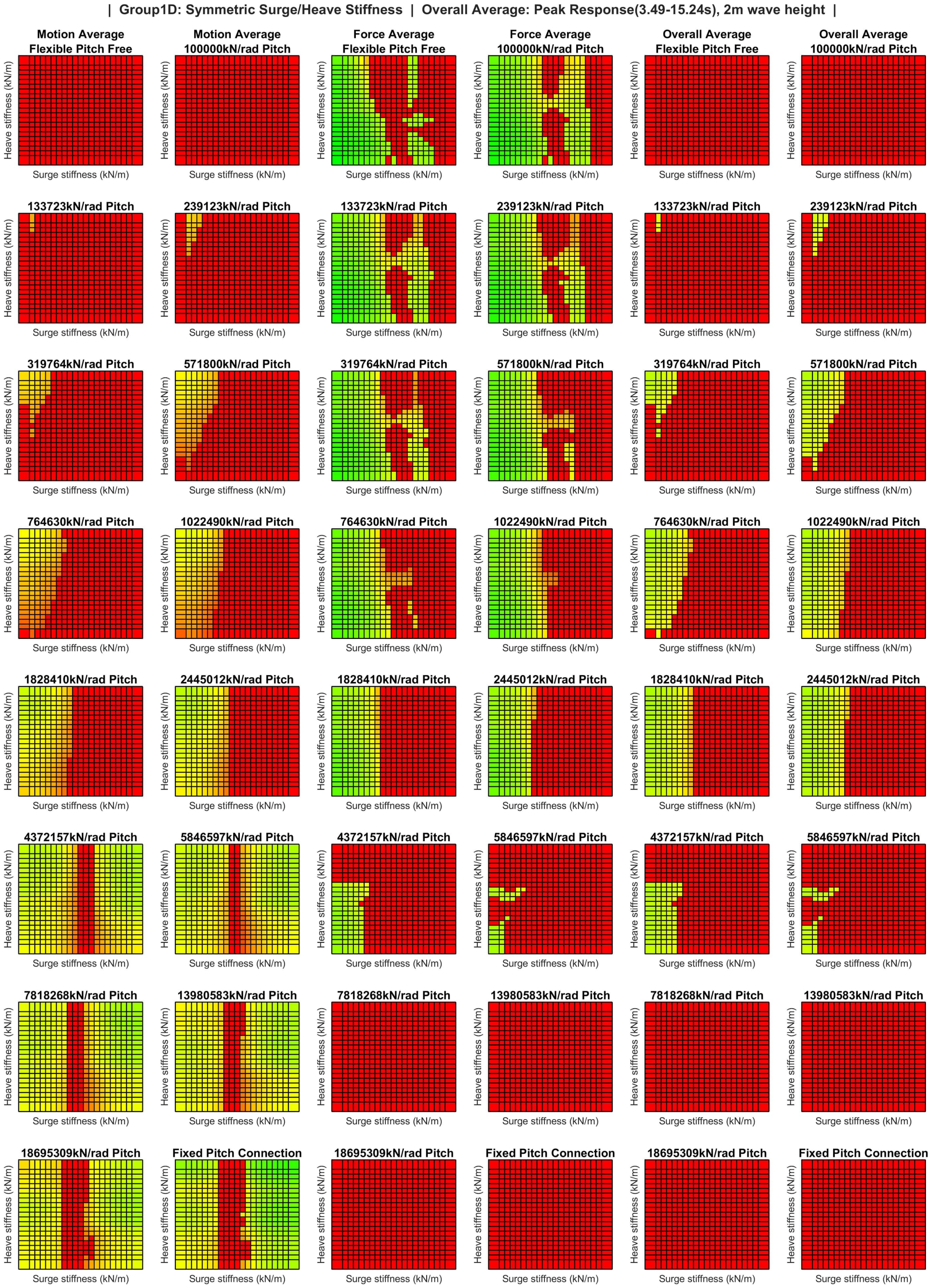

| Group1D: Symmetric Surge/Heave Stiffness | Overall Average: Peak Response(3.49-15.24s), 2m wave height |

Motion Average Flexible Pitch Free; Motion Average 100000kN/rad Pitch; Force Average Flexible Pitch Free; Force Average 100000kN/rad Pitch; Overall Average Flexible Pitch Free; Overall Average 100000kN/rad Pitch

133723kN/rad Pitch; 239123kN/rad Pitch; 133723kN/rad Pitch; 239123kN/rad Pitch; 133723kN/rad Pitch; 239123kN/rad Pitch

319764kN/rad Pitch; 571800kN/rad Pitch; 319764kN/rad Pitch; 571800kN/rad Pitch; 319764kN/rad Pitch; 571800kN/rad Pitch

764630kN/rad Pitch; 1022490kN/rad Pitch; 764630kN/rad Pitch; 1022490kN/rad Pitch; 764630kN/rad Pitch; 1022490kN/rad Pitch

1828410kN/rad Pitch; 2445012kN/rad Pitch; 1828410kN/rad Pitch; 2445012kN/rad Pitch; 1828410kN/rad Pitch; 2445012kN/rad Pitch

4372157kN/rad Pitch; 5846597kN/rad Pitch; 4372157kN/rad Pitch; 5846597kN/rad Pitch; 4372157kN/rad Pitch; 5846597kN/rad Pitch

7818268kN/rad Pitch; 13980583kN/rad Pitch; 7818268kN/rad Pitch; 13980583kN/rad Pitch; 7818268kN/rad Pitch; 13980583kN/rad Pitch

18695309kN/rad Pitch; Fixed Pitch Connection; 18695309kN/rad Pitch; Fixed Pitch Connection; 18695309kN/rad Pitch; Fixed Pitch Connection

Figure C.19: Group 1D: Surge Heave Coupling Overall Average (16 variations)

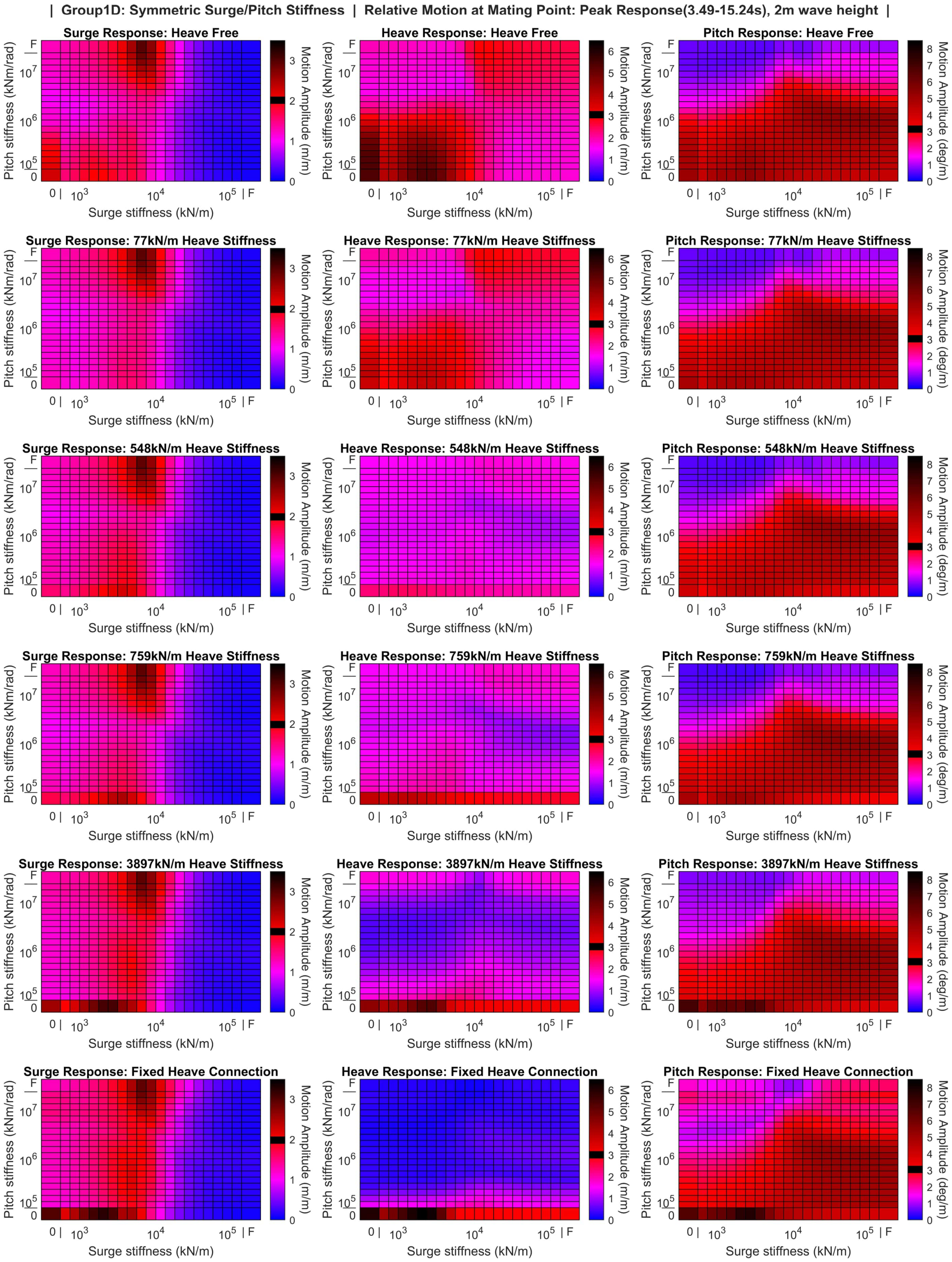

Figure C.20: Group 1D: Surge Pitch Coupling Motions

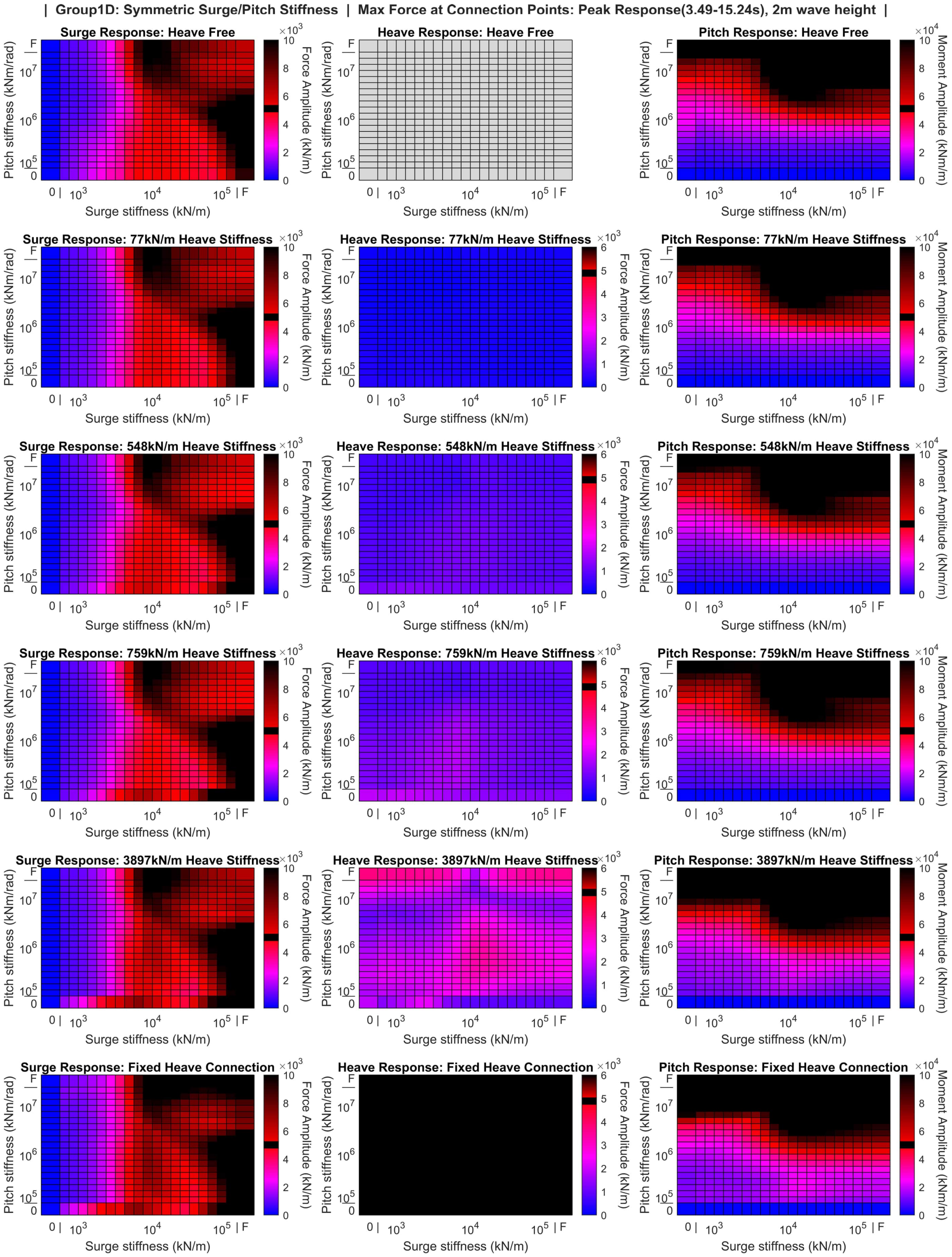

Figure C.21: Group 1D: Surge Pitch Coupling Force

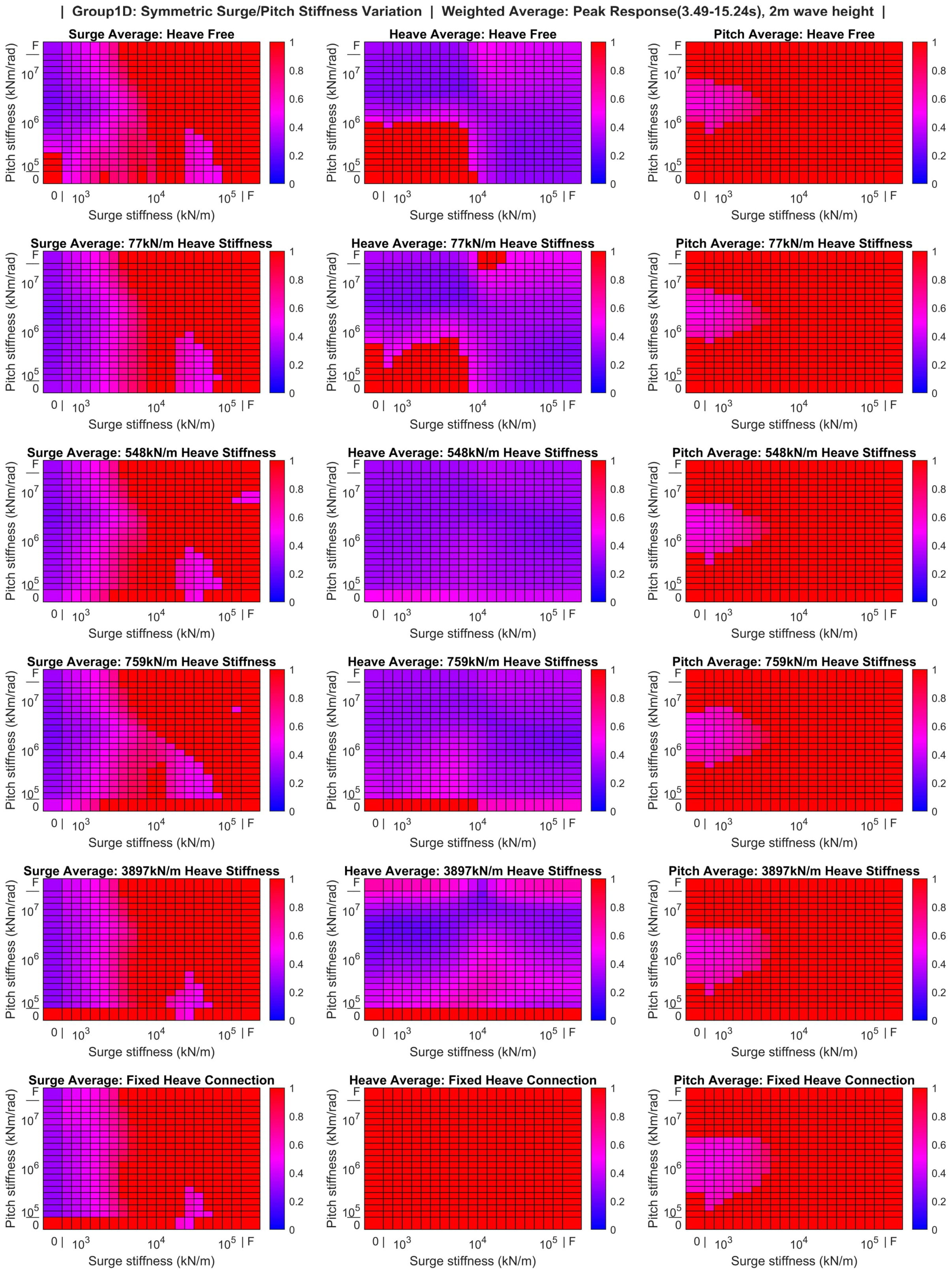
| Group1D: Symmetric Surge/Pitch Stiffness Variation | Weighted Average: Peak Response(3.49-15.24s), 2m wave height |

Surge Average: Heave Free
Heave Average: Heave Free
Pitch Average: Heave Free
Surge Average: 77kN/m Heave Stiffness
Heave Average: 77kN/m Heave Stiffness
Pitch Average: 77kN/m Heave Stiffness
Surge Average: 548kN/m Heave Stiffness
Heave Average: 548kN/m Heave Stiffness
Pitch Average: 548kN/m Heave Stiffness
Surge Average: 759kN/m Heave Stiffness
Heave Average: 759kN/m Heave Stiffness
Pitch Average: 759kN/m Heave Stiffness
Surge Average: 3897kN/m Heave Stiffness
Heave Average: 3897kN/m Heave Stiffness
Pitch Average: 3897kN/m Heave Stiffness
Surge Average: Fixed Heave Connection
Heave Average: Fixed Heave Connection
Pitch Average: Fixed Heave Connection

Figure C.22: Group 1D: Surge Pitch Coupling Weighted Average

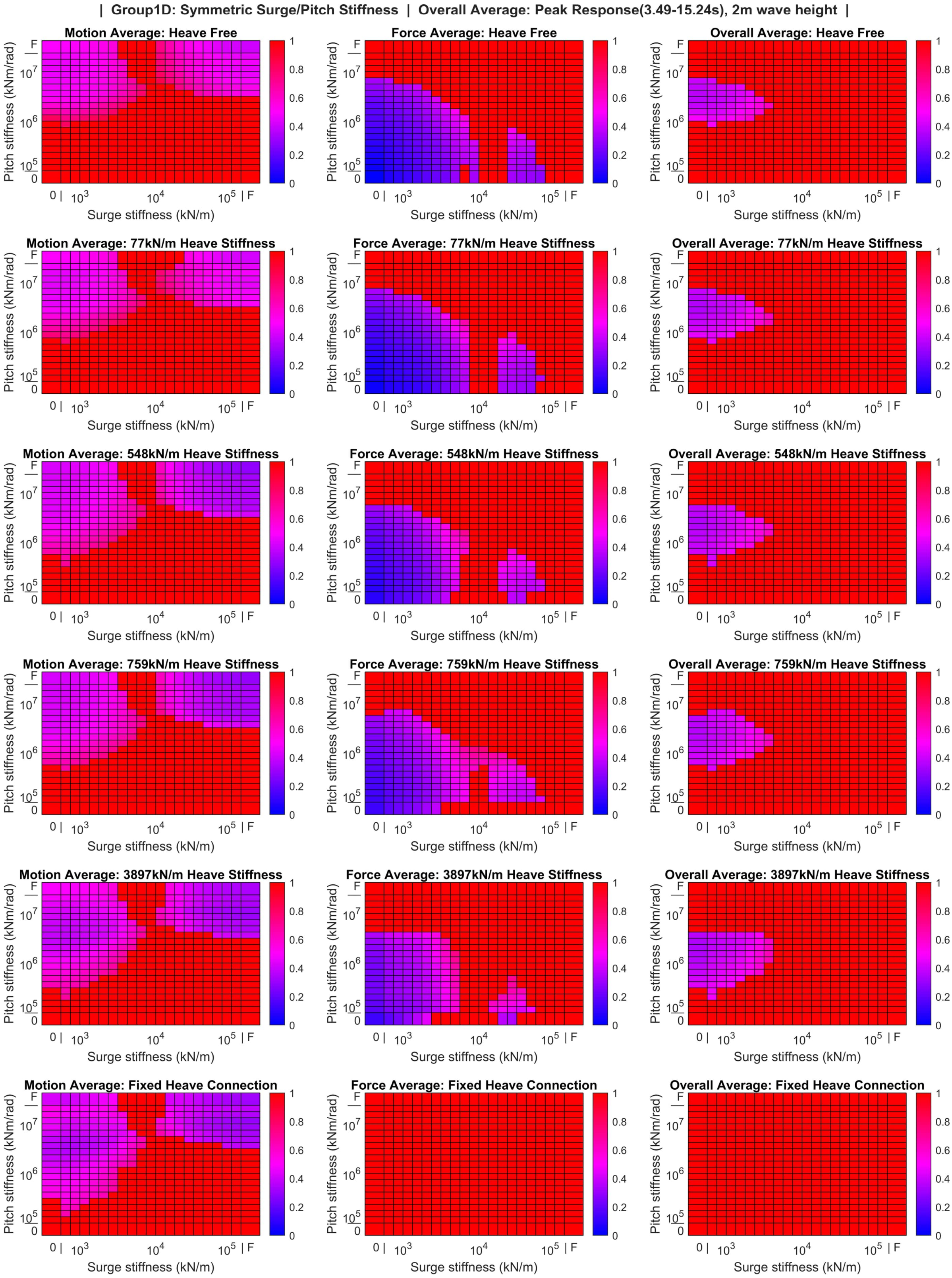

Figure C.23: Group 1D: Surge Pitch Coupling Overall Average

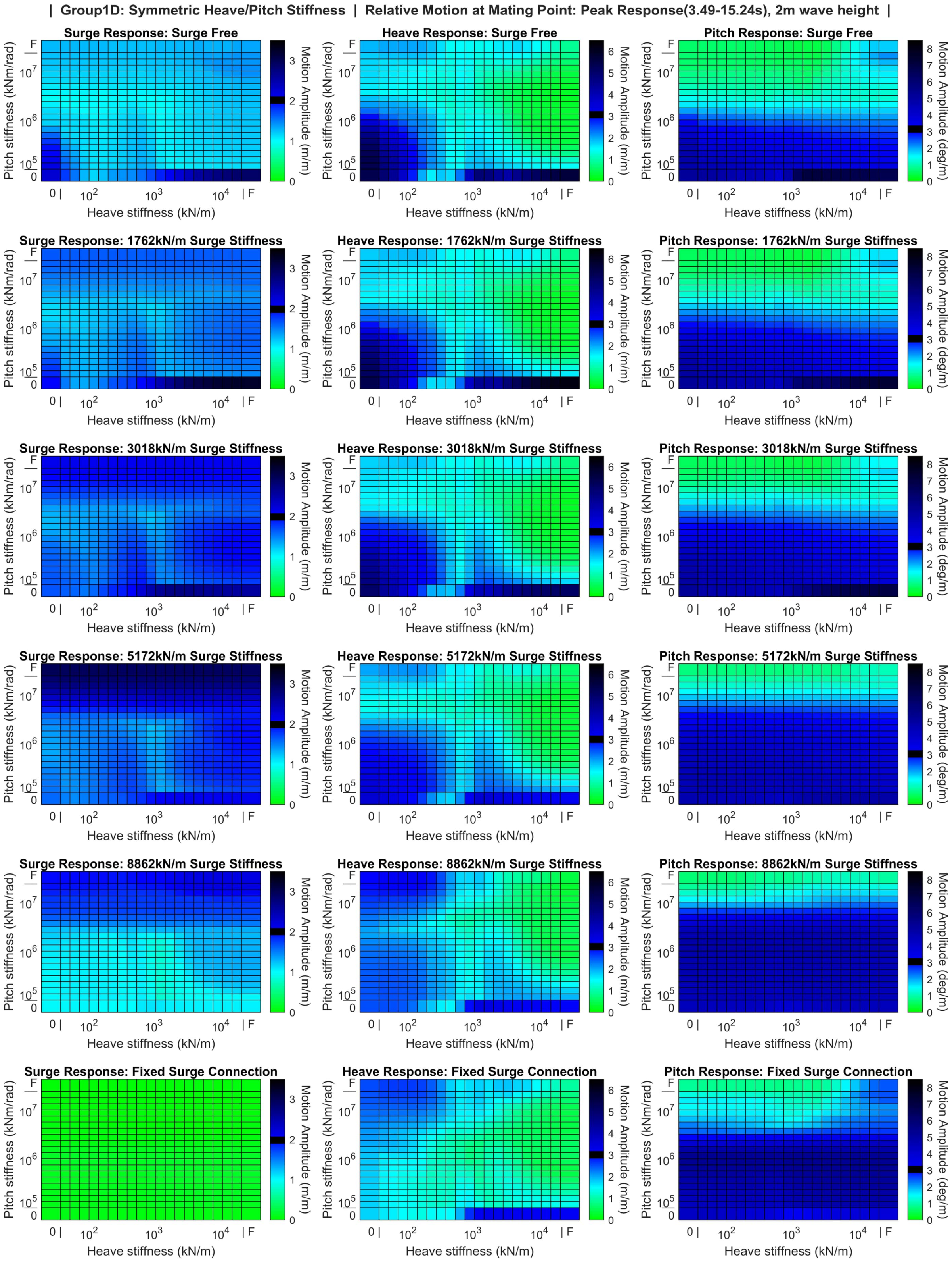

Figure C.24: Group 1D: Heave Pitch Coupling Motions

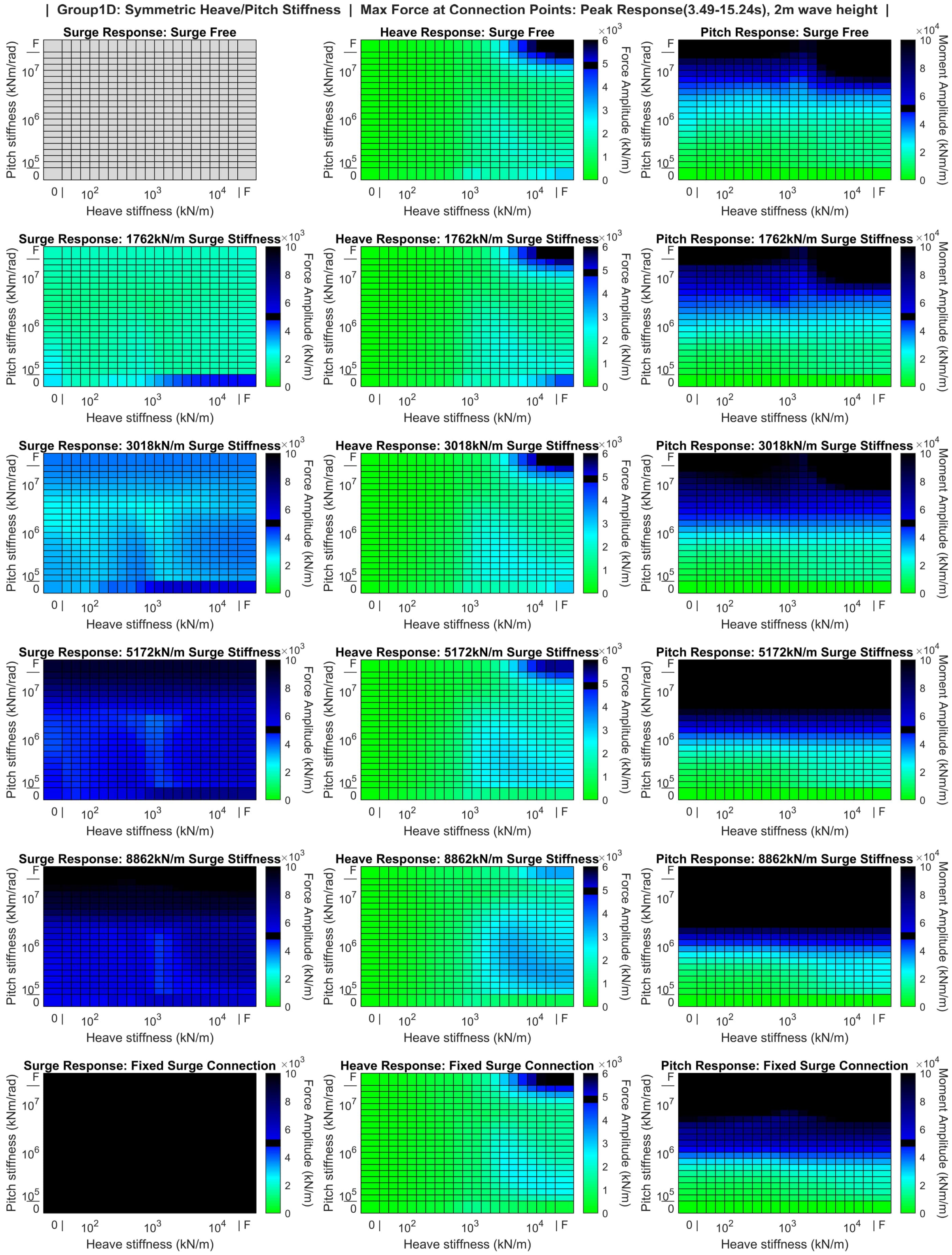

Figure C.25: Group 1D: Heave Pitch Coupling Force

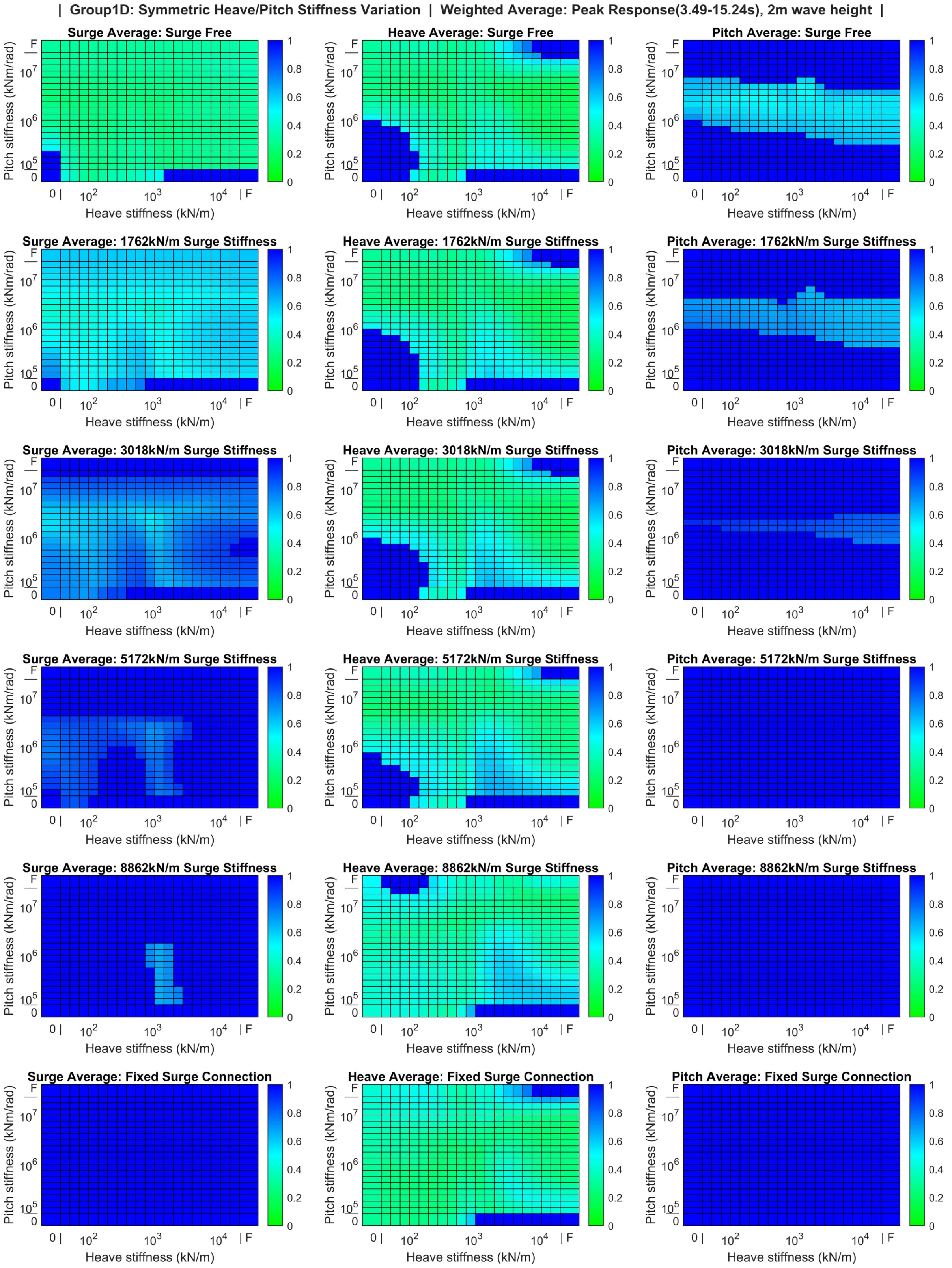

Figure C.26: Group 1D: Heave Pitch Coupling Weighted Average

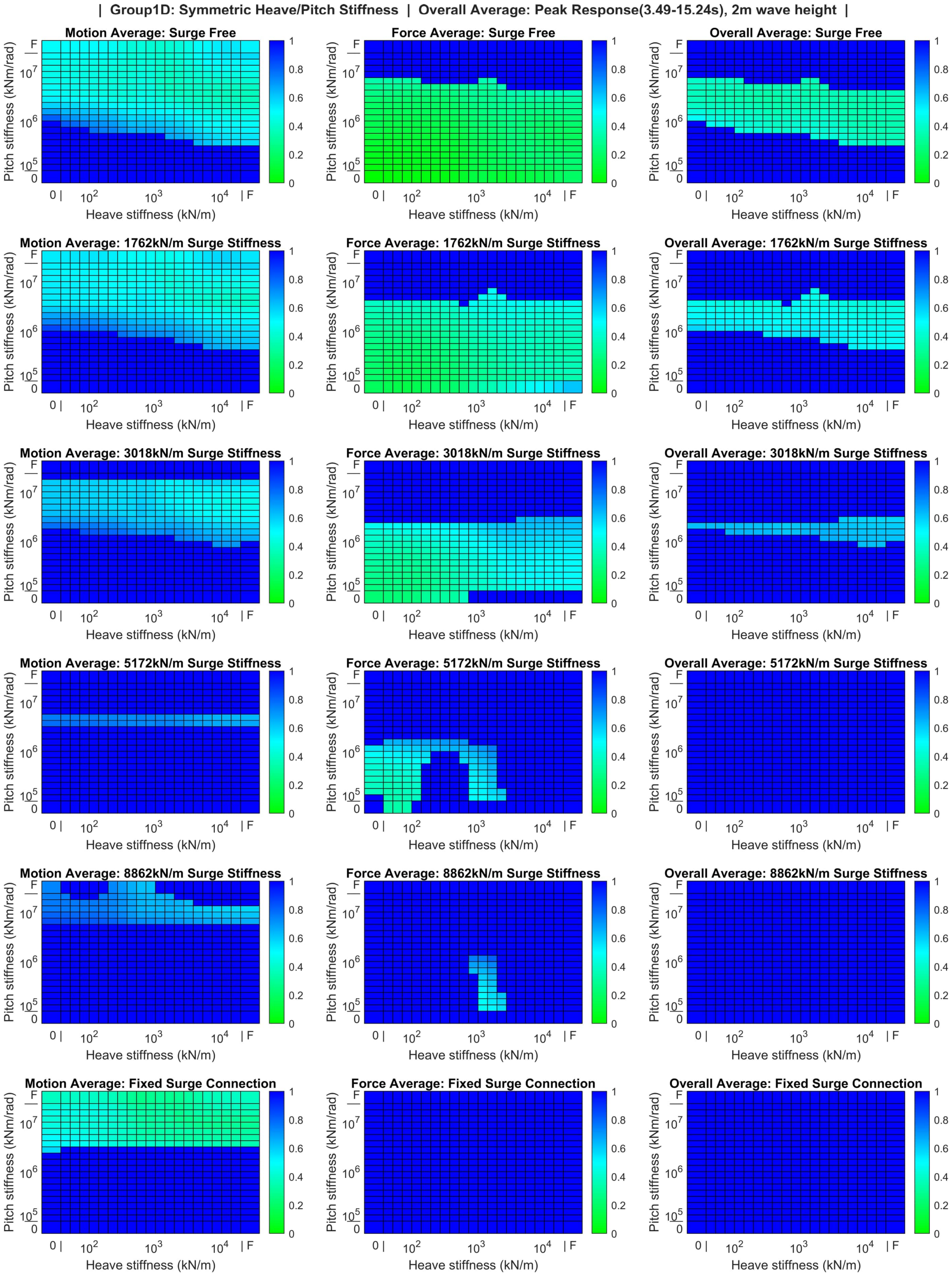

Figure C.27: Group 1D: Heave Pitch Coupling Overall Average

D

Analysis Group 2 Extended Results

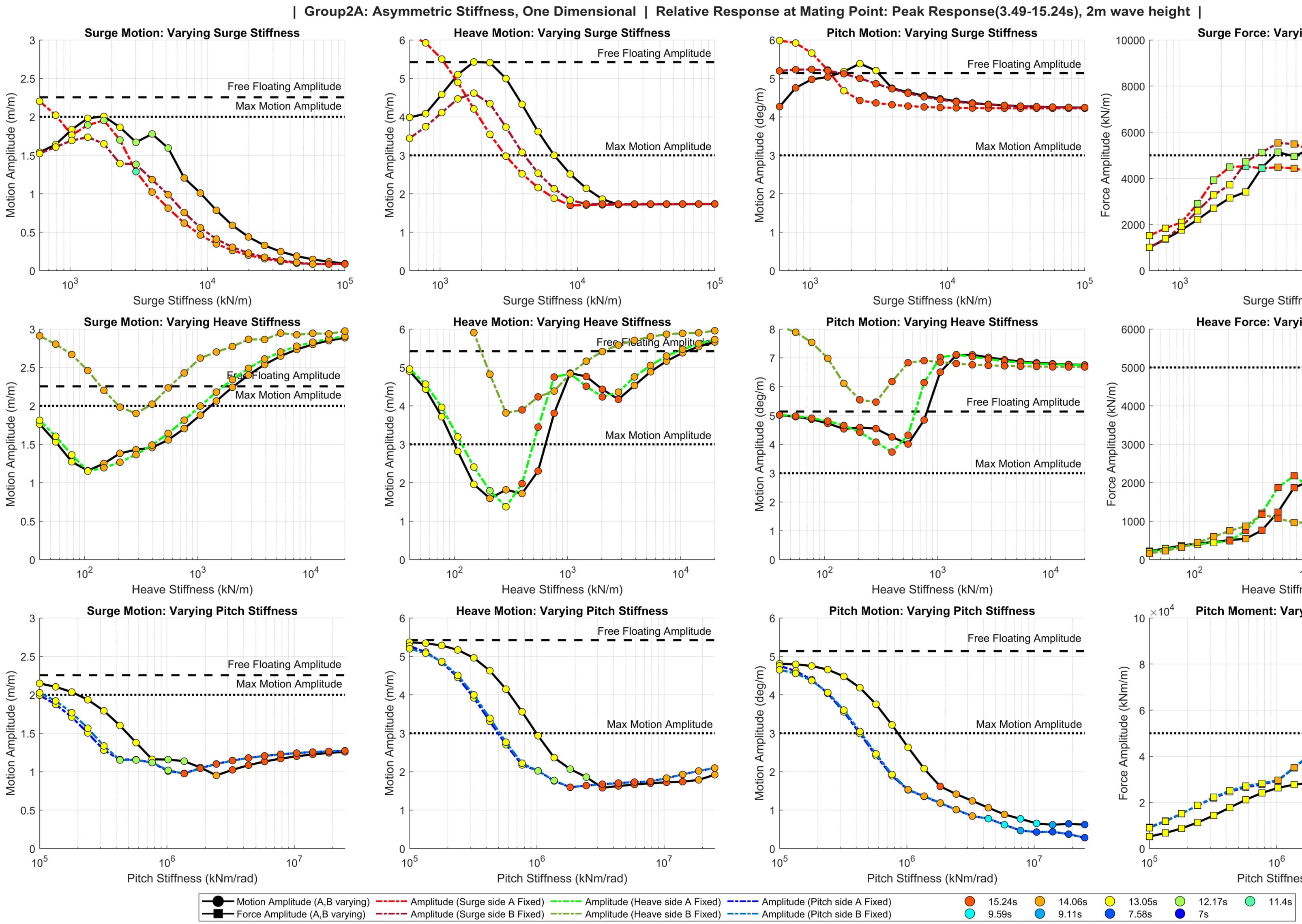

Figure D.1: Group 2A One-Dimensional two sided variation

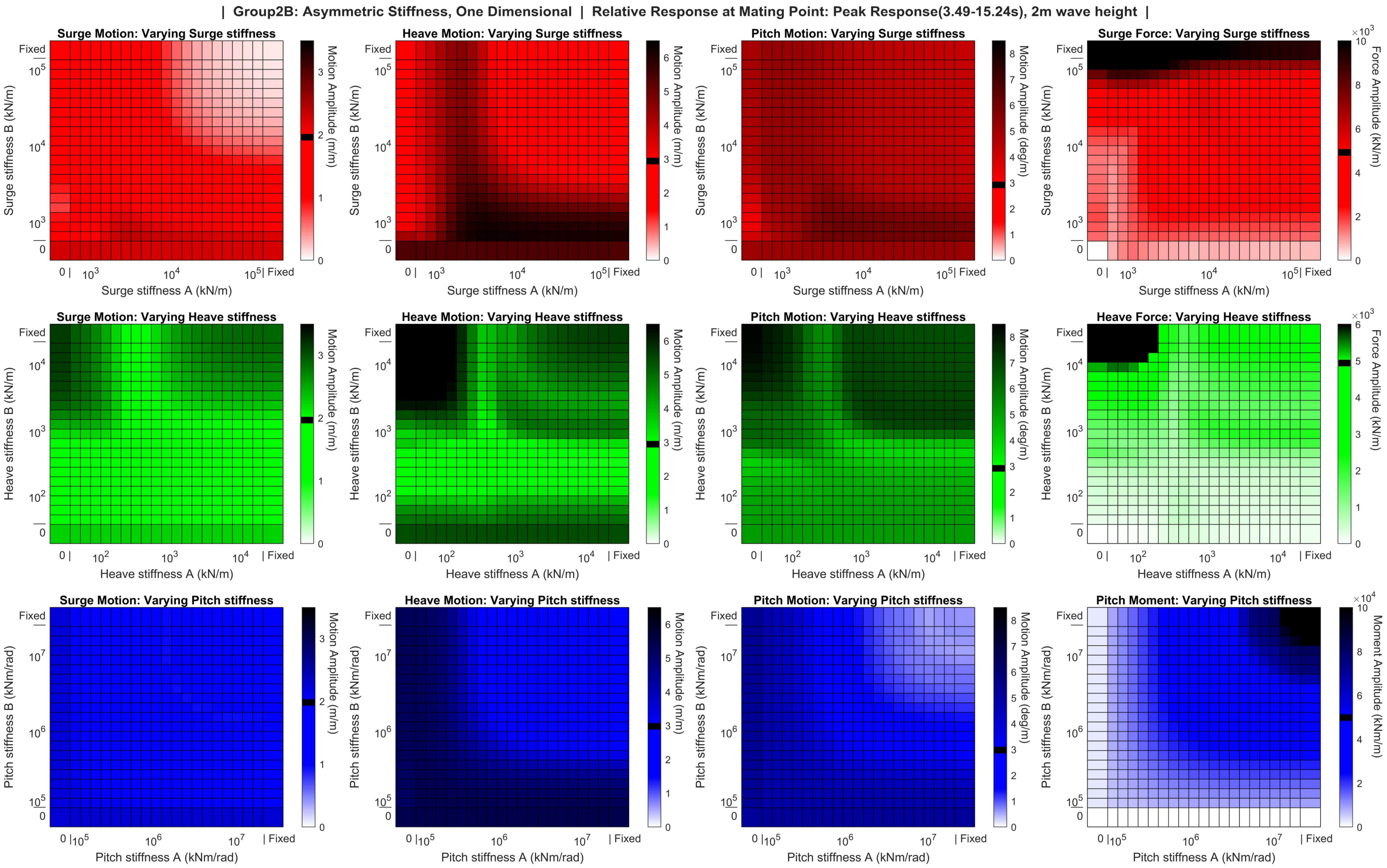

Figure D.2: Group 2B: One-Dimensional two sided variation

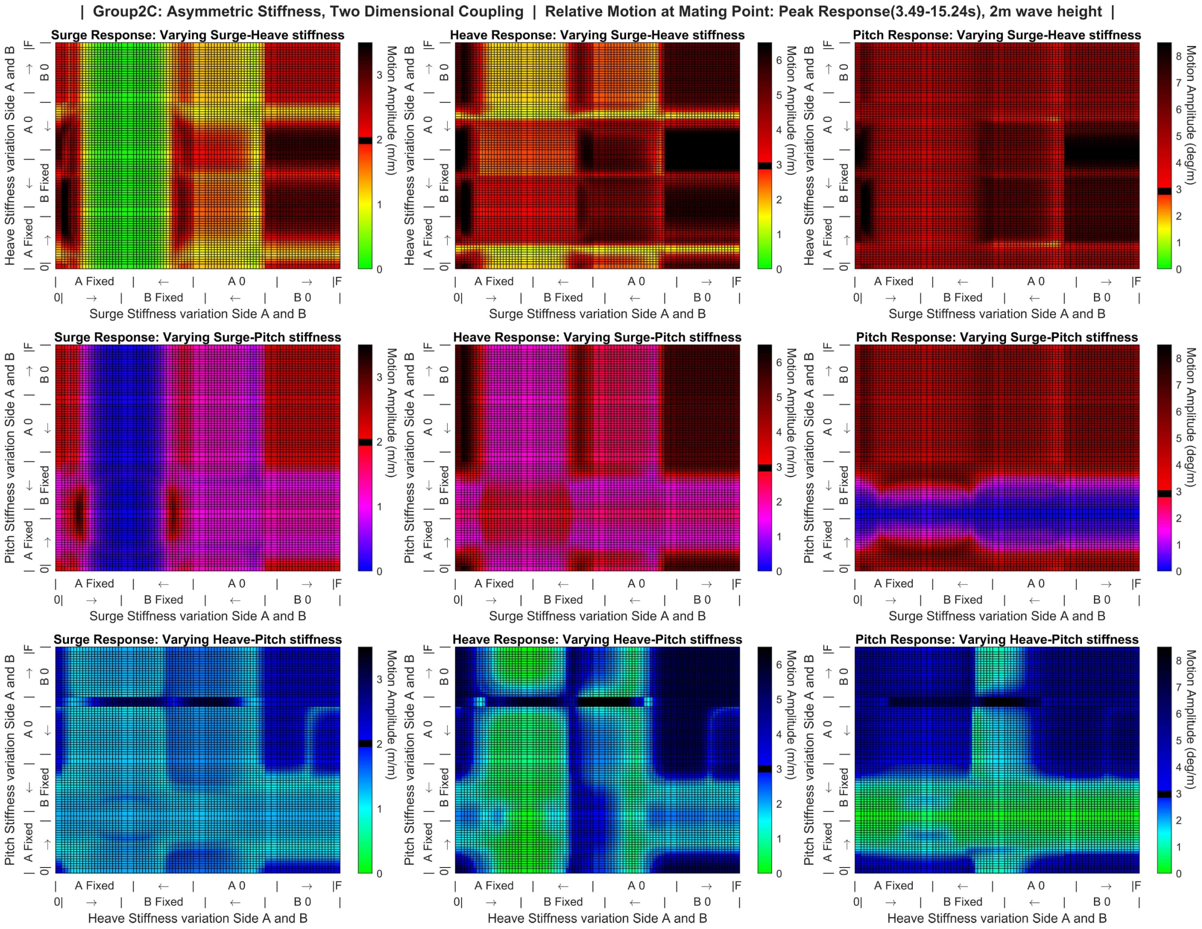

Figure D.3: Group 2C: Relative Motions

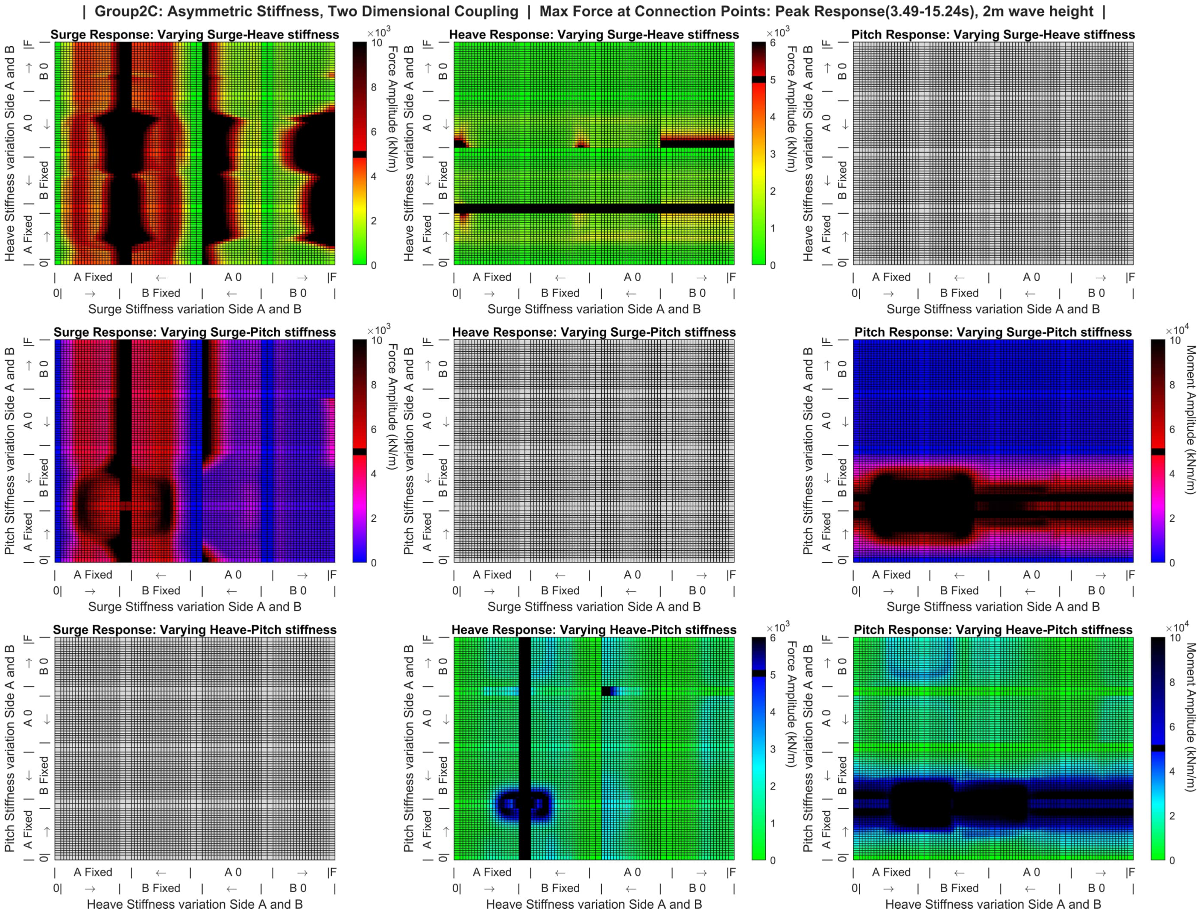

Figure D.4: Group 2C: Coupling Force

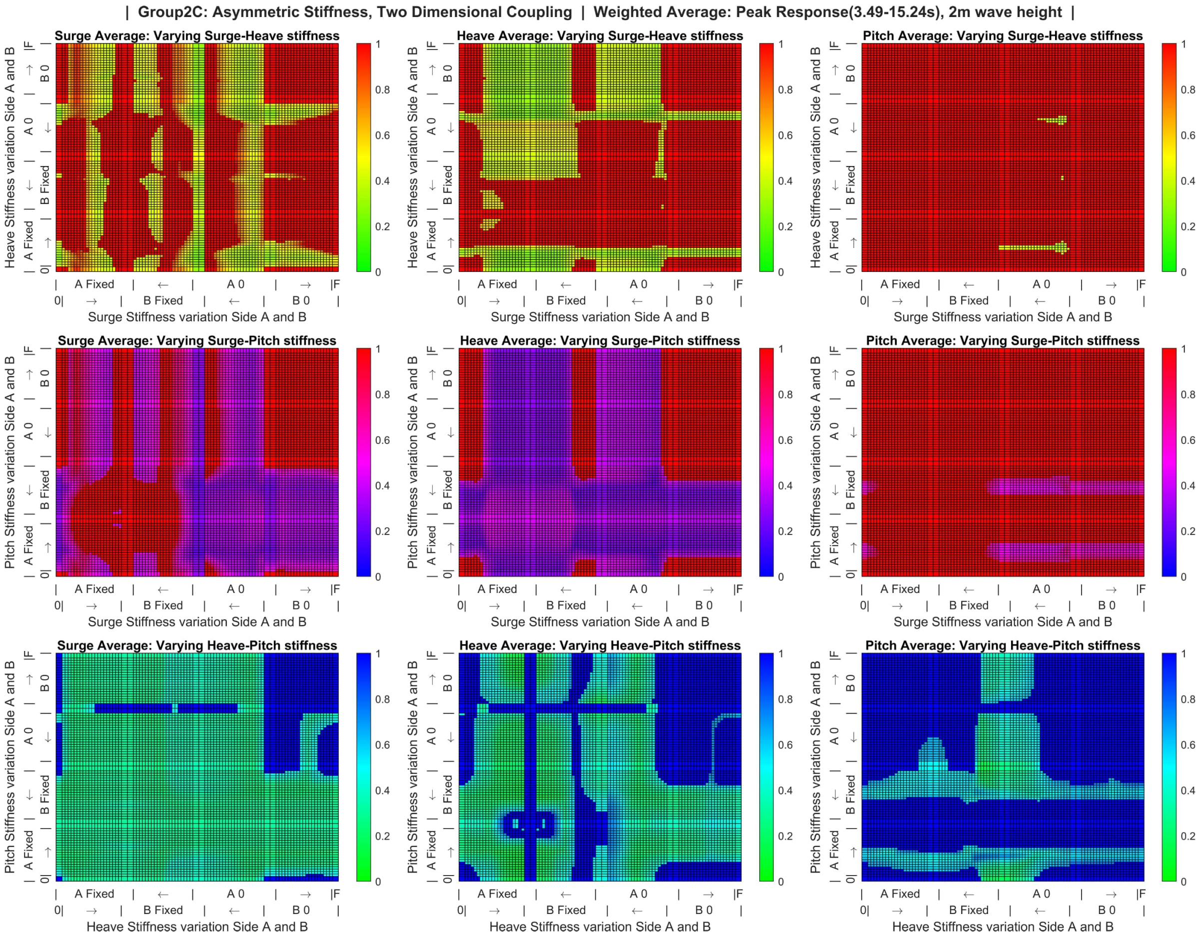

Figure D.5: Group 2C: Weighted Average

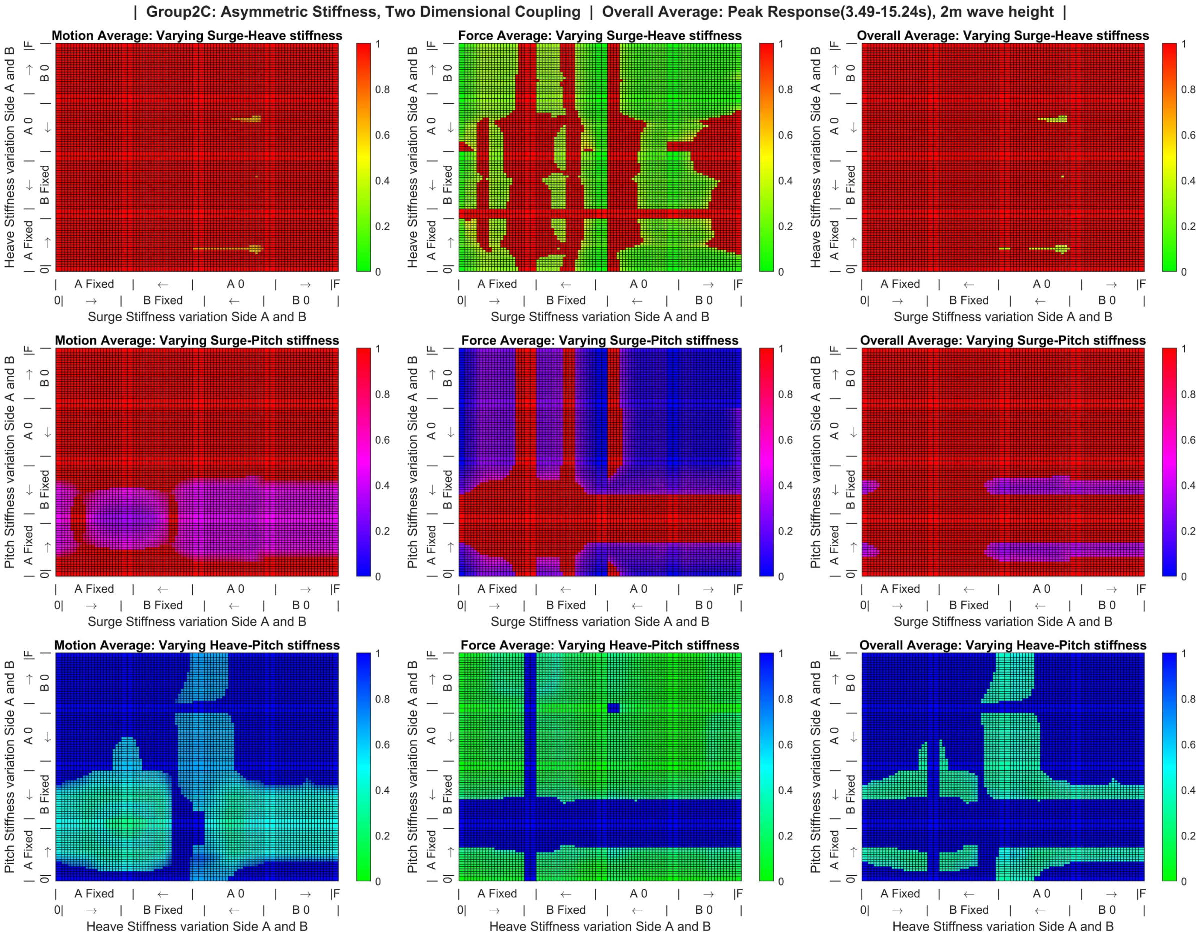

Figure D.6: Group 2C: Overall Average

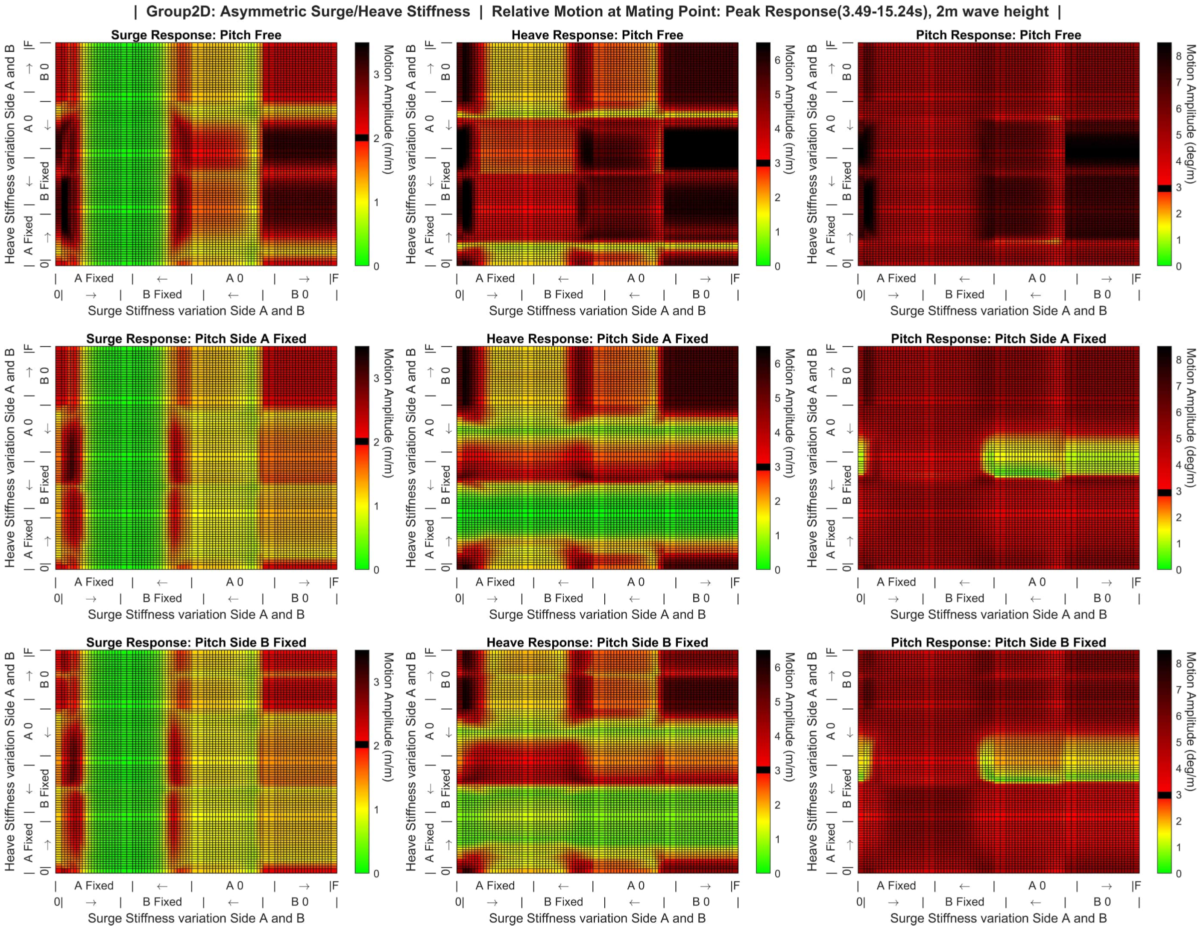

| Group2D: Asymmetric Surge/Heave Stiffness | Relative Motion at Mating Point: Peak Response(3.49-15.24s), 2m wave height |

Surge Response: Pitch Free

Heave Response: Pitch Free

Pitch Response: Pitch Free

Surge Response: Pitch Side A Fixed

Heave Response: Pitch Side A Fixed

Pitch Response: Pitch Side A Fixed

Surge Response: Pitch Side B Fixed

Heave Response: Pitch Side B Fixed

Pitch Response: Pitch Side B Fixed

Figure D.7: Group 2D: Surge Heave Coupling Motions

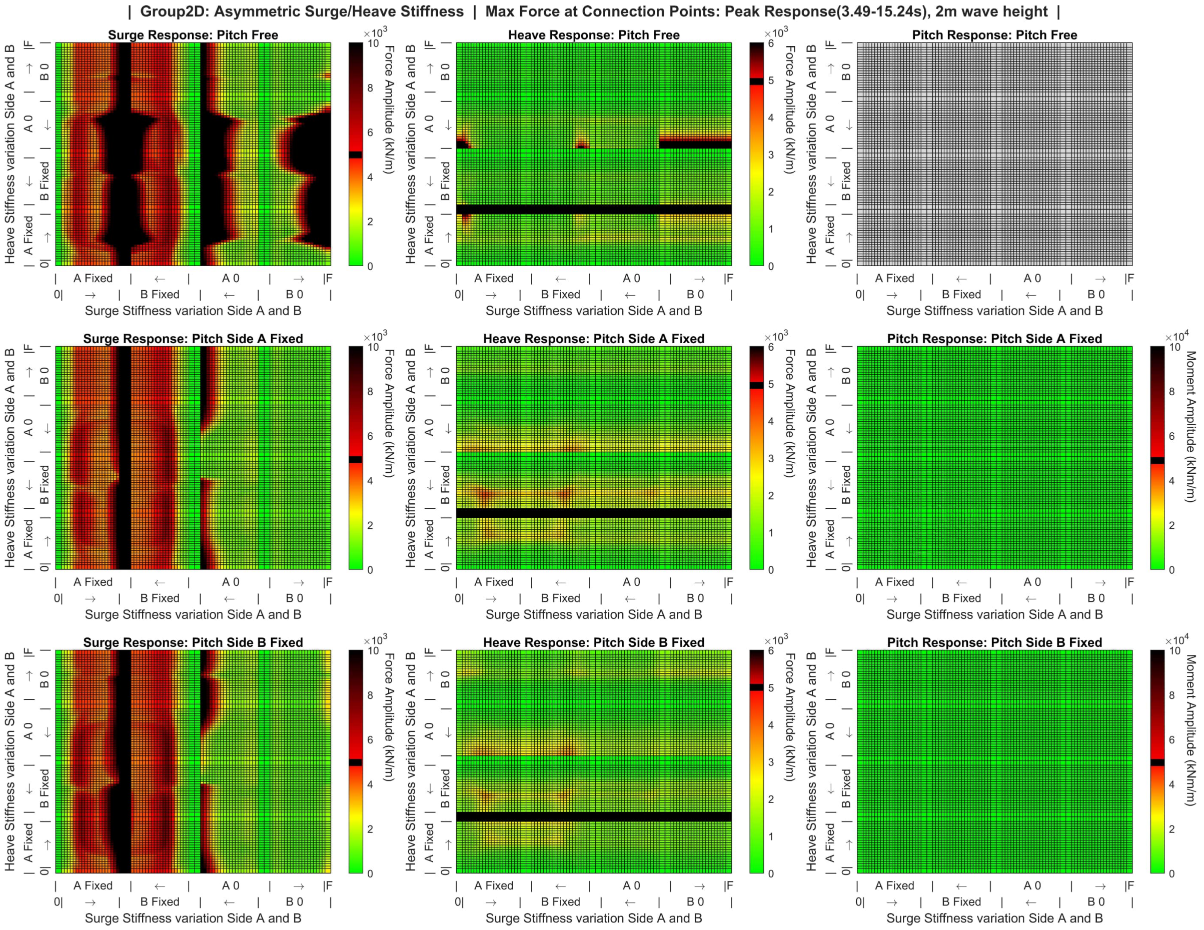

| Group2D: Asymmetric Surge/Heave Stiffness | Max Force at Connection Points: Peak Response(3.49-15.24s), 2m wave height |

Surge Response: Pitch Free

Heave Response: Pitch Free

Pitch Response: Pitch Free

Surge Response: Pitch Side A Fixed

Heave Response: Pitch Side A Fixed

Pitch Response: Pitch Side A Fixed

Surge Response: Pitch Side B Fixed

Heave Response: Pitch Side B Fixed

Pitch Response: Pitch Side B Fixed

Figure D.8: Group 2D: Surge Heave Coupling Force

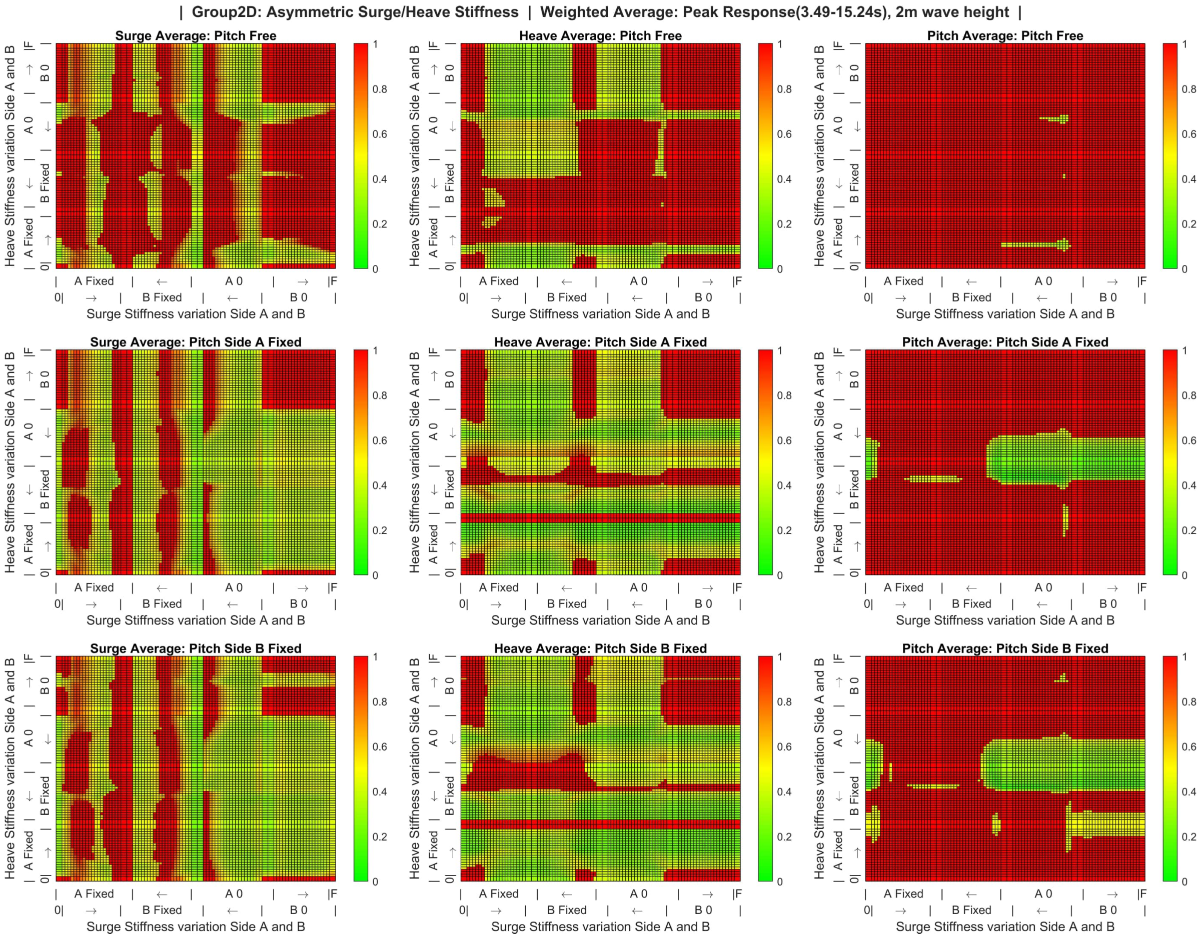

| Group2D: Asymmetric Surge/Heave Stiffness | Weighted Average: Peak Response(3.49-15.24s), 2m wave height |

Surge Average: Pitch Free

Heave Average: Pitch Free

Pitch Average: Pitch Free

Surge Average: Pitch Side A Fixed

Heave Average: Pitch Side A Fixed

Pitch Average: Pitch Side A Fixed

Surge Average: Pitch Side B Fixed

Heave Average: Pitch Side B Fixed

Pitch Average: Pitch Side B Fixed

Figure D.9: Group 2D: Surge Heave Coupling Weighted Average

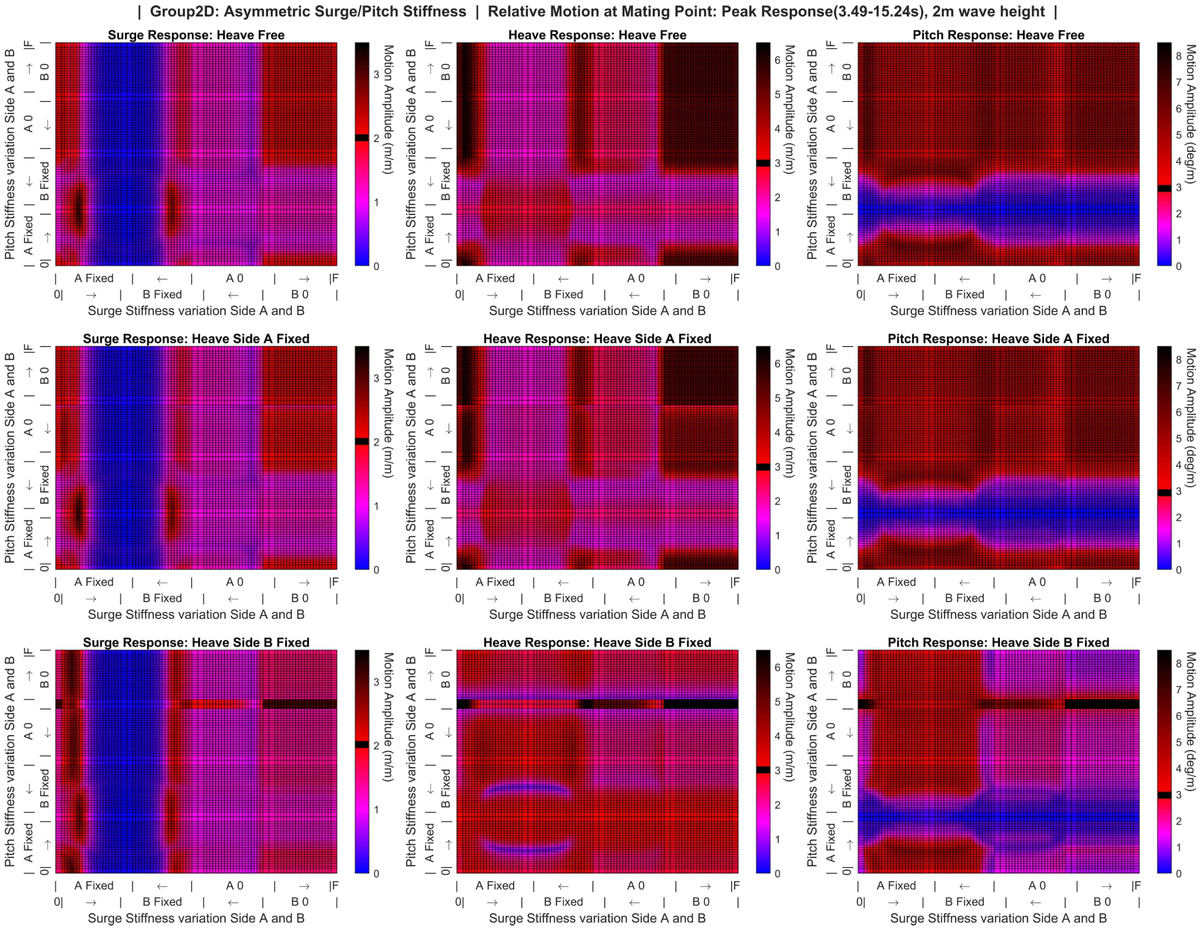

| Group2D: Asymmetric Surge/Pitch Stiffness | Relative Motion at Mating Point: Peak Response(3.49-15.24s), 2m wave height |

Surge Response: Heave Free

Heave Response: Heave Free

Pitch Response: Heave Free

Surge Response: Heave Side A Fixed

Heave Response: Heave Side A Fixed

Pitch Response: Heave Side A Fixed

Surge Response: Heave Side B Fixed

Heave Response: Heave Side B Fixed

Pitch Response: Heave Side B Fixed

Figure D.10: Group 2D: Surge Pitch Coupling Motions

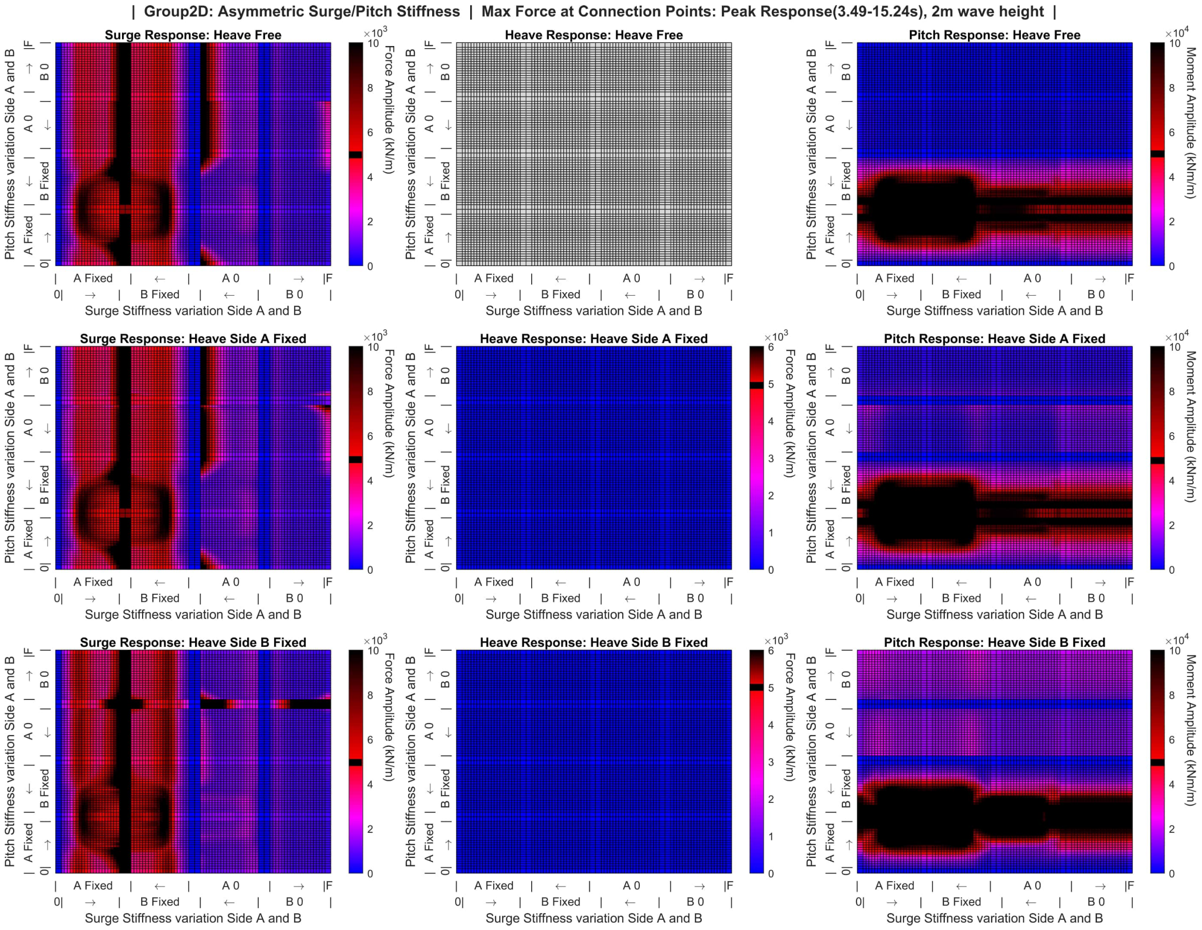

Figure D.11: Group 2D: Surge Pitch Coupling Force

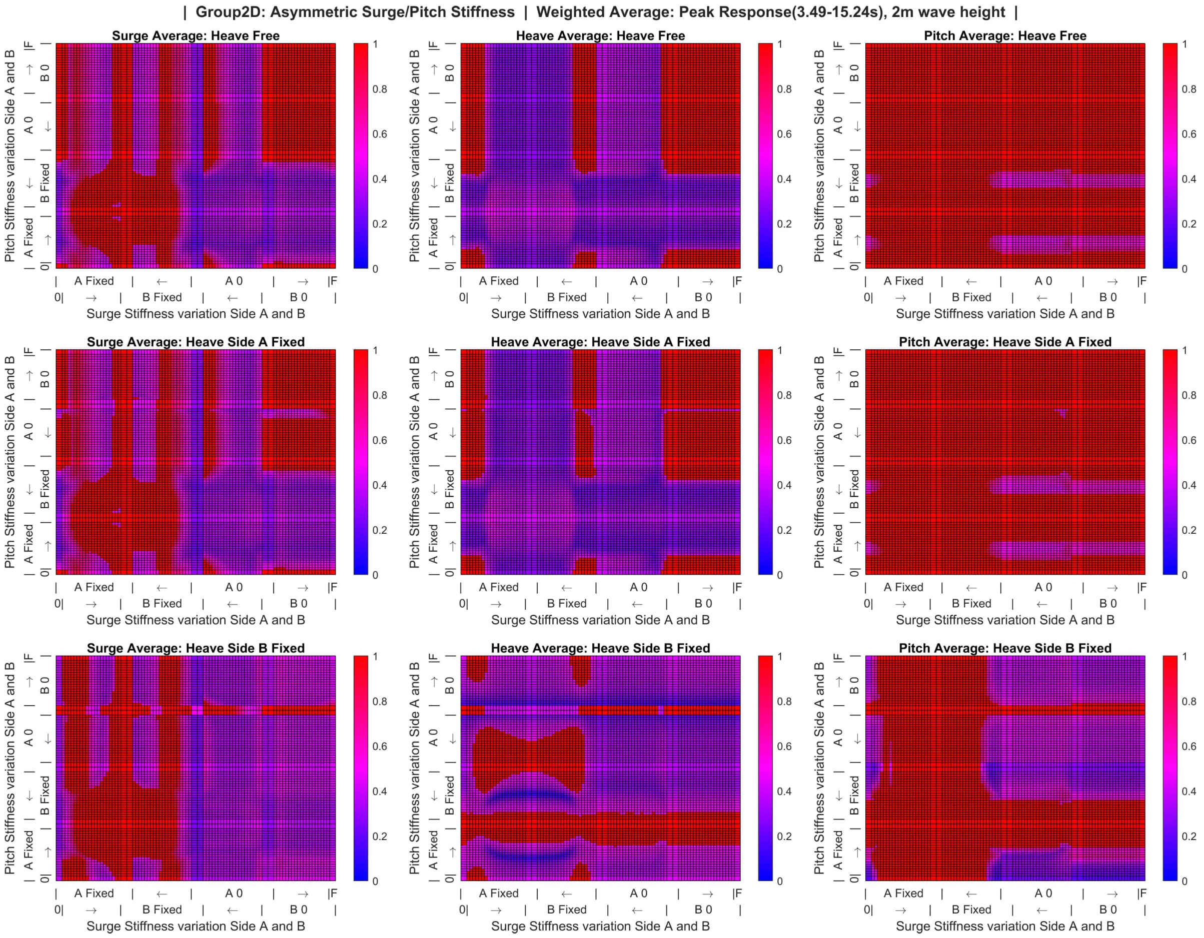
| Group2D: Asymmetric Surge/Pitch Stiffness | Weighted Average: Peak Response(3.49-15.24s), 2m wave height |

Surge Average: Heave Free

Heave Average: Heave Free

Pitch Average: Heave Free

Surge Average: Heave Side A Fixed

Heave Average: Heave Side A Fixed

Pitch Average: Heave Side A Fixed

Surge Average: Heave Side B Fixed

Heave Average: Heave Side B Fixed

Pitch Average: Heave Side B Fixed

Figure D.12: Group 2D: Surge Pitch Coupling Weighted Average

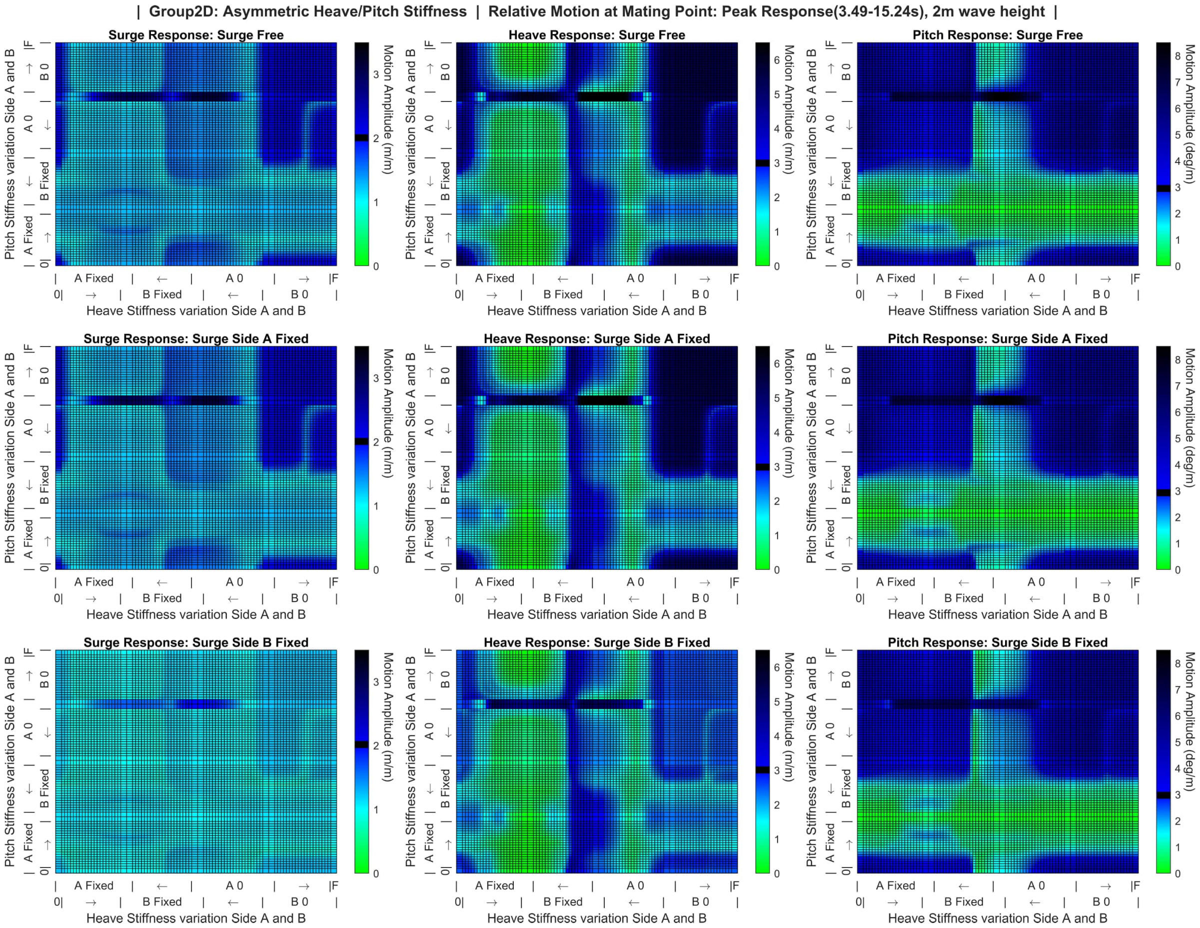

Figure D.13: Group 2D: Heave Pitch Coupling Motions

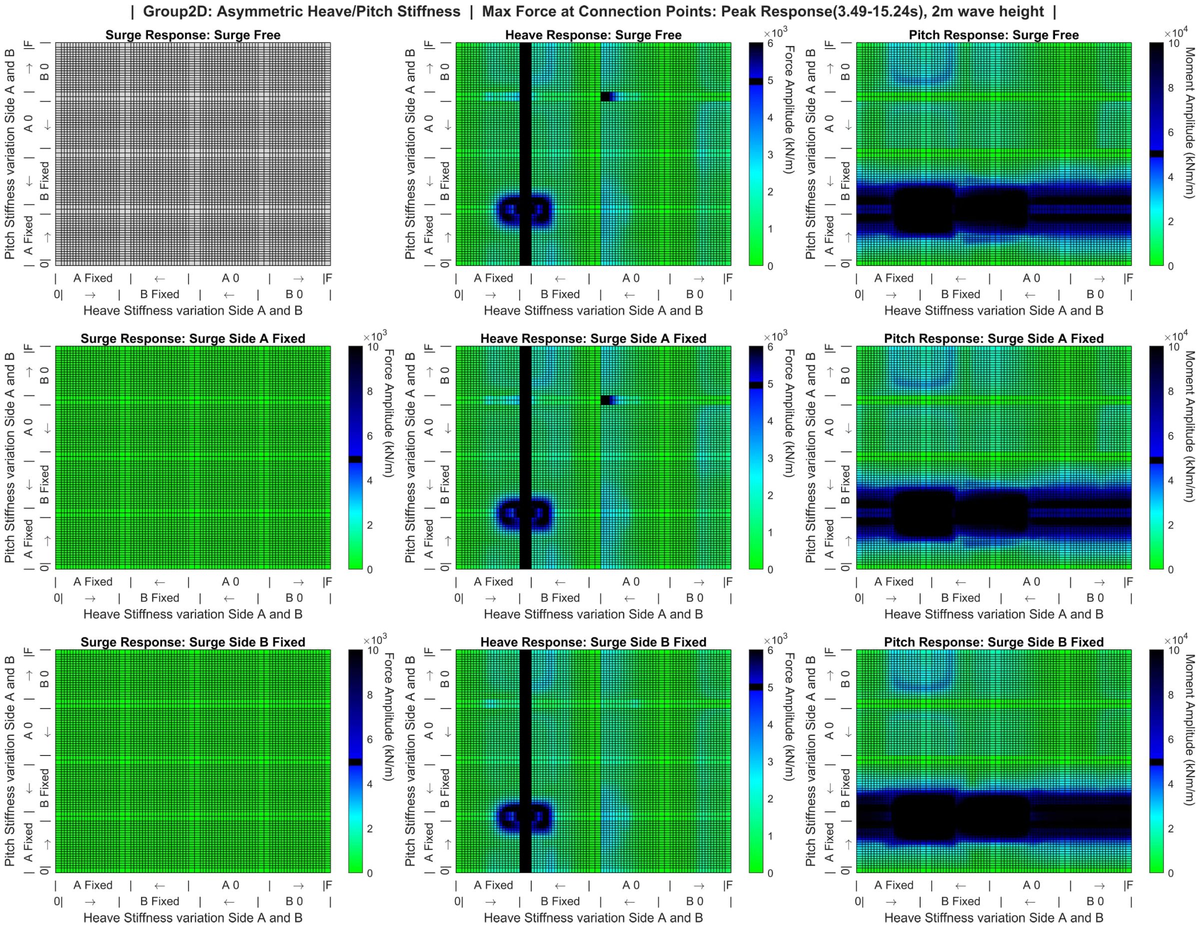

Figure D.14: Group 2D: Heave Pitch Coupling Force

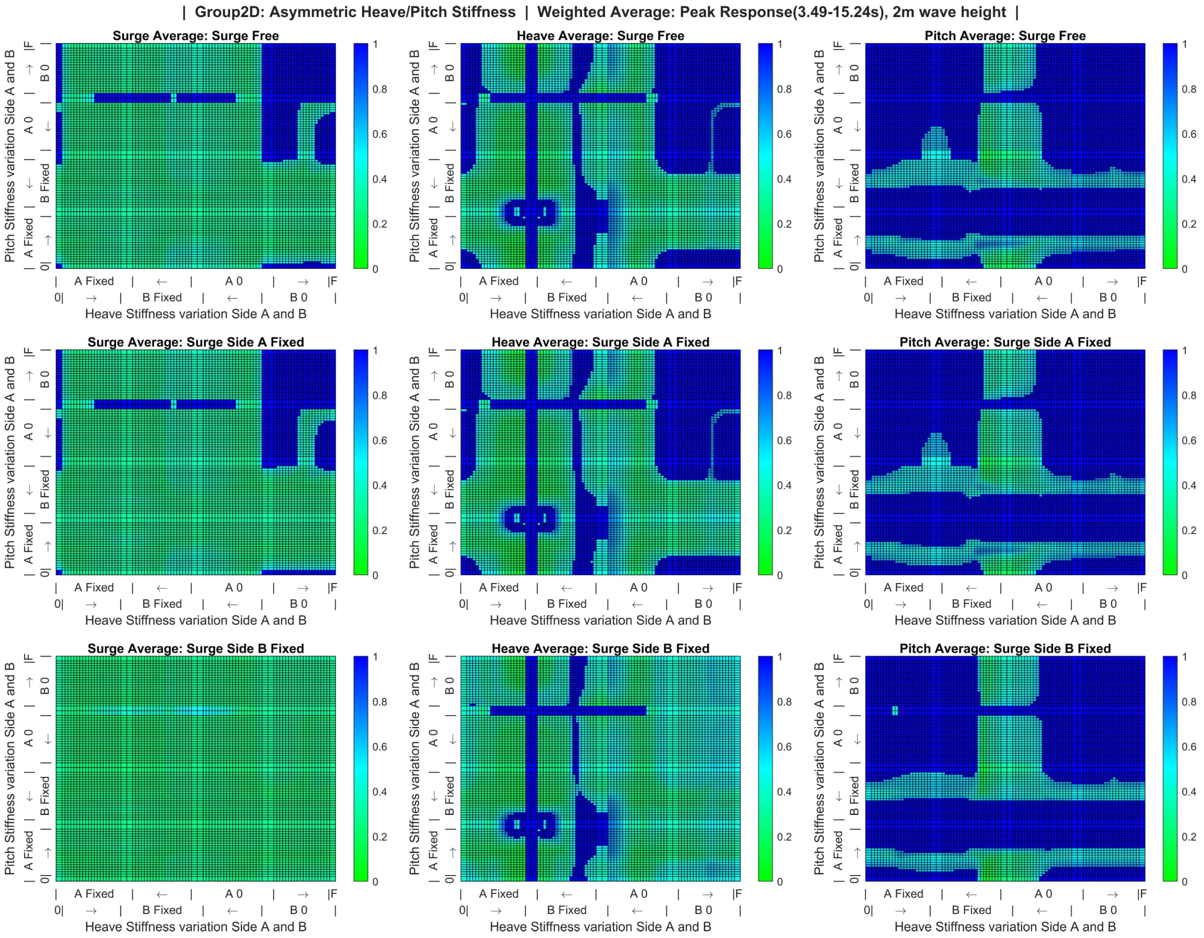

Figure D.15: Group 2D: Heave Pitch Coupling Weighted Average

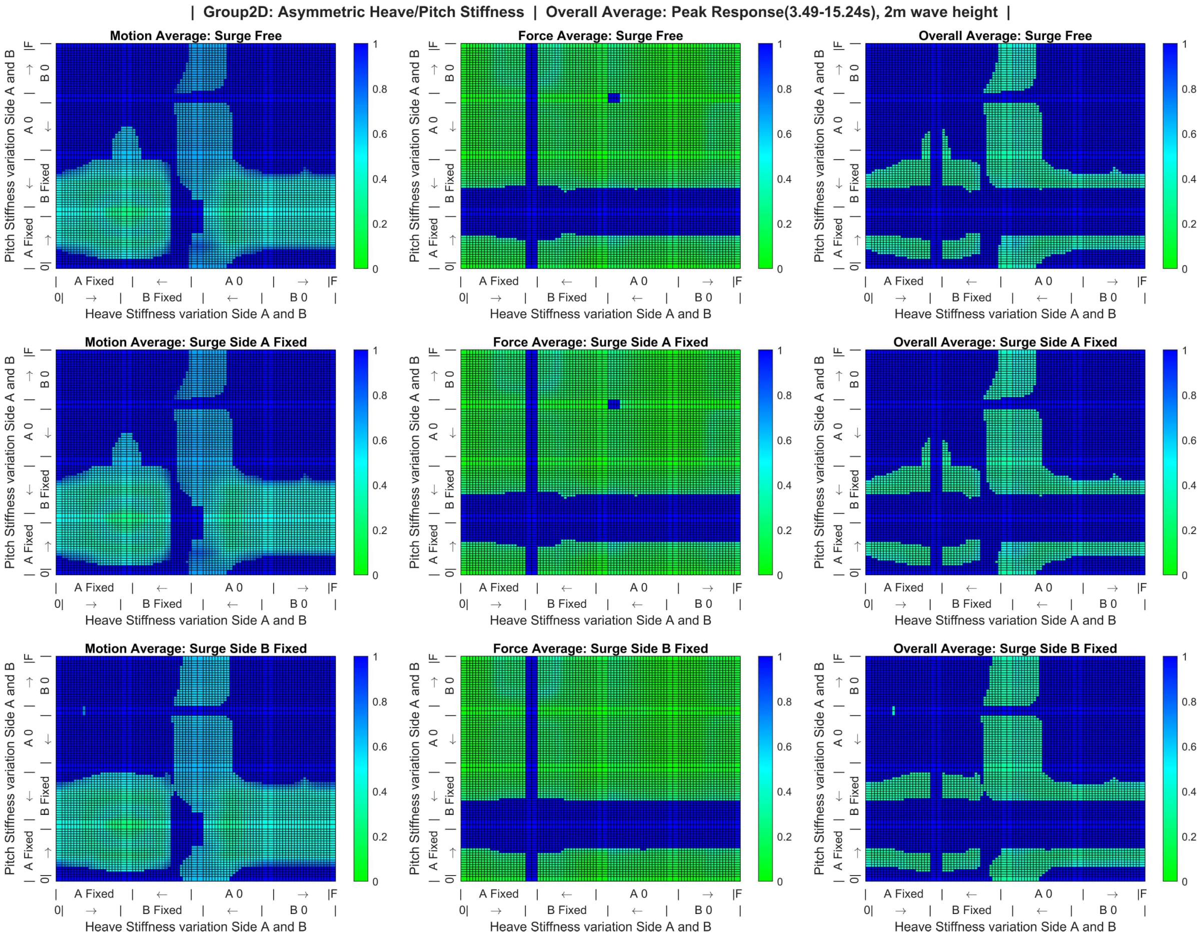

Figure D.16: Group 2D: Heave Pitch Coupling Overall Average

Bibliography

Acteon. Floating wind: What are the mooring options?, 2020. URL https://acteon.com/wp-content/uploads/2020/11/Floating-Assets-Render_1.jpg.

M. Borg and M. Collu. A comparison between the dynamics of horizontal and vertical axis offshore floating wind turbines. *Philosophical Transactions of the Royal Society A: Mathematical, Physical and Engineering Sciences*, 373, 2 2015. ISSN 1364503X. doi: 10.1098/rsta.2014.0076.

Jonathan Bosch, Iain Staffell, and Adam D. Hawkes. Temporally explicit and spatially resolved global offshore wind energy potentials. *Energy*, 163:766–781, 11 2018. ISSN 03605442. doi: 10.1016/j.energy.2018.08.153.

bp. *Statistical Review of World Energy 2021*, 2021. URL https://www.bp.com/content/dam/bp/business-sites/en/global/corporate/pdfs/energy-economics/statistical-review/bp-stats-review-2021-full-report.pdf.

Adrijana Buljan. Ge, glosten present 12 mw floating wind turbine concept, 2022. URL https://www.offshorewind.biz/2021/05/25/ge-glosten-present-12-mw-floating-wind-turbine-concept/.

BW Ideol. Bw ideol technology, 2022. URL https://www.bw-ideol.com/en/technology.

Young Myung Choi, Bo Woo Nam, and Sa Young Hong. Numerical modeling of load transfer unit of the float-over installation. *Proceedings of the Twenty-fourth (2014) International Ocean and Polar Engineering ConferenceBusan, Korea, June 15-20*, 2014.

A P Crowle and P R Thies. Installation innovation for floating offshore wind. *Maritime Innovation and Emerging Technologies Online Conference 2021, 17-18 March*, 2021. URL http://hdl.handle.net/10871/125194.

A. P. Crowle and P. R. Thies. Floating offshore wind turbines port requirements for construction. *Proceedings of the Institution of Mechanical Engineers Part M: Journal of Engineering for the Maritime Environment*, 2022. ISSN 20413084. doi: 10.1177/14750902221078425.

Alan Crowle and R. Thies Philipp. Port and shipyard requirements for the installation of floating wind turbines [conference presentation]. *RINA London Branch 21 Oct 2021, London, UK*, 2021. URL http://hdl.handle.net/10871/127588.

DNV. *Floating wind: The power to commercialize*, 12 2020. URL https://www.dnv.com/focus-areas/floating-offshore-wind/commercialize-floating-wind-report.html#:~:text=Floating%20Wind%3A%20The%20Power%20to%20Commercialize&text=DNV%20predicts%20that%20the%20installed,of%2040%20EUR%20per%20MWh.

DNV. *Energy Transition Outlook 2021: Main Report*, 2021. URL https://download.dnv.com/eto-2021-download?_ga=2.144924989.860795736.1652170803-500799932.1651569107#about.

DNV. *Floating offshore wind: The next five years*, 2022. URL https://www.dnv.com/focus-areas/floating-offshore-wind/floating-offshore-wind-the-next-five-years.html.

Adnan Durakovic. Ge haliade-x prototype completes second year in operation, 11 2021a. URL https://www.offshorewind.biz/2021/11/09/ge-haliade-x-prototype-completes-second-year-in-operation/.

Adnan Durakovic. World's largest, most powerful wind turbine stands complete, 11 2021b. URL https://www.offshorewind.biz/2021/11/12/worlds-largest-most-powerful-wind-turbine-stands-complete/#:~:text=With%20the%20final%20blade%20in,Port%20of%20Rotterdam%2C%20the%20Netherlands.

Luke Eatough. Floating offshore wind technology and operations review. *Catapult Offshore Renewable Energy*, 1 2021. URL https://f.hubspotusercontent20.net/hubfs/4351574/7523%20Catapult%20Report%20%E2%80%93%20FOW%20Technology%20and%20Operations%20Review%20%E2%80%93%2027.10.21.pdf?__hstc=&__hssc=&hsCtaTracking=17ada39c-b9e9-4278-98c7-440c74781190%7C9706834e-54fb-4332-802d-54dca6be0131.

Equinor. Hywind scotland remains the uk's best performing offshore wind farm, 2021. URL https://www.equinor.com/news/archive/20210323-hywind-scotland-uk-best-performing-offshore-wind-farm.

Equinor. Hywind scotland, 2022a. URL https://www.equinor.com/energy/hywind-scotland.

Equinor. First power from hywind tampen, 2022b. URL https://www.equinor.com/news/20221114-first-power-from-hywind-tampen.

European Environment Agency. *Electric vehicles and the energy sector - impacts on Europe's future emissions*, 9 2016. URL https://www.eea.europa.eu/publications/electric-vehicles-and-the-energy.

(Nexans) Frédéric Grizaud. Impact of the floating foundations on a standard offshore substation topside general arrangement [conference presentation]. *FOWT 2022, Montpellier*, 16-18 May 2022.

Tom Fulton, Yusuf Arikan, H Offshore, Regan Miller, and Jonathan Kent Longridge. Design and installation of leading edge, practical and economic mooring systems for commercial scale floating offshore wind energy. *Offshore Technology Conference held in Houston, TX, USA, 16 - 19 August 2021*, 8 2022. doi: https://doi-org.tudelft.idm.oclc.org/10.4043/31318-MS. URL http://onepetro.org/OTCONF/proceedings-pdf/21OTC/2-21OTC/D022S060R014/2525776/otc-31318-ms.pdf/1.

Evan Gaertner, Jennifer Rinker, Latha Sethuraman, Frederik Zahle, Benjamin Anderson, Garrett Barter, Nikhar Abbas, Fanzhong Meng, Pietro Bortolotti, Witold Skrzypinski, George Scott, Roland Feil, Henrik Bredmose, Katherine Dykes, Matt Shields, Christopher Allen, and Anthony Viselli. Definition of the iea 15-megawatt offshore reference wind. *National Renewable Energy Laboratory*, NREL/TP-5000-75698, 3 2020. URL https://www.nrel.gov/docs/fy20osti/75698.pdf.

Global Wind Energy Council. Global wind report 2022. *Global Wind Energy Council*, 4 2022.

Andrew J Goupee, Bonjun Koo, Kostas F Lambrakos, and Habib J Dagher. Experimental comparison of three floating wind turbine concepts. *31st International Conference on Ocean, Offshore and Arctic Engineering OMAE2012 Rio de Janeiro, Brazil June 10-15*, 2012. URL https://asmedigitalcollection-asme-org.tudelft.idm.oclc.org/offshoremechanics/article/136/2/020906/375202/Experimental-Comparison-of-Three-Floating-Wind.

Yaohua Guo, Haijun Wang, and Jijian Lian. Review of integrated installation technologies for offshore wind turbines: Current progress and future development trends. *Energy Conversion and Management*, 255:115319, 3 2022. ISSN 01968904. doi: 10.1016/j.enconman.2022.115319.

Kwangtae Ha, Hoai Vu Anh Truong, Tri Dung Dang, and Kyoung Kwan Ahn. Recent control technologies for floating offshore wind energy system: A review. *International Journal of Precision Engineering and Manufacturing - Green Technology*, 8:281–301, 1 2021. ISSN 21980810. doi: 10.1007/s40684-020-00269-5.

Y. J. Ha, B. W. Nam, S. Y. Hong, D. W. Jung, and H. J. Kim. Experimental and numerical study on mating operation of a topside module by a floating crane vessel in waves. *Ocean Engineering*, 154: 375–388, 2018. ISSN 00298018. doi: 10.1016/j.oceaneng.2018.01.074.

Lars Ivar Hatledal, Houxiang Zhang, Karl Henning Halse, and Hans Petter Hildre. Numerical study for a catamaran gripper-monopile mechanism of a novel offshore wind turbine assembly installation procedure. *Proceedings of the ASME 2017 36th International Conference on Ocean, Offshore and Arctic Engineering. Volume 9: Offshore Geotechnics; Torgeir Moan Honoring Symposium. Trondheim, Norway. June 25–30*, 2017. URL https://doi-org.tudelft.idm.oclc.org/10.1115/OMAE2017-62342.

Sunghun Hong, David Vagnes, Karl Henning Halse, and Torodd Skjerve Nord. Mechanical coupling effect on the horizontal response of floating offshore wind turbine installation using a catamaran with a low height lifting system. *Proceedings of the Thirty-first (2021) International Ocean and Polar Engineering Conference Rhodes, Greece, June 20 – 25*, 2021.

Sunghun Hong, Houxiang Zhang, Torodd Skjerve Nord, and Karl Henning Halse. Effect of fender system on the dynamic response of onsite installation of floating offshore wind turbines. *Ocean Engineering*, 259, 2022. ISSN 00298018. doi: 10.1016/j.oceaneng.2022.111830.

Huisman. Ulstein windlifter, 2022. URL https://www.huismanequipment.com/en/products/renewables/offshore_wind/windfarm-installation-vessel.

D. Jiang, K. H. Tan, C. M. Wang, and J. Dai. Research and development in connector systems for very large floating structures. *Ocean Engineering*, 232, 2021. ISSN 00298018. doi: 10.1016/j.oceaneng.2021.109150.

Zhiyu Jiang, Lin Li, Zhen Gao, Karl Henning Halse, and Peter Christian Sandvik. Dynamic response analysis of a catamaran installation vessel during the positioning of a wind turbine assembly onto a spar foundation. *Marine Structures*, 61:1–24, 9 2018a. ISSN 09518339. doi: 10.1016/j.marstruc.2018.04.010.

Zhiyu Jiang, Zhengru Ren, Zhen Gao, Peter Christian Sandvik, Karl Henning Halse, and Roger Skjetne. Mating control of a wind turbine tower-nacelle-rotor assembly for a catamaran installation vessel. *Proceedings of the Twenty-eighth (2018) International Ocean and Polar Engineering ConferenceSapporo, Japan, June 10-15*, 2018b. ISSN 1098-6189. URL https://ntnuopen.ntnu.no/ntnu-xmlui/handle/11250/2583101.

Zhiyu Jiang, Rune Yttervik, Zhen Gao, and Peter Christian Sandvik. Design, modelling, and analysis of a large floating dock for spar floating wind turbine installation. *Marine Structures*, 72, 7 2020. ISSN 09518339. doi: 10.1016/j.marstruc.2020.102781.

Jingzhe Jin, Zhiyu Jiang, Sigrid Ringdalen Vatne, Zhengru Ren, Yuna Zhao, and Zhen Gao. Installation of pre-assembled offshore wind turbines using a catamaran vessel and an active gripper motion control method. *GRAND RENEWABLE ENERGY 2018 Proceedings June 17 (Sun) - 22(Fri), Pacifico Yokohama, Yokohama, Japan*, 2018. doi: 10.24752/gre.1.0_156. URL https://www.jstage.jst.go.jp/article/gre/1/0/1_156/_article.

(London Marine Consultants (LMC)) Jon Dunstan. ”plug and play” mooring and power cable connection and disconnection buoy system [conference presentation]. *FOWT 2022, Montpellier*, 16-18 May 2022.

J. M. Jonkman and D. Matha. Dynamics of offshore floating wind turbines-analysis of three concepts. *Wind Energy*, 14:557–569, 5 2011. ISSN 10954244. doi: 10.1002/we.442.

S.J. Jung, H.U. Kwak, S.H. Oh, Y.J. Kwon, B.W. Nam, N.W. Kim, Kangsu Lee, and H.G. Sung. Mating analysis for float-over installation of a large topside in various load transfer stages. *Proceedings of the Twenty-eighth (2018) International Ocean and Polar Engineering Conference Sapporo, Japan, June 10-15*, 2018.

Georgios Katsouris and Andrew Marina. Cost modelling of floating wind farms. *ECN*, 2016.

Rakesh Kumar, Kaamran Raahemifar, and Alan S. Fung. A critical review of vertical axis wind turbines for urban applications. *Renewable and Sustainable Energy Reviews*, 89:281–291, 6 2018. ISSN 1364-0321. doi: 10.1016/J.RSER.2018.03.033.

Roberto Lacal-Arántegui, José M. Yusta, and José Antonio Domínguez-Navarro. Offshore wind installation: Analysing the evidence behind improvements in installation time. *Renewable and Sustainable Energy Reviews*, 92:133–145, 9 2018. ISSN 18790690. doi: 10.1016/j.rser.2018.04.044.

Trond Landbo. Floating wind will be cheaper than bottom-fixed: wait and see. *Quest Floating Wind Energy*, 11 2017. URL https://questfwe.com/wp-content/uploads/2018/02/Floating-wind-will-be-cheaper-than-bottom-fixed-wait-and-see-Recharge.pdf.

Binbin Li, Kun Liu, Gongwei Yan, and Jinping Ou. Hydrodynamic comparison of a semi-submersible, tlp, and spar: Numerical study in the south china sea environment. *Journal of Marine Science and Application*, 10:306–314, 9 2011. ISSN 16719433. doi: 10.1007/s11804-011-1073-2.

Ting Liu, Karl H. Halse, Bernt J. Leira, and Zhiyu Jiang. Comparative study of the mating process for a spar-type floating wind turbine using two alternative installation vessels. *Applied Ocean Research*, 132:103452, 3 2023. ISSN 01411187. doi: 10.1016/j.apor.2022.103452.

Ye Lu, Qijia Shi, Yuchao Chen, Wenhui Zheng, and Ye Zhou. Response suppression of multiple hinged floating structures by using rubber cushion. *Shock and Vibration*, 2021, 2021. ISSN 10709622. doi: 10.1155/2021/1208336.

Denis Matha, Christopher Brons-Illig, Alexander Mitzlaff, and Ron Scheffler. Fabrication and installation constraints for floating wind and implications on current infrastructure and design. *Energy Procedia*, 137:299–306, 2017. ISSN 18766102. doi: 10.1016/j.egypro.2017.10.354.

Anders Myhr, Catho Bjerkseter, Anders Ågotnes, and Tor A. Nygaard. Levelised cost of energy for offshore floating wind turbines in a lifecycle perspective. *Renewable Energy*, 66:714–728, 2014. ISSN 09601481. doi: 10.1016/j.renene.2014.01.017.

Ocean Energy Resources. Cutting mooring costs for floating wind significantly, 2022. URL https://ocean-energyresources.com/2022/02/15/cutting-mooring-costs-for-floating-wind-significantly/.

offshoreWIND.biz. French floating wind project lags behind, 2014. URL https://www.offshorewind.biz/2014/02/06/french-floating-wind-project-lags-behind/.

offshoreWIND.biz, Jan Arne Wold, and Equinor. First turbines assembled for hywind tampen floating offshore wind farm, 2022. URL https://cdn.offshorewind.biz/wp-content/uploads/sites/2/2022/05/23124003/Hywind-Tampen-Turbine-Assembly.png.

Orsted. *Making green energy affordable*, 6 2019. URL https://orsted.com/-/media/WWW/Docs/Corp/COM/explore/Making-green-energy-affordable-June-2019.pdf.

Principle Power. The first floating wind farm in continental europe is now fully operational, digital image, 7 2020. URL https://www.principlepower.com/news/the-first-floating-wind-farm-in-continental-europe-is-now-fully-operational.

Principle Power. The windfloat advantage: Performance, 2022a. URL https://www.principlepower.com/windfloat/advantage/performance.

Principle Power. Kincardine offshore wind farm, 2022b. URL https://www.principlepower.com/projects/kincardine-offshore-wind-farm.

Principle Power. Windfloat atlantic, 2022c. URL https://www.principlepower.com/projects/windfloat-atlantic.

Principle Power. The windfloat advantage: Performance, 2022d. URL https://www.principlepower.com/_next/image?url=https%3A%2F%2Fimages.prismic.io%2Fprinciplepower%2F934556a7-052b-4a9c-b929-5aa8756738f4_windfloat_advantage_performance_turbine_agnostic.jpg%3Fauto%3Dcompress%2Cformat&w=2048&q=75.

Rahul Chitteth Ramachandran, Cian Desmond, Frances Judge, Jorrit-Jan Serraris, and Jimmy Murphy. Floating wind turbines: marine operations challenges and opportunities. *Wind Energy Science*, 7:903–924, 4 2022. ISSN 2366-7451. doi: 10.5194/wes-7-903-2022. URL https://wes.copernicus.org/articles/7/903/2022/.

Lizet Ramirez, Mattia Cecchinato, and Sabina Potestio. Ports: a key enabler for the floating offshore wind sector. *WindEurope*, 9 2020. URL https://windeurope.org/intelligence-platform/product/ports-a-key-enabler-for-the-floating-offshore-wind-sector/.

(Nautilus Floating Solutions) Raúl Rodríguez. Designing semi-submersible floater for floating offshore substation (foss) [conference presentation]. *FOWT 2022, Montpellier*, 16-18 May 2022.

H. R. Riggs and R. C. Ertekin. Approximate methods for dynamic response of multi-module floating structures. *Marine Structures*, 6, 1993. ISSN 09518339. doi: 10.1016/0951-8339(93)90016-V.

Silvio Rodrigues, Carlos Restrepo, George Katsouris, Rodrigo Teixeira Pinto, Maryam Soleimanzadeh, Peter Bosman, and Pavol Bauer. A multi-objective optimization framework for offshorewind farm layouts and electric infrastructures. *Energies*, 9, 3 2016. ISSN 19961073. doi: 10.3390/en9030216.

Jan Rosenow. Electrification: Using more to emit less. *EnergyMonitor*, 7 2021. URL https://www.energymonitor.ai/tech/electrification/electrification-using-more-to-emit-less.

Tom Salic, Jean Frédéric Charpentier, Mohamed Benbouzid, and Marc Le Boulluec. Control strategies for floating offshore wind turbine: Challenges and trends. *Electronics (Switzerland)*, 8, 10 2019. ISSN 20799292. doi: 10.3390/electronics8101185.

J A Schneider and M Senders. Foundation design-a comparison of oil and gas platforms with offshore wind turbines. *Journal of the Marine Technology Society*, 44:32–51, 2010.

SENSEWind. Engineering to reduce the cost of wind energy, 2022. URL https://sensewind.com/.

SFI MOVE. *SFI MOVE Annual Report 2021*, 3 2021. URL https://www.ntnu.edu/documents/1266972546/1312147025/SFI_MOVE_%C3%85rsrapport_2021_30.03+%28002%29.pdf/ee81960c-5399-3257-eda5-8b2fac16fade?t=1648815540862.

Q. J. Shi, D. L. Xu, H. C. Zhang, H. Zhao, and Y. S. Wu. Optimized stiffness combination of a flexible-base hinged connector for very large floating structures. *Marine Structures*, 60:151–164, 2018. ISSN 09518339. doi: 10.1016/j.marstruc.2018.03.014.

Sergio Sánchez, José Santos López-Gutiérrez, Vicente Negro, and M. Dolores Esteban. Foundations in offshore wind farms: Evolution, characteristics and range of use. analysis of main dimensional parameters in monopile foundations. *Journal of Marine Science and Engineering*, 7, 12 2019. ISSN 20771312. doi: 10.3390/JMSE7120441.

K. P. Thiagarajan and H. J. Dagher. A review of floating platform concepts for offshore wind energy generation. *Journal of Offshore Mechanics and Arctic Engineering*, 136, 3 2014. ISSN 1528896X. doi: 10.1115/1.4026607.

United Nations Climate Change. Updated climate commitments ahead of cop26 summit fall short, but net-zero pledges provide hope, 10 2021. URL https://unfccc.int/news/updated-climate-commitments-ahead-of-cop26-summit-fall-far-short-but-net-zero-pledges

United Nations Environment Programme. *Emissions Gap Report 2021*, 10 2021. URL https://www.unep.org/resources/emissions-gap-report-2021.

Vattenfall. Vattenfall bouwt windpark hollandse kust zuid, 2022. URL https://vattenfall-hollandsekust.nl/.

Wei Wang and Yong Bai. Investigation on installation of offshore wind turbines. *Journal of Marine Science and Application*, 9:175–180, 2010. ISSN 16719433. doi: 10.1007/s11804-010-9076-y.

Windcrete. Windcrete concrete floating platform for wind turbines., 2022. URL https://www.windcrete.com/.

World Forum Offshore Wind. *Offshore Wind Energy Report 2021*, 2 2022. URL https://wfo-global.org/?jet_download=4814.

Huai Zhao, Daolin Xu, Haicheng Zhang, Shuyan Xia, Qijia Shi, Rui Ding, and Yousheng Wu. An optimization method for stiffness configuration of flexible connectors for multi-modular floating systems. *Ocean Engineering*, 181:134–144, 2019. ISSN 00298018. doi: 10.1016/j.oceaneng.2019.03.039.

Øyvind Gravås. The hywind scotland floating wind farm, digital image, 10 2017. URL https://www.equinor.com/news/archive/worlds-first-floating-wind-farm-started-production.